Dissertation zur Erlangung des Doktorgrades

Measurement of Higgs boson production via gluon fusion and vector-boson fusion in the $H \to WW^*$ decay mode with the ATLAS experiment at the LHC at $\sqrt{s} = 13$ TeV

Ralf Gugel

Fakultät für Mathematik und Physik
Albert-Ludwigs-Universität Freiburg

Measurement of Higgs boson production via gluon fusion and vector-boson fusion in the $H \to WW^*$ decay mode with the ATLAS experiment at the LHC at $\sqrt{s} = 13$ TeV

Dissertation zur Erlangung des Doktorgrades

vorgelegt von

Ralf Gugel

Prof. Dr. Karl Jakobs, Dr. Christian Weiser

Fakultät für Mathematik und Physik

der

Albert-Ludwigs-Universität

Freiburg im Breisgau

30.09.2019

Dekan:	Prof. Dr. Michael Thoss
Betreuer:	Prof. Dr. Karl Jakobs, Dr. Christian Weiser
1. Gutachter:	Dr. Christian Weiser
2. Gutachter:	Prof. Dr. Beate Heinemann
Verkündung des Prüfungsergebnisses:	12.12.2019
1. Prüfer:	Prof. Dr. Gregor Herten
2. Prüfer:	Dr. Christian Weiser
3. Prüfer:	Prof. Dr. Stefan Dittmaier

"I can live with doubt and uncertainty and not knowing. I think it's much more interesting to live not knowing than to have answers that might be wrong."

– Richard P. Feynman

Abstract

On the 4th of July 2012 the observation of a new neutral particle was announced by the ATLAS [1] and CMS [2] Collaborations. This particle is by now generally considered as the Higgs boson H predicted [3,4] in the Standard Model of particle physics. Its mass of $m_H = 125.09 \pm 0.24\,\mathrm{GeV}$ [5] implies a rich set of final states which allow for experimental studies in regards to this particle and searches for deviations from the properties predicted by the Standard Model.

In this thesis a measurement of the gluon-fusion and vector-boson fusion production cross sections times $H \to WW^*$ branching ratio is presented using final states with one electron and one muon. The measurement is based on proton-proton collisions with an integrated luminosity of $36.1\,\mathrm{fb}^{-1}$ recorded with the ATLAS detector at the CERN Large Hadron Collider (LHC) at $\sqrt{s} = 13\,\mathrm{TeV}$ in 2015 and 2016. Signal-like events are selected in categories with different jet multiplicities. The results are extracted by means of a binned maximum-likelihood fit. To this end, either distributions in multiple discriminant variables or the response of a multivariate classifier are used depending on the category. The results are found to be well compatible with the Standard Model predictions.

This analysis is extrapolated to estimate the future precision of such a measurement at the end of the High-Luminosity LHC programme [6]. This extrapolated analysis is combined with analogously extrapolated analyses targeting other production and decay modes of the Higgs boson. Based on this combination the expected precision is determined for future measurements of couplings between the Higgs boson and other particles. Thereby an estimation is given for the anticipated sensitivity of these analyses to signs of physics beyond the Standard Model.

In addition studies are presented to identify sources of electron charge misidentification in the reconstruction algorithms employed in the ATLAS Collaboration.

Zusammenfassung

Am 4. Juli 2012 wurde die Beobachtung eines neuen, neutralen Teilchens von den ATLAS [1] und CMS [2] Kollaborationen bekannt gegeben. Dieses Teilchen wird heute als das Higgs-Boson H angesehen, dessen Existenz im Standardmodel der Teilchenphysik vorhergesagt wird [3,4]. Seine Masse von $m_H = 125.09 \pm 0.24$ GeV [5] impliziert eine große Anzahl von Endzuständen in welchen dieses Teilchen experimentell untersucht werden kann.

In der vorliegenden Dissertation wird eine Messung des Produkts der Produktionwirkungsquerschnitte des Higgs-Bosons in Gluonfusion und Vektorbosonfusion, und des $H \to WW^*$ Verzweigungsverhältnisses dargestellt. Die hierfür betrachteten Endzustände beinhalten ein Elektron und ein Myon. Die Messung basiert auf Proton-Proton-Kollisionen bei $\sqrt{s} = 13$ TeV mit einer integrierten Luminosität von 36.1 fb^{-1}, welche durch den ATLAS Detektor am CERN *Large Hadron Collider* (LHC) in den Jahren 2015 und 2016 aufgezeichnet wurden. Signalartige Ereignise werden in Kategorien mit verschiedenen Jetmultiplizitäten selektiert. Die Extraktion der Ergebnise erfolgt mittels einer gebinnten Maximum-Likelihood-Anpassung. Hierbei werden je nach Jetmultiplizität Verteilungen in entweder mehreren diskriminierenden Variablen oder eines multivariaten Klassifizierungsalgorithmus verwendet. Die Ergebnisse zeigen gute Kompatibilität mit den Vorhersagen des Standardmodels.

Mittels einer Extrapolation dieser Analyse wird die zukünftige Präzision abgeschätzt, die am Ende des *High-Luminosity* LHC-Projekts [6] mit einem erwarteten Datensatz von 3000 fb^{-1} erreicht werden kann. Diese extrapolierte Analyse wird mit weiteren extrapolierten Analysen anderer Produktions- und Zerfallskanäle kombiniert. Basierend auf dieser Kombination wird die erwartete Präzision der Messung der Kopplung des Higgs-Bosons mit anderen Teilchen bestimmt. Hierdurch wird auch die erwartete Sensitivität auf Physik jenseits des Standardmodels abgeschätzt.

Des Weiteren werden Studien vorgestellt, in welchen Ursachen fü Ladungsfehlidentifikation von Elektronen in den Rekonstruktionsalgorithmen der ATLAS Kollaboration untersucht werden. Aufbauend auf diesen Studien werden potentielle Verbesserungen kurz erläutert.

Preface

The latest addition to the set of experimentally discovered elementary particles of the Standard Model (SM) of particle physics was announced on July 4$^{\text{th}}$, 2012 by the ATLAS [1] and CMS [2] Collaborations: a neutral resonance with a mass of about 125 GeV consistent with the SM Higgs Boson. In the few years since this discovery many improved and extended measurements related to this resonance have been performed without a clear sign of a deviation from the SM prediction. Yet it remains one of the most promising candidates for finding hints of potential physics beyond the SM. With the Large Hadron Collider (LHC) program (and its high luminosity extension HL-LHC) having delivered only a fraction of the total expected dataset, the ultimate precision for measurements in this sector is yet to be reached - a journey requiring efforts of many.

In this thesis steps in this journey are presented which I had the great opportunity to contribute to as part of the ATLAS Collaboration.

Acknowledgements

While a thesis such as this one is formally the work of an individual the science presented in it is directly or indirectly influenced by several people. Overall sincere gratitude shall be expressed for the work of the various groups in the ATLAS Collaboration without which most aspects presented here would have been impossible to study in the time available. In particular the very fruitful and constructive collaboration with the ATLAS HWW, Higgs Prospects and Combination, and e/γ groups is greatly appreciated. Within these groups there are several people additionally deserving to be mentioned explicitly.

Prof. Karl Jakobs and Dr. Christian Weiser as group leaders hosting and supervising this thesis.

PD Karsten Köneke for his supervision, support and expertise in concerns of physics as well as many technical aspects.

Dr. Benedict Winter for stimulating discussions on various topics.

The CAF Team including Dr. Carsten Burgard, Frank Sauberburger, David Shope, and others for their enthusiasm and creativity to find and implement helpful technical solutions greatly benefiting the here presented $H \to WW^*$ analysis and several others.

Dr. Carsten Burgard additionally for his expertise in regards to various technical oddities of statistics tools.

Dr. Kathrin Becker for her expertise and helpful discussions in regards to theoretical modeling uncertainties.

Dr. Christos Anastopoulos and Dr. Philip Sommer
for their help and discussions in regards to electron reconstruction and identification.

Freiburg BFG The team behind the Freiburg ATLAS computing infrastructure (*Black Forest Grid*) for providing countless CPU hours and prompt support in case of technical issues cruical for many of the studies presented in this thesis.

Finally the efforts leading up to this thesis were hugely supported over many years by my parents, Ursula and Werner Gugel, who cannot be thanked enough for this.

Table of Contents

1 Introduction

Fundamental research is frequently questioned for its necessity and answers from first principles are often inherently challenging: the unknown would not deserve its name if the outcome of its exploration was trivially predictable. A more pragmatic approach to these questions is of empirical nature. Einstein's theory of general relativity [7] is inevitable for the accuracy of satellite based localization and navigation. Quantum mechanics is of ever increasing importance in modern technology: structure sizes in integrated circuits are approaching sizes of a few atoms. The discovery of the Giant Magnetoresistance effect was awarded the 2007 Nobel Price in physics [8] and is vital for the capacity of magnetic data storage devices. At the time the underlying theories were developed their eventual area of application, let alone their particular use could hardly be dreamt of.

Other benefits from fundamental research may be loosely summarized as spin-offs. Extensive experience with particle accelerators allowed for advances in cancer therapy such as Ref. [9]. The famous proposal [10] of Timothy Berners-Lee at the European Organization for Nuclear Research (CERN) emerged from the need to efficiently provide and exchange information amongst scientists. Today the *web* may be considered as one of the most important economic factors world wide. While advancing the frontier of human knowledge, large scale fundamental research and research centers such as CERN also inherently provide benefits outside the scientific and technological realms. The research of the most fundamental aspects of the universe joins people from all across the world in a common endeavor. The thereby emerging international collaborations greatly benefit cultural exchange and mutual understanding.

The first concept of fundamental constituents of matter is often attributed to the Greek philosopher Democritus coining the term "ατομος" (*atomos*), meaning uncut, indivisible. Objects denoted by the modern term *atom* derived from this are by now well known not to be indivisible. The concept of indivisible instances, however, is still valid although names other than *atom* are employed for what are today considered to be *elementary particles*.

Crucial aspects of our current understanding of the universe at its smallest scales have already been developed in the early 20$^{\text{th}}$ century. Max Planck's work regarding black body radiation [11] and Einstein's description of the photoelectric effect [12] started the development of quantum mechanics. The 1918, and 1921 Nobel Prizes were therefore awarded to Max Planck [13], and Albert Einstein [14] respectively. An insight from these works is that probing small length scales implies large quantities of energy. A description of the smallest length scales therefore also needs to incorporate Einstein's theory of special relativity [15]. The mathematical framework combining the principles from both, quantum mechanics and special relativity, is referred to as *quantum field theory* (QFT).

The interplay of theoretical descriptions and predictions on one side and experimental observations at often increasingly high energies on the other side has since lead to the development of a QFT that is today called the *Standard Model of particle physics* (SM). It describes a vast set of phenomena often expressed in terms of the *strong*, *electromagnetic*, and *weak* forces. On for elementary particle physics almost macroscopic scales these are responsible, for example, for the bound structure of protons, neutrons, and nuclei (strong), as well as atoms and molecules (electromagnetic). The weak force is responsible for the nuclear β-decay.

The first description of the β-decay by Enrico Fermi [16] in 1934 is today known to be a low energy approximation of a more general description of the interaction. With the unification into an electroweak theory pioneered by Glashow [17], Salam [18] and Weinberg [19] in the 1960s, the β-decay can be described as the emission of a charged vector boson $W^{\pm}$. The newly predicted weak neutral current [20] was first observed in 1973. The corresponding Z boson [21, 22] and the charged $W^{\pm}$ bosons [23] were finally discovered in 1983 at CERN. The development of the electroweak theory and the discovery of the W and Z bosons were honored by the Nobel Prices in 1979 [24] and 1984 [25] respectively.

Unifying the electroweak interactions in a consistent theory required another crucial ingredient: a mechanism breaking the original symmetry associated with the electroweak interaction and thereby allowing for the W and Z bosons to be massive. This *Brout-Englert-Higgs* (BEH) *mechanism* was developed by François Englert, Robert Brout [26], and Peter Higgs [3, 4] as well as Gerald Guralnik, Carl Hagen, and Tom Kibble [27] and Philip Anderson [28]. Peter Higgs explicitly pointed out that this mechanism implies the existence of another, massive boson: the Higgs boson. The experimental confirmation of this prediction required the construction of the largest and most powerful particle accelerator to date, the *Large Hadron Collider* (LHC) situated at CERN in a circular tunnel of about 27 km circumference. Almost five decades after the prediction of the Higgs boson the ATLAS [1] and CMS [2] Collaborations announced on July 4$^{\text{th}}$ 2012 the observation of a new particle with mass $m \approx 125\,\text{GeV}$. After further investigations its properties were found to be in agreement with those expected for the predicted Higgs boson. Following the discovery, Higgs and Englert received the 2013 Nobel Price in physics [29].

In the few years since its discovery the Higgs boson has already been studied in great detail by the ATLAS and CMS experiments. Today all major production and decay mechanisms of the Higgs boson H at the LHC have been observed. The latest additions to this set of observed processes are the production together with a pair of top quarks, $t\bar{t}H$ [30, 31], an additional vector boson, VH [32], and the decay to a pair of bottom quarks $H \to b\bar{b}$ [32, 33]. Still large efforts are ongoing to put the Higgs boson to even more stringent tests. Deviations from the predictions are implicative of new physics for which experimental guidance is highly sought after.

While the discovery of the Higgs boson is said to complete the Standard Model, the model is known to have imperfections. Neutrinos are treated as massless particles in contradiction to experimental evidence [34]. The rotation of galaxies suggests the presence of *dark matter* [35] which hardly interacts with known force carriers and constituents of matter. While the Standard Model describes all known forces relevant at microscopic scales it does not account for gravity: while it is consistent with the theory of special relativity it does not incorporate effects of general relativity [7]. The quest to address these open questions and advance our understanding of the universe involves thousands of physicists around the world. The pursuit of ever more precise measurements in the context of the Higgs boson represents one of the many aspects which may shed additional light on some of these matters.

In this thesis contributions to this endeavor are documented with focus on measurements in the $H \to WW^*$ decay channel. Amongst the different decay modes of the Higgs boson the most precise ATLAS measurement based on the first data taking campaign at the LHC was obtained in the $H \to WW^*$ channel [36]. Also with the second data taking campaign this channel provides excellent opportunities despite various challenges connected with it. In this thesis a measurement of the Higgs-boson production cross sections times $H \to WW^*$ branching ratios in the gluon fusion and vector-boson fusion production modes is documented. The results are the most precise measurements of these quantities at the time of their first publication. The measured production modes are the two most common Higgs-boson production modes and the results are extracted from a large number of candidate events. To this end a complex maximum-likelihood fit is discussed by means of which the results are extracted.

The scattering of two same-charge $W^{\pm}$ bosons is closely related to the $H \to WW^*$ process. Measurements of this process involve an experimental challenge in terms of accurate charge reconstruction of leptons emerging from the decays of the W bosons. Cases of charge misreconstruction represent sources of significant uncertainties for these measurements. In this thesis reasons for charge misidentification of electrons and potential improvements are investigated. Such improvements will benefit the precision of future analyses sensitive to charge misreconstruction.

Following this introduction, a brief introduction to quantum field theory and the Standard Model is given in Chap. 2, including also a summary of statistical methods employed in other parts of this thesis. The experimental setup is described in Chap. 3, including the LHC, the ATLAS detector, and algorithms used to reconstruct the proton-proton collisions studied from the detector signals. Studies identifying sources of the charge misidentification of electrons in the ATLAS detector are also presented in this chapter. The measurement of the gluon-fusion and vector-boson fusion production cross sections times branching ratio of the Higgs boson in the $H \to WW^*$ decay mode is presented in Chap. 4. While this measurement is only based on data recorded in 2015 and 2016, in Chap. 5 an extrapolation is performed estimating the future precision of such an analysis and identifying limiting factors at the end of the High-Luminosity LHC programme [6]. In addition to the extrapolation of the $H \to WW^*$ analysis, it is combined with extrapolations of other recent ATLAS analyses regarding the Higgs boson. Based on this combination the expected precisions of measurements of Higgs boson production cross sections, branching ratios, and coupling strengths are presented. The main results are finally summarized in Chap. 6.

In regards to the $H \to WW^*$ analysis the author's contributions include the construction and optimization of the maximum-likelihood fit for the ggF categories including the development of sanitization strategies for systematic uncertainties estimated from finite samples. A leading role was assumed in the development of the analysis software jointly used by the ATLAS $H \to WW^*$ analysis group. Even if one is not directly involved in an particular study this task requires foreseeing technical and functional needs of the analysis team to ensure steady progress. The author is the main analyzer for the projections of the $H \to WW^*$ analysis for the HL-LHC and has performed various validation and auxiliary studies for the combination of the projections of the different Higgs boson analyses. The author's studies regarding the electron charge misidentification presented in this thesis were initially proposed by the ATLAS e/γ group and kindly supported by the groups feedback.

2 Theoretical Overview

The description of fundamental particles and their interactions at high energies requires the combination of two sets of principles developed in the early 20^{th} century: those of quantum mechanics and special relativity. Theories written based on these principles are generally referred to as *quantum field theories* (QFTs). One particular QFT is the *Standard Model* (SM) of particle physics, a theory consistent with a comprehensive set of experimental measurements (see, *e.g.*, Ref. [37]). In Section 2.1 a brief introduction to quantum field theories is given followed by a summary of the particles, fields, and their interactions in the SM in Section 2.2. Additional, phenomenological considerations with focus on proton-proton collisions are briefly addressed in Section 2.3. These summaries are largely based on Refs. [38–40]. Throughout this thesis *natural units* are used, such that $c = \hbar = 1$. Additionally Einstein's sum convention is used in the following, *i.e.*, summation over doubly appearing indices is implied.

2.1. Quantum Field Theory

2.1.1. Equations of Motion and Lagrangian Densities

Both, relativistic and non-relativistic quantum theories incorporate the energy-momentum relation of their non-quantum counterpart through a procedure commonly referred to as *quantization.* In this ansatz observable quantities are replaced by suitable operators eventually acting on a wave function ψ. In the non-relativistic case of a free particle of mass m ($E = \vec{p}^{\,2}/(2m)$) the so obtained operator relation is the *Schrödinger equation*

$$\frac{-\vec{\nabla}^2}{2m}\psi = i\partial_t\psi,$$

with $\hat{\vec{p}} = -i\vec{\nabla}$, and $\hat{E} = i\partial_t$.

In the relativistic case more than one quantized version of $p^\mu p_\mu - m^2 = 0$ is of relevance. The *Klein-Gordon equation*[1]

$$\left(\partial^\mu \partial_\mu + m^2\right) \phi = 0 \tag{2.1}$$

can be solved by scalar fields ϕ and is therefore found to describe spin-0 particles. The *Dirac equation*

$$\left(\gamma^\mu p_\mu - m\right) \Psi = 0 \tag{2.2}$$

can be obtained from the linearized ansatz $p^\mu p_\mu - m^2 = (\gamma^\nu p_\nu + m)(\gamma^\omega p_\omega - m)$. This ansatz, however, requires the γ^ν to be matrices and therefore also Ψ to be a higher dimensional object. One suitable set of γ^ν is given by the 4×4 matrices

$$\gamma^0 = \begin{pmatrix} 1 & 0 \\ 0 & -1 \end{pmatrix}, \qquad \gamma^i = \begin{pmatrix} 0 & \sigma^i \\ -\sigma^i & 0 \end{pmatrix}$$

where the entries $0, 1$, and σ^i represent the 2×2 matrices with only zero entries, the 2×2 identity matrix, and the *Pauli matrices*. The four-component object Ψ is called a *Dirac spinor*. Its components can be associated with the spin states of spin-$1/2$ particles and corresponding anti-particles thus describing fermions and anti-fermions. The latter ones correspond to solutions of (seemingly) negative energy which would imply a spectrum unbounded from below. This is overcome by re-interpretation of these solutions as positive energy solutions going backward in time.

Instead of using explicitly the equations of motion (EOM) such as the Klein-Gordon or Dirac equations, quantum field theories are often expressed in the form of a *Lagrange density* $\mathcal{L}$ (commonly shortened to *Lagrangian*) from which the equations of motion can be derived similarly to the classical Euler-Lagrange formalism:

$$\partial_\mu \left(\frac{\partial \mathcal{L}}{\partial(\partial_\mu \phi_i)} \right) = \frac{\partial \mathcal{L}}{\partial \phi_i}. \tag{2.3}$$

A Lagrangian corresponding to the Klein-Gordon equation (2.1) reads

$$\mathcal{L} = \frac{1}{2} \left(\partial_\mu \phi\right) \left(\partial^\mu \phi\right) - \frac{1}{2} m_\phi^2 \phi^2 \quad [38].$$

The Lagrangian corresponding to the Dirac equation (2.2) commonly reads

$$\mathcal{L} = i\bar{\Psi}\gamma^\mu \partial_\mu \Psi - m_\Psi \bar{\Psi}\Psi, \text{ with } \bar{\Psi} = \Psi^\dagger \gamma^0,\ \Psi^\dagger = (\Psi^T)^* \quad [38]. \tag{2.4}$$

[1] obtained through replacements $p_\mu \to i\partial_\mu = i\frac{\partial}{\partial x^\mu}$

Another important type of Lagrangian is the (free) *Proca* Lagrangian describing a vector (spin-1) field A^μ:

$$\begin{aligned}\mathcal{L} &= -\tfrac{1}{16\pi}\underbrace{\left(\partial^\mu A^\nu - \partial^\nu A^\mu\right)}_{F^{\mu\nu}}\underbrace{\left(\partial_\mu A_\nu - \partial_\nu A_\mu\right)}_{F_{\mu\nu}} + \tfrac{1}{8\pi}m_A^2 A^\mu A_\mu \\ &= -\tfrac{1}{16\pi}\, F^{\mu\nu}\, F_{\mu\nu} + \tfrac{1}{8\pi}m_A^2 A^\mu A_\mu \;\; [38].\end{aligned} \tag{2.5}$$

2.1.2. Gauge Symmetries and Interactions

The Lagrangian of a free Dirac field (2.4) is invariant under the global transformation $\Psi \to e^{iq\cdot\theta}\Psi$ for a real valued constant θ and the generator q of a symmetry group. Such a transformation which leaves the resulting physical observables invariant is called a *gauge transformation*. In case of the symmetry group $U(1)$, q is just a real valued constant as well. In order for the Lagrangian to be invariant under a local $U(1)$ gauge transformation $\Psi \to e^{iq\cdot\theta(x)}\Psi$, *i.e.*, θ being dependent on the coordinate x, the derivative ∂_μ is replaced by the so called *covariant derivative*

$$D_\mu = \partial_\mu + iqA_\mu,$$

with the thereby introduced vector field transforming as $A_\mu \to A_\mu + \frac{1}{q}\partial_\mu\theta(x)$. Due to the introduction of the vector field A^μ the Lagrangian also needs to be extended with free terms from Eq. (2.5) and becomes

$$\begin{aligned}\mathcal{L} &= -\frac{1}{16\pi}F^{\mu\nu}F_{\mu\nu} - m_\Psi\bar{\Psi}\Psi + i\bar{\Psi}\gamma^\mu\left(\partial_\mu + iqA_\mu\right)\Psi \\ &= -\frac{1}{16\pi}F^{\mu\nu}F_{\mu\nu} - m_\Psi\bar{\Psi}\Psi + i\bar{\Psi}\gamma^\mu D_\mu\Psi.\end{aligned}$$

The mass term $\frac{1}{2}m_A^2A^\mu A_\mu$ from Eq. (2.5) would violate the demanded symmetry such that the mass of the *gauge field* A^μ must be zero. The injection of the covariant derivative also introduces the *interaction term*

$$\mathcal{L}_{\text{int}} = -q\bar{\Psi}\gamma^\mu\Psi A_\mu$$

coupling the fields Ψ and A_μ with a *coupling strength* (or *coupling constant*) proportional to the *charge* q.

Besides potentially introducing interactions, symmetries are connected to conservation laws via *Noether's theorem* [41]. It states that every unbroken, continuous symmetry implies a conserved current j^μ with $\partial_\mu j^\mu = 0$ and a corresponding conserved charge. For example, in the just discussed $U(1)$ example, this conserved current is

$$j^\mu = \frac{iq}{2}\left(\frac{\partial\mathcal{L}}{\partial(\partial_\mu\psi)}\cdot\psi - \bar{\psi}\cdot\frac{\partial\mathcal{L}}{\partial(\partial_\mu\bar{\psi})}\right) = -q\bar{\psi}\gamma^\mu\psi,$$

and the conserved charge $Q = \int d^3x\, j^0$. Other examples include the invariance of a system with respect to translations in space-time leading to conservation of the systems four-momentum, and a rotational invariance leading to conservation of angular momentum.

2.1.3. Perturbative Expansion via Feynman Calculus

The transition of an initial state $|i(t=-\infty)\rangle$ to a final state $|f(t=\infty)\rangle$ given the interaction Hamiltonian density $\mathcal{H}_{int} = -\mathcal{L}_{int}$ is described by the $\mathcal{S}$ matrix

$$\langle f|T\left(\exp\left[-i\int d^4x\,\mathcal{H}_{int}(x)\right]\right)|i\rangle = \langle f|\mathcal{S}|i\rangle$$

with the time ordering operator $T(...)$. When expanding the exponential term the ever increasing powers of the coupling parameters from the Hamiltonian/Lagrangian are suggestive of a perturbative expansion. In fact, as for example discussed in great detail in Ref. [40], a perturbative treatment can be applied for sufficiently small coupling constants. The terms of such a perturbative series can be derived from *Feynman graphs* in which the couplings appear at vertices connecting multiple lines which represent the fields/particles involved. The number of vertices in a graph correspond to the perturbative order of the term, *i.e.*, the power of the coupling constant. External lines with one end not connected to some vertex represent initial or final state particles. In this thesis the time axis in Feynman graphs is running from left to right, *i.e.*, initial state particles enter from the left and final state particles leave to the right. Internal lines with both ends connected are referred to as *propagators*. To obtain the matrix element at nth order all connected graphs with the same external lines and up to n vertices need to be summed. Examples for a vertex and a leading-order (LO) diagram are shown in Fig. 2.1 based on the $U(1)$ gauge theory from Sec. 2.1.2. The leading order (LO) refers to the non-trivial order with minimal number of vertices n. Diagrams with next-to-minimal number of vertices are referred to as next-to-leading order (NLO), even higher orders being denoted by, *e.g.*, NNLO (or N2LO), and N3LO. Rotating a valid graph by multiples of $90°$ produces again a valid graph. If such a rotation inverts the direction of a line with respect to the time axis its interpretation in terms of particle/anti-particle is inverted as well.

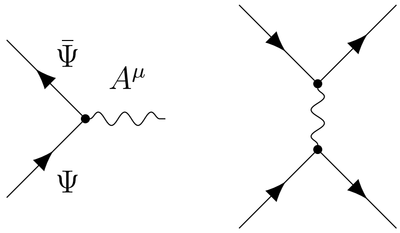

Figure 2.1.: A single vertex (left) with indication of the fields associated with different line styles, and a basic example for a leading-order Feynman graph (right) representing a simple fermion-fermion scattering process based on the example $U(1)$ theory in Sec. 2.1.2.

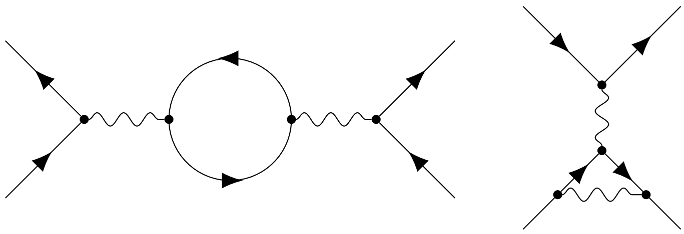

Figure 2.2.: Examples for divergent Feynman graphs based on the example $U(1)$ theory in Sec. 2.1.2 requiring the introduction of renormalized coupling parameters. Based on Ref. [40].

Divergent integrals are encountered in diagrams like the ones shown in Fig. 2.2. These can be solved by introducing a regularisation factor as presented, *e.g.*, in Ref. [38]. However, this still leads to finite and infinite contributions modifying the original masses and couplings when taking a limit in the regularisation parameter such that the regularisation term disappears again. The infinite contributions can be absorbed through a redefinition (*renormalization*) of the masses and couplings while the finite contributions introduce four-momentum dependencies. As a consequence the masses and coupling "constants" are said to be *running*. A theory for which such a treatment can be applied is called a *renormalizable theory*.

2.1.4. Cross Sections and Decay Widths

A typical way of studying fundamental interactions is using accelerators such as the *Large Hadron Collider* LHC described in Sec. 3.1. In these machines series of bunches of particles, in sum referred to as *beams*, collide with other particles at high energies. The collision partners are either other bunches or so called *fixed targets*. In order to compare results between different experiments and to theoretical calculations the number of transitions $n(i \to f)$ in these collisions are converted to cross sections σ. These are constructed to be independent from beam parameters such as the overlap of the colliding beams and number density ρ of particles contained in the beams. For colliding bunches A, B with bunch lengths ℓ_A, ℓ_B one finds the relation [40]

$$n(i \to f) = \sigma \ell_A \ell_B \int d^2x \, \rho_A(x) \rho_B(x),$$

where the integration is performed over the plane transverse to the beam direction and number densities in the bunches are assumed constant along the longitudinal direction. Analogously, differential cross sections $\frac{d\sigma}{dX}$ for some observable X are used to describe transitions to final states with particular kinematic properties such as emission angles or momenta of final state particles.

Using the $\mathcal{T}$ matrix given by $\mathcal{S} = 1 + i\mathcal{T}$ the *invariant matrix element* $\mathcal{M}(i \to f)$ can be defined through

$$\langle i|\mathcal{T}|f\rangle = (2\pi)^4 \delta^{(4)} \left(\sum_i p_i - \sum_f p_f \right) \cdot i\mathcal{M}(i \to f), \tag{2.6}$$

where the sums run over the initial (i) and final (f) state particles respectively. The cross section of a process with initial state particles $1, 2$ is then obtained from (see, *e.g.*, Ref. [38])

$$d\sigma = \frac{S}{4\sqrt{(p_1 p_2)^2 - (m_1 m_2)^2}} \cdot |\mathcal{M}|^2 \cdot \left(\prod_f \frac{d^3\vec{p}_f}{(2\pi)^3 2E_f} \right) \cdot (2\pi)^4 \delta^{(4)}(p_1 + p_2 - \sum_f p_f).$$

The decay rate Γ is used to describe the decay of a particle. For a given number N of particles of the same type the decay rate and average life time τ are given by

$$\Gamma = \frac{1}{N}\frac{dN}{dt}, \qquad \tau = \frac{1}{\Gamma}.$$

For a particle at rest with mass m it can be expressed in terms of the invariant matrix element $\mathcal{M}$ through

$$d\Gamma = \frac{S}{2m} \cdot |\mathcal{M}|^2 \cdot \left(\prod_f \frac{d^3\vec{p}_f}{(2\pi)^3 2E_f} \right) \cdot (2\pi)^4 \delta^{(4)}(p - \sum_f p_f).$$

In both cases S is a statistical factor: each group of j identical particles in the final state contributing a factor $(1/j!)$. Cross section and decay rate are additive. For example the total decay rate of a particle which can decay to final states $1, 2, 3, ...$ is $\Gamma = \Gamma_1 + \Gamma_2 + \Gamma_3 + ...$.

2.2. The Standard Model of Particle Physics

The Standard Model comprises all known elementary particles and their interactions with the exception of gravity. Its gauge symmetry group is $SU(3)_c \times SU(2)_L \times U(1)_Y$ giving rise to two main sectors of interactions that are briefly summarized in the following sections: the strong interaction corresponding to $SU(3)_c$ and the electroweak (EW) interaction corresponding to $SU(2)_L \times U(1)_Y$. The elementary particle content of the Standard Model is summarized in Fig. 2.3. Fermions are arranged in three generations: every particle in one generation has a correspondent in each other generation which only differs by mass. The individual types of particles are often referred to as (quark or lepton) *flavors*. The sets of quarks with same electric charge are often referred to by their first generation element as *up-type* or *down-type* quarks.

2.2.1. Quantum Chromo Dynamics

The *strong force* described by quantum chromo dynamics is mediated by gluons. The index c of the $SU(3)_c$ group refers to the *color charge* which is responsible for a particle to couple to a gluon gauge field. While quarks[2] carry color, denoted as r, g, or b for red, green, or blue, anti-quarks carry anti-colors $\bar{r}$, $\bar{g}$, or $\bar{b}$. The quark sector therefore consists of color triplets. Gluons form a color octet carrying a combination of color and anti-color. The gluon color-singlet $1/\sqrt{3}|r\bar{r} + g\bar{g} + b\bar{b}\rangle$ is not realized.

The terms of the SM Lagrangian relevant for QCD are

$$\mathcal{L}_{\text{SM}} \supset \mathcal{L}_{QCD} = \bar{q}\left(i\gamma^{\mu}\partial_{\mu} - m\right) q - g_s \left(\bar{q}\gamma^{\mu}T_a q\right) G^a_{\mu} - \frac{1}{4} G^a_{\mu\nu} G^{\mu\nu}_a,$$
$$G^a_{\mu\nu} = \partial_{\mu} G^a_{\nu} - \partial_{\nu} G^a_{\mu} - g_s f_{abc} G^b_{\mu} G^c_{\nu},$$

where the T_a are the eight generators of the $SU(3)_C$ group with structure constants f_{abc} defined via the commutators $[T_a, T_b] = i f_{abc} T_c$. The gluon field operators are denoted as G^{μ}_a and $g_s = \sqrt{4\pi\alpha_s}$ is the coupling strength. The resulting vertices are shown in Fig. 2.4.

The running of the strong coupling α_s is influenced by two types of loop diagrams similar to those shown in Fig. 2.2. Quark loops lead to an increase of α_s with increasing momentum transfer q while contributions from gluon loops have the opposite sign. The contributions from these two types of diagrams depend on the number of quark flavors and colors, respectively. In the Standard Model with six quark flavors and three colors the gluon loops dominate. That is, the strong

[2] The concept of quarks with fractal electric charge was suggested in Ref. [43] and Ref. [44] .

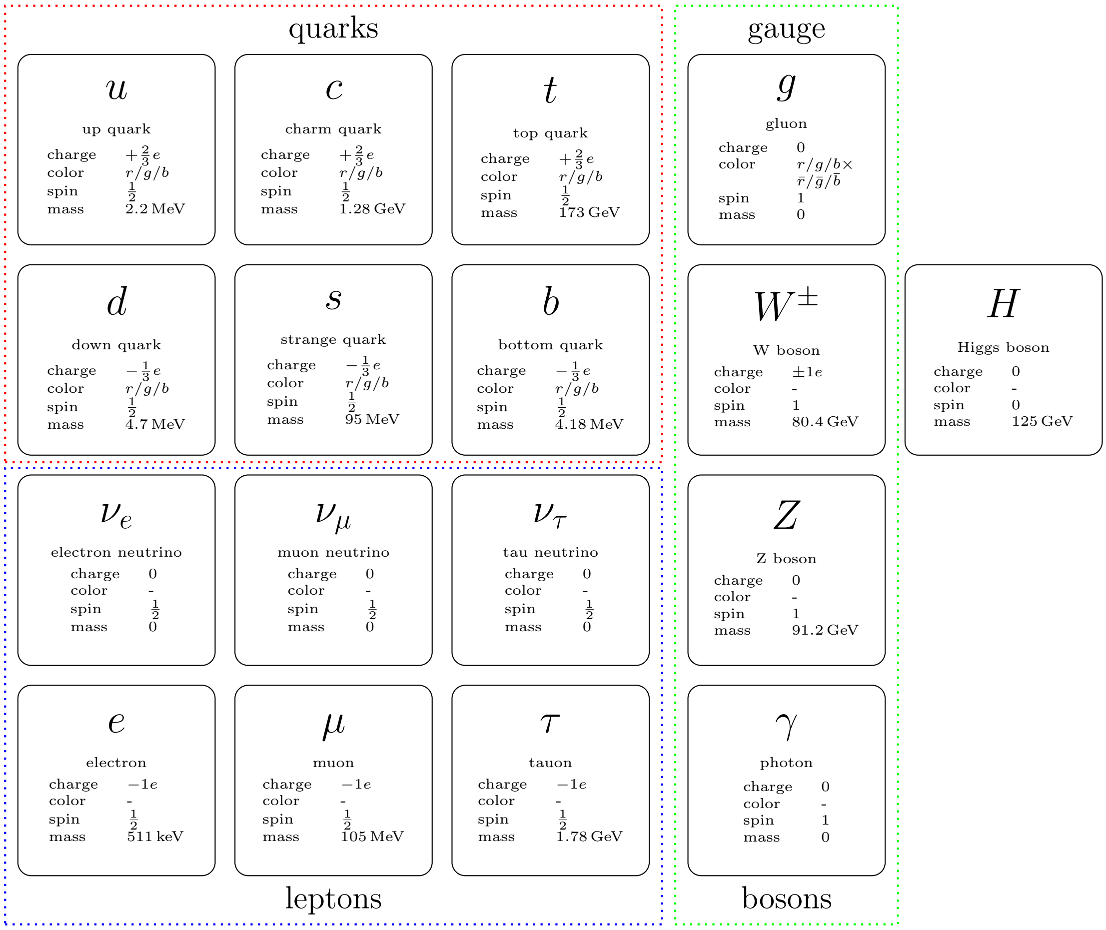

Figure 2.3.: Simplified overview of the particle content of the Standard Model. For fermions only particles but no anti-particles are shown. The latter posses charges conjugate to those of particles. Based on Ref. [42].

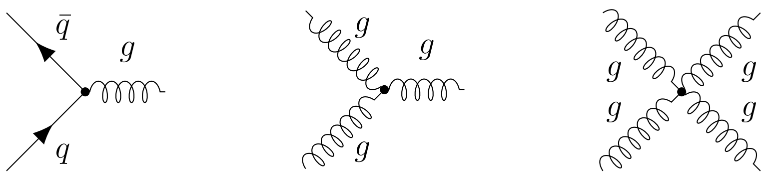

Figure 2.4.: Vertices in quantum chromo dynamics. The three-legged vertices are proportional to the coupling strength $g_s = \sqrt{4\pi\alpha_s}$, the four-gluon vertex is proportional to g_s^2. The quark-gluon vertex is flavor diagonal, *i.e.*, always involves two (anti) quarks of the same flavor.

interaction becomes weaker at high momentum transfer (or equivalently short distances) leading to *asymptotic freedom*. At low momentum transfer (or large distances), however, α_s becomes large preventing the use of Feynman calculus in this regime. An important consequence of this running is *confinement*, *i.e.*, particles charged under $SU(3)_c$ rapidly form bound, color-neutral (*white*) states denoted as hadrons. The most prominent subsets of hadrons are mesons (quark + anti-quark) and baryons (three quarks).

2.2.2. Electroweak Interaction

Fermi [16] described the nuclear beta decay by means of a direct coupling of a proton, a neutron, an electron, and a neutrino of strength G_F. In regards to, *e.g.*, total decay rates this description turns out to be a low energy approximation of what today is called the electroweak Standard Model. This gauge theory unifying the description of electromagnetic and weak interactions was largely developed by Glashow [17], Salam [18], and Weinberg [19]. It is summarized in this section although incomplete without the Brout-Englert-Higgs (BEH) mechanism which is described in a subsequent section.

The electroweak interaction is based on the symmetry group $SU(2)_L \times U(1)_Y$ with gauge fields $W^i_\mu,\ i = 1, 2, 3$ and B_μ. The subscript Y refers to the *hypercharge* responsible for a coupling to B_μ. The subscript L refers to the *left-handed* coupling structure of the $SU(2)_L$ subgroup and the corresponding W^i_μ.

The weak currents corresponding to $SU(2)_L$ read

$$J^i_\mu = \bar{\chi}\frac{1}{2}\tau_i\gamma_\mu\frac{1}{2}(1-\gamma^5)\chi = \bar{\chi}_L\frac{1}{2}\tau_i\gamma_\mu\chi_L, \qquad \gamma^5 = i\gamma^0\gamma^1\gamma^2\gamma^3,$$

where χ is a *(weak) isospin* doublet of Dirac spinors and τ_i are the Pauli matrices and generators of $SU(2)_L$. In the lepton sector the doublets are $\chi = (\nu_\ell, \ell)^T,\ \ell = e, \mu, \tau$. The iso spin doublets in the quark sector connect up and down type quarks. The operator $\frac{1}{2}(1-\gamma^5)$ projects the Dirac spinors of fermions (anti-fermions) onto their left (right) chiral components. The weak $SU(2)_L$ currents therefore only couple to left chiral fermions and right chiral anti-fermions.

While γ^μ transforms under the parity operator (spatial inversion) P like a vector, $P(\gamma^\mu) = -\gamma^\mu$, the product $\gamma^\mu\gamma^5$ transforms like an axial vector $P(\gamma^\mu\gamma^5) = \gamma^\mu\gamma^5$. An inherent property of weak currents is therefore the so called V-A structure implying parity violation.

With the step operators $\tau_\pm = \frac{1}{2}(\tau_1 \pm i\tau_2)$ the charged currents [39]

$$J^\pm_\mu = \bar{\chi}\tau^\pm\gamma_\mu(1-\gamma^5)\chi = \left(J^1_\mu \pm iJ^2_\mu\right)$$

Table 2.1.: Charges relevant in electroweak interactions for left (L) and right (R) chiral fermions: isospin T, its third component T^3, hypercharge Y, and electric charge Q. The values for second and third generation particles are identical to their first generation correspondents. Right chiral neutrinos are not contained in the Standard Model. Reproduced from [39].

	T	T^3	Y	Q
$(\nu_e)_L$	$\frac{1}{2}$	$\frac{1}{2}$	-1	0
e_L	$\frac{1}{2}$	$-\frac{1}{2}$	-1	-1
e_R	0	0	-2	-1

	T	T^3	Y	Q
u_L	$\frac{1}{2}$	$\frac{1}{2}$	$\frac{1}{3}$	$\frac{2}{3}$
d_L	$\frac{1}{2}$	$-\frac{1}{2}$	$\frac{1}{3}$	$-\frac{1}{3}$
u_R	0	0	$\frac{4}{3}$	$\frac{2}{3}$
d_R	0	0	$-\frac{2}{3}$	$-\frac{1}{3}$

describe transitions between the two components of the isospin doublets. These are the currents the physical, eventually massive gauge bosons $W_\mu^\pm = \frac{1}{\sqrt{2}}(W_\mu^1 \mp iW_\mu^2)$ couple to.

The electroweak section of the SM Lagrangian can be expressed as[3] [39]

$$\begin{aligned}\mathcal{L} \supset \mathcal{L}_{\mathrm{EW}} =& \bar{\chi}_L\gamma^\mu \left(i\partial_\mu - g\frac{1}{2}\vec{\tau}\vec{W}_\mu - g'\frac{Y_L}{2}B_\mu\right)\chi_L \\ &+ \bar{f}_R\gamma^\mu\left(i\partial_\mu - g'\frac{Y_R}{2}B_\mu\right)f_R - \frac{1}{4}\vec{W}_{\mu\nu}\vec{W}^{\mu\nu} - \frac{1}{4}B_{\mu\nu}B^{\mu\nu},\end{aligned} \tag{2.7}$$

where $B_{\mu\nu} = \partial_\mu B_\nu - \partial_\nu B_\mu$, and $\vec{W}_{\mu\nu} = \partial_\mu\vec{W}_\nu - \partial_\nu\vec{W}_\mu - g\vec{W}_\mu \times \vec{W}_\nu$. The coupling constants are g and g'. The left (right) chiral fermion doublets (singlets) are denoted as χ_L (f_R) and their corresponding hypercharge as Y_L (Y_R). Besides the fields W_μ^1, W_μ^2 mixing to the physical fields $W_\mu^\pm$ the electroweak section of the SM Lagrangian contains two more fields W_μ^3 and B_μ mixing to the physical fields

$$\begin{aligned}A_\mu =& \quad B_\mu\cos\theta_w + W_\mu^3\sin\theta_w, \\ Z_\mu =& -B_\mu\sin\theta_w + W_\mu^3\cos\theta_w.\end{aligned}$$

This choice of mixing is arbitrary up until the introduction of the BEH mechanism. Identifying A_μ as the (eventually massless) photon field, the weak mixing angle θ_w allows to relate the coupling strengths g, and g' to the electric unit charge:

$$g\sin\theta_w = g'\cos\theta_w = e,$$

[3]Mass terms are omitted up until the introduction of the BEH mechanism.

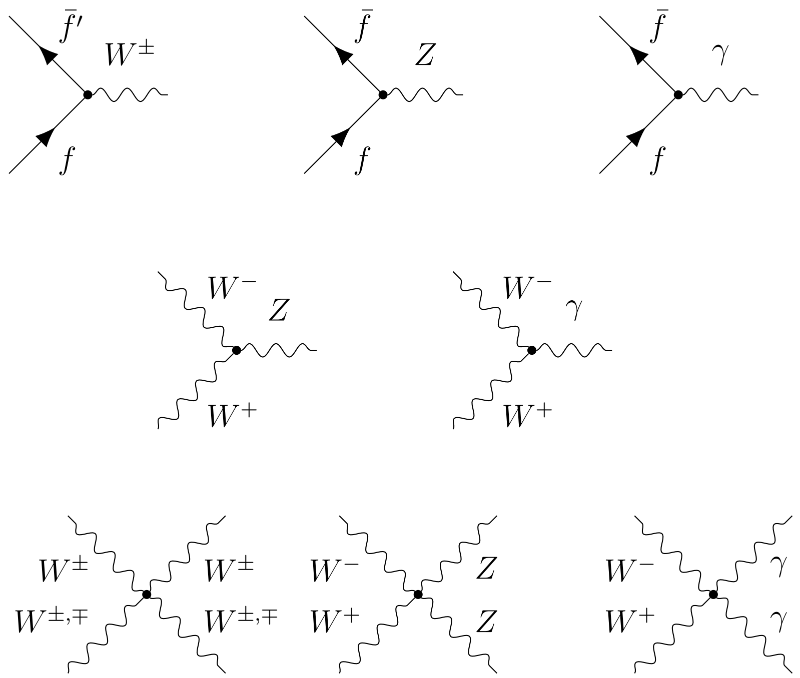

Figure 2.5.: Vertices of the electroweak interaction based on the $SU(2)_L \times U(1)_Y$ group.

where values of the hypercharge Y are constructed such that the dimensionless charges obey the relation

$$Q = T^3 + \frac{Y}{2}.$$

Thus, the photon field couples to particles irrespective of their chirality and in turn conserves parity. The *weak neutral current* couples to Z_μ in a vertex described by

$$-i\frac{g}{\cos\theta_w}\gamma^\mu\frac{1}{2}\left(c_V - c_A\gamma^5\right), \text{ with } c_v = T^3 - 2\sin^2\theta_w Q, \text{ and } c_A = T^3.$$

The charges of fermions under these here discussed symmetry groups are summarized in Tab. 2.1. The vertices of the electroweak sector discussed thus far are shown in Fig. 2.5. Triple and quartic gauge vertices occur as the gauge fields W^i_μ carry isospin $T = 1$ themselves.

2.2.3. The Brout-Englert-Higgs Mechanism

In the $U(1)$ example in Sec. 2.1 adding a mass term for the gauge field breaks the demanded $U(1)$ symmetry. Similarly, introducing mass into Eq.(2.7) for fermions or gauge bosons violates the $SU(2)_L$ symmetry. Massless gauge bosons and fermions, however, are in clear contradiction to experimental results $m_W = 80.379 \pm 0.012\,\text{GeV}$

and $m_Z = 91.1876 \pm 0.0021\,\text{GeV}$ [42]. Furthermore the scattering of vector bosons $WW \to WW$ is bound to violate unitarity at sufficiently high energies when only considering Feynman diagrams constructed from the vertices shown in Fig. 2.5 (see, *e.g.*, Ref. [45]). These shortcomings are addressed by a mechanism leading to spontaneous symmetry breaking, namely the *Brout-Englert-Higgs* (BEH) *mechanism* [3, 4, 26].

This mechanism introduces a complex isospin doublet

$$\phi = \begin{pmatrix} \phi^+ \\ \phi^0 \end{pmatrix} = \frac{1}{\sqrt{2}} \begin{pmatrix} \phi_1 + i\phi_2 \\ \phi_3 + i\phi_4 \end{pmatrix}$$

with hypercharge $Y = 1$. The relevant part of the Lagrangian is

$$\mathcal{L} \supset \mathcal{L}_H = (D_\mu \phi)^\dagger (D^\mu \phi) - V(\phi), \text{ with } V(\phi) = \mu^2 \phi^\dagger \phi + \lambda \left(\phi^\dagger \phi\right)^2, \tag{2.8}$$

and the covariant derivative (as already implicitly used in Eq. 2.7)

$$D_\mu = \partial_\mu + ig\frac{\tau_a}{2} W_\mu^a + ig'\frac{Y}{2} B_\mu.$$

The potential $V(\phi)$ exhibits the *Mexican hat* shape shown in Fig. 2.6 for $\mu^2 < 0,\ \lambda > 0$. In this case its minima[4] fulfill the condition

$$\phi^\dagger \phi = -\frac{\mu^2}{2\lambda} \equiv \frac{1}{2} v^2,$$

where v is referred to as *vacuum expectation value*. The field ϕ can then be expanded around a chosen minimum $\phi_1 = \phi_2 = \phi_4 = 0$, $\phi_3 = v$

$$\phi = \frac{1}{\sqrt{2}} \begin{pmatrix} 0 \\ v + H(x) \end{pmatrix}. \tag{2.9}$$

Any other value of ϕ can be obtained by means of $SU(2)$ rotations while the Lagrangian is invariant under these. The only physical field emerging is therefore the *Higgs field* $H(x)$ giving rise to the Higgs boson H. Inserting the expansion (2.9) into

[4] As $V(\phi)$ only depends on $|\phi|^2 = \phi^\dagger \phi$ the minima form a hyper sphere in the space spanned by the $\phi_i,\ i = 1, ..., 4$.

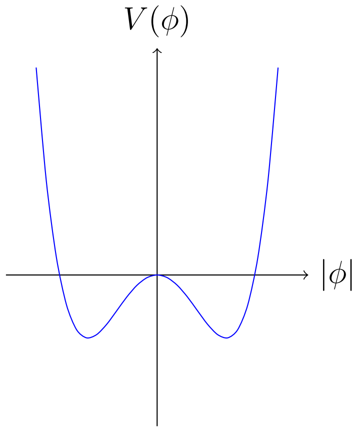

Figure 2.6.: Shape of the potential $V(\phi)$ in the BEH mechanism.

the Lagrangian (2.8) mass terms can be identified for the electroweak bosons [39]:

$$\begin{array}{rcrcl} v^2\lambda H^2 & \Rightarrow & m_H & = & \sqrt{2v^2\lambda}, \\ \left(\frac{1}{2}vg\right)^2 W_\mu^+ W^{-\mu} & \Rightarrow & m_W & = & \frac{1}{2}vg, \\ \frac{1}{8}\left(W_\mu^3, B_\mu\right)\begin{pmatrix} g^2 & -gg' \\ -gg' & g'^2 \end{pmatrix}\begin{pmatrix} W^{3\mu} \\ B^\mu \end{pmatrix} & \Rightarrow & \begin{array}{r} m_Z \\ m_A \end{array} & \begin{array}{c} = \\ = \end{array} & \begin{array}{l} \frac{1}{2}v\sqrt{g^2+g'^2} \\ 0 \end{array} \end{array}$$

The basis transformation diagonalizing the W^3, B mass matrix defines the composition of the physical fields Z^μ and A^μ. It is also the reason for the mass difference between the $W^\pm$ and Z bosons which are related to the weak mixing angle through

$$\cos\theta_w = \frac{m_W}{m_Z}.$$

The *propagator* term corresponding to internal, massive vector boson lines $-i(g_{\mu\nu} - p_\mu p_\nu/m_V^2)/(p^2 - m_V^2)$ in the low energy limit $p^2 \ll m_V^2$ allows to relate G_F, g, and m_W and thereby determine the vacuum expectation value $v \approx 246\,\mathrm{GeV}$ using results from low energy experiments such as muon decays:

$$\frac{G_F}{\sqrt{2}} = \frac{g^2}{8m_W^2} = \frac{1}{2v^2}.$$

The value of λ and thereby the mass of the Higgs boson m_H, however, are not predicted.

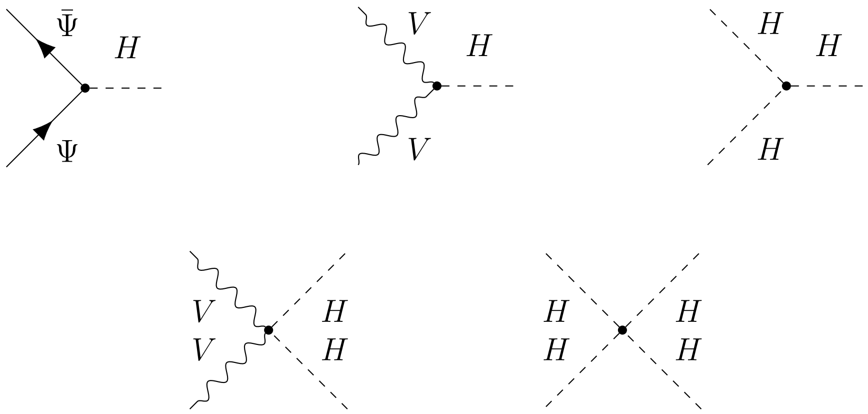

Figure 2.7.: Vertices involving the SM Higgs boson. Ψ refers to massive fermions (quarks, charged leptons), V to massive vector bosons (W, Z) and H to the Higgs boson.

Fermionic mass terms can be included in the Lagrangian via *Yukawa couplings*[5] of the Higgs field to the fermion fields. With $\tilde{\phi} = i\tau_2\phi$ the additional terms read (see, *e.g.*, [47])

$$\mathcal{L}_F = -\lambda_e \bar{L}_L \phi e_R - \lambda_d \bar{Q}_L \phi d_R - \lambda_u \bar{Q} \tilde{\phi} u_R + \text{h.c.}$$

for each fermion generation. Inserting ϕ after spontaneous symmetry breaking fermion mass terms can be identified:

$$-\frac{1}{\sqrt{2}}\lambda_e v \bar{e}_L e_R \quad \Rightarrow \quad m_e = \frac{1}{\sqrt{2}}\lambda_e v.$$

The parameters λ_x are not predicted and, hence, fermion masses need experimental determination.

Together with the mass terms for both, fermions and massive gauge bosons, interaction terms of the respective fields with the Higgs field are introduced leading to the vertices shown in Fig. 2.7. While couplings of Higgs bosons to fermions are proportional to the respective fermion mass m_f the couplings to W and Z bosons are proportional to m_V^2.

The isospin doublets of the quark sector already mentioned in Sec. 2.2.2 exhibit the particularity that the elements of the doublets are no mass eigenstates but instead related to these via a unitary transformation U_{CKM}. By convention states

[5]The coupling of fermion fields to a scalar field was first introduced by Hideki Yukawa to describe the attraction between neutrons and protons in nuclei in Ref. [46].

modified by this transformation are taken to be the down-type ones:

$$\chi = \begin{pmatrix} u \\ d' \end{pmatrix}, \begin{pmatrix} c \\ s' \end{pmatrix}, \begin{pmatrix} t \\ b' \end{pmatrix}, \text{ where } \begin{pmatrix} d' \\ s' \\ b' \end{pmatrix} = \underbrace{\begin{pmatrix} U_{ud} & U_{us} & U_{ub} \\ U_{cd} & U_{cs} & U_{cb} \\ U_{td} & U_{ts} & U_{tb} \end{pmatrix}}_{U_{CKM}} \begin{pmatrix} d \\ s \\ b \end{pmatrix}.$$

The matrix U_{CKM} is known as the *Cabibbo-Kobayashi-Maskawa matrix* [48, 49]. Its values are not predicted and therefore require experimental determination, a summary of which can be found in [42]. The absolute values of the diagonal elements are close to one. Still all off-diagonal elements are found to be non vanishing. The presence of a complex phase in U_{CKM} leads to violation of CP-symmetry where C is the charge-conjugation operator interchanging particles and anti-particles.

2.3. Phenomenology of Proton-Proton Collisions

In the preceding sections only interactions between free, elementary particles were considered. In case of proton-proton collisions, however, the initial states are complex compound states. The fundamental constituents of the protons are collectively referred to as *partons*. In the deep inelastic scatter (DIS) regime it is those partons which are considered as the initial state particles for the *hard scatter* described by Eq. (2.6).

While the quantum numbers of protons can be constructed from those of the three *valence quarks* (*uud*) the set of partons which can enter the hard scatter exceeds these three quarks. In addition to the valence quarks, the omnipresent emission and absorption of gluons, together with the creation and annihilation of quark-anti-quarks pairs (*sea quarks*) need to be considered. To account for this composite structure so called *parton distribution functions* (PDF) $f_a(x, \mu^2)$ are determined from fits of theoretical models to previous experiments, *e.g.*, from electron-proton collisions or even proton-proton collisions other than the datasets to make predictions for. The PDFs describe the density of partons a carrying the fraction x of the total proton momentum when probed at a scale given by μ^2. The evolution to different scales μ^2 can be performed by means of a DGLAP[6] equation [42]

$$\frac{\partial f_a}{\partial \ln \mu^2} \sim \frac{\alpha_s(\mu^2)}{2\pi} \sum (P_{ab} \otimes f_b),$$

where the sum runs over convolutional integrals where P_{ab} describes the production of parton a from parton b, *e.g.*, the production of a quark and an anti quark

[6]Named after Dokshitzer [50], Gribov and Lipatov [51], and Altarelli and Parisi [52].

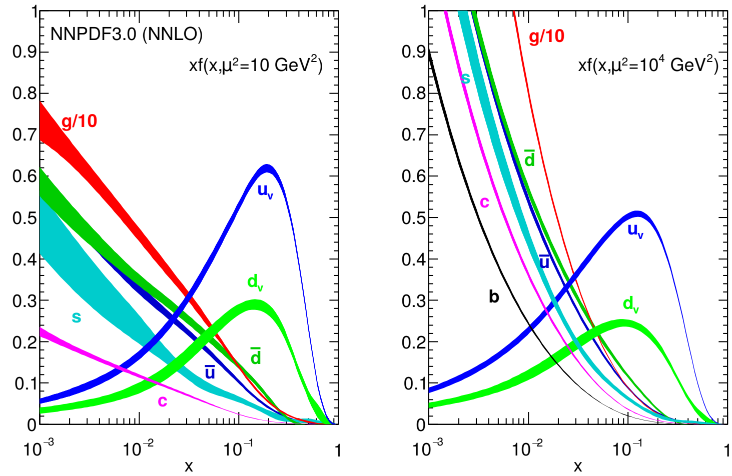

Figure 2.8.: Examples for parton distributions (PDFs) $xf(x, \mu^2)$ at different scales μ^2 for protons. Uncertainties are indicated by the width of the lines. The gluon PDFs are scaled by 1/10. The valence quarks u and d carry larger momentum fractions on average compared to sea quarks and anti-quarks. For the same reason a distinction between $u/\bar{u}$ and $d/\bar{d}$ is made. From Ref. [42].

from a gluon $g \to q\bar{q}$. Examples for PDFs are shown in Fig. 2.8. The soft, phenomenologically treated proton substructure factorizes from the perturbatively treated hard scatter process. The scale $\mu = \mu_F$ that separates these two domains is therefore called *factorization scale*. The hadronic cross section σ for a process emerging from a proton-proton collision is then given based on the considered hard scatter cross sections $\hat{\sigma}_{ij}$ by (see, *e.g.*, [53])

$$\sigma(p_1, p_2) = \sum_{i,j} \int dx_1 dx_2 \; f_i(x_1, \mu_F^2) f_j(x_2, \mu_F^2) \hat{\sigma}_{ij}(x_1 p_1, x_2 p_2, Q^2/\mu_F^2).$$

Here, $p_{1,2}$ denote the proton momenta, Q^2 the scale of the hard scatter process, and the sum runs over possible initial state partons with momentum fractions $x_{1,2}$. As a consequence the initial state momenta with respect to the hard scatter are experimentally not accessible for individual collisions[7]. The initial state parton momenta transverse to the axis defined by the direction of the incident protons (in the center-of-mass frame) is typically negligible compared to their longitudinal momenta. Hence, at hadron colliders, quantities in the transverse plane such as the transverse momenta p_T of final state particles are frequently used.

[7] Activity from proton remnants is strongly focused in the direction of the original protons and therefore outside of the main geometric acceptance of the experiments.

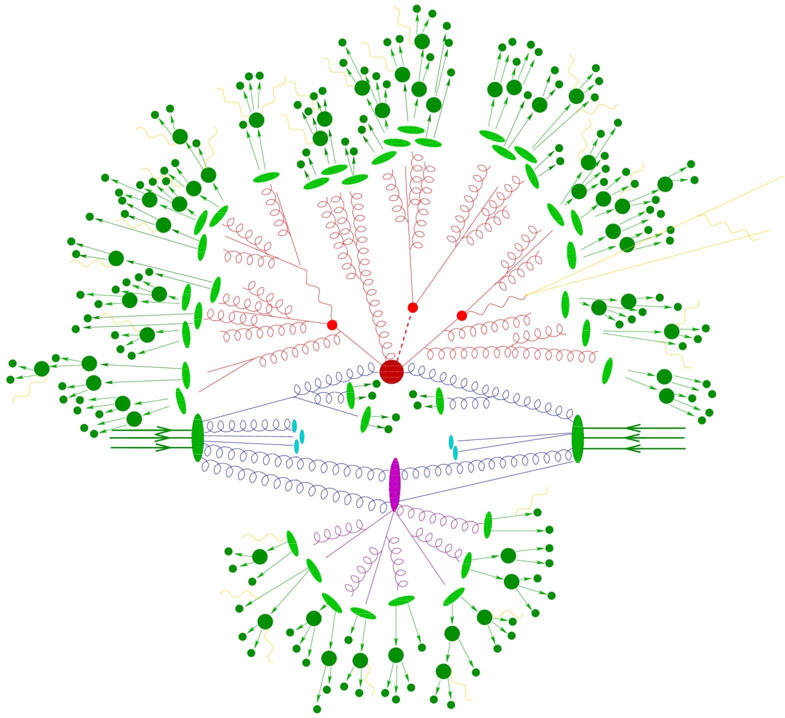

Figure 2.9.: Visual representation of the structure of proton-proton collisions. Initial state partons are drawn in blue. The main hard scatter is indicated by the large red circle, a second hard scatter is drawn in purple. Both are surrounded by parton showers eventually transitioning to hadronization (formation of color neutral bound states, light green) and eventually decays of these hadrons (dark green). Emissions of (soft) photons and leptons are drawn in yellow. From Ref. [54].

The confining property of QCD leads to additional effects in proton-proton collisions visualized in Fig. 2.9. The main hard scatter is accompanied by the so called *underlying event* (UE). It originates from additional parton interactions besides the main hard scatter as well as partons created in the *color reconnection* process in between the various color charged particles emerging from the collision. Additionally (soft) initial/final state radiation like emissions are accounted under the term of *parton shower*. More in-depth studies and discussions regarding the underlying event and parton showers can, for example, be found in Refs. [54, 55]. The process of forming bound hadronic states (color singlets) is finally referred to as *hadronization*. One exception to the formation of hadrons is given by the top quark. Given its extremely short life time of $\sim 0.5 \cdot 10^{-24}\,\mathrm{s}$ [42] it generally decays before the formation of hadrons.

At the macroscopic level hadrons formed as a result of the scatter fly out from the point of collision as collimated sprays of particles called *jets*. The exact definition of a jet depends on the algorithm chosen to perform the clustering of individual jet constituents. In order to allow comparisons between theory and experiment the chosen algorithm must be *infrared/collinear safe*, *i.e.*, the resulting jets' properties must be robust against emission of additional soft particles such as gluons (and hence additional/different hadrons) within the jet. A popular example for such an algorithm is the *anti-k_t algorithm* [56]. A brief description of this algorithm and its use in the ATLAS detector is given in Sec. 3.3.2.

In order to join results from perturbation theory, phenomenological treatment, and eventually even interactions with complex detectors a *Monte Carlo* (MC) approach is used. Individual collisions are simulated in chains of software tools, each responsible for a subset of aspects to be accounted for. Such steps include simulation of the hard scatter, parton showers and underlying event, hadronization, further decays and interaction with detector material. Uncertainties, in particular on phenomenological treatments, can be estimated from comparison of results obtained from different tools for a particular aspect or by varying tuning parameters of a tool itself. At the LHC multiple collisions are produced essentially simultaneously. These additional collisions are referred to as *pile up*. Additional collisions in the same bunch crossing as the collision of interest are referred to as *in-time pile up*, collisions in preceding or subsequent bunch crossings as *out-of-time pile up* if produced within the detector's temporal resolution. In simulations this is accounted for by means of overlaying multiple, individual scatters randomly distributed over the collision region. The number of simultaneous collisions for unchanged beam properties follows a Poisson distribution. Within the ATLAS Collaboration the effect of pile-up interactions in simulated events is taken into account by overlaying mostly soft QCD interactions generated with PYTHIA8 [57, 58].

2.3.1. Signatures of Electroweak Processes

The cross sections for various SM processes at different proton-proton center-of-mass energies $\sqrt{s}$[8] are shown in Fig. 2.10. The vast majority of collisions, often called *events*, are produced due to the strong interaction. Electroweak processes in which W,Z[9], γ, or H bosons are produced, however, can produce (charged) leptons in the final state. Due to the probabilistic nature of the collisions and processes involved therein, experimental studies regarding a particular *signal* process typically require handles to enrich the signal with respect to other *background* processes. Hence, leptonic decays of weak bosons are of great importance. The relative decay widths

[8] s denotes one of the three Mandelstam variables s, t, u. For a process with four-momenta $p_1, p_2 \to p_3, p_4$ these are given by $s = (p_1 + p_2)^2$, $t = (p_1 - p_3)^2$, and $u = (p_1 - p_4)^2$.

[9] Including processes with *off-shell* electroweak currents with $q^2 \neq 0, m_W^2, m_Z^2$, the neutral currents often being denoted as Z/γ^*.

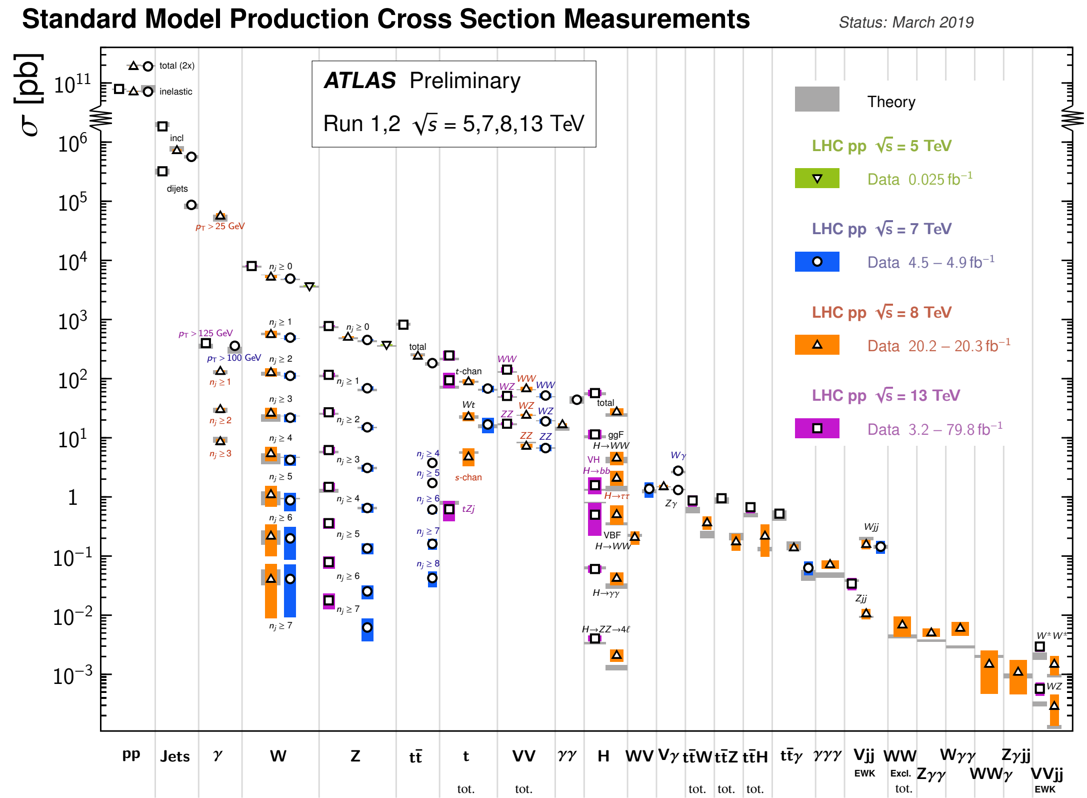

Figure 2.10.: Summary of predicted and measured cross sections in proton-proton collisions for various processes in the SM. From Ref. [59].

called *branching ratios* $\mathcal{B}_i = \Gamma_i/\Gamma_{\text{total}}$ of W, and Z bosons are shown in Fig. 2.11. Branching ratios specify the probability of a decay to a particular final state. While electrons are stable and muons can be considered as stable on typical experimental distances (proper life time $c \cdot \tau_\mu \approx 660\,\text{m}$) tau leptons ($c \cdot \tau_\tau \approx 87\,\mu\text{m}$) decay well within the instrumented area $\mathcal{O}(1\,\text{cm} - 10\,\text{m})$.

Although Higgs bosons only couple to massive particles the main production mode at the LHC is from a pair of gluons. In this process referred to as *gluon fusion* (ggF) the gluons produce a Higgs boson via a loop of heavy quarks, predominantly top quarks, as shown in Fig. 2.12 together with some of the subdominant production modes. The production cross sections of the SM Higgs boson with mass $m_H = 125\,\text{GeV}$ are shown in Fig. 2.13. Branching ratios of the SM Higgs boson with a mass of 125 GeV are shown in Fig. 2.14, a subset of its decay modes (*decay channels*) is illustrated in Fig. 2.15.

At the LHC Higgs bosons produced via gluon fusion are most commonly accompanied by only little additional activity from the hard scatter besides the

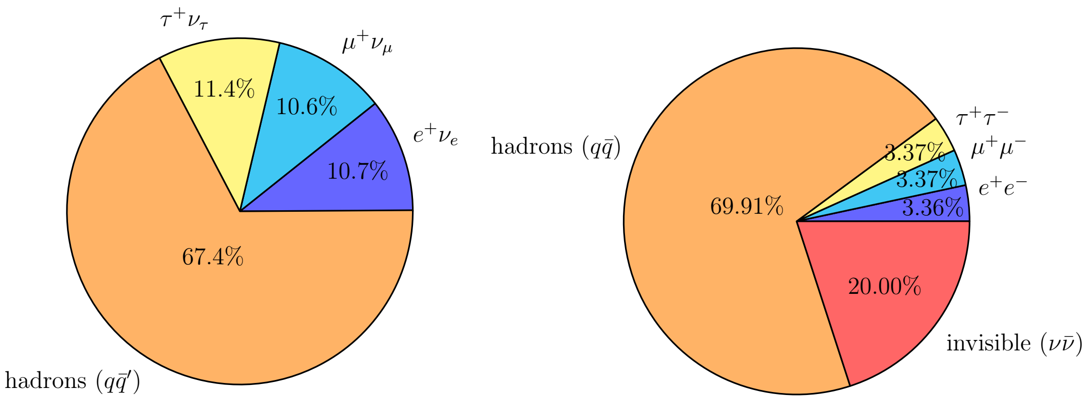

Figure 2.11.: Branching ratios Γ_i/Γ_{total} of W^+ (left) and Z bosons (right) based on Ref. [42] for the main decay modes. The W^- decay modes are charge conjugate to those of W^+.

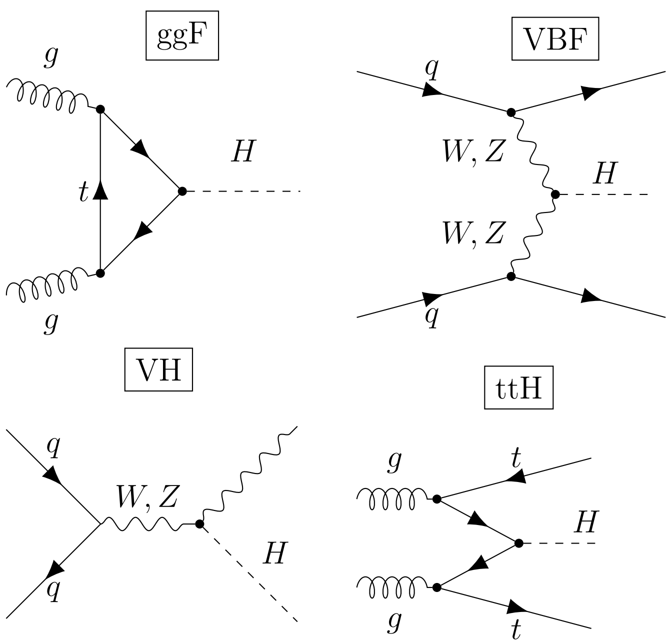

Figure 2.12.: Feynman diagrams for the most prominent production modes of Higgs bosons: gluon fusion (ggF), vector-boson fusion (VBF), Higgs strahlung (VH), and top associated production (ttH). Processes not shown include gluon induced Higgs strahlung ($gg \to ZH$) and production in association with a single top quark or a pair of bottom quarks.

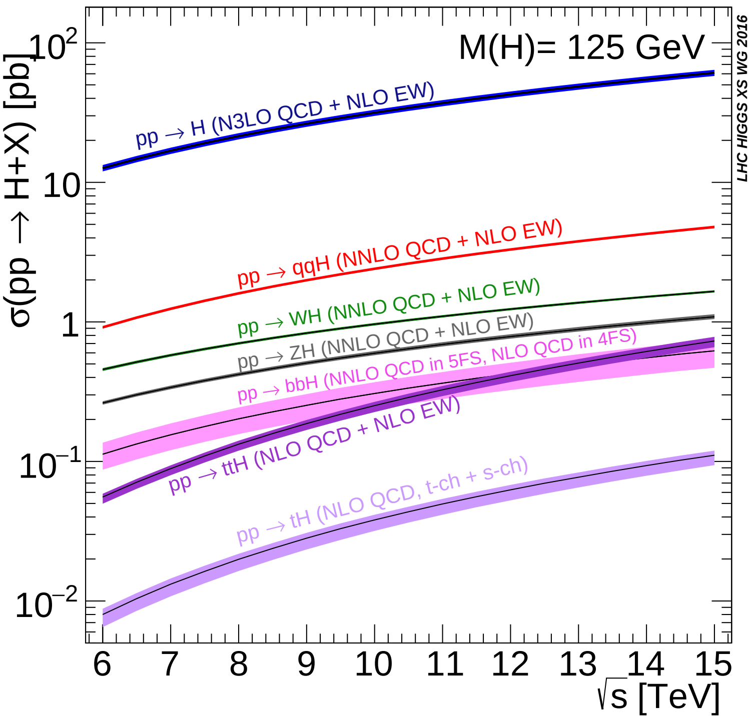

Figure 2.13.: Cross sections of different production modes of a 125 GeV Higgs boson in the SM depending on the center-of-mass energy of the proton-proton collision. Theoretical uncertainties are indicated by the line widths. The label of the process with the largest cross section $pp \to H$ is often referred to as ggF, the second largest ($pp \to qqH$) as VBF. From Ref. [60].

decay products from the Higgs boson itself. Hence, this production process is experimentally most accessible in well distinguished decay modes of the Higgs boson such as $H \to WW^* \to \ell\nu\ell'\nu'$, $H \to ZZ^* \to \ell\ell\ell'\ell'$ ($\ell = e, \mu$), and $H \to \gamma\gamma$. Examples for ggF production of Higgs bosons together with additional partons are shown in Fig. 2.16 including an example for production from a qg initial state. The production cross section quickly decreases with the number of additionally created jets [60].

The VBF production mode is characterized by the presence of two highly energetic jets from the quarks emitting the fusing vector bosons. As typically the quark momenta are only moderately changed in this process the emerging jets are emitted in the so called *forward* direction, i.e., close to the beam direction. These characteristic jets feature large values of the dijet invariant mass m_{jj} and a large

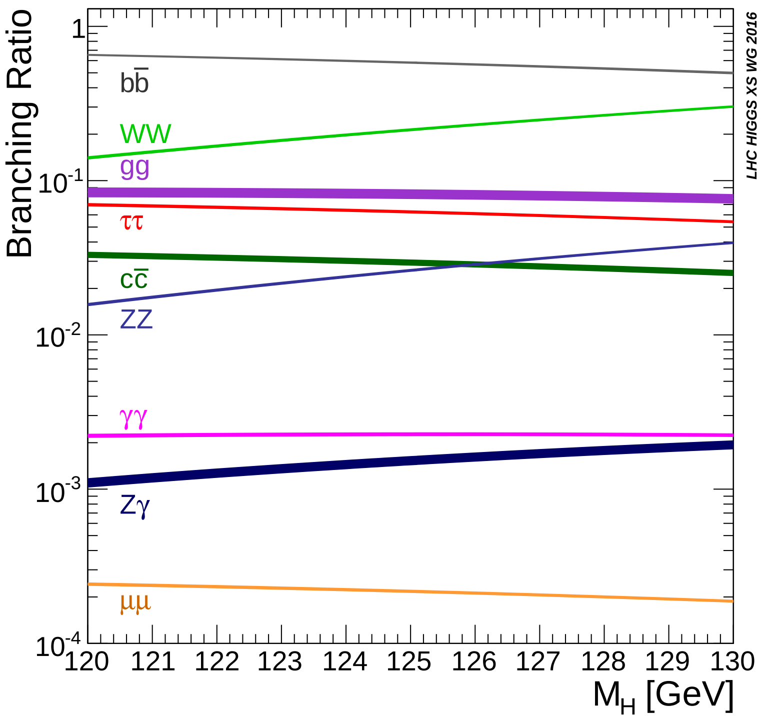

Figure 2.14.: Branching ratios of different decay modes of the SM Higgs boson depending on the mass m_H of the Higgs boson. From Ref. [60].

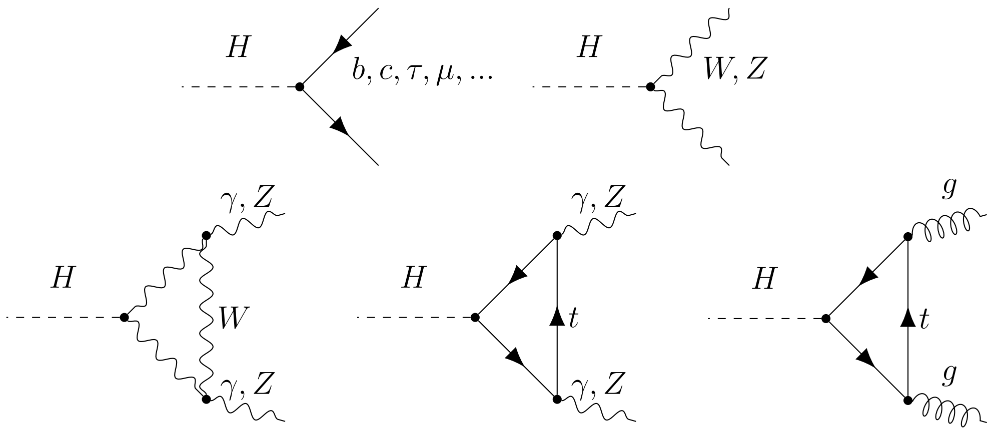

Figure 2.15.: Leading order Feynman diagrams for decay modes of Higgs bosons to pairs of fermions, W bosons, Z bosons, photons, $Z\gamma$, and gluons.

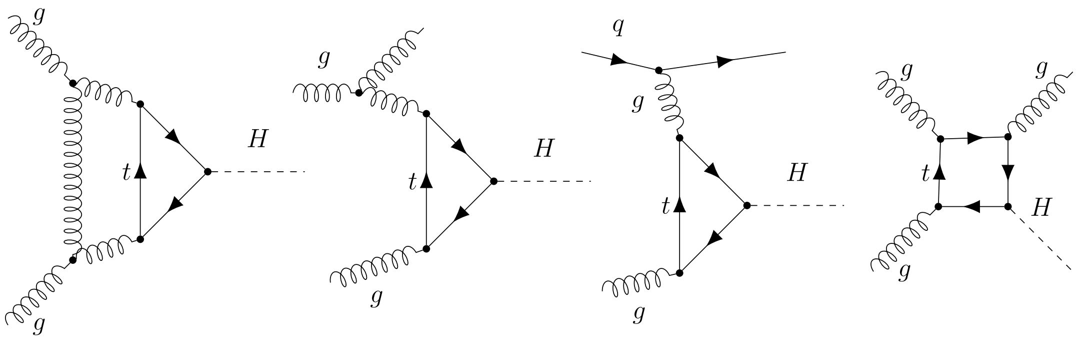

Figure 2.16.: Example diagrams of the ggF Higgs production with higher order corrections or emission of additional partons leading to additional jets. In place of the top quark any quark can occur in the loop. The largest contribution, however, is from the heaviest, *i.e.*, top quark.

rapidity gap $\Delta y = |y_1 - y_2|$ with

$$y = \frac{1}{2} \log \left(\frac{E + p_z}{E - p_z} \right)$$

where the z axis parallel to the direction of the momenta of the initial protons. While the rapidity y itself is not invariant under Lorentz boosts the rapidity difference between two objects Δy is invariant under boosts along the z axis. Exploiting these additional features can enhance the experimental sensitivity to decays such as $H \to \tau\tau$ [61, 62] even beyond the sensitivity to the same decay with ggF production despite the reduced event rate.

The Higgs strahlung production modes where the vector boson produces charged leptons are particularly interesting for studies of decays of Higgs bosons to pairs of b quarks. The low cross section of these production modes (with the additional restriction to $V \to \ell\ell, \ell\nu, \nu\nu,\ \ell = e, \mu$) is paired with the most frequent decay of Higgs bosons to b quarks to achieve observations of the latter [63, 64].

The $H \to \gamma\gamma$ and $H \to ZZ^* \to \ell\ell\ell'\ell'$ decay modes allow for full reconstruction of the mass of the Higgs boson candidates with high resolution. Recent measurements by the ATLAS [65] and CMS [66] collaborations report the mass as $m_H = 124.97 \pm 0.24\,\text{GeV}$ (ATLAS) and $m_H = 125.26 \pm 0.21\,\text{GeV}$ (CMS, using $H \to ZZ^* \to 4\ell$ only) respectively. While the mass has already been measured with great precision, resolutions considered experimentally achievable prohibit direct measurements of the total width. For a Higgs boson with $m_H \approx 125\,\text{GeV}$ it is predicted to be $\Gamma_H \approx 4\,\text{MeV}$ [60] in the SM while the aforementioned measurement by the CMS collaboration reports only an upper limit of $\Gamma_H < 1.1\,\text{GeV}$ at 95% confidence level (CL).

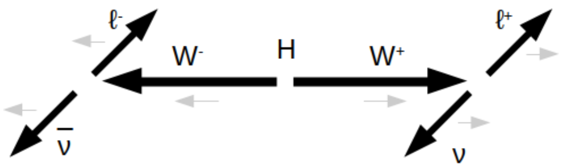

Figure 2.17.: Illustration of the spin correlation in the $H \to WW^* \to \ell\nu\ell'\nu'$ channel. Large, black arrows indicate the particles direction (in the rest frame of the Higgs boson), small gray arrows their spin projected onto the decay axis of the Higgs boson for one possible spin configuration.

The $H \to WW^* \to \ell\nu\ell'\nu'$ decay mode comprises $(1.007 \pm 0.022)\%$ [60] of all decays of Higgs bosons[10]. An important feature of this mode is illustrated in Fig. 2.17. Due to the Higgs boson carrying spin-0 the spins of the W bosons along the decay axis are anti-parallel: $m_s(W^+) = +1/0/-1 = -m_s(W^-)$. For non-vanishing m_s the spins of neutrino and anti-neutrino are therefore anti-aligned as well. The helicity defined through the operator $h = \frac{1}{2}\vec{\sigma}\frac{\vec{p}}{|\vec{p}|}$ is the projection of a particle's spin onto its direction of motion. Its eigenstates with eigenvalues $\pm\frac{1}{2}$ coincide for massless fermions ψ with those of of chiral projection operators. As the SM only contains massless, left (right) chiral (anti-)neutrinos this implies that the neutrino and anti-neutrino produced in the $H \to WW^* \to \ell^+\nu\ell^{-\prime}\bar{\nu}'$ must posses opposite helicities. As their spins are already anti-aligned their momenta must be aligned and they are, hence, emitted in the same hemisphere in the rest frame of the Higgs boson. Momentum conservation then requires also the charged leptons $\ell^+, \ell^{-\prime}$ to be emitted in the opposite hemisphere with small angular separation with respect to each other. As a consequence this dilepton system also features a smaller values of its invariant mass $m_{\ell\ell}$ compared to, *e.g.*, the case of non-resonant WW production.

2.4. Maximum Likelihood Method

Comparisons of predicted and measured distributions at complex experiments such as the ATLAS experiment often involve many parameters and measurements thereof. A commonly used method to extract parameters of interest (POI) such as cross sections and to compare different hypotheses is the *maximum likelihood method* (see, *e.g.*, Refs. [67–69]). An exhaustive discussion of all aspects of likelihoods is well beyond the scope of this document. Hence, only the most relevant aspects

[10] For $m_H = 125\,\text{GeV}$ and $\ell = e, \mu$. Decays via $W \to \tau\nu \to \nu\nu\ell\nu$ are neglected here. In addition to the reduced event yield due to the $\tau \to \nu\ell\nu$ branching ratio, the additional neutrinos dilute the experimental signature compared to the $H \to WW^* \to \ell\nu\ell'\nu'$ process.

for analyses such as those presented in Chap. 4 are discussed here. The software packages RooFit [70] and HistFactory [71] are frequently used in LHC experiments in this context. Terminology and notation used here are loosely adapted from these packages. For simplicity a binned counting experiment is assumed, *i.e.*, measurements are event yields d_i in multiple orthogonal regions i of phase space, *i.e.*, bins in one or more histograms.

Let $n_i(\vec{\theta})$ denote the expected event yield in each bin as a function of a set of parameters $\vec{\theta}$. The parameters $\vec{\theta}$ include one or more POIs as well as so called *nuisance parameters*. The likelihood is eventually to be maximized with respect to $\vec{\theta}$. Nuisance parameters are of no immediate interest for an analysis at hand but required to construct an adequate statistical model including uncertainties associated with said parameters. A typical likelihood L has the form

$$L = \prod_{\text{bins } i} P(d_i|n_i(\vec{\theta})) \cdot \prod_{\theta_k} C_k(\theta_k), \tag{2.10}$$

where P is the Poisson probability

$$P(d|n) = \frac{n^d}{d!} e^{-n}.$$

For $d \notin \mathbb{N}$ it is generalized through the replacement of the factorial $d!$ with the gamma function $\Gamma(d+1)$. The C_k are constraint terms representing external measurements for the θ_k[11] which are assumed to be initially uncorrelated[12].

- For systematic uncertainties such as ones related to the theoretical modeling or calibrations common choices for the C_k are normal or log-normal distributions. Calibrations are generally obtained from other measurements involving several uncertain, *i.e.*, random quantities. The use of (log-)normal constraints is therefore motivated by the central limit theorem [67].
- For parameters purely determined *in-situ* C_k is a constant. Parameters frequently found in this category include the POIs and normalization parameters for background processes.
- The case of nominal yields $n_{i,\text{nom}}$ being obtained from finite samples such as MC simulation is discussed in Ref. [72]. The corresponding constraint term is then usually taken as a Poisson distribution. In case events in the

[11] In Ref. [68] the likelihood is formulated such that nuisance parameters are constrained by expanding the set of bins to include data suitable for determination of the θ_k. Such a treatment, however, is often not feasible, *e.g.*, in case of parameters describing uncertainties on theoretical predictions or experimental parameters determined in dedicated external measurements.

[12] In case of complex external measurements their potentially correlated uncertainties can be transformed to uncorrelated ones by means of eigenvalue decompositions.

samples are weighted the mean of the Poisson distribution is rescaled to match the estimated variance of the MC sample in the respective bin. In the default implementation in HistFactory [71] the approximation is made to only use a single parameter per bin for the sum of multiple processes instead of individual parameters for each process and bin.

Estimates for the POIs are obtained by maximizing the likelihood with respect to $\vec{\theta}$. Equivalently the negative log-likelihood (NLL), $-\log L$, can be minimized which is often computationally preferable. The maximization or minimization respectively are summarized as fitting a dataset. The resulting shifts of parameters with respect to their nominal values $\hat{\theta}_k - \theta_{k,\text{nom}}$ are referred to as *pulls*. For parameters with Gaussian constraint terms the parametrization is usually chosen such that the constraint term is a unit Gaussian with central value $\theta_{k,\text{nom}} = 0$ and standard deviation 1.

2.4.1. Hypothesis Testing

The absolute value of L has no meaning. In order to test two hypotheses, H_0 and H_1 with parameters $\vec{\theta}_0$ and $\vec{\theta}_1$, against each other the *log-likelihood ratio*

$$2\Delta\text{NLL} = -2 \cdot \log \lambda, \text{ with } \lambda = \frac{L(\hat{\vec{\theta}}_0)}{L(\hat{\vec{\theta}}_1)}$$

can serve as a test statistic[13]. Here $L(\hat{\vec{\theta}}_i)$ denote the value fo the likelihood maximized with respect to the parameters $\hat{\vec{\theta}}_i$. Two hypotheses are nested if the set of parameters of one is a subset of the parameters of the other. The hyothesis with fewer parameters can be seen as a *conditional* version of the other. The *conditional* maximum likelihood denoted as $L(\hat{\vec{\theta}}_{\text{cond}})$ is the value of the likelihood maximized with respect to all but m elements of $\vec{\theta}_{\text{uncond}}$ for which fixed values of the conditional hypothesis H are to be tested. The *unconditional* maximum likelihood denoted as $L(\hat{\vec{\theta}}_{\text{uncond}})$ is maximized with respect to all elements of $\vec{\theta}$. Then, in the so called *asymptotic limit* of large samples $d_i, n_i \to \infty$, the log-likelihood ratio 2ΔNLL is distributed according to a χ^2 distribution with m degrees of freedom if H is true [68, 69]. In the following the applicability of this asymptotic approximation is assumed.

[13] In Ref. [68] additionally multiple variants of such test statistics are discussed where the POI and/or the test statistic are truncated at some point motivated by the test to be performed. While the distributions of the test statistics differ slightly the overall procedure laid out here remains the same.

For establishing the presence of a signal one often uses a *signal strength* parameter μ as POI. Writing out μ explicitly $n_i(\mu, \vec{\theta}) = b(\vec{\theta}) + \mu s(\vec{\theta})$ where s and b denote the expected event yields from the signal and background processes. The conditional or null-hypothesis H_0 then corresponds to $\mu = 0$ and $L(\mu = 0, \hat{\hat{\vec{\theta}}}_0)$, the unconditional or alternative hypothesis H_1 to $\mu = \hat{\mu}$ and $L(\mu = \hat{\mu}, \hat{\hat{\vec{\theta}}}_\mu)$ where quantities with hats are *best fit* values maximizing L under the given hypothesis. Using the asymptotic approximation or by creating pseudo experiments[14] the probability p can be determined to find a value of 2ΔNLL larger than the one found for the present dataset if H_0 is true. If p is below a certain threshold the hypothesis H_0 is considered rejected in favor of H_1. For $m = 1$ degree of freedom as in the example just considered it is customary to convert p to a number Z of standard deviations σ of a standard normal distribution such that

$$1 - p = \int_{-\infty}^{Z} \frac{1}{\sqrt{2\pi}} e^{-x^2/2}\, dx. \tag{2.11}$$

By convention for an *observation* of a new signal in particle physics the significance is required to exceed $Z = 5$ corresponding to a probability of $p = 2.87 \cdot 10^{-7}$ for the null-hypothesis being true. For the exclusion of a potential new signal the threshold for the signal hypothesis being true is usually taken to be $p = 5\%$ corresponding to a 95% confidence level (CL) for the rejection of the signal hypothesis (see, *e.g.*, Ref. [68]).

2.4.2. Uncertainty Estimates

Uncertainty estimates of parameters in a likelihood fit can be obtained from the diagonal elements of the covariance matrix $V_{k\ell} = \mathrm{cov}(\hat{\theta}_k, \hat{\theta}_\ell)$ which is related to the Hessian of the NLL

$$(V^{-1})_{k\ell} = -\frac{\partial^2 \log L(\hat{\vec{\theta}})}{\partial\theta_k \partial\theta_\ell}.$$

The so obtained covariance only describes the shape of the NLL near the minimum. An alternative approach to estimating an individual parameter's *post-fit* uncertainty is connected to the profile log-likelihood ratio

$$2\Delta\mathrm{NLL}(\theta'_k) = -2 \log \frac{L\left(\hat{\hat{\vec{\theta}}}(\theta_k = \theta'_k)\right)}{L\left(\hat{\hat{\vec{\theta}}}(\theta_k = \hat{\theta}_k)\right)},$$

[14] Pseudo-datasets $\tilde{d}_i$ are created by randomly sampling the expected yields according to the distributions given by the constraint terms of nuisance parameters and the Poisson distributions of the n_i themselves.

where the fit is performed under the condition that $\theta_k = \theta'_k$ in the numerator and unconditionally in the denominator. As before, if θ'_k was the true value then $2\Delta\mathrm{NLL}$ is distributed according to a χ^2 distribution. Here it is convenient to express confidence levels in terms of symmetric, two-sided confidence intervals of a normal distribution with standard deviation σ. As detailed in App. A the confidence interval corresponding to $n \cdot \sigma$ of a normal distribution is given by the *crossing points* where

$$\sqrt{2\Delta\mathrm{NLL}} = n.$$

A common definition of a parameter's possibly asymmetric post-fit uncertainty is therefore given by the differences between the best-fit value and the upper and lower limit of the surrounding 1σ confidence interval[15] often written in the form $\hat{\theta}_k \,{}^{+\sigma_k^+}_{-\sigma_k^-}$. In the implementation provided in Ref. [70] the Minos algorithm determines the crossing points by iterative means. Nuisance parameters with dedicated constraint terms are called *overconstrained* if their so obtained *post-fit uncertainty* is much smaller than the *pre-fit uncertainty* implied by the constraint term.

2.4.3. Ranking of Uncertainties

When performing a complex measurement with several sources of uncertainties it is desirable to quantify the *effect* of individual or groups of sources of uncertainties on the total uncertainty of a POI μ. To this end two prescriptions are commonly used, referred to as *impacts* and *breakdowns* in the following.

The impact method quantifies the effect of an uncertainty based on the best fit values of μ. To determine the impact of a nuisance parameter θ_k an unconditional fit giving $\hat{\theta}_k$ as well as conditional fits with fixed $\theta_k = \hat{\theta}_k \pm \sigma_{\theta_k}$ are performed. The positive and negative impacts $I_k^\pm$ are then given by the shifts of $\hat{\mu}$ with respect to the unconditional fit

$$I_k^\pm(\theta_k) = \mu(\hat{\theta}_{k,\mathrm{nom}} \pm \sigma_{\theta_k}) - \hat{\mu}(\theta_k = \hat{\theta}_k).$$

In the conditional fit other parameters may adjust to partially compensate the shift of θ_k. Depending on whether pre- or post-fit values of σ_{θ_k} are used the impacts are called *pre-* or *post-fit impacts.*

The breakdown prescription uses the post-fit uncertainties of the POI. For a group of one or more nuisance parameters $\{\theta_k\}$ the uncertainties of the POI are

[15] The profile log-likelihood ratio $2\Delta\mathrm{NLL}$ can, in general, exhibit multiple minima. In such a case the "confidence interval" is not necessarily a single, continuous interval but the union of multiple such intervals for which $\sqrt{2\Delta\mathrm{NLL}} < n$ where $2\Delta\mathrm{NLL}$ is taken with respect to the global minimum.

determined from an unconditional likelihood where the $\{\theta_k\}$ are variable and a conditional likelihood where the $\{\theta_k\}$ are treated as constant at their best fit values from the unconditional fit. The latter leads to a more narrow minimum in the profiled log-likelihood of the POI, that is, the uncertainty of the POI is reduced. The breakdown $B^{\pm}_{\{\theta_k\}}$ is then given by

$$B^{\pm}_{\{\theta_k\}} = \sqrt{(\sigma^{\pm}_{\mathrm{POI,uncond}})^2 - (\sigma^{\pm}_{\mathrm{POI,cond}})^2}. \tag{2.12}$$

Statistical uncertainties due to the finite size of the dataset are not represented by a parameter in the likelihood. Their effect is therefore usually taken to be the residual uncertainty of the POI when fixing all nuisance parameters with dedicated, external constraint terms $C_k \neq const.$ to their best fit values.

The breakdown method requires the definition of a confidence interval for the POI, usually chosen to be the 1σ interval. In case of low sensitivity of a measurement to the POI this may not be well defined. In contrast the impact method only requires such intervals only for nuisance parameters for which this is in practice guaranteed by the C_k. An asset of the breakdown method, however, is that it can be applied in the same way to single or multiple parameters at once. This allows for the comparison of their effects based on a consistent prescription. In general there is no prescription how the signs of different parameters relate to each other. Assessing a combined impact for a set of parameters by constructing an envelope would require to consider all combinations of shifting each parameter in the set by $+1\sigma_k$ and $-1\sigma_k$. Hence, such an impact-like prescription leads to exponential complexity. Further more such a treatment in general does not take correlations of these parameters correctly into account.

In cases such as statistical uncertainties of simulated MC samples the resulting uncertainties are represented by one or more parameters per bin. Simulating larger MC samples reduces the statistical uncertainties in not just one bin but in many or all. In comparisons to other sources of uncertainties it is therefore adequate to consider the combined effect of all nuisance parameters representing the bin-wise MC statistical uncertainties. Similarly comparisons of systematic uncertainties to the effect of the statistical uncertainty of the dataset fitted are more methodologically consistent when comparing to breakdown-based values for the effects of systematic uncertainties. Ranking of sources of uncertainties based on either prescription generally differ for different POIs.

2.4.4. Asimov Dataset

The use of an artificial dataset, the so called *Asimov dataset*, is suggested in Ref. [68]. This dataset is defined as the set of $d_i = n_i(\vec{\theta})$ where the parameters $\vec{\theta}$ are taken at their nominal value. Vanishing pulls are obtained from fitting a likelihood constructed from this dataset. The Asimov dataset allows to study, *e.g.*, the expected sensitivity of a measurement or expected post-fit correlations. To this end It is also crucial for thorough optimizations of analyses as optimizations based on the observed dataset would introduce potential biases to the final result.

2.4.5. Post-fit Distributions and Uncertainties

So called *post-fit* distributions and event yields refer to those including modifications to the initially (*pre-fit*) predicted distributions implied by maximizing the likelihood. In the following prescriptions to obtain such distributions are outlined as used in this thesis, in particular in Chap. 4.

For distributions used directly in the construction of the likelihood the post-fit distribution is given by $n_{i,\mathrm{post-fit}} = n_i(\hat{\vec{\theta}}_{\mathrm{uncond}})$. For distributions in different variables or with different bin boundaries than the distributions used in the construction of L an exact treatment is often not feasible[16]. The effects of pulls to an arbitrary distribution of events after the same event selection as used for a region in the likelihood fit are therefore approximated. To this end effective scale factors for individual processes can be calculated as the ratio $n_{\mathrm{post-fit}}/n_{\mathrm{pre-fit}}$ of the modeled yields integrated over the region in question. These scale factors are then applied to the nominal distribution of the respective process.

Post-fit yield uncertainties $\Delta_{\mathrm{post-fit}}$ are calculated taking into account linear correlation coefficients $\mathrm{corr}(i,j)$ obtained from the covariance matrix described in Sec. 2.4.2:

$$\Delta^2_{\mathrm{post-fit}} = \delta n(\theta_i)\,\mathrm{corr}(i,j)\delta n(\theta_j).$$

Here, $\delta n(\theta_i)$ represents the symmetrized yield change of one or the sum of multiple processes

$$\delta n(\theta_i) = \left[n\left(\hat{\theta}_i + 1\sigma_{\mathrm{post-fit}}(\theta_i)\right) - n\left(\hat{\theta}_i - 1\sigma_{\mathrm{post-fit}}(\theta_i)\right)\right]/2.$$

[16] *e.g.*, due to the lack of templates needed in the modeling of changes of modeled yields due to pulls

3 The Large Hadron Collider and the ATLAS Detector

3.1. The Large Hadron Collider

The Large Hadron Collider LHC [73] is the largest and most powerful particle accelerator built to date. It is situated in a tunnel of about 27 km circumference in the Geneva area spanning across the border of Switzerland and France. The tunnel was previously housing the Large Electron Positron Collider LEP [74]. The collider complex the LHC is part of, and which is illustrated in Fig. 3.1, is built, maintained, and operated by the European Organisation for Nuclear Research CERN (named after the *Conseil Européen pour la Recherche Nucléaire*). At its design specifications it is capable of accelerating and colliding two counter rotating beams of protons at an energy of up to 7 TeV and lead ions at up to 2.8 TeV per nucleon. In proton-proton collision mode it has thus far been operated[1] at beam energies of 3.5 TeV in 2011, 4 TeV in 2012 (collectively called *Run 1*) and 6.5 TeV from 2015 through 2018 (*Run 2*) corresponding to center-of-mass energies of $\sqrt{s} = 7,\ 8,$ and 13 TeV. The protons are created through ionization of hydrogen before being injected to LINAC2 and gradually accelerated further in the Booster, Proton Synchrotron (PS) and Super Proton Synchrotron (SPS) up to the LHC injection energy of 450 GeV. Despite the common parlance of *beams* the accelerated particles typically do not form a continuous stream but are accelerated in *bunches*.

The proportionality factor between the cross section σ of a process and the event rate unit per time n introduced in a simplified form in Sec. 2.1.4 is called *instantaneous luminosity* $\mathcal{L}(t)$, its time integrated value simply *luminosity* $\mathcal{L} = \int \mathcal{L}(t)\,dt$. For accelerators such as the LHC it can be expressed as [42, 73]

$$\mathcal{L}(t) = \frac{N_1 N_2 n_b f_{\mathrm{rev}}}{4\pi\sigma_x^*\sigma_y^*} \cdot F, \quad F = \sqrt{\frac{1}{1 + \left(\frac{\theta_c\sigma_z}{2\sigma_x^*}\right)^2}}. \tag{3.1}$$

[1] Only operational periods with major data recording by the main LHC experiments are considered here.

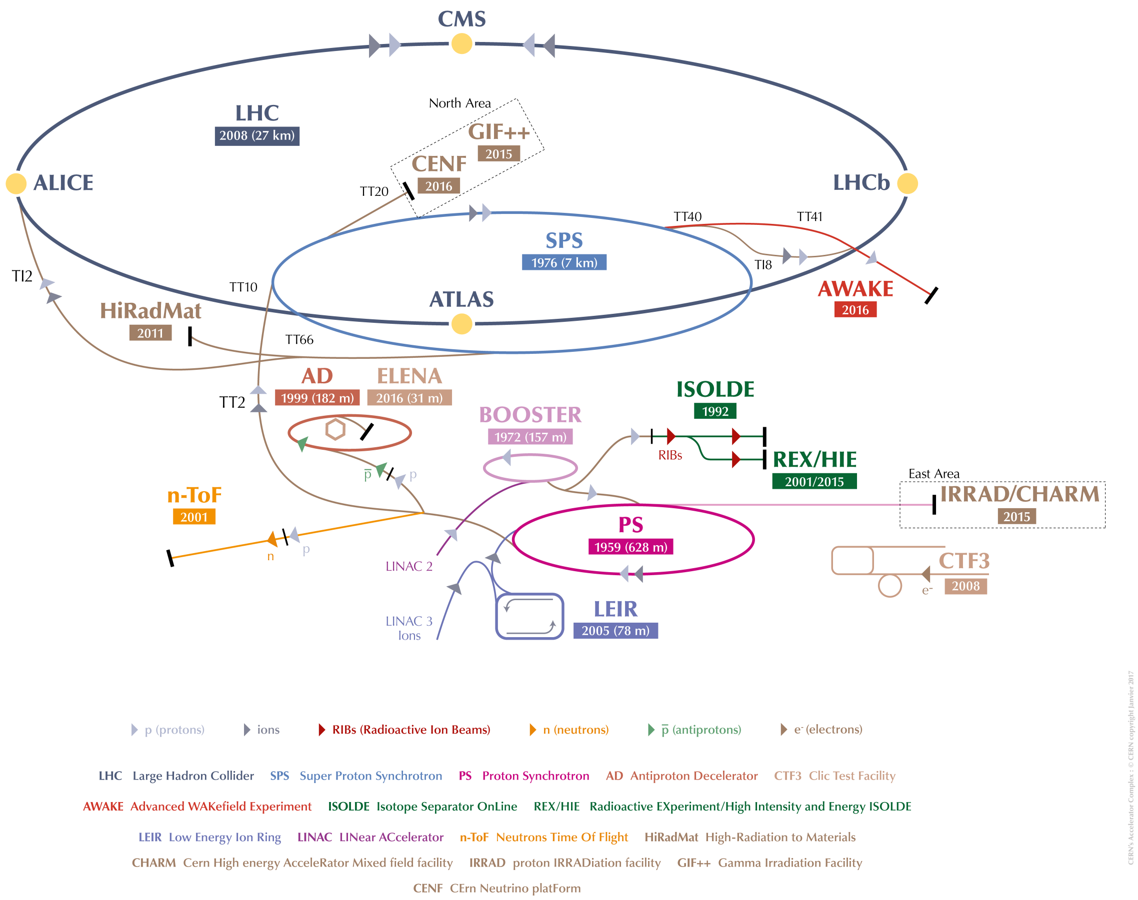

Figure 3.1.: Overview of the CERN accelerator complex including the LHC and the locations of its four main experiments: ALICE, ATLAS, CMS, and LHCb. From [75].

The individual variables in this equation are summarized in Tab. 3.1 together with their typical values at the LHC. The factor F accounts for reduced geometric overlap due to the beams not colliding head on but instead under a small angle. In Eq. (3.1) this crossing is assumed to be in the $x - z$ plane. While the design luminosity of the LHC inside the ATLAS and CMS experiments is $10^{34}\,\mathrm{cm}^{-2}\,\mathrm{s}^{-1}$ [73], measurements, *e.g.*, with the ATLAS detector, report up to $2.1 \cdot 10^{34}\,\mathrm{cm}^{-2}\,\mathrm{s}^{-1}$ [76] during Run 2. While high instantaneous luminosity is required for studies of rare processes it does impose challenges to the experiments in the form of pile up. The mean numbers of interactions per bunch crossing during the Run 2 data taking with the ATLAS detector are shown in Fig. 3.2.

Table 3.1.: Parameters in the luminosity equation (3.1) and their typical values at the LHC in 2016. Values may vary between operational periods. Based on [42, 73, 77].

description	symbol	typical value
protons per bunch (at start)	N_1, N_2	$1.1 \cdot 10^{11}$
bunches per beam	n_b	2200
revolution frequency	f_{rev}	11 kHz
transverse beam size (rms) at collision point	σ_x^*, σ_y^*	$11\,\mu$m
bunch length (rms)	σ_z	6 cm
full beam crossing angle	θ_c	$280 - 370\,\mu$rad
geometric reduction factor	F	0.65
instantaneous luminosity	$\mathcal{L}(t)$	$1.4 \cdot 10^{34}\,\mathrm{cm}^{-2}\,\mathrm{s}^{-1}$

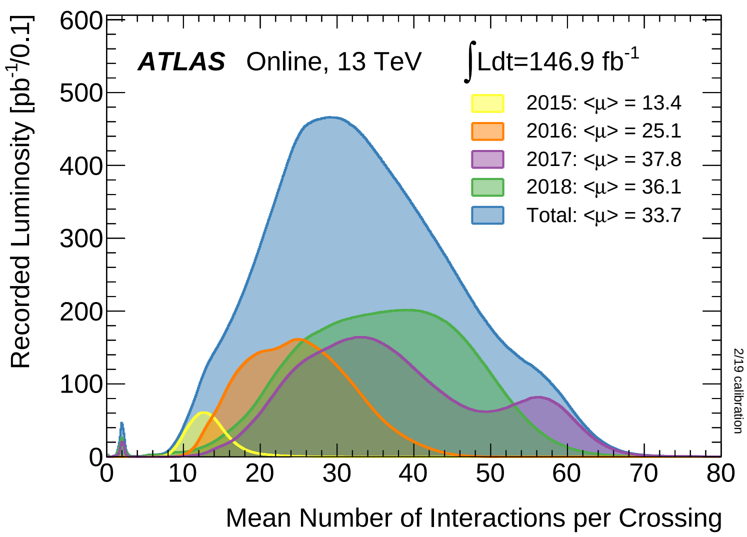

Figure 3.2.: Mean number of inelastic interactions per bunch crossing in the ATLAS detector during the LHC Run 2. The double-peak structure for the year 2017 is due to changed bunch train sequences circumventing technical difficulties during the operation [78]. From [76].

While during Run 2 the ATLAS experiment (and similarly the CMS experiment) were required to handle about $50 - 60$ simultaneous inelastic interactions this number is anticipated to increase to $140 - 200$ at the planned upgrade of the LHC, the High Luminosity LHC or HL-LHC for short [6]. During its operation planned for 2026-2040 it is foreseen to deliver $3000 - 4000\,\mathrm{fb}^{-1}$ to the ATLAS and CMS experiments each.

3.2. The ATLAS Detector

The ATLAS detector [79] (*A Toroidal LHC ApparatuS*) is located in the *point 1* cavern of the LHC near Meyrin, Switzerland. In contrast to the more specialized LHC detectors LHCb[2] [80] and ALICE[3] [81] the ATLAS as well as the CMS[4] [82] detectors are designed to cover a broad range of physics processes to be studied. In this section a summary of the most important subdetectors of the ATLAS detector is given. A comprehensive description of the initial design can be found in Ref. [79], the most significant modifications between the Run 1 and Run 2 detector being the addition of the insertable b-layer [83] (IBL) and an upgrade of the trigger system [84]. An overview of the entire detector is shown in Fig. 3.3.

3.2.1. The ATLAS Coordinate System

The origin of the ATLAS coordinate system is chosen to be at the nominal interaction point. The positive x, and y axes point towards the center of the LHC ring, and upward, respectively. The z axis is given by the beam axis forming a right-handed coordinate system. The angle ϕ is measured in the *transverse plane* spanned by the x and y axes. The angle with respect to the z axis is denoted by θ. More commonly, however, the *rapidity* y or the *pseudorapidity* $\eta = -\log\tan(\theta/2)$ are used instead of θ. For massless particles one finds $\eta = y$. An angle of $\theta = 90°$ to the beam axis corresponds to $\eta = 0$ while the beam axis itself corresponds to $\eta = \pm\infty$. Angular distances in the $\eta - \phi$ space are often expressed in terms of $\Delta R = \sqrt{\Delta\eta^2 + \Delta\phi^2}$.

[2] *Large Hadron Collider beauty*, targeting CP violation and rare decays of hadrons containing b quarks

[3] *A Large Ion Collider Experiment*, targeting studies of the quark-gluon plasma in heavy ion collisions

[4] *Compact Muon Solenoid*

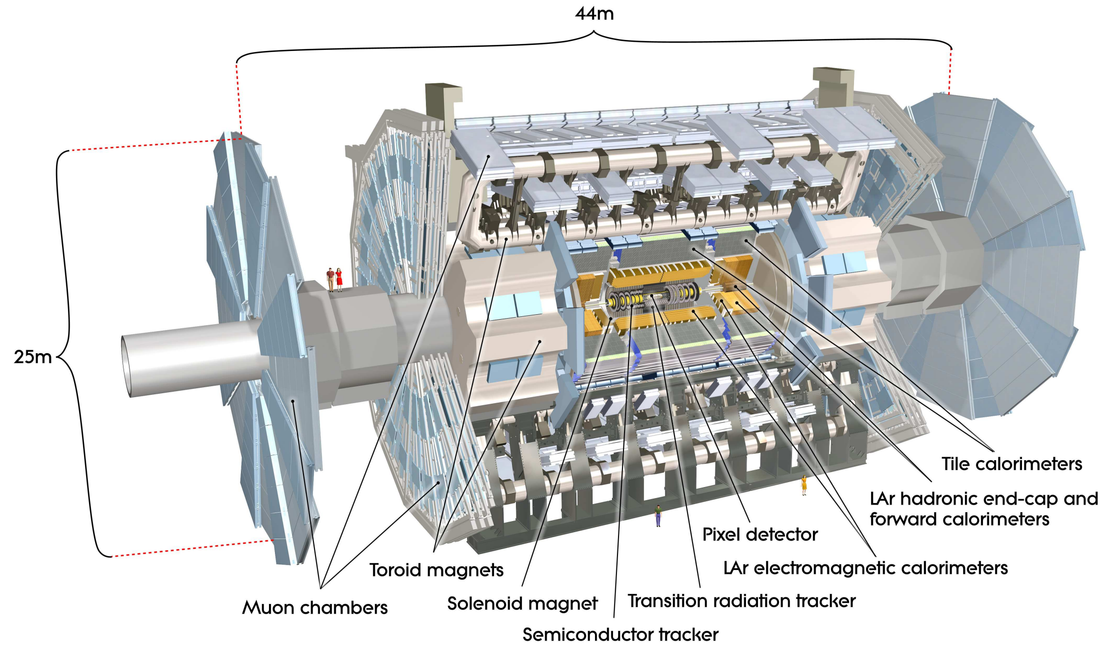

Figure 3.3.: Cutaway illustration of the original ATLAS detector design. From [79].

3.2.2. The Inner Detector

The ATLAS inner detector is shown in Fig. 3.4 and is targeted at recording the trajectories of charged particles[5] emerging from the collisions at its center. In order to measure the particles' momenta and charges it is immersed in a 2 T magnetic field created by the surrounding superconducting solenoid magnet. The different subsystems of the inner detector are arranged in a cylindrical shape in the *barrel* region (low $|\eta|$) and in a disk shape (normal to the beam axis) or radial direction in the forward directions (higher $|\eta|$).

Multiple layers of silicon pixel detectors are installed at the center of the detector starting at a radius of $r = 33.5\,\mathrm{mm}$ from the interaction point [83]. The pixel size is $50 \times 400\,\mu\mathrm{m}^2$ ($50 \times 250\,\mu\mathrm{m}^2$ for the IBL) with the longer edge oriented parallel to the beam axis (barrel) and in radial direction (disks) providing high resolution in $r - \phi$ (barrel) and $z - \phi$ (disks). A particle originating from the interaction point typically passes through four layers of silicon pixel sensors in the barrel.

Following outwards from the pixel detector silicon strip detectors are installed. In the barrel region four double layers provide space points with accuracies of $17\,\mu\mathrm{m}$ and $580\,\mu\mathrm{m}$ in $r - \phi$ and z directions respectively. In each double layer one set of

[5] In the context of detectors and interactions therewith "charged" refers to electrical charge unless indicated differently.

strips is oriented parallel to the z direction while the other is rotated by 40 mrad to allow for the accuracy of the z coordinate measurement despite the much longer strip length of several centimeters. Larger stereo angles would allow for even more accurate determination of the z coordinate this leads to ambiguities when multiple particles pass the same module. In the forward region nine layers of similar strip detectors can be found with strips facing in radial direction[6]. The two types of silicon based detectors cover the pseudorapidity range $|\eta| < 2.5$.

The last part of the inner detector is the *Transition Radiation Tracker* (TRT) which consists of straws of 4 mm diameter and a length of 144 cm (barrel, parallel to the beam axis) and 37 cm (forward, radial orientation). The straws are filled with a gas mixture originally based on xenon which allows for detection of transition radiation benefiting the identification of electrons. The barrel part of the TRT is split in two halves near $\eta = 0$. The TRT provides typically 36 measurement points with an accuracy per straw of 130 μm in $r - \phi$ direction and no significant information in z direction. It covers the range $|\eta| < 2.0$.

The inner detector without the IBL was designed [79] to achieve a (transverse) momentum resolution in the central region that can roughly be parametrized as

$$\frac{\sigma_{p_\mathrm{T}}}{p_\mathrm{T}} = 0.05\% \cdot p_\mathrm{T} \cdot \mathrm{GeV}^{-1} \oplus 1\% \tag{3.2}$$

where $\oplus$ means addition in quadrature. In the limit of large values of p_T, i.e., where the constant term due to multiple scattering becomes negligible, an intrinsic resolution of $\frac{\sigma_p}{p} = (0.0483 \pm 0.0016)\,\% \cdot p_\mathrm{T} \cdot \mathrm{GeV}^{-1}$ was measured [85] using cosmic rays prior to the start of collision data taking. The addition of the IBL left the momentum resolution essentially unchanged while improving the resolution of the impact parameters d_0 and z_0 [86].

3.2.3. The Calorimeter System

The calorimeter system of the ATLAS detector surrounds the inner detector and the solenoid magnet. Over most of the covered pseudorapidity range it is subdivided radially into an electromagnetic calorimeter followed by a hadronic calorimeter. Both, electromagnetic and hadronic calorimeters are sampling calorimeters. They are subdivided in different ranges of pseudorapidity using different types of calorimeter technology. The calorimeter system is illustrated in Fig. 3.5. The total coverage of the calorimeter system extends up to $|\eta| = 4.9$.

The electromagnetic calorimeter is based on liquid argon (LAr) as a scintillator with lead plates as absorbers. The barrel part of the electromagnetic calorimeter

[6] or rotated by 40 mrad with respect to this direction

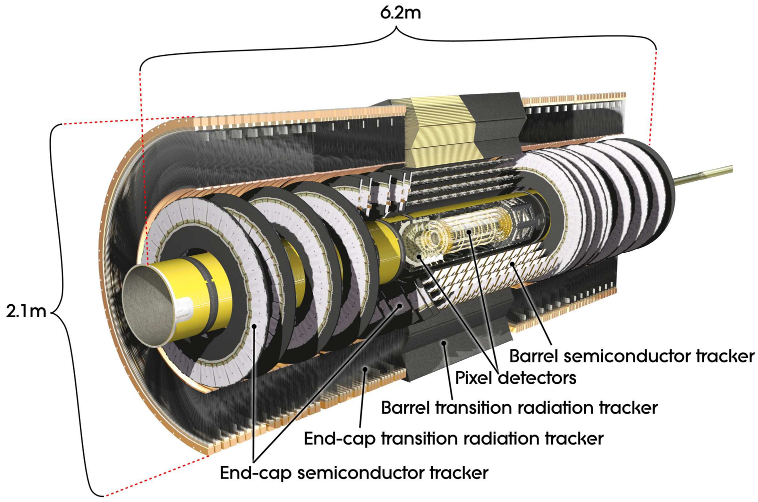

Figure 3.4.: Cutaway illustration of the original ATLAS inner detector design. The insertable b-layer (IBL) installed between Run 1 and Run 2 of the LHC is missing in this depiction. From [79].

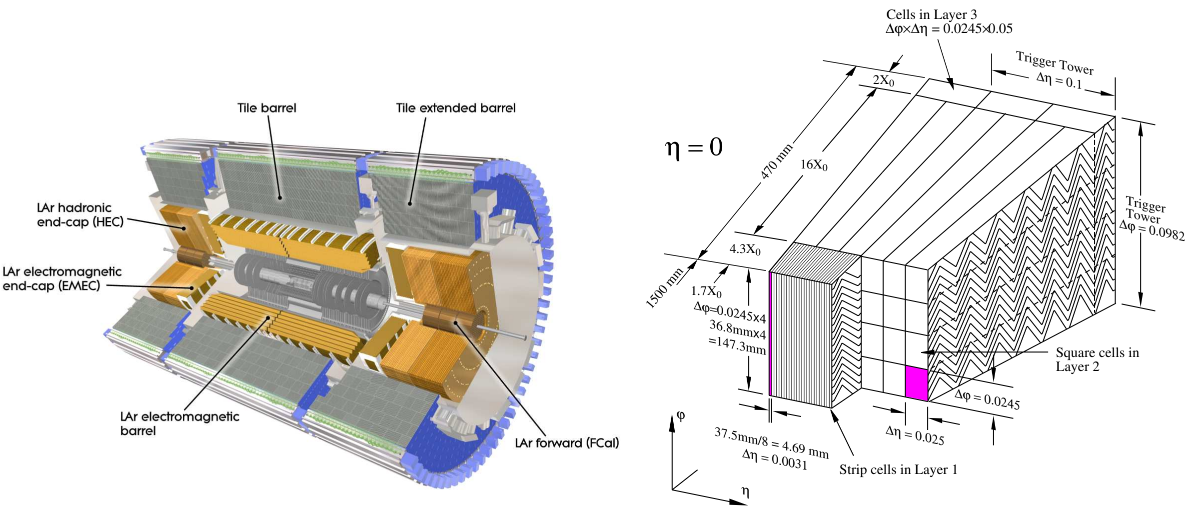

Figure 3.5.: Cutaway illustration of the ATLAS calorimeter system (left) and schematic of layers one to three of the electromagnetic calorimeter (right). From [79].

Table 3.2.: Cell granularities $\Delta\eta \times \Delta\phi$ of the ATLAS electromagnetic calorimeter. Reproduced from [79].

layer	barrel		end-cap	
	$\Delta\eta \times \Delta\phi$	η range	$\Delta\eta \times \Delta\phi$	η range
presampler	0.025×0.100	$\|\eta\| < 1.52$	0.025×0.1	$1.5 < \|\eta\| < 1.8$
first layer	0.003×0.100	$\|\eta\| < 1.40$	0.050×0.100	$1.375 < \|\eta\| < 1.425$
	0.025×0.025	$1.40 < \|\eta\| < 1.475$	0.025×0.100	$1.425 < \|\eta\| < 1.5$
			0.003×0.100	$1.5 < \|\eta\| < 1.8$
			0.004×0.100	$1.8 < \|\eta\| < 2.0$
			0.006×0.100	$2.0 < \|\eta\| < 2.4$
			0.025×0.100	$2.4 < \|\eta\| < 2.5$
			0.100×0.100	$2.5 < \|\eta\| < 3.2$
second layer	0.025×0.025	$\|\eta\| < 1.40$	0.050×0.025	$1.375 < \|\eta\| < 1.425$
	0.075×0.025	$1.40 < \|\eta\| < 1.475$	0.025×0.025	$1.425 < \|\eta\| < 2.5$
			0.100×0.100	$2.5 < \|\eta\| < 3.2$
third layer	0.100×0.100	$\|\eta\| < 1.35$	0.050×0.025	$1.5 < \|\eta\| < 2.5$

consists of two parts split at $\eta = 0$ and covers $|\eta| < 1.475$ providing > 22 radiation lengths X_0[7]. The two end caps cover $1.375 < |\eta| < 3.2$ with an additional split at $|\eta| = 2.5$ and provide $> 24X_0$. In radial direction it is split in a presampler without absorbers and three sampling layers with different granularities in $\Delta\eta$ and $\Delta\phi$ depending on the layer and $|\eta|$. The first layer, while providing rather coarse granularity of $\Delta\phi = 0.1$, features the highest granularity in η with up to 8 cells per $\Delta\eta = 0.025$ interval. These intervals are matched to the η span of cells in the second layer which provides higher granularity in ϕ direction with sizes down to $\Delta\eta \times \Delta\phi = 0.025 \times 0.025$. The arrangement of the different layers is schematically shown in Fig. 3.5. A more comprehensive overview of the different granularities is given in Tab. 3.2.

Hadronic calorimetry is realized in the barrel up to $|\eta| = 1.7$ using scintillating tiles interleaved with steel plates as absorbers. This part of the hadronic calorimeter is subdivided into a central part $|\eta| < 1.0$ and two extended barrels covering $0.8 < |\eta| < 1.7$. At the outer edge of the tile calorimeter the entire detector corresponds to 9.7 interaction lengths λ[8]. Including material of the outer support structure the muon system, described in Sec. 3.2.4, is shielded against hadronic leakage, so called *punch through*, by a total of eleven interaction lengths at $\eta = 0$ [79]. In the end-cap region LAr with copper absorbers is used to cover $1.5 < |\eta| < 3.2$.

[7] The radiation length specifies the mean path traversed by electrons between inelastic interactions with the surrounding material.

[8] The interaction length for hadrons is analogous to the radiation length for electrons the mean distance between inelastic interactions.

The forward calorimeters use again LAr with a copper plate for the electromagnetic part followed by two tungsten plates for hadronic measurements. It covers the range $3.1 < |\eta| < 4.9$ with about ten interaction lengths λ.

The design energy resolution of the electromagnetic calorimeter within $|\eta| < 3.2$ is parametrized as $\frac{\sigma_E}{E} = \frac{10\%}{\sqrt{E/\mathrm{GeV}}} \oplus 0.7\%$. In the same range of pseudorapidity the resolution of the hadronic calorimeter is targeted at $\frac{\sigma_E}{E} = \frac{50\%}{\sqrt{E/\mathrm{GeV}}} \oplus 3\%$ while in the forward calorimeter it is $\frac{\sigma_E}{E} = \frac{100\%}{\sqrt{E/\mathrm{GeV}}} \oplus 10\%$ [79]. The first term in these parametrizations accounts for the statistical evolution of the particle showers in the calorimeter. The constant second term is attributed to local inhomogeneities.

3.2.4. The Muon Spectrometer

The only particles with non-negligible interaction with the detector which regularly escape even the hadronic calorimeter are muons. Making use of this property the outermost layers of the ATLAS detector are dedicated to the measurement of these particles. The muon trajectories are bent in the magnetic field created by the toroid magnets. The toroid magnet system consists of one barrel toroid covering $|\eta| < 1.4$ and two end-cap toroids covering primarily $1.6 < |\eta| < 2.7$ with eight coils each. The bending of muons in the region between $|\eta| = 1.4$ and $|\eta| = 1.6$ is subject to relevant contributions from barrel and end-cap toroid fields. The toroid magnets provide bending power $\int B\,d\ell$ in the instrumented range[9] between 1 and 7.5 Tm. The muon system is designed to allow muon momenta of $p_{\mathrm{T}} = 1\,\mathrm{TeV}$ to be measured with a resolution of 10%.

Similarly to the tracking in the inner detector the muon trajectories are determined from multiple layers of sensors providing position information. As in case of the preceding subdetectors the individual modules of the muon system form three cylindrical layers centered around the beam axis in the barrel region. In the forward regions the modules form wheels perpendicular to the beam axis. Monitored drift tubes (MDT) are installed in the range $|\eta| < 2.7$, cathode strip chambers (CSC) in the range $2.0 < |\eta| < 2.7$. Additionally resistive plate chambers (RPC) and thing gap chambers (TGC) provide measurements with high temporal resolution in the ranges $|\eta| < 1.05$ and $1.05 < |\eta| < 2.7$ respectively. The jitter of the RPCs is specified to be $\leq 10\,\mathrm{ns}$ and the TGCs measure 99% of all signals within 25 ns [79].

[9] from innermost to outermost measurement point of the muon spectrometer

3.2.5. Trigger

The time between two subsequent bunch crossings of 25 ns and the corresponding event rate[10] not only exceed the read-out capabilities of many detector subsystems but recording every event would also vastly exceed the bandwidth to and the storage capabilities at the CERN computing center. Therefore a multi-stage trigger system is used to select interesting events which exhibit features of relatively rare processes with cross sections several orders lower than the total inelastic pp cross section. An overview over the ATLAS trigger system used during Run 2 of the LHC can be found in Ref. [84] and some high-level aspects of it are summarized in the following.

The trigger system is split into two levels, the *Level-1* trigger L1 being implemented in custom electronic circuits. The second, *high level trigger* HLT, is realized in software running on a dedicated farm with several thousand CPU cores. The L1 trigger reduces the maximum rate of events to be further processed to about 100 kHz within a delay of 2.5 μs, the HLT reduces this further to an averaged rate of 1 kHz within 200 ms [84].

The L1 trigger uses information from resistive plate chambers and thin gap chambers in the muon system as well as calorimeter information at a reduced granularity. While the former are used to select events with muons the latter can be used for a variety of signatures. These include the presence of electron, photon, or tau lepton candidates, highly energetic jets, and large transverse momentum imbalance. Detector regions causing the L1 to accept an event are called *regions of interest* (RoIs) and forwarded to the HLT. The HLT uses reconstruction algorithms close to the ones used for offline reconstruction in the RoIs identified by the L1 using full detector information. It therefore bases its decision on improved estimates of the kinematics of the objects required by a particular trigger chain.

3.2.6. Luminosity Measurement

A simple expression such as given in Eq. (3.1) for the instantaneous luminosity makes some idealizing assumptions. In practice the luminosity is measured, which also provides important feedback for optimization and adjustments of the beams. One subdetector in ATLAS dedicated to the determination of luminosity is LUCID2 [87] (*Luminosity Cherenkov Integrating Detector*). It is integrated with the beam pipe at roughly 17 m from the interaction point and consists of photo multiplier tubes with quartz windows in which Cherenkov radiation is produced. The luminosity is determined from the inelastic proton-proton cross section and

[10] Due to the technical necessity of empty bunches the average event rate is about 30 MHz instead of $1/(25\,\text{ns}) = 40\,\text{MHz}$.

number of simultaneous interactions visible to the detector. The latter is derived from the number of signals in the detector, the exact relation depends on the algorithm used to count the number of signals, *i.e.*, what requirements are placed on coincident signals from different photo multiplier tubes. The cross section of inelastic collisions within the subdetectors acceptance is determined in dedicated *van der Meer* runs in which the beams' relative displacements in the x and y direction are scanned. From these runs the absolute luminosity values can be determined.

3.3. Object Reconstruction in ATLAS

Making a connection from signals from individual detector components to the physics processes in the collisions imposes a significant challenge which is approached in several steps. One important step is the reconstruction of particles produced in the collision, and their identification. The algorithms and procedures for every type of object, *e.g.*, electrons, photons, muons, and jets, are each the result of the work of many and are subject to constant revision and improvements. Therefore, in most of this section only a high-level summary is given. One exception is Sec. 3.3.6 in which also original research is presented in regards to origins of charge misidentification of electrons.

The procedures used for reconstruction and calibration of objects are, with a few exceptions, applied in the same way to events from measured data and MC simulation. In the latter case the interaction of particles with the detector and the detector response is simulated based on GEANT4 [88, 89].

The different reconstruction methods are subject to continuous improvements. The following sections summarize the methods and their performance as used for the analysis of data recorded in 2015 and 2016 corresponding to an integrated luminosity of approximately $36\,\mathrm{fb}^{-1}$.

3.3.1. Track and Vertex Reconstruction

Signals[11] created through interactions of charged particles with the sensitive material of the tracking detectors are referred to as *hits*, each corresponding to a point in space. Individual hits are then combined to reconstruct the particles' trajectories, or *tracks* for short, using an algorithm as described, *e.g.*, in Ref. [90]. In multiple steps track candidates are build from seeds of three silicon hits. A Kalman filter is then used to expand the sets of seed hits with hits compatible with the trajectory

[11] possibly spread over multiple pixels or strips

expected from the seed hits. Hits are removed from tracks if they are already included in two other tracks which are deemed to be of higher quality. The track parameters are then estimated based on a fit to the selected hits. Besides direction and momentum these include the *transverse* and *longitudinal impact parameters* d_0 and z_0. The d_0 parameter is the minimal distance in the transverse plane between the beam axis and the particle's trajectory. The parameter z_0 refers to the longitudinal position of the trajectories closest approach to the beam axis.

In order to discriminate tracks from different collisions a vertex finding algorithm in employed [91]. An initial seed vertex position is iteratively updated by weighting tracks based on their geometric compatibility with the vertex position in each iteration. Eventually tracks considered compatible with the vertex position are assigned to that vertex and removed from the set of tracks considered by the algorithm. The algorithm is then repeated to form the next vertex. The hard scatter primary vertex is then chosen to be the vertex with the largest sum of squared tracks' transverse momenta associated with it [86]. Following the choice of this primary vertex the values of the z_0 and d_0 parameters are adjusted such that they represent the longitudinal and transverse distances with respect to the chosen primary vertex.

3.3.2. Jet Reconstruction

Jets are reconstructed by combining individual topological clusters [92] of energy deposited in the calorimeter using the anti-k_t algorithm [56]. This algorithm performs an iterative combination of constituents by defining distances d_{ij} between two objects as well as a distance d_i of each object to the beam:

$$\begin{aligned} d_{ij} &= \min(k_{t,i}^{-2}, k_{t,j}^{-2}) \cdot \frac{\Delta_{ij}^2}{R^2}, \quad \Delta_{ij}^2 = \Delta y_{ij}^2 + \Delta\phi_{ij}^2, \\ d_i &= k_{t,i}^{-2}. \end{aligned}$$

Here the transverse momentum of the constituents is denoted by k_t and R is a radius parameter. In each iteration, if the minimal distance is a d_{ij}, the two constituents i, j are replaced by their combination. If the minimal distance is a d_i it is considered a jet and removed from the set of constituents. Besides being safe with respect to collinear emissions it produces the most cone-like jet shapes when compared to other algorithms such as the k_t or Cambridge/Aachen algorithms [56].

Unless indicated otherwise in this thesis *jets* are assumed to be constructed by the anti-k_t algorithm with a radius parameter $R = 0.4$ and based on the aforementioned topological clusters[12]. The *jet energy scale* JES describes the translation from measured energy depositions in the calorimeter to the energy of the jet responsible for these deposits. A determination of the JES, using data recorded with the ATLAS detector in 2015 is documented in Ref. [94]. The calibration steps performed therein are as follows: after changing the direction of the jet's four-momentum to originate from the primary vertex, corrections for pile-up are applied. The jet's four-momentum is then modified by scale factors derived from simulated samples. Finally, for detector data only, a residual calibration is applied *in situ* using jets recoiling against well-identified additional objects such as photons or Z bosons decaying to pairs of electrons or muons. An *η-intercalibration* is applied correcting the JES in the range $0.8 < |\eta| < 4.5$ to the JES determined for $|\eta| < 0.8$. Measurements of the *jet energy resolution* (JER) are presented in Ref. [95].

Flavor Tagging

Jets of hadrons can be produced from different sources at the hard scatter level. Of frequent interest is the identification of b-jets, that is, jets produced from b-quarks and thus containing b-hadrons. Such jets are indicative of processes producing heavy quarks such as top or bottom quarks. As the decay $b \to W^* c$ is strongly suppressed by the corresponding CKM matrix element (V_{cb}) b-hadrons are rather long lived compared to other hadrons with $c\tau_{b-\text{hadron}} \sim 0.5\,\text{mm}$. Their identification, also referred to as *b-tagging*, is therefore largely based on the presence and properties of a secondary vertex displaced from the primary one as well as the significance of transverse and longitudinal impact parameters of tracks associated to the jet. These discriminating features are combined in the MV2c10 algorithm [96] by means of a boosted decision tree (BDT). As it crucially depends on precise tracking information it is limited to jets within the acceptance of the inner tracking detectors $|\eta| < 2.5$. To correct for different b-tagging efficiencies and inefficiencies between data and simulated samples *scale factors* $\epsilon_\text{d}/\epsilon_\text{MC}$ are derived in bins of jet p_T and $|\eta|$ where ϵ is the efficiency in data and simulation, respectively, for a chosen threshold (*working point*) above which a jet is considered to be b-tagged. These scale factors are then used to correct simulated samples through weighting of their individual jets and thereby the events the jets are part of. For a working point selecting b-jets with an efficiency of 85% the MV2c10 algorithm is found to provide a rejection factor of about three for c-jets and 30 for light flavor (u, d, s, g) jets [96].

[12] An alternative jet definition becoming increasingly popular is given by *particle flow* jets which additionally exploit the momentum measurement of charged constituents in the inner tracker [93].

3.3.3. Muon Reconstruction

Muons are close to minimally ionizing particles over a large range of energies relevant at the LHC. They are therefore the only charged particles regularly reaching the muon spectrometer. Their trajectories can be reconstructed in both the inner detector as well as in the muon system. The so obtained trajectories are then extrapolated to the respective other subdetector where they are matched with their counterparts of the subdetector extrapolated to [97]. Besides so reconstructed *combined muons* additional reconstruction strategies are employed to mitigate inefficiencies due to, *e.g.*, reduced instrumentation in some detector regions. Muons are reconstructed up to $|\eta| = 2.5$ with about 99% efficiency in the p_{T} range between 5 and 100 GeV [97]. Muons reconstructed only in the muon spectrometer are mainly used to increase acceptance outside the coverage of the inner detector in the range $2.5 < |\eta| < 2.7$.

Multiple working points[13] for muon identification are centrally provided [97] in the ATLAS Collaboration. The identification is largely based on requirements on the track quality in terms of missing hits[14] and the track fit's χ^2 as well as compatibility of track parameters estimated from muon spectrometer and inner detector. For the most restrictive *tight* working point only combined muons are considered yielding efficiencies between 90 and 98% for most of the range $|\eta| < 2.5$[15].

Muons originating from the decay of promptly produced weak bosons typically feature much lower activity in their vicinity compared to muons produced in secondary decays of hadrons. Therefore Ref. [97] reports on a set of working points for muon *isolation* criteria. The isolation variables are based on either the scalar sum of p_{T} of tracks consistent with originating from the primary vertex or calorimeter clusters' $E_{\mathrm{T}} = E \sin\theta$ in ΔR cones of different sizes around the muon. In both cases contributions from the muon itself are removed and for the calorimeter based quantity corrections for pile-up contributions to the measured energy are applied. For the $H \to WW^*$ analysis presented in Chap. 4 a custom working point has been created requiring $p_{\mathrm{T}}^{\mathrm{varcone30}}/p_{\mathrm{T}}{}^{\mu} < 0.06$ and $E_{\mathrm{T}}^{\mathrm{topocone20}}/p_{\mathrm{T}}{}^{\mu} < 0.09$. The cone sizes are $\Delta R = \min(10\,\mathrm{GeV}/p_{\mathrm{T}}{}^{\mu}, R_{\mathrm{max}} = 0.3)$ for the track based isolation ($p_{\mathrm{T}}^{\mathrm{varcone30}}$) and $\Delta R = 0.2$ for the calorimeter based isolation ($E_{\mathrm{T}}^{\mathrm{topocone20}}$).

Again, small differences between measured data and simulation in terms of reconstruction, identification, and isolation efficiencies are corrected for by means of scale factors applied to simulated events.

[13] labeled *loose*, *medium*, *tight*, and *high-p_{T}* where tight muons are also medium muons which in turn are a subset of loose muons

[14] A hit is considered missing if a tracking detector module was supposedly passed without leaving a hit consistent with the track in question is found in that module.

[15] the main exception being the very central region $|\eta| < 0.1$ where an efficiency around 55-60% is found due to reduced instrumentation in the muon spectrometer

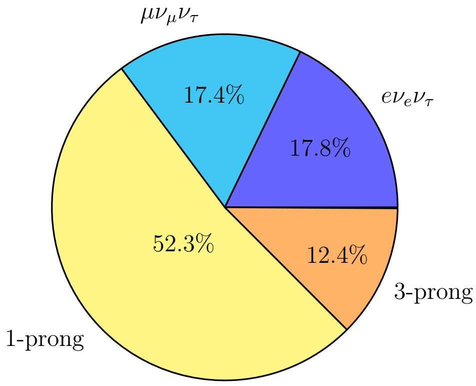

Figure 3.6.: Branching ratios Γ_i/Γ_{total} of τ leptons based on Ref. [42] for the main decay modes. The n-prong modes refer to τ decays in which n charged hadrons are produced. Decay modes with five or more charged hadrons are omitted.

3.3.4. Tau Lepton Reconstruction

While τ leptons decaying to electrons or muons are just reconstructed as such, a dedicated reconstruction and identification of hadronically decaying τ leptons is employed. The branching ratios of τ leptons to electrons, muons, and different multiplicities of charged hadrons (*prongness*) are shown in Fig. 3.6. The reconstruction of hadronically decaying τ leptons is seeded from anti-k_t 0.4 jets with $p_{\mathrm{T}} > 10\,\mathrm{GeV}$, and $|\eta| < 1.37$ or $1.52 < |\eta| < 2.5$. Tracks within $\Delta R < 0.2$ from the jet's barycenter, $p_{\mathrm{T}} > 1\,\mathrm{GeV}$, and passing additional requirements on impact parameters and hits in the inner detector are used to form a τ vertex. Tracks with $0.2 < \Delta R < 0.4$ are used to define isolation criteria which in turn are used in a multivariate identification algorithm. A dedicated energy calibration is performed using calorimeter clusters within $\Delta R < 0.2$ using simulations to account for neutral hadronic components and unmeasured energy carried by the ν_τ. Alternatively the contribution from charged decay products is measured from tracking information. Identification is provided depending on the prongness, *i.e.*, the number of tracks, with working point efficiencies from $30 - 60\%$. Details on τ reconstruction, triggering, calibration, and identification can be found in Ref. [98].

3.3.5. Overview of Electron and Photon Reconstruction

In this section the reconstruction and identification of electrons and photons is briefly summarized. A more detailed description with regards to the reconstruction of electrons is given in Sec. 3.3.6.

The reconstruction and, to some extent, also the identification of electrons and photons are closely related. Their reconstruction starts from clusters of energy deposits in the second layer of the electromagnetic calorimeter within $|\eta| < 2.47$. The clusters are constructed using a sliding-window algorithm searching for local energy maxima within a window size of 3×5 cells in $\eta \times \phi$ [99, 100]. The so found clusters are eventually expanded to 3×7 cells in the barrel part and 5×5 cells in the end caps. Such a cluster is considered as an unconverted photon if no tracks are associated with it. If a track is associated with it it is considered as a converted photon if the track is compatible with originating from a photon conversion inside the detector material. An electron is assumed if the track's parameters are in agreement with the hypothesis of the particle being produced in the collision region. In simulation the reconstruction efficiencies of electron clusters are close to 100% above a true electron $p_{\mathrm{T}} > 10\,\mathrm{GeV}$. The total reconstruction efficiency, including tracking and track-to-cluster matching efficiencies, with respect to the cluster efficiency is in excess of 98% at $E_{\mathrm{T}} = 20\,\mathrm{GeV}$ with a further increase towards higher values of E_{T} [99].

The energy calibration of electrons and photons uses multivariate regression techniques and is performed in multiple steps taking into account different energy scales in different layers of the calorimeter and local detector effects [100]. These local effects as well as the overall energy scale are determined using primarily $Z \to ee$ events. The total energy scale uncertainty for electrons and photons is below 1% over a large range of transverse energy E_{T} and $|\eta|$. The energy resolution of electrons improves from $7-15\%$ at low E_{T} to $1-3\%$ at $E_{\mathrm{T}} = 100\,\mathrm{GeV}$. At low E_{T} the resolutions of converted and unconverted photons are superior to the resolution of electrons by around $2-3\%$ depending on $|\eta|$. Towards high E_{T} their resolutions become more similar. Worst resolutions are found in the region $1.37 < |\eta| < 1.52$ corresponding to the transition from the barrel to the end-cap electromagnetic calorimeter. This regions also contains large amounts of uninstrumented material in front of the electromagnetic calorimeter.

The final identification of photons is largely based on shower shapes in the electromagnetic calorimeter. The identification of electrons additionally makes use of tracking information including information from the TRT. The calorimeter based criteria include energy leakage to the hadronic calorimeter, and the fractions of energies in the different layers of the electromagnetic calorimeter. Tracking-based information comprises numbers of hits in different parts of silicon detectors as well as the transverse impact parameter, its significance and the loss of momentum while traversing the inner detector. Additionally the geometric agreement between the cluster's barycenter and the position of the track extrapolated to the calorimeter is used. Here $\Delta\eta$ is taken at the first layer of the electromagnetic calorimeter, $\Delta\phi_{\mathrm{res}}$ is taken at the middle of the second layer. For the latter the track's momentum is rescaled to the cluster energy and the rescaled track is then extrapolated using otherwise unchanged track parameters at the perigee[16]. The extrapolation of the trajectory is performed based on a map of the magnetic field in the detector. The response of the TRT provides additional discrimination against charged hadrons such as charged pions. The full set of quantities used can be found in Ref. [99]. Depending on the final working point selection requirements are placed on, *e.g.*, information regarding the number of hits in particular subdetectors and individual detector layers. Most quantities are combined via a likelihood method using the probability density functions (*pdf*s) of signal and background candidates. While the signal is given by promptly produced electrons the background is composed of a mixture of light and heavy quark induced jets and converted photons. The signal and background likelihoods $L_{S/B}$ are then taken as the product of the corresponding pdfs and the discriminant is[17] $L_S/(L_S + L_B)$. The provided working points are referred to as VeryLoose, Loose, Medium and Tight. The average efficiencies with respect to the number of reconstructed electrons of the Loose, Medium and Tight working points are 93%, 88%, and 80% for electrons with $E_\mathrm{T} = 40\,\mathrm{GeV}$ and improve with larger E_T [99].

Isolation criteria for electrons are similar to those for muons: the calorimeter based isolation considers clusters other than the one created by the electron inside a fixed $\Delta R = 0.2$ cone, the track based isolation uses a p_T dependent cone size with $R_\mathrm{max} = 0.2$. Several working points with different intentions[18] are given in Ref. [99].

Scale factors and corresponding uncertainties correcting for different efficiencies in simulation and measured data are derived in Ref. [99] for identification, isolation, as well as the different steps in the reconstruction: cluster efficiency, tracking efficiency, and track-to-cluster matching efficiency.

3.3.6. Electron Reconstruction and Origin of Charge Misidentification

While being an important signature of rare physics processes electrons also introduce significant experimental challenges. Being the lightest charged particles they are particularly prone to the emission of hard bremsstrahlung in the presence of detector material. While the ATLAS Global χ^2 Track Fitter [101] does account for some energy loss in material it is not well suited for sudden, significant momentum changes in both magnitude and direction. Therefore, tracks passing the loose criteria in Tab. 3.3 with respect to an electron-like calorimeter cluster are refit

[16]point of closest approach to the beam line

[17]up to monotonous transformations

[18]e.g., constant efficiencies in η and p_T, constant in η but dependent on p_T, or fixed thresholds

using a so called *Gaussian Sum Filter* (GSF) [102], which uses a more sophisticated way to account for radiative losses. It thereby allows to account for up to one hard emission of a bremsstrahlung photon. More than one hard emission is not considered due to the increased computational complexity of an even more flexible fit model. The set of space points the track parameters are estimated from stays unchanged. A clear improvement in the estimation of various track parameters is found as shown for two examples in Fig. 3.7. As the Global χ^2 Track Fitter is optimized for the majority of tracks found in the ATLAS detector its parameter estimate is often referred to as a *pion-hypothesis* fit. As radiative energy losses of electrons are typically emitted to the away side of the electron trajectories curvature the pion-hypothesis fit tends to underestimate the trajectory's radius and thereby the corresponding p_{T}. As the curvature is dependent on the charge of the electron the transverse impact parameter is also biased in a direction depending on the electron's charge.

After the GSF refit the tight criteria in Tab. 3.3 are applied for tracks to be considered matching to the calorimeter cluster. The asymmetric window in the $q \times \Delta\phi$ requirements accounts for bremsstrahlung and the resulting increased curvature and deflection due to the detector's magnetic field. An illustration of the effect is included in Fig. 3.8. If multiple tracks pass the selection for one cluster an ambiguity resolution algorithm is employed. Tracks with hits in the innermost detector layer, *i.e.*, the IBL are preferred to those without. If more than one track remains after this criterion the ΔR distances at the second calorimeter layer and a score based on the number of hits in different silicon detector layers are considered. This ambiguity resolution algorithm is referred to as the *conventional* algorithm in the following. The direction of curvature of a track defines the charge associated with it. In turn the charge of the track selected as the best match according to the employed ambiguity resolution algorithm defines the electron's charge.

Several distributions shown in the following including those in Fig. 3.7 are based on simulated samples of single-electron events with overlaid pile-up as described in Sec. 2.3. The simulated electrons are produced in the center of the detector, *i.e.*, representing prompt electrons. The spectrum of electrons[19] in this sample is flat in η in the range $|\eta| < 2.5$. In terms of transverse momentum it raises sharply around ${p_{\mathrm{T}}}^{\mathrm{truth}} = 1\,\mathrm{GeV}$ to a flat top and declines smoothly in the range $150\,\mathrm{GeV} \lesssim {p_{\mathrm{T}}}^{\mathrm{truth}} \lesssim 250\,\mathrm{GeV}$ with a small tail up to 300 GeV. The shape of this ${p_{\mathrm{T}}}^{\mathrm{truth}}$ distribution is approximately equal to that of the "chosen (electron)" distribution in Fig. 3.10. The sample comprises positively and negatively charged electrons in equal parts. Reconstructed electrons and their matched tracks are considered only if they are within $\Delta R = 0.1$ of a true electron and

[19] As throughout most of this document *electrons* refer to particles of positive and negative electric charge equally.

Table 3.3.: Criteria for matching tracks to calorimeter clusters during electron reconstruction. Loose criteria are applied before the GSF refit, tight criteria after. All coordinates in these criteria are taken at the second layer of the electromagnetic calorimeter. $\phi_{\text{track,rescaled}}$ is determined by re-extrapolating the track from the perigee after rescaling its momentum to the energy of the cluster.

distance measure	loose range	tight range	
$\lvert\eta_{\text{track}} - \eta_{\text{cluster}}\rvert$	$[0, 0.05]$	$[0, 0.05]$	and either
$q \times \Delta(\phi_{\text{cluster}}, \phi_{\text{track}})$	$[-0.20, 0.05]$	$[-0.10, 0.05]$	or
$q \times \Delta(\phi_{\text{cluster}}, \phi_{\text{track,rescaled}})$	$[-0.10, 0.05]$	$[-0.10, 0.05]$	

their reconstructed p_{T} is in excess of 3.5 GeV. Lower thresholds would introduce significant amounts of fake electron candidates as for these studies no identification or isolation requirements are applied. During initial studies the p_{T} threshold was set to 5 GeV, no significant differences in this regard were found between the two thresholds. For charge-sensitive analyses like the one in Ref. [103], the threshold is even much higher. Furthermore, only tracks with more than three hits in silicon detectors are considered.

Truth Classification of Tracks and Particles

For detailed studies of various processes, in particular of potential inefficiencies of reconstruction algorithms, a connection between aspects of the true process and the reconstructed process is highly desirable. Knowing the true process implies that such connections are restricted to simulated samples of events. An association between *truth* particles produced by the MC generator or the detector simulation and reconstructed objects is provided in the main ATLAS software framework ATHENA [104]. Of particular relevance in regards of electrons is the link between truth particles and reconstructed tracks. The truth particle assigned to a track is determined based on the hits the track is composed of and that are attributed to a particular truth particle. The so called *truth-match probability* is given as the weighted fraction[20] of hits of a track that are attributed to the truth particle [105]:

$$\text{TMP} = \max_{\text{particles } x} \left(\frac{\sum_{\text{hit } i \text{ from particle x}} w_i}{\sum_{\text{all hits i}} w_i} \right) .$$

[20] For the inner detector the weights per hit are 10 for pixel hits, 5 for silicon strip hits and 1 for TRT hits.

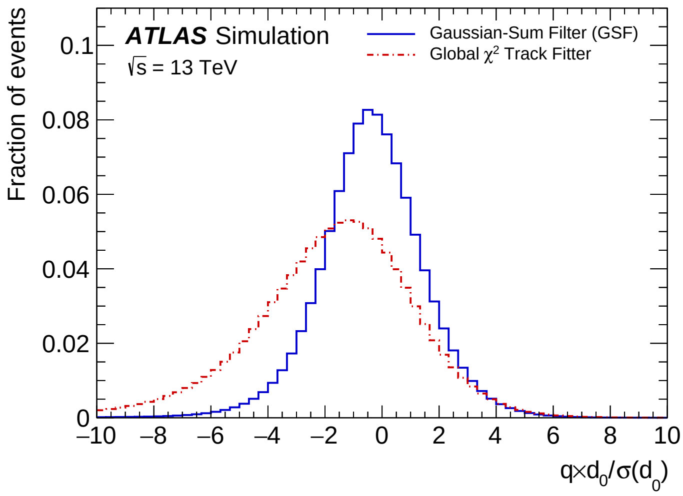

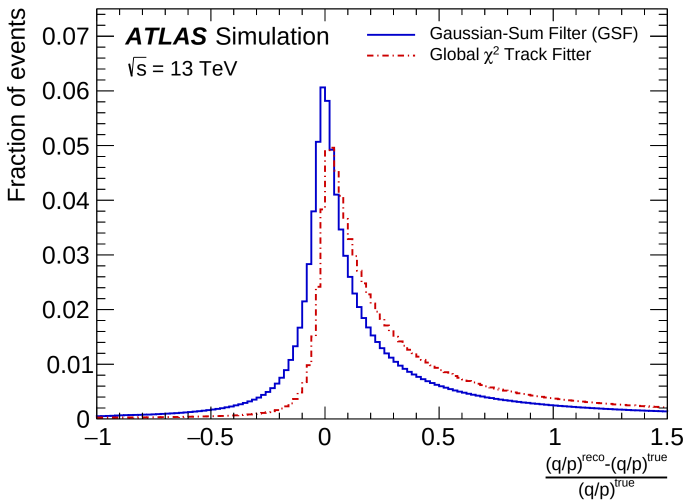

Figure 3.7.: Comparisons of track parameters of electrons estimated by the pion-hypothesis and the GSF fits in the simulated single-electron sample. The graphic at the top shows the transverse impact parameter significance times reconstructed charge $q \times d_0/\sigma(d_0)$. In the graphic at the bottom the track's charge times inverse momentum difference between true and reconstructed values is shown. In both cases the parameters estimated by the GSF fit show improved resolution and reduced bias. Published in [99].

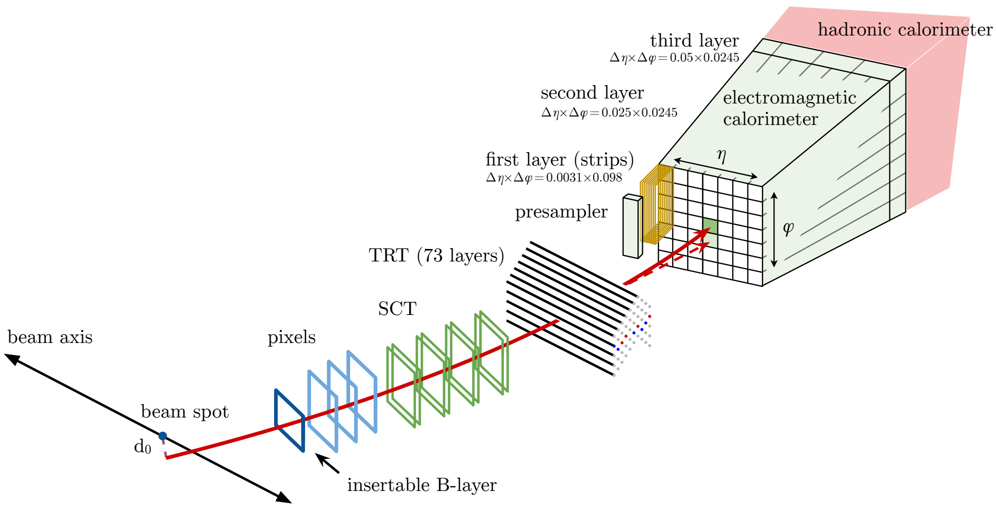

Figure 3.8.: Schematic illustration of detector parts and concepts involved in the reconstruction of electrons in the ATLAS detector. The solid red line indicates the path of an electron, the dashed red line a bremsstrahlung photon. The track's curvature and the deflection due to the emission of the bremsstrahlung photon are supposed to be in ϕ direction. From [99].

Additionally a classification in terms of *truth type*[21] and *truth origin*[22] is provided.

Implications of Charge Misidentification

The presence of two leptons in an event represents a clear signature of rare electroweak process such as the production of a Z boson. However, Fig. 2.10 includes even more rare electroweak processes to be studied such as vector-boson scattering (VBS) denoted as $VVjj$. Amongst the processes in this category the production of two same-charge W bosons [103] ($W^{\pm}W^{\pm}$) allows to exploit a particularly rare signature of two same-charge leptons to greatly reduce the contribution of events from other processes. Similar signatures are used, *e.g.*, by searches for effects of new physics beyond the Standard Model (BSM) such as Ref. [106]. Contamination from opposite-charge dilepton final states to a same-charge selection can occur due to inefficiencies in charge reconstruction. In a recent ATLAS publication regarding electron reconstruction and identification [99] a boosted decision tree (BDT) is presented to identify electrons which are likely to have undergone charge misidentification. Vetoing events based on such a multivariate discriminant is shown to largely suppress events with charge misidentification. Besides reducing the signal acceptance, however, it requires the introduction of additional corrections

[21] such as isolated e, non-isolated e, background e (including photon conversion), hadrons, ...
[22] such as single e, e from W, Z, or H bosons, or various types of hadrons, ...

and corresponding systematic uncertainties to account for discrepancies between simulation and data.

Origins of Charge Misidentification

The sign of the charge of a reconstructed particle is determined from the direction of curvature of its track in a known magnetic field. With increasing p_{T} tracks become more straight and the efficiency of reconstructing the correct charge degrades. From Eq. (3.2) the q/p_{T} resolution in the inner detector can be estimated to be around 50% at $p_{\mathrm{T}} = 1\,\mathrm{TeV}$. Reconstructing the wrong charge due to a straight track corresponds to a sign change of q/p_{T}. Assuming the resolution can be interpreted as the standard deviation of a Gaussian distribution, the charge misidentification at $p_{\mathrm{T}} = 1\,\mathrm{TeV}$ can be estimated to be about $2-3\%$. Hence, up to multiple hundred GeV the charge misidentification due to straight tracks can be expected to be well below 1%. In the $W^{\pm}W^{\pm}$ analysis [103], for example, the p_{T} of the charged leptons is roughly at the electroweak scale $\mathcal{O}(100\,\mathrm{GeV})$. In this region the charge misidentification of electrons is dominated by misreconstruction as a consequence of hard bremsstrahlung where the prompt electron looses a significant fraction of its momentum due to interaction with the detector material. In case of a conversion of the bremsstrahlung photon an additional electron-positron pair and potentially additional tracks near the prompt electron are created. Charge misidentification can therefore arise from the resulting ambiguities during reconstruction. Studies regarding these ambiguities are presented in the following using the simulated sample of single electron events described earlier.

In the following the track considered as the best match to a calorimeter cluster is referred to as the *primary* or *chosen* track. All non-primary candidate tracks also satisfying the matching criteria in Tab. 3.3 for the same calorimeter cluster are summarized as *subordinate* tracks. All tracks matched to a calorimeter cluster are further labeled based on their best truth match as:

electron (track) if the track is matched to a prompt truth electron. If multiple tracks assigned to the same reconstructed electron are truth matched to a prompt electron only the truth matched track ranked highest by the track selection algorithm under study is labeled as an *electron* track while the lower ranked ones are labeled as *additional electron* tracks.

conversion (track) if the track is truth matched to an electron produced from photon conversion.

other (track) if the track falls in neither of the previous categories. These tracks largely originate from pile-up collisions for the sample used.

Table 3.4.: Meta parameters used for the track selection BDT.

meta parameter	setting
boost type	gradient boost
number of trees	500
max. tree depth	5
min. node site	2.5%
bagged boost	yes
shrinkage	0.05
bagging fraction	0.1
separation type	misclassification error

In the following the terms (*additional*) *electron*, *conversion*, and *other track* refer to these categories. With exception of "additional electron tracks" these can be chosen or subordinate tracks. The truth electron η_{truth} and $p_{T,\text{truth}}$ distributions for these different types of tracks are shown in Figs. 3.9 and 3.10. In addition the amount of material in the inner detector is shown, as well as the fractions of correctly or incorrectly reconstructed electron charge when selecting different types of tracks. The largest charge identification inefficiencies are found at high $|\eta|$ due to the larger amounts of material traversed[23]. A slight increase in the fraction of erroneously chosen conversion tracks is found with increasing $p_{T,\text{truth}}$ of the generated electron while the overall number of conversion tracks increasing more strongly with $p_{T,\text{truth}}$. In case a conversion track is chosen the reconstructed charge is found random with a slight bias towards the wrong charge $q_{\text{truth}} \times q_{\text{GSF track}} = -1$.

A reduction of charge misidentification of electrons can therefore be expected if the selection of the primary track is improved. In the ambiguity resolution algorithm described earlier only a subset of the information available is used. Hence, the possibility was studied to include additional information and better exploit correlations amongst discriminants. To this end a *boosted decision tree* (BDT) was trained trying to identify electron tracks. The training was performed using TMVA [107] with meta parameters given in Tab. 3.4. The training targets are $+1$ for electron tracks and -1 for tracks of different categories. Due to the prospective nature of these studies the training sample used comprises only $\sim 1 \cdot 10^6$ tracks randomly selected from the sample. These correspond to about 2% of the available dataset.

Distributions of quantities provided as inputs to the BDT are shown in Figs. B.1-B.4 in the Appendix and are briefly described in the following.

[23]The exact shapes are not expected to be identical as the location of the hard emission of bremsstrahlung is random and the track selection inefficiency may depend on the number of tracking detector layers traversed before the bremsstrahlung emission.

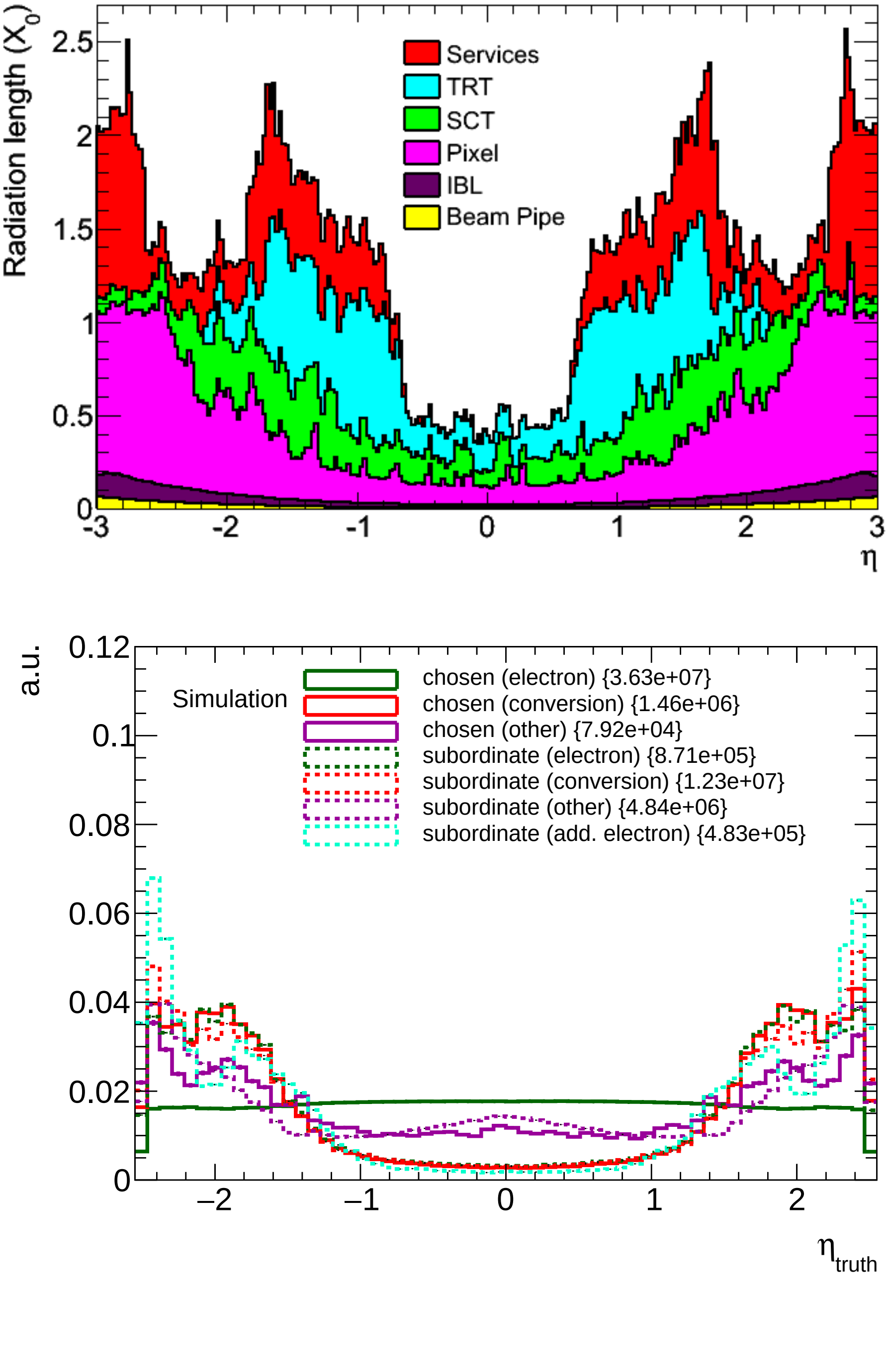

Figure 3.9.: The material in terms of radiation lengths between the interaction point and the calorimeter is shown in the top (from [86]). It can be loosely correlated with track selection inefficiencies represented by the solid red and purple distributions in the bottom. There, the normalized distributions of different types of tracks are shown depending on η of the truth electron. The integral of each type of track before normalization is given in the legends. Values shown are unweighted number of tracks.

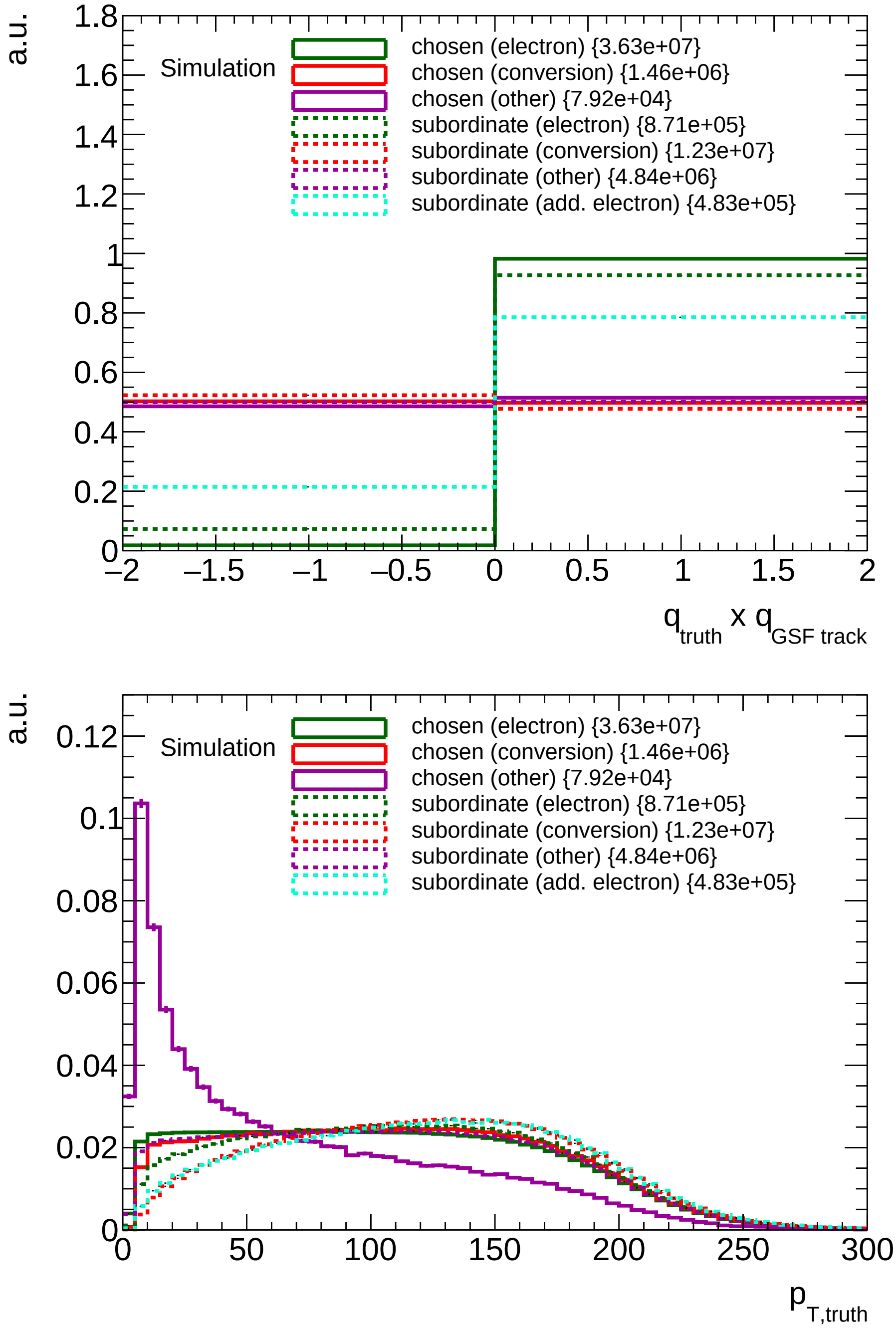

Figure 3.10.: Charge of the truth electron times reconstructed track's charge (top), and truth electron p_T distributions (top) for different types of tracks. The distributions of different types of tracks are normalized, the integral of each type of track before normalization is given in the legends. Values shown are unweighted number of tracks.

Hits, holes and dead modules The numbers of measured hits, expected but missing hits (*holes*) as well as number of disabled or *dead* modules traversed by the hypothesized track are provided. As shown, *e.g.*, in Ref. [108], prompt charged particles produce a hit in the innermost and next-to-innermost layers of the pixel detector with probability of $\gtrsim 98\%$ per layer. Unless emission of the hard bremsstrahlung photon and its conversion to an electron pair already occur in the beam pipe, tracks from these conversion electrons should not have an innermost hit. In addition to the numbers in these two individual layers the total numbers for the pixel detector and the silicon strip detector are provided as inputs.

Distances The distances $\Delta\phi$ and $\Delta\eta$ between the track position and the barycenter of the $\eta \times \phi = 3 \times 5$ cells sized calorimeter cluster are included in the set of features. As in the existing selection algorithm they are evaluated at the second layer of the electromagnetic calorimeter and the track parameters of the GSF fit are used. Two variants of extrapolation of the track to the calorimeter are used: extrapolation from perigee with and without rescaling the tracks momentum to the calorimeter based energy measurement. All four resulting distances to the calorimeter cluster are provided to the BDT.

Track-fit quality, impact parameters For tracks purely constructed from conversion hits the conversion represents a largely displaced vertex such that a larger significance of the transverse impact parameter $d_0/\sigma(d_0)$ is expected compared to tracks from prompt electrons. The parametrization used in the GSF fit is such that it can include up to one kink in the trajectory corresponding to the emission of a hard bremsstrahlung photon. While this leads to more accurate parameter estimates for electron tracks, the changes of several track parameters between the pion-hypothesis fit and the GSF fit are found to be even larger for erroneously chosen conversion tracks. Due to the high relevance of hits in the innermost and next-to-innermost detector layers, chosen conversion tracks typically have such hits even if these hits were originally created from, *e.g.*, the prompt electron. Such a track predominantly constructed from conversion hits but also including hits from a prompt electron is therefore unphysical. As a consequence the reduced χ^2, χ^2/NDoF for short, of the pion-hypothesis fit is larger for these tracks compared to others and provided as an input to the BDT. The GSF fit appears to compensate for this leading also to larger changes of χ^2 from pion to GSF fit denoted as $\Delta(\chi^2/\mathrm{NDoF})_{\mathrm{GSF}-\pi\ \mathrm{track}}$ providing additional discrimination power in the BDT. The track parameter estimates from the pion-hypothesis fit for the unphysical conversion tracks are often very poor. Therefore $E_{35}/p_{\pi\ \mathrm{track}}$ and $\Delta p^{\mathrm{T}}_{\mathrm{GSF}-\pi\ \mathrm{track}}/E^{T}_{35}$ are used as additional input quantities. E_{35} is the energy of the 3×5 calorimeter cluster, $E^{T}_{35} = E_{35}\cdot\sin\theta$, and $\Delta p^{\mathrm{T}}_{\mathrm{GSF}-\pi\ \mathrm{track}}$ the difference between the track's p_{T} estimated from the GSF and pion-hypothesis fits. As an example for this group of quantities, distributions of the track's charge times transverse impact parameter significance are shown in Fig. 3.15.

The response of the so created BDT is shown in Fig. 3.11 for tracks yielding the correct charge and tracks yielding the wrong charge. A strong separation power is expected as already with the conventional algorithm an electron track is selected for $95.935\% \pm 0.003\%$(stat.) of the reconstructed electrons in the sample under study. The tracks associated with a reconstructed electron are resorted according to the BDT response. Based on this sorting the labeling scheme of *BDT chosen* and *BDT subordinate* tracks is applied where the chosen track is the one with the highest BDT response amongst the set of candidate tracks. The resulting migration between primary and subordinate tracks is shown in Fig. 3.12 for electron and conversions tracks. The number of electron tracks being *promoted* from a subordinate to a primary track exceeds the number of such conversion tracks across the entire $p_{T,\mathrm{truth}}$ spectrum and almost the entire η range. As the number of electron tracks being *demoted* is much lower than the number of demoted conversion tracks a net improvement is found across the entire η range.

The recoverable inefficiency is given by electron tracks which are not selected as primary tracks[24]. It is compared for the two track selection algorithms in Fig. 3.13. The BDT based selection yields improvements of up to $\sim 25\%$ in the central detector region. Changes in the distributions of features used in the BDT due to the BDT based track selection are small for quantities which are already used in the conventional selection algorithm. More prominent differences in distributions when using either of the two selection algorithms can be found in the variables related to the track quality. While other features used in the BDT are already used in the conventional algorithm, these track quality variables represent additional information. As an example the transverse impact parameter significance is compared in Fig. 3.15. After the BDT based sorting the remaining subordinate electron tracks are distributed more similarly to conversion tracks than with the conventional sorting. This implies that when switching from conventional to BDT based sorting tracks with low absolute transverse impact parameter significance are preferentially promoted to a primary track. The total selection efficiency of electron tracks is increased from $95.935\% \pm 0.003\%$ to $96.292\% \pm 0.003\%$. The charge misidentification rate in the sample under study is reduced from $3.760\% \pm 0.003\%$ to $3.584\% \pm 0.003\%$. The given uncertainties are statistical uncertainties only. It should also be noted that the selection of an electron track and a correct charge identification are strongly, yet not fully correlated. A comparison of the charge

[24]and no other electron track matched to the same reconstructed electron is selected as a primary track either

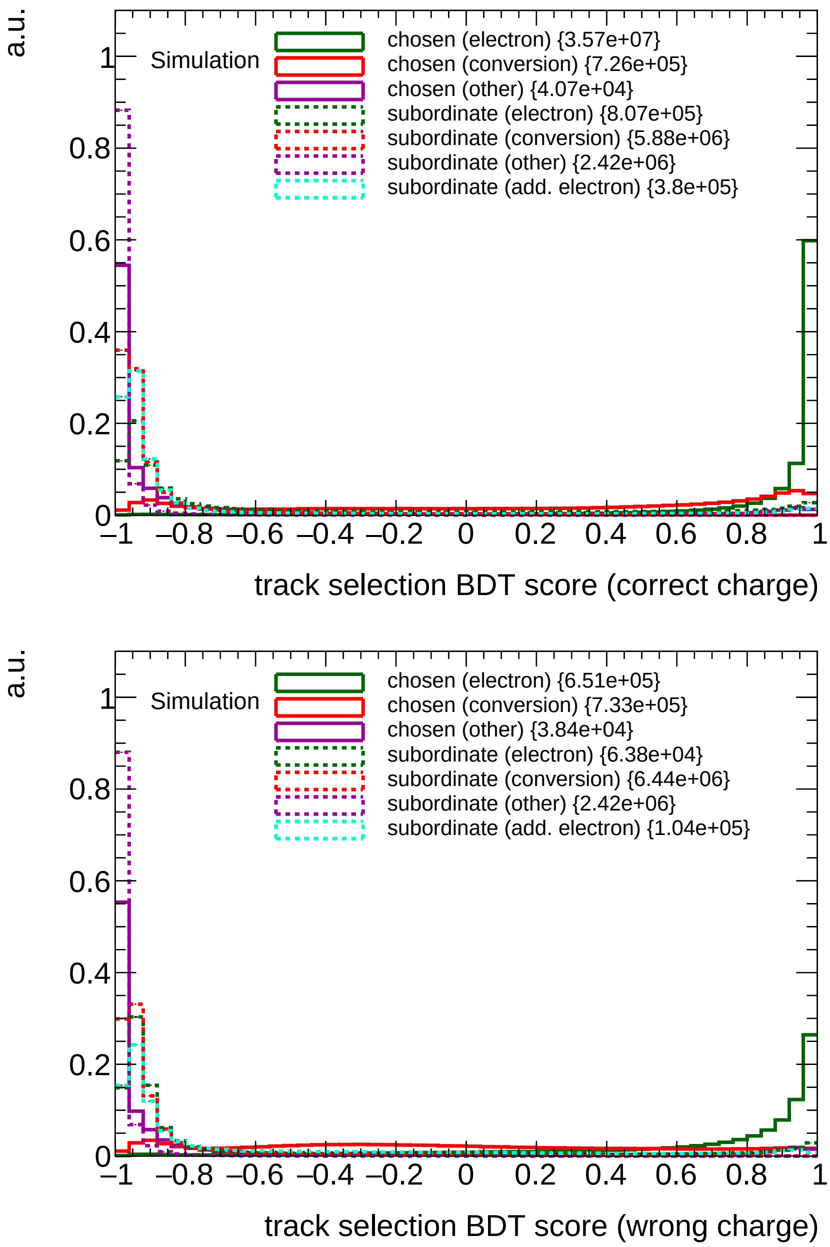

Figure 3.11.: Response of the track selection BDT split into tracks with charge identical to the original truth electron in the top graphic and those with differing charge shown in the bottom graphic. The integral of each type of track before normalization is given in the legends. Values shown are unweighted number of tracks.

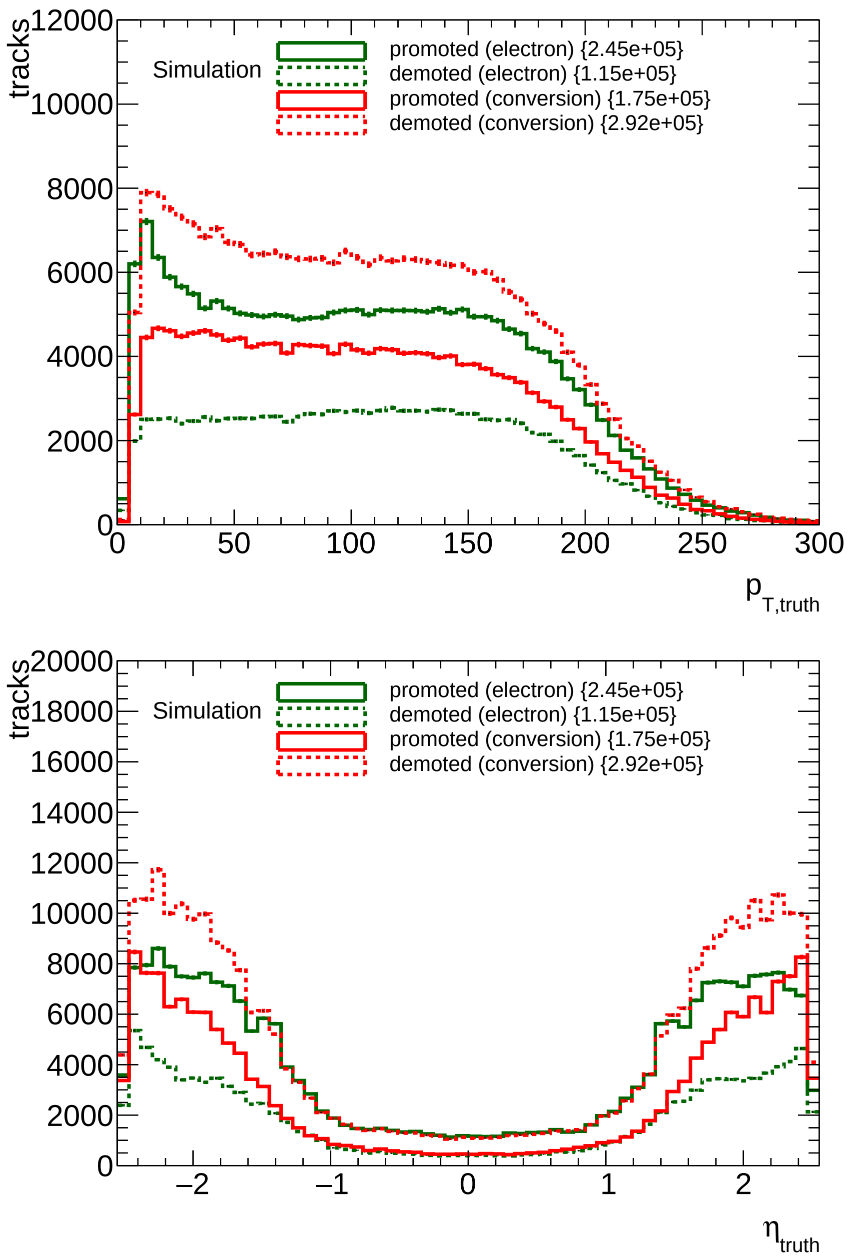

Figure 3.12.: Promotion and demotion of tracks due to BDT based track selection as functions of p_{T} (top) and η (bottom) of the truth electron. A *promoted* track is subordinate according to the conventional sorting and becomes a primary track when using the BDT based ranking. A *demoted* track follows the inverse logic. Values shown are unweighted number of tracks.

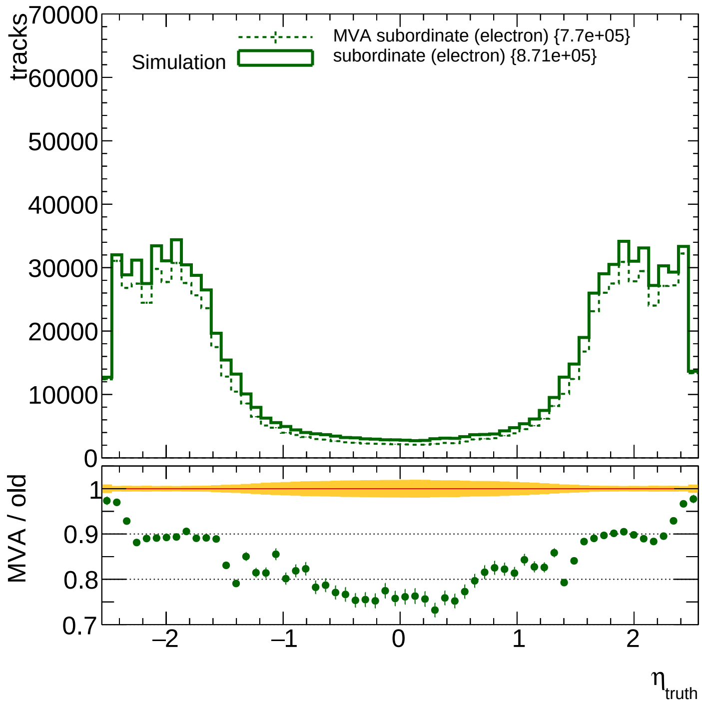

Figure 3.13.: Comparison of number of tracks constituting the recoverable inefficiencies with the conventional and the BDT based selection. Ratios shown in the bottom panels below unity correspond to a reduced inefficiency and therefore an improved selection. The yellow band in the bottom panel indicates the statistical uncertainty of the denominator, the error bars the statistical uncertainties of the numerator.

misidentification between the conventional and the BDT based algorithm depending on η^{truth} and $p_{\text{T}}{}^{\text{truth}}$ is shown in Fig. 3.14.

Given the only moderate increase in selection efficiency and charge identification the question arises if further optimization of the track selection is possible. Potential improvements include

- thorough optimization of BDT meta parameters and input features, and
- direct comparison of selection candidates against each other instead of individual scores and ranking by these scores. In the BDT used here a score is assigned to each track without regard to the other, competing candidates matched to the same calorimeter cluster.
- In this regard a different choice of machine learning algorithm, *e.g.*, usage of (deep) neural networks instead of a BDT, may be beneficial.

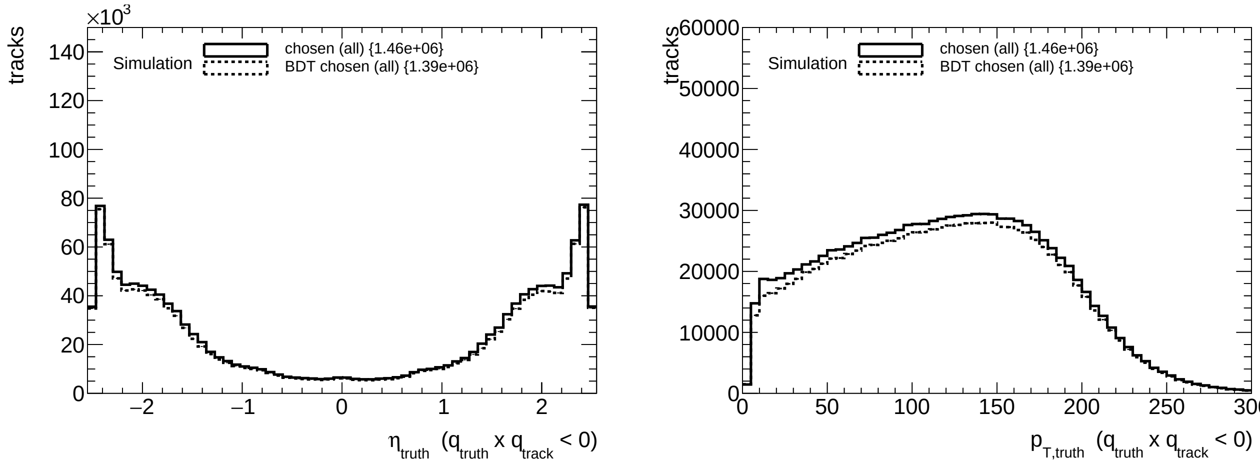

Figure 3.14.: Comparisons of distributions of true electron p_{T} (right) and η (left) where the electron's charge is incorrectly reconstructed when using the conventional or the BDT based track selection. The distributions are obtained from the same dataset and entries are unweighted number of primary tracks of the reconstructed electrons without regard to their truth classification.

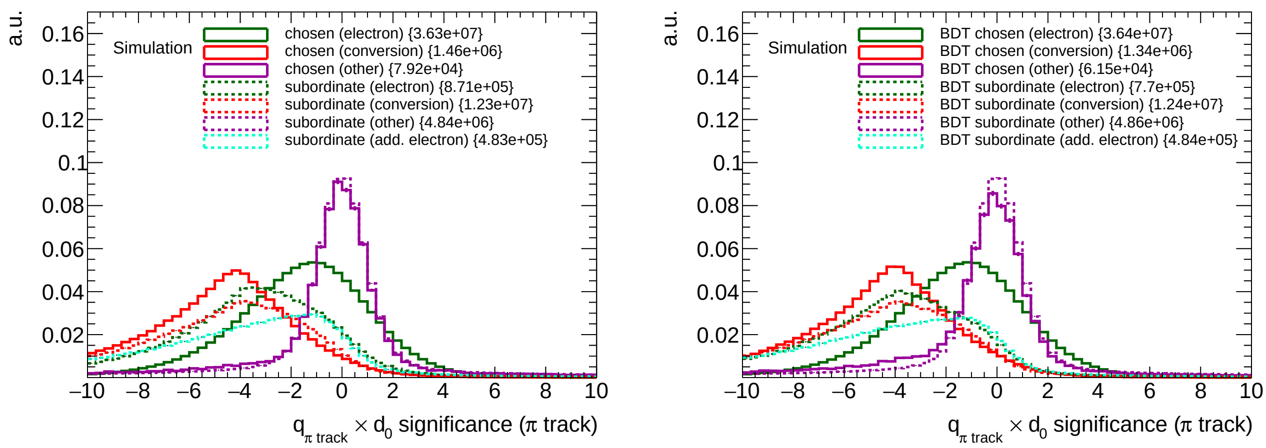

Figure 3.15.: Comparison of distributions using conventional (left) and BDT based (right) track selection for the charge times transverse impact parameter significance. With the BDT based track selection subordinate electron and conversion tracks are more similar to each other than in the conventional case. The integral of each type of track before normalization is given in the legends. Values shown are unweighted number of tracks.

Another highly relevant aspect is given by the definition of the set of correct track choices and thereby the training target. As described earlier an electron track is defined by the weighted majority of its hits originating from a true electron. That is electron tracks, just like all other categories of tracks, can be composed of hits from two or more particles. The truth match probability can be qualitatively interpreted as the purity of a track and is shown in Fig. 3.16. From the truth match probability distributions shown in Fig. 3.16 several observations can be made:

- selected electron tracks with correct charge feature high purity,
- selected electron tracks with incorrect charge are often highly impure,
- selected non-electron tracks are rarely pure, irrespective of their charge, and
- non-selected electron tracks feature high purity.

In particular with respect to the last bullet it should be noted that the truth match probability is not symmetric: it only accounts for the fraction of hits of a track originating from a particular truth particle. It does not, however, account for the fraction of a truth particles hits being included in a particular track. The presence of an innermost hit and the number of pixel hits shown in Fig. 3.17 after BDT sorting are already highly important features in the conventional track selection algorithm. Electron tracks which are not selected by the BDT often lack an innermost hit and have less pixel hits while chosen conversion tracks do exhibit these features. This is indicative of what has also been shown explicitly for individual events in Ref. [109]: hits created by the prompt electron in the first few detector layers are combined with hits created by conversion electrons in the subsequent layers. The truth classification of these hybrid tracks is then effectively dependent on the detector layer in which the bremsstrahlung photon is emitted, eventually creating a pair of conversion electrons. In case of an early emission and conversion the conversion electrons traverse a larger number of tracking detector layers resulting in a larger fraction of hits of the hybrid track stemming from conversion electrons. Hence, the track is classified as a conversion track. As the emission and conversion of bremsstrahlung happens only rarely before the prompt electron even reaches the first pixel layer[25] the resulting track is bound to be impure.

Modest improvements seem possible through thorough optimization of the track selection. Significant improvements to charge reconstruction of electrons, however, must already start at the track building. Modifications to the existing track building are subject to strong constraints due to finite computing resources. A second pattern recognition algorithm starting from individual hits is therefore practically excluded. Additionally, tracks represent a crucial input to various other areas of reconstruction. In these areas performance could be easily degraded by a generally modified track building. For improvements it is therefore required

[25] *c.f.* material distribution of different components shown in Fig. 3.9

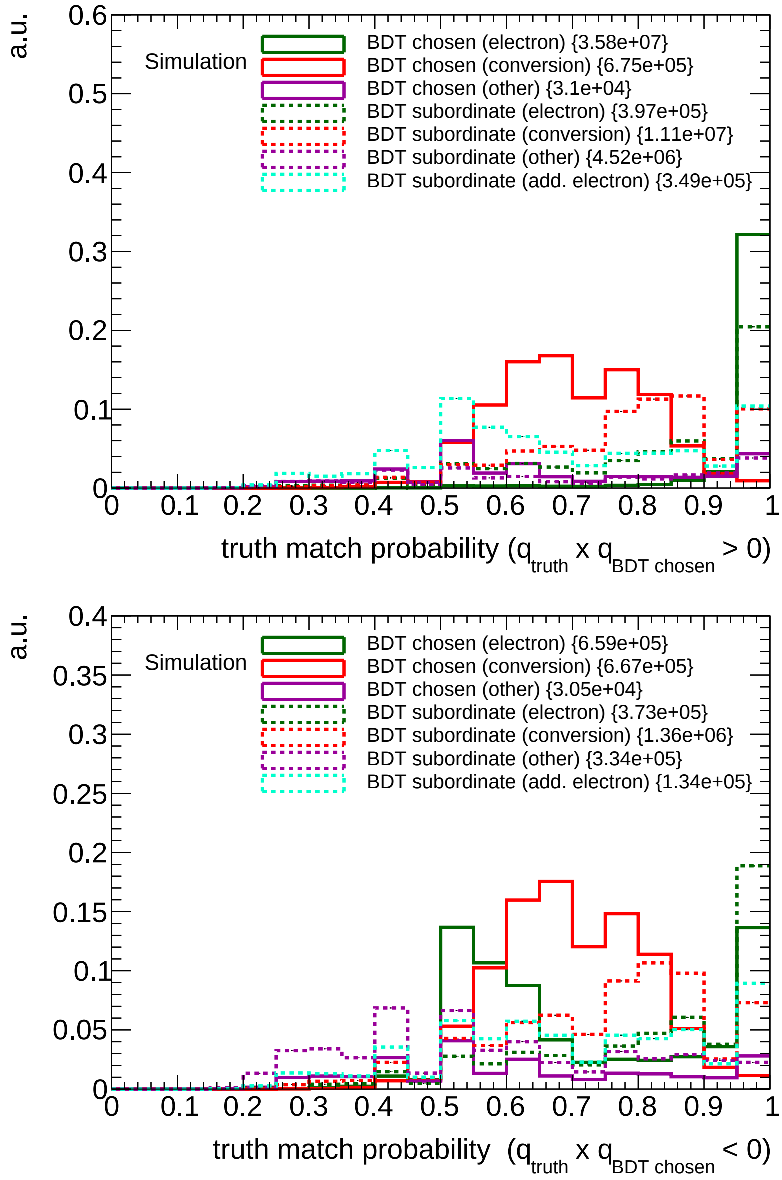

Figure 3.16.: Truth match probability distributions of different types of tracks. The graphic on the left includes tracks of electron candidates where the track selected by the BDT has the same charge as the truth electron. On the right only those tracks are included where the selected track's charge is different from the charge of the truth electron. The reduction below ~ 0.5 is due to the truth match probability being defined for best truth match - values below 0.5 require the track to include multiple hits from at least three different sources. The integral of each type of track before normalization is given in the legends. Values shown are unweighted number of tracks.

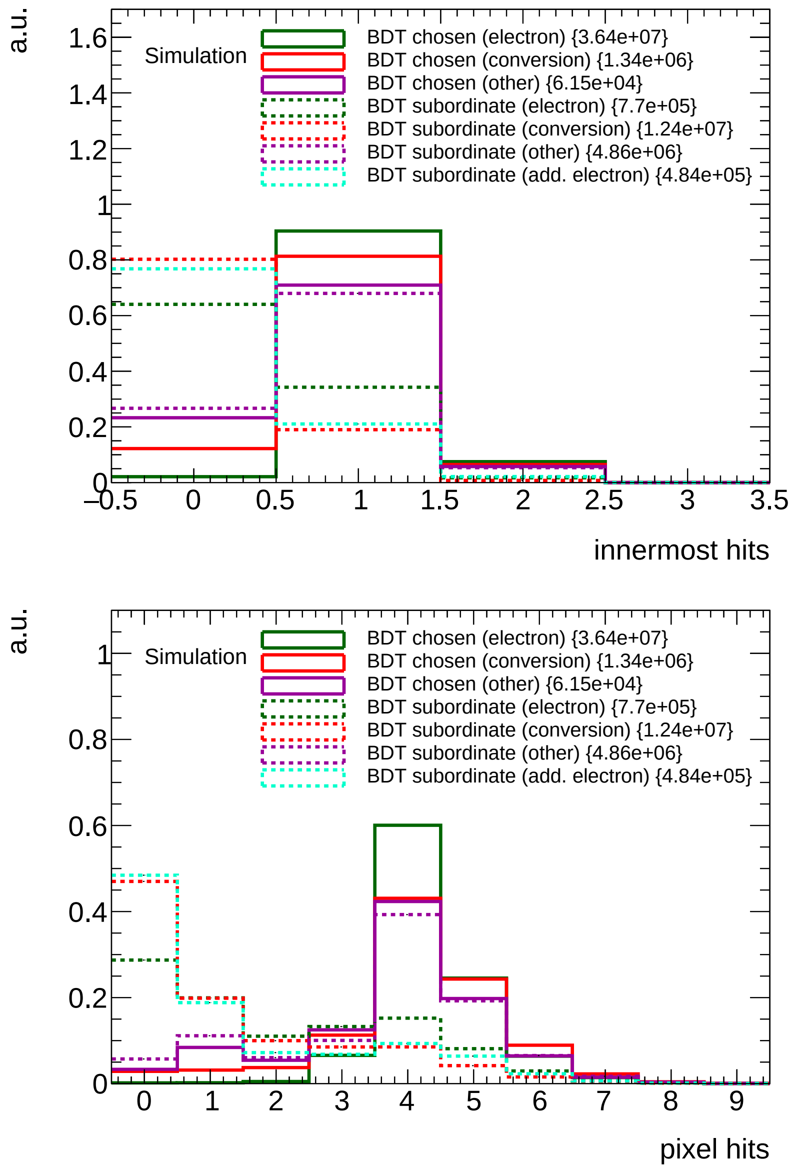

Figure 3.17.: Number of hits in the innermost detector layer and number of pixel hits after BDT sorting. More than one innermost hit can be found due to small overlaps of the individual detector modules. The integral of each type of track before normalization is given in the legends. Values shown are unweighted number of tracks.

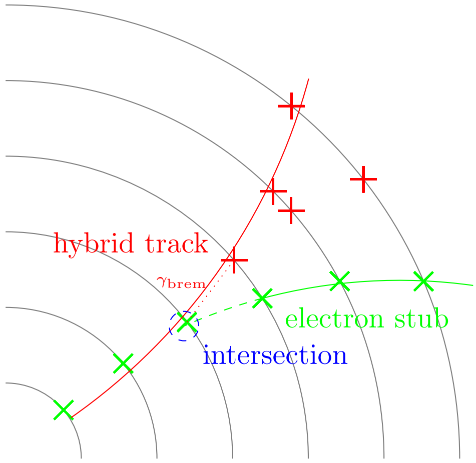

Figure 3.18.: Schematic illustration of hybrid track (red solid line) with additional electron stub track (green solid line). Green 'X' markers represent hits from the prompt electron, red '+' markers those from conversion electrons. The blue circle indicates an approximate intersection around which the longer tracks could be split in an attempt to find tracks which are in better agreement with physical hypothesis by recombination of the so created track segments. Angular distances are vastly enlarged for illustration purposes. For the same reason a potentially reconstructed track on the second conversion branch is not shown.

that they are lightweight and highly restrictive to cases where hybrid tracks are suspected. A conceptual idea is sketched in Fig. 3.18. The challenging cases are found to often include one long hybrid track with hits in inner and outer detector layers as well as a short track with only hits in outer layers. By searching amongst tracks matched to an electromagnetic calorimeter cluster for potential intersections between a long and a short track a recombination of track segments before and after the intersection could be performed followed by fitting the new tracks' parameters. If the recombination turns a hybrid track plus electron stub into a physically sensible prompt electron track plus conversion stub, *e.g.*, the total χ^2 can be expected to improve with respect to the track fits before the recombination. Such an approach - if feasible - does not depend on the initial track building algorithm used. The approach could therefore even be combined with other developments in terms of tracking algorithms such as the use of modern machine learning techniques for pattern recognition. Such techniques have recently been developed in the TrackML Challenge [110] also in view of the upcoming challenges at the HL-LHC.

3.3.7. Missing Transverse Energy

Neutrinos escape the detector without measurable interactions. Their kinematics are therefore not directly accessible. However, the momentum carried by undetected particles creates a transverse momentum imbalance in the transverse plane. The sum of transverse momenta carried by undetected particles can be reconstructed under the assumption that the vectorial sum of momenta in the transverse plane, *i.e.*, the transverse momenta of the initial state partons, is vanishing. The so called missing transverse energy $\vec{E}_{\mathrm{T}}^{\mathrm{miss}}$ (with magnitude $E_{\mathrm{T}}^{\mathrm{miss}}$) is therefore defined as the negative vectorial sum of transverse momenta of reconstructed objects associated with the primary vertex. These objects include electrons, photons, muons, jets, as well as the visible component of hadronically decaying τ leptons. The so called *soft contribution* is given by the transverse momenta of tracks associated with the primary vertex without being used in the reconstruction of the aforementioned objects. An ambiguity resolution algorithm is applied to prevent double counting contributions reconstructed as multiple, different objects. In the $H \to WW^*$ analysis presented in Chap. 4 additionally a quantity denoted $\vec{p}_{\mathrm{T}}^{\mathrm{miss}}$ (with magnitude $p_{\mathrm{T}}^{\mathrm{miss}}$) is used where the momenta of tracks associated with jets are used in place of the calorimeter based jet energy measurement. A comprehensive comparison of different $E_{\mathrm{T}}^{\mathrm{miss}}$ variants and their performance using early Run 2 data can be found in Ref. [111].

4 Measurement of the $H \to WW^*$ Cross Section in Production via Gluon Fusion and Vector-Boson Fusion

In this chapter the measurement of the inclusive cross sections times branching ratio for the gluon-fusion and vector boson fusion production of Higgs bosons with subsequent decay to a pair of W bosons is presented. The measurement is based on proton-proton collisions amounting to an integrated luminosity $\int L\ dt = 36\,\mathrm{fb}^{-1}$ of data recorded with the ATLAS detector in 2015 and 2016 at the LHC at $\sqrt{s} = 13\,\mathrm{TeV}$. The signal final state used is $e^{\pm}\nu\mu^{\mp}\nu$. This chapter is structured as follows: in Sec. 4.1 definitions and selection criteria for objects considered in the analysis are given. In Sec. 4.2 and 4.3 signal and background processes relevant to the analysis are described, the latter of these sections addressing background contributions due to misidentified leptons specifically. The main event selection is presented in Sec. 4.4, followed by the statistical interpretation of the so selected events described in Sec. 4.5. The results of the analysis are shown in Sec. 4.6 including a discussion of the most important sources of uncertainties. The analysis has been performed in collaboration with the ATLAS HWW subgroup and published in Ref. [112]. Throughout this chapter the term *leptons* refers to electrons and muons including those produced in decays of τ leptons.

4.1. Object Definitions

Objects considered in this analysis are reconstructed as described in Sec. 3.3. The reconstruction of jets, electrons, and muons can lead to ambiguities in the sense that activity in a detector region is reconstructed as more than one object candidate. Therefore an overlap removal procedure is applied using objects passing preselection criteria. For leptons these are given in Tab. 4.1. The photon ambiguity refers to the electron's calorimeter cluster also being reconstructed as a photon.

Jets are preselected by requiring $p_\mathrm{T} > 20\,\mathrm{GeV}$ and $|\eta| < 4.5$. Jets from pile-up collisions are suppressed by means of multivariate criteria described in Ref. [113] for jets with $|\eta| < 2.4$, and $p_\mathrm{T} < 60\,\mathrm{GeV}$ and in Ref. [114] for jets with $|\eta| > 2.5$, and $p_\mathrm{T} < 50\,\mathrm{GeV}$, also referred to as (forward) jet vertex taggers (f)JVT. Overlaps between objects passing these criteria are then removed as follows: in case an electron and a muon have a shared inner detector track, the electron is removed. As an exception this preference is inverted if the muon is *calorimeter tagged* [97]. Such muons are only included in the *loose* identification category in the range $|\eta| < 0.1$. Jets are removed if they are within $\Delta R < 0.2$ of an electron. Jets are also removed if they are within the same ΔR cone around a muon if the jet in question has less than three tracks with $p_\mathrm{T} > 500\,\mathrm{MeV}$, or $p_{\mathrm{T},\mu}/p_{\mathrm{T,jet}} > 0.5$ and $p_{\mathrm{T},\mu}/p_{\mathrm{T,jet\ tracks}} > 0.7$. The denominator in the latter ratio is the p_T sum of the jet's tracks with $p_\mathrm{T} > 500\,\mathrm{MeV}$. Finally, leptons within $\Delta R < \min(0.4, 0.04 + 10\,\mathrm{GeV}/p_\mathrm{T}^\ell)$ of a remaining jet are removed where p_T^ℓ is the p_T of the lepton. For the construction of $\vec{p}_\mathrm{T}^{\,\mathrm{miss}}$ and $\vec{E}_\mathrm{T}^{\,\mathrm{miss}}$ objects passing the preselection criteria are used.

Leptons finally considered in the analysis are those matching any of the remaining categories in Tab. 4.1. The ID and anti-ID leptons with the highest and second highest p_T are referred to as the *leading* and *subleading lepton* with transverse momenta $p_\mathrm{T}^{\ell 0}$ and $p_\mathrm{T}^{\ell 1}$ respectively. An analogous p_T sorting and index labeling is used for jets.

For the jet multiplicity N_jets of an event only jets with $p_\mathrm{T} > 30\,\mathrm{GeV}$ are considered[1]. For the identification of b-jets the 85% efficiency working point [96] is used. The numbers of so tagged jets are denoted as $N_{b-\mathrm{jets},20}$, $N_{b-\mathrm{jets},30}$, and $N_{b-\mathrm{jets},20-30}$ when counting tagged jets with $p_\mathrm{T} > 20\,\mathrm{GeV}$, $p_\mathrm{T} > 30\,\mathrm{GeV}$, and $20\,\mathrm{GeV} < p_\mathrm{T} < 30\,\mathrm{GeV}$, respectively.

4.2. Signal and Background Processes and Samples

The processes estimated via simulation are summarized in Tab. 4.2 together with corresponding generators, PDF sets, showering tools, and perturbative order of the calculation of their predicted total cross section. Alternatives given for generators and showering tools are used to derive systematic uncertainties.

The ggF and VBF signal samples used comprise all leptonic decays of W bosons including those to τ leptons with potential subsequent decays to electrons or muons. The ggF samples are simulated in Powheg-Boxv2 NNLOPS [116, 117] reweighting

[1] In the corresponding ATLAS analysis [115] based on the Run 1 dataset the p_T threshold is 25 GeV for $|\eta| < 2.5$ and 30 GeV for $|\eta| > 2.5$.

Table 4.1.: Lepton selection criteria for the $H \to WW^*$ analysis. The combination of the listed criteria is a logical *and* of each criterion. The shorthand LH indicates a likelihood based discriminant. Identification and isolation requirements are abbreviated as "id" and "iso". Names of working points in quotation marks refer to those in Ref. [99] for electrons and Ref. [97] for muons. The custom muon isolation working point is described in Sec. 3.3.3. For anti-ID muons the preselection requirements on muons' transverse impact parameter are loosened to the thresholds given in parentheses.

	electrons	muons
Preselection	$p_{\mathrm{T}} > 10\,\mathrm{GeV}$	$p_{\mathrm{T}} > 10\,\mathrm{GeV}$
	$\lvert\eta\rvert < 2.47$	$\lvert\eta\rvert < 2.7$
	id: "Loose" LH	id: "Loose"
	$\lvert z_0 \cdot \sin\theta\rvert < 0.5\,\mathrm{mm}$	$\lvert z_0 \cdot \sin\theta\rvert < 0.5\,\mathrm{mm}$
	$\lvert d_0\rvert/\sigma_{d_0} < 5$	$\lvert d_0\rvert/\sigma_{d_0} < 5$ (< 15)
ID	Preselection	Preselection
	veto $1.37 < \lvert\eta\rvert < 1.52$	
	id: "Tight" LH ($p_{\mathrm{T}} < 25\,\mathrm{GeV}$), "Medium" LH ($p_{\mathrm{T}} > 25\,\mathrm{GeV}$)	id: "Tight"
	iso: "Fixed (Tight)" ($p_{\mathrm{T}} < 25\,\mathrm{GeV}$), "Gradient" ($p_{\mathrm{T}} > 25\,\mathrm{GeV}$)	iso: custom (see Sec. 3.3.3)
	veto photon ambiguity	
anti-ID	Preselection	Preselection
	id: "Loose" LH	id: "Medium"
	veto $1.37 < \lvert\eta\rvert < 1.52$	
	veto photon ambiguity	
	veto ID	veto ID
3rd lepton veto	Preselection	Preselection
	$p_{\mathrm{T}} > 15\,\mathrm{GeV}$	$p_{\mathrm{T}} > 15\,\mathrm{GeV}$
	id: "Tight" LH ($p_{\mathrm{T}} < 25\,\mathrm{GeV}$), "Medium" LH ($p_{\mathrm{T}} > 25\,\mathrm{GeV}$)	
	iso: "Gradient (Loose)"	iso: "Gradient (Loose)"

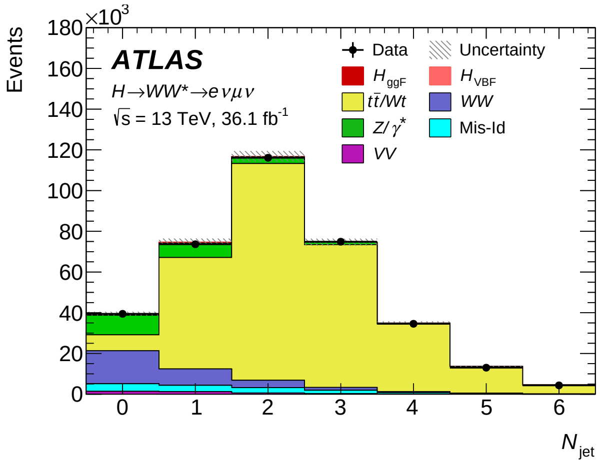

Figure 4.1.: Jet multiplicity distribution in the $H \to WW^*$ analysis after the event-level preselection criteria described in Sec. 4.4 are applied. The hatched band represents statistical and experimental systematic uncertainties. Published in Ref. [112].

the rapidity spectrum of the Higgs bosons to the spectrum in Ref. [118] resulting in NNLO accuracy in QCD. The PDF set used is PDF4LHC15 NNLO [119]. Similarly the VBF process is simulated in POWHEG-BOXv2 [116,117,120,121] at NLO accuracy in QCD. The PDF set used is PDF4LHC15 NLO [119]. In both cases the mass of the Higgs boson is set to 125 GeV and parton showers, hadronization, and underlying event are simulated by PYTHIA8 [57][2] with the AZNLO parameter set [122]. The branching ratio of $H \to WW^*$ is taken as 0.214 [60] as computed for the Standard Model in HDecay v6.50 [123, 124]. The inclusive cross section of the ggF process is calculated at N3LO in QCD including EW corrections up to NLO [125–129]. For VBF the cross section includes NLO EW corrections and approximates NNLO in QCD [125, 130–132].

Contributions from other production or decay modes of the Higgs boson (*other* H) are small after the selection presented in Sec. 4.4. They are treated as backgrounds and fixed to their SM predictions (VH, $H \to WW^*$ and ggF, VBF, and VH, $H \to \tau\tau$) or neglected. While contributions from $H \to \tau\tau$ and VH, $H \to WW^*/\tau\tau$ are considered in the statistical analysis described in Sec. 4.5 they are too small to be visible in graphics presented here and therefore omitted in these. An overview of the main background processes relevant for this analysis is shown in Fig. 4.1 after a loose preselection. At low jet multiplicities the $WW(\to e\nu\mu\nu)$ and $Z/\gamma^* \to \tau\tau(\to \nu e\nu\nu\mu\nu)$ backgrounds are dominant. The latter is eventually strongly suppressed by the selection criteria. Contributions from $Z/\gamma^* \to ee/\mu\mu$

[2] version 8.210 for ggF, version 8.186 for VBF

are even more suppressed due to the restriction to the $e\nu\mu\nu$ signature. At higher jet multiplicities the production of top quark pairs ($t\bar{t}$) and single top quarks (Wt), summarized as the *top* background, are dominant. As only decay modes producing two prompt leptons are considered for the top background other single top processes are not included. Other processes estimated from MC simulation are WZ, ZZ, $V\gamma^*$ ($V = W, Z$), and $V\gamma$ jointly denoted as VV.

4.3. Estimation of Contributions from Misidentified Leptons

Only processes yielding at least two prompt leptons are considered in Sec. 4.2. Remaining background contributions relevant to this analysis are events with misidentified leptons denoted as *mis-ID* in Fig. 4.1. These misidentified leptons, or *fakes* for short, comprise lepton candidates reconstructed from jets and non-prompt decays of c- and b-hadrons. For the selection detailed in Sec. 4.4 the main contribution to this category is from the production of a W boson in association with jets (W+jets), the former decaying via $W \to \ell\nu$ and the latter being misidentified as a second lepton. A smaller contribution can be associated with multijet production resulting in two misidentified leptons. A precise and accurate estimation of these backgrounds from simulation is facing several challenges. The acceptance for such events is very low after the criteria discussed in Sec. 4.1 are applied. Yet, the contribution is non-negligible due to the large cross sections of the processes involved (see Fig. 2.10). Achieving sufficient statistical precision using simulated events would therefore require huge computing resources. The probability of a jet being misidentified as a lepton depends on the flavor of the jet. The accuracy of a MC based prediction is therefore limited to that of the theoretical prediction of the jets' composition. Hence, a data-driven method, often referred to as *fake-factor method*, is employed to estimate the mis-ID background and is presented in this section.

4.3.1. The Fake-Factor Method

For the fake-factor method two categories of reconstructed leptons are defined. In the analysis at hand these are given by the ID and anti-ID categories in Tab. 4.1. The anti-ID category employs looser selection criteria compared to ID while explicitly vetoing leptons passing criteria for the latter. It is, hence, enriched in mis-ID leptons compared to the ID category. The *fake factor* FF is the ratio of the number of misidentified leptons of a particular type $\ell = e, \mu$ in these categories in

Table 4.2.: Summary of tools used to simulate signal and background processes in the $H \to WW^*$ analysis and perturbative order of total cross section computation. Alternative implementations and configurations are given in parentheses.

Process	Total cross section order of prediction	Hard scatter matrix element	PDF set	Underlying event, parton shower
ggF	N3LO(QCD), NLO(EW) [125–129]	Powheg-Box v2 NNLOPS [116–118] (MG5_aMC@NLO [133, 134])	PDF4LHC15 NNLO [119]	Pythia8 [57] (Herwig 7 [135])
VBF	NNLO(QCD), NLO(EW) [125, 130–132]	Powheg-Box v2	PDF4LHC15 NLO	Pythia8 (Herwig 7)
VH	NNLO(QCD), NLO(EW) [136–138]	Powheg-Box v2 [139]	PDF4LHC15 NLO	Pythia8
$qq \to WW$	NLO [140]	Sherpa 2.2.2 [141, 142] (Powheg-Box v2, MG5_aMC@NLO)	NNPDF3.0NNLO [143]	Sherpa 2.2.2 [144, 145] (Herwig++ [135], Pythia8)
$gg \to WW$	NLO [146]	Sherpa 2.1.1 [140]	CT10 [147]	Sherpa 2.1.1
$WZ, ZZ, V\gamma^*$	NLO [140]	Sherpa 2.1	CT10	Sherpa 2.1
$V\gamma$	NLO [140]	Sherpa 2.2.2 (MG5_aMC@NLO)	NNPDF3.0NNLO	Sherpa 2.2.2 (CSS variation [144, 148])
$t\bar{t}$	NNLO+NNLL [149]	Powheg-Box v2 [150] (Sherpa 2.2.1)	NNPDF3.0NLO	Pythia8 (Herwig 7)
Wt	NLO [151]	Powheg-Box v1 [151] (MG5_aMC@NLO)	CT10	Pythia 6.428 [152] (Herwig++)
Z/γ^*	NNLO [153, 154]	Sherpa 2.2.1 (MG5_aMC@NLO)	NNPDF3.0NNLO	Sherpa 2.2.1 (Pythia8)

bins of p_{T} and η

$$FF(p_{\mathrm{T}}, \eta) = \frac{N^{\mathrm{misID}}_{\mathrm{ID}}}{N^{\mathrm{misID}}_{\mathrm{anti-ID}}}.$$

The number of mis-ID events contributing in a data sample requiring two ID leptons can then be conceptually expressed as

$$N^{\mathrm{misID}}_{\mathrm{ID,ID}} = FF \cdot N^{\mathrm{misID}}_{\mathrm{ID,anti-ID}} - FF_0 \cdot FF_1 \cdot N^{\mathrm{misID}}_{\mathrm{anti-ID,anti-ID}}. \tag{4.1}$$

Here, the FF denotes the fake factor corresponding to the anti-ID lepton in events with one ID and one anti-ID lepton. In events with two anti-ID leptons FF_0, and FF_1 are the fake factors corresponding to each one of the anti-ID leptons. The N^{misID} are the number of events with misidentified leptons obtained from

$$N^{\mathrm{misID}}_{\mathrm{x,y}} = N^{\mathrm{data}}_{\mathrm{x,y}} - N^{\mathrm{MC}}_{\mathrm{x,y}},$$

where $N^{\mathrm{data}}_{\mathrm{x,y}}$ is the number of measured events with lepton candidates belonging to the ID/anti-ID categories indicated by the x and y subscripts. The number of events in such a category with more real leptons than ID leptons is denoted by $N^{\mathrm{MC}}_{\mathrm{x,y}}$ and subtracted using MC samples. That is, for $N_{\mathrm{ID,anti-ID}}$ only processes resulting in two real leptons are subtracted while also simulated W+jets events are subtracted for $N_{\mathrm{anti-ID,anti-ID}}$. The term is referred to as *electroweak correction* in the remainder of this document.

The double anti-ID term in Eq. (4.1) corrects for double accounting in the first term: the ID lepton can itself be a misidentified lepton. As either of the misidentified leptons can pass the ID criteria for the event to enter the "ID,anti-ID" category the contribution of events with two misidentified leptons in the "ID,ID" category is doubly accounted for by the first term and corrected by the second. In the analysis discussed in this chapter the correction is only applied for kinematic regions targeting the VBF production mode as it is found to be negligible in other regions.

As the fake factors only apply to events where the corresponding anti-ID lepton matches the fake factor's p_{T} and η bin the full expression of Eq. (4.1) includes a summation over all such bins for each occurrence of a fake factor in the term to be summed:

$$\begin{aligned} N^{\mathrm{misID}}_{\mathrm{ID,ID}} = &\sum_{(p_{\mathrm{T}},\eta)} FF(p_{\mathrm{T}}, \eta) \cdot N^{\mathrm{misID}}_{\mathrm{ID,anti-ID}}(p_{\mathrm{T}}, \eta) \\ &- \sum_{(p_{\mathrm{T}0},\eta_0)} \sum_{(p_{\mathrm{T}1},\eta_1)} FF_0(p_{\mathrm{T}0}, \eta_0) \cdot FF_1(p_{\mathrm{T}1}, \eta_1) \cdot N^{\mathrm{misID}}_{\mathrm{anti-ID,anti-ID}}(p_{\mathrm{T}0}, \eta_0, p_{\mathrm{T}1}, \eta_1). \end{aligned}$$

Generalizing this to arbitrary distributions the FF are applied as weights to each event based on its anti-ID leptons and including a factor -1 for MC events constituting the EW correction. In the so obtained extrapolation the anti-ID leptons are then treated as if they were ID leptons for all other aspects of the analysis.

4.3.2. Estimation of Fake Factors

In order to estimate the mis-ID background in a region enriched in events from the signal processes an orthogonal set of events is required to determine the fake factors from data. To this end a data sample enriched in Z+jets events is selected requiring three lepton candidates. The Z candidate is taken as the opposite-charge ee or $\mu\mu$ pair with invariant mass $m_{\ell\ell}$ closest to the Z boson mass. Both of these are required to belong to the ID category. If the third lepton candidate is an electron candidate the requirement $80\,\text{GeV} < m_{\ell\ell} < 110\,\text{GeV}$ is imposed. If it is a muon candidate the requirement is $70\,\text{GeV} < m_{\ell\ell} < 110\,\text{GeV}$. Additionally, at least one of the Z candidate leptons must be associated to the online object selected by one of the single-lepton triggers used in the analysis and described in Sec. 4.4. The remaining lepton is then considered as the fake candidate. In order to further reduce the contamination with real leptons from WZ production the transverse mass of the fake candidate

$$m_{\mathrm{T}}^{\ell} = \sqrt{2p_{\mathrm{T}}^{\ell}E_{\mathrm{T}}^{\mathrm{miss}}(1 - \cos\Delta\phi_{\vec{p}_{\mathrm{T}}^{\ell},\vec{E}_{\mathrm{T}}^{\mathrm{miss}}})} \tag{4.2}$$

is required to be $m_{\mathrm{T}}^{\ell} < 50\,\text{GeV}$. The p_{T} distributions of the fake candidate in the so constructed regions are shown in Fig. 4.2. For the estimation of the fake factors contributions from real leptons are subtracted using MC simulation. The dominant WZ contribution is normalized to data in a control region. The control region requires the third lepton to be in the ID category and inverts the m_{T}^{ℓ} requirement. Uncertainties from the normalization of the WZ process in the control region and its extrapolation to regions the fake factors are estimated from are summarized as the EW subtraction uncertainty.

The fake factors

$$FF = \frac{N_{\mathrm{ID}}^{\mathrm{data}} - N_{\mathrm{ID}}^{\mathrm{true}}}{N_{\mathrm{anti-ID}}^{\mathrm{data}} - N_{\mathrm{anti-ID}}^{\mathrm{true}}}$$

are finally derived in bins with $p_{\mathrm{T}}/\,\text{GeV}$ boundaries $[15, 20, 25, 35, \infty]$. For misidentified electrons the fake factors are additionally split in two $|\eta|$ bins separated at 1.5 [3]. The highest p_{T} bin of the muon fake factor already starts at 25 GeV and only a single inclusive bin in η is used. The granularity of the respective binning is

[3] The region $1.37 < |\eta| < 1.52$ is implicitly excluded by the ID and anti-ID criteria.

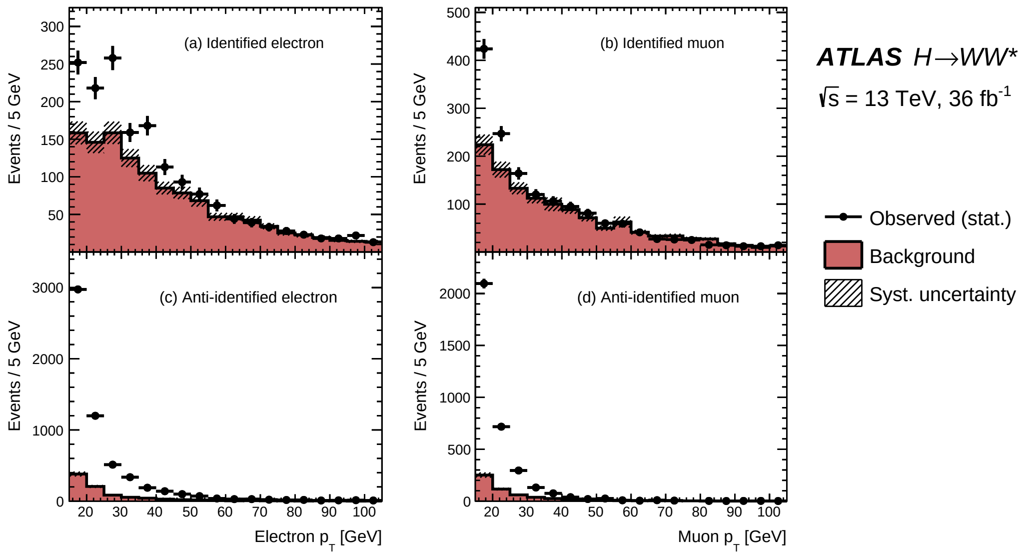

Figure 4.2.: Fake candidate p_{T} distribution in the $Z(\to \ell\ell)$+fake region. Contributions due to misidentified leptons are given by the difference between the observed yields and the MC based background estimate. Published as auxiliary material with Ref. [112].

limited by the size of the available data and MC samples. The resulting fake factors as functions of the misidentified lepton's p_{T} are shown in Fig. 4.3.

The flavor composition of jets produced in association with a Z boson differs from the composition of jets produced in association with a W boson. Therefore correction factors CF are derived for the electron and muon fake factors in two bins of the misidentified lepton's p_{T}. The correction factors are given by the ratio of fake factors derived from MC of the W+jets and Z+jets samples

$$CF = \frac{FF_{W+\text{jets}}}{FF_{Z+\text{jets}}},$$

where for the W+jets fake factor events are required to be reconstructed with two leptons of opposite charge. The central value of the correction factors are obtained from samples simulated with Powheg and Pythia8 [57, 155]. A systematic uncertainty regarding the predicted flavor composition is estimated via comparison to correction factors obtained from samples simulated using Alpgen together with Pythia6 [152, 156]. For all of these samples the CTEQ6L1 PDF set [157] is used. The resulting correction factors and uncertainties are given in Tab. 4.3.

The isolation and identification requirements of trigger chains (*triggers*) used in this analysis are tighter than the anti-ID requirements. Hence, a bias can be

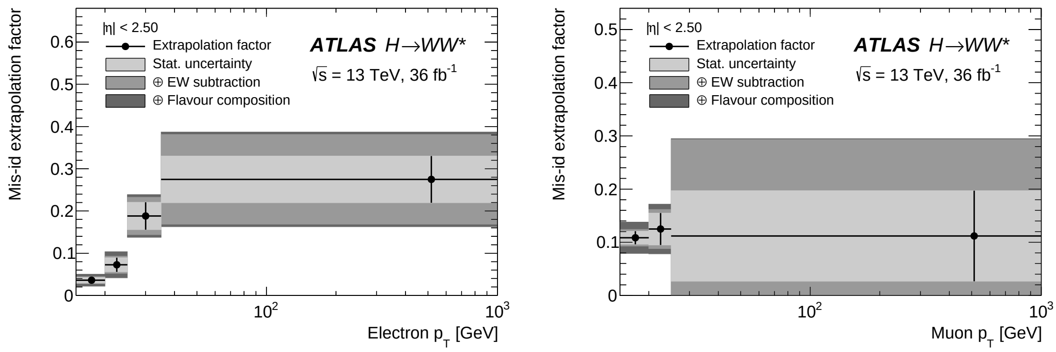

Figure 4.3.: Electron (left) and muon (right) fake factors (extrapolation factors) derived from the Z+jets enriched sample as a function of the p_{T} of the misidentified lepton and the full $|\eta|$ range. The shown uncertainties represent the finite size of the used data and MC samples (*stat.*), uncertainties on the subtraction of contributions of real leptons (*EW subtraction*) and uncertainties due to the different flavor composition of jets produced in association with Z ($\to \ell\ell$+fake) and $W(\to \ell\nu$+fake) bosons. Summation in quadrature is denoted by $\oplus$. Published as auxiliary material with Ref. [112].

Table 4.3.: Correction factors used in the estimation of background contributions due to misidentified leptons in the $H \to WW^*$ analysis. Statistical uncertainties originate from finite sizes of simulated samples used.

	$p_{\mathrm{T}} < 25\,\mathrm{GeV}$	$p_{\mathrm{T}} > 25\,\mathrm{GeV}$
e	$0.96 \pm 0.13(\mathrm{stat.}) \pm 0.28(\mathrm{syst.})$	$1.15 \pm 0.15(\mathrm{stat.}) \pm 0.02(\mathrm{syst.})$
μ	$1.34 \pm 0.17(\mathrm{stat.}) \pm 0.25(\mathrm{syst.})$	$1.83 \pm 0.38(\mathrm{stat.}) \pm 0.20(\mathrm{syst.})$

expected in events where exclusively the misidentified lepton causes the event to be selected by the trigger system. The available sample sizes for estimating a dedicated fake factor from Z+jets events are very small. Instead a sample enriched in dijet events is used to estimate *triggered fake factors* to be applied in the aforementioned cases in place of the regular fake factors. The sample is selected by requiring exactly one potentially misidentified lepton being also the one selected by one of the single lepton triggers used in the main analysis. Additionally, the requirements of at least one jet with $p_{\mathrm{T}} > 22\,\mathrm{GeV}$ and $m_T + E_{\mathrm{T}}^{\mathrm{miss}} < 50\,\mathrm{GeV}$ are imposed. The fake factors are estimated analogously to the ones based on the Z+jets enriched sample including simulation based subtraction of processes with at least one real lepton. The resulting fake factors are approximately between 0.4 and 1.7 depending on p_{T}, $|\eta|$ and the flavor of the misidentified lepton.

4.4. Event Selection

For the analysis presented in this chapter single and dilepton triggers are used. The individual single electron and single muon triggers use different E_{T} or p_{T} thresholds where triggers with higher thresholds for the same type of object require looser online[4] identification and isolation criteria to be passed. The lowest single electron trigger used requires $E_{\mathrm{T}} > 24\,\mathrm{GeV}$ for data recorded in 2015 and early 2016 and $E_{\mathrm{T}} > 26\,\mathrm{GeV}$ for the remainder of the data taken in 2016. The lowest p_{T} thresholds of the single muon triggers are 20 GeV (2015), 24 GeV (early 2016), and 26 GeV (late 2016). For the dilepton trigger to accept an event both an electron and muon are required. As the thresholds $E_{\mathrm{T}} > 17\,\mathrm{GeV}$ (electron) and $p_{\mathrm{T}} > 14\,\mathrm{GeV}$ (muon) are lower than those of the single lepton triggers, the acceptance for signal-like events is increased. The largest increase of signal acceptance is found to be about 22% in the ggF enriched $N_{\mathrm{jets}} = 0$ category for events where the electron is the leading lepton. All thresholds listed here refer to HLT requirements which exceed the corresponding L1 thresholds by multiple GeV.

In the offline event selection an electron and a muon of opposite charge are required which must be matched to the objects selected by a trigger responsible for the event to be recorded. The offline object's E_{T}, or p_{T}, respectively, must additionally exceed the matched triggers threshold by at least 1 GeV for electrons and 5% of the threshold for muons. The two signal leptons are required to be ID leptons as defined in Tab. 4.1 with exception of events used in the estimation of the mis-ID background. Events are rejected if a third lepton according to the 3$^{\mathrm{rd}}$ *lepton veto* category in Tab. 4.1 is present in the event. The two signal leptons must satisfy $p_{\mathrm{T}}^{\ell 0} > 22\,\mathrm{GeV}$ and $p_{\mathrm{T}}^{\ell 1} > 15\,\mathrm{GeV}$. The latter requirement is raised from 10 GeV to 15 GeV compared to the corresponding analysis of the Run 1 dataset [115]. The change is mainly due to the more challenging estimation of the mis-ID contribution at low transverse momenta. Potential contaminations from hadronic resonances such as J/Ψ not explicitly modeled in this analysis are suppressed by a lower requirement on the invariant mass of the dilepton system $m_{\ell\ell} > 10\,\mathrm{GeV}$.

Following this event-level preselection the analysis is split into three jet categories with $N_{\mathrm{jets}} = 0$, $N_{\mathrm{jets}} = 1$, and $N_{\mathrm{jets}} \geq 2$ where additionally $p_{\mathrm{T}}^{\mathrm{miss}} > 20\,\mathrm{GeV}$ is required in the $N_{\mathrm{jets}} = 0, 1$ categories. The first two N_{jets} categories target primarily the ggF production mode while the highest jet multiplicity bin is focused on the VBF production mode. In the following the terms ggF *analysis*, and VBF *analysis* refer to these categories. This split is not only motivated by the different signatures of the Higgs-boson production modes under study, but also the significantly different

[4] Online criteria applied during data taking are generally preliminary working points and calibrations. Offline criteria applied to recorded data can therefore slightly differ from their online pendants.

Table 4.4.: Event selection criteria used in the $H \to WW^*$ analysis. The first block is referred to as the preselection.

$N_{\text{jets}} = 0$ (ggF)	$N_{\text{jets}} = 1$ (ggF)	$N_{\text{jets}} \geq 2$ (VBF)
One electron, one opposite charge muon		
$p_{\text{T}}^{\ell 0} > 22\,\text{GeV}$		
$p_{\text{T}}^{\ell 1} > 15\,\text{GeV}$		
$m_{\ell\ell} > 10\,\text{GeV}$		
$p_{\text{T}}^{\text{miss}} > 20\,\text{GeV}$		
$N_{b-\text{jets},20} = 0$		
$\Delta\phi^{\ell\ell,\text{MET}} > \pi/2$	$\max(m_{\text{T}}^{\ell}) > 50\,\text{GeV}$	
$p_{\text{T}}^{\ell\ell} > 30\,\text{GeV}$	$m_{\tau\tau} < m_Z - 25\,\text{GeV}$	
$m_{\ell\ell} < 55\,\text{GeV}$		central jet veto
$\Delta\phi_{\ell\ell} < 1.8$		outside lepton veto

background composition in each category as shown in Fig. 4.1. The event-selection criteria in the three N_{jets} categories are summarized in Tab. 4.4.

4.4.1. Categories Targeting Production via Gluon Fusion

Despite the jet veto in the 0-jet category a sizeable number of top background events are found in this category. The inevitable b-jets from the decays of the top quarks are either outside of the detector acceptance or have sufficiently low p_{T} to not be counted towards the jet multiplicity. In the latter case the top background can still be reduced by vetoing b-tagged jets with $p_{\text{T}} > 20\,\text{GeV}$. Distributions of the number of such b-tagged jets per event are shown in Fig. 4.4 after the preselection criteria. Distributions of remaining quantities used to define the 0-jet *signal region* are shown in Fig. 4.5 where each distribution is shown at a selection level just before a selection based on the quantity shown is applied. The angle between the $\vec{p}_{\text{T}}$ of the dilepton system ($\vec{p}_{\text{T}}^{\,\ell\ell}$) and $\vec{E}_{\text{T}}^{\text{miss}}$ is denoted as $\Delta\phi^{\ell\ell,\text{MET}}$ and is distributed slightly more narrowly near π for the signal process compared to the distribution for background processes. Stronger separation with respect to background processes is given by the transverse momentum of the dilepton system $p_{\text{T}}^{\ell\ell}$. This difference is due to the spin correlation in the $H \to WW^*$ decay described in Sec. 2.3.1 leading to a collimated emission of the leptons and thereby closely aligned momenta. For the same reason $H \to WW^*$ events are enriched at small angles $\Delta\phi_{\ell\ell}$ between the leptons' transverse momenta and low $m_{\ell\ell}$. Yet, the non-resonant WW production remains as the largest background.

In order to constrain the total rates from the WW, top and Z/γ^* backgrounds dedicated control regions (CR) are defined which are enriched in events from the

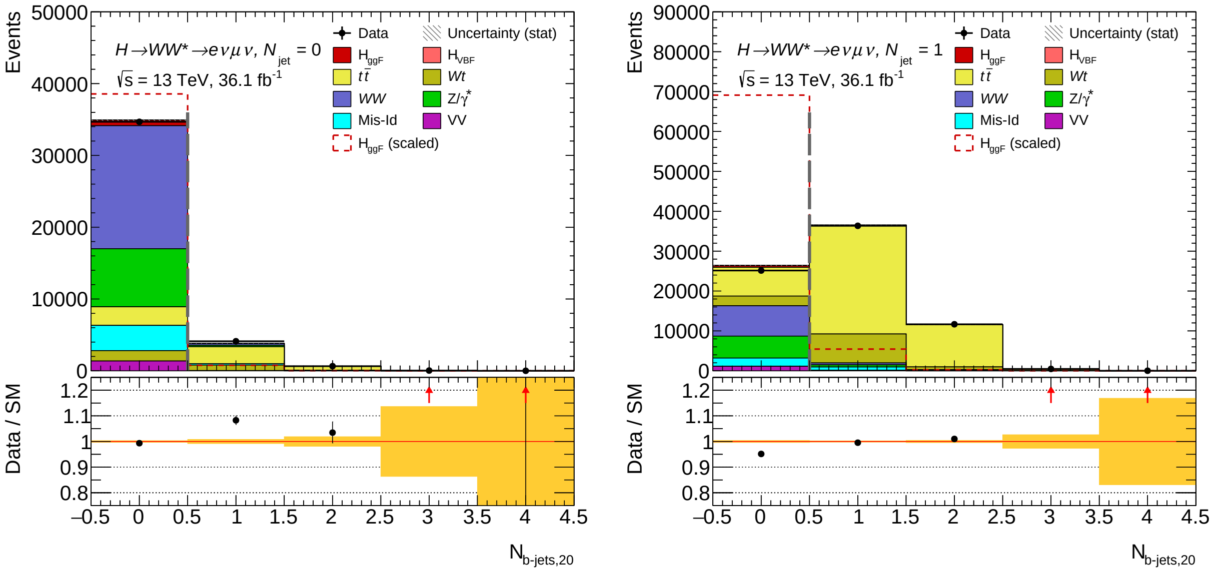

Figure 4.4.: Distributions of the number of b-tagged jets after preselection in the 0-jet and 1-jet categories. The distributions are shown at a selection level just before the selection based on the number of b-tagged jets is applied. The order of these selections follows that of Tab. 4.4. Stacked estimates are normalized to their prediction with exception of WW, top, and Z/γ^* which are scaled to measured data in control regions, resulting in scaling factors listed in Tab. 4.5. Selection thresholds for the signal regions are indicated by the vertical gray dashed line. Uncertainties shown include statistical uncertainties only. The overlaid ggF signal distribution is scaled to the integral of the stacked contributions. Red arrows in the bottom panels indicate the direction of ratio points outside the range shown.

respective background. They are ideally close to the just discussed signal region (SR) in order to reduce extrapolation uncertainties. For the 0-jet category the differences with respect to the selection criteria for the signal region are summarized in the following, where criteria ensuring orthogonality between signal and control regions are enquoted.

0-jet WW **CR** No requirements on $p_{\mathrm{T}}^{\ell\ell}$, and $\Delta\phi^{\ell\ell,\mathrm{MET}}$, loosened requirement $\Delta\phi_{\ell\ell} < 2.6$, and "$55\,\mathrm{GeV} < m_{\ell\ell} < 110\,\mathrm{GeV}$".

0-jet top CR No requirement on $m_{\ell\ell}$, loosened requirement $\Delta\phi_{\ell\ell} < 2.8$, and "$N_{b\mathrm{-jets},20-30} > 0$".

0-jet Z/γ^* **CR** No requirement on $p_{\mathrm{T}}^{\mathrm{miss}}$, $\Delta\phi^{\ell\ell,\mathrm{MET}}$, and $p_{\mathrm{T}}^{\ell\ell}$, loosened requirement $m_{\ell\ell} < 80\,\mathrm{GeV}$, and "$\Delta\phi_{\ell\ell} > 2.8$".

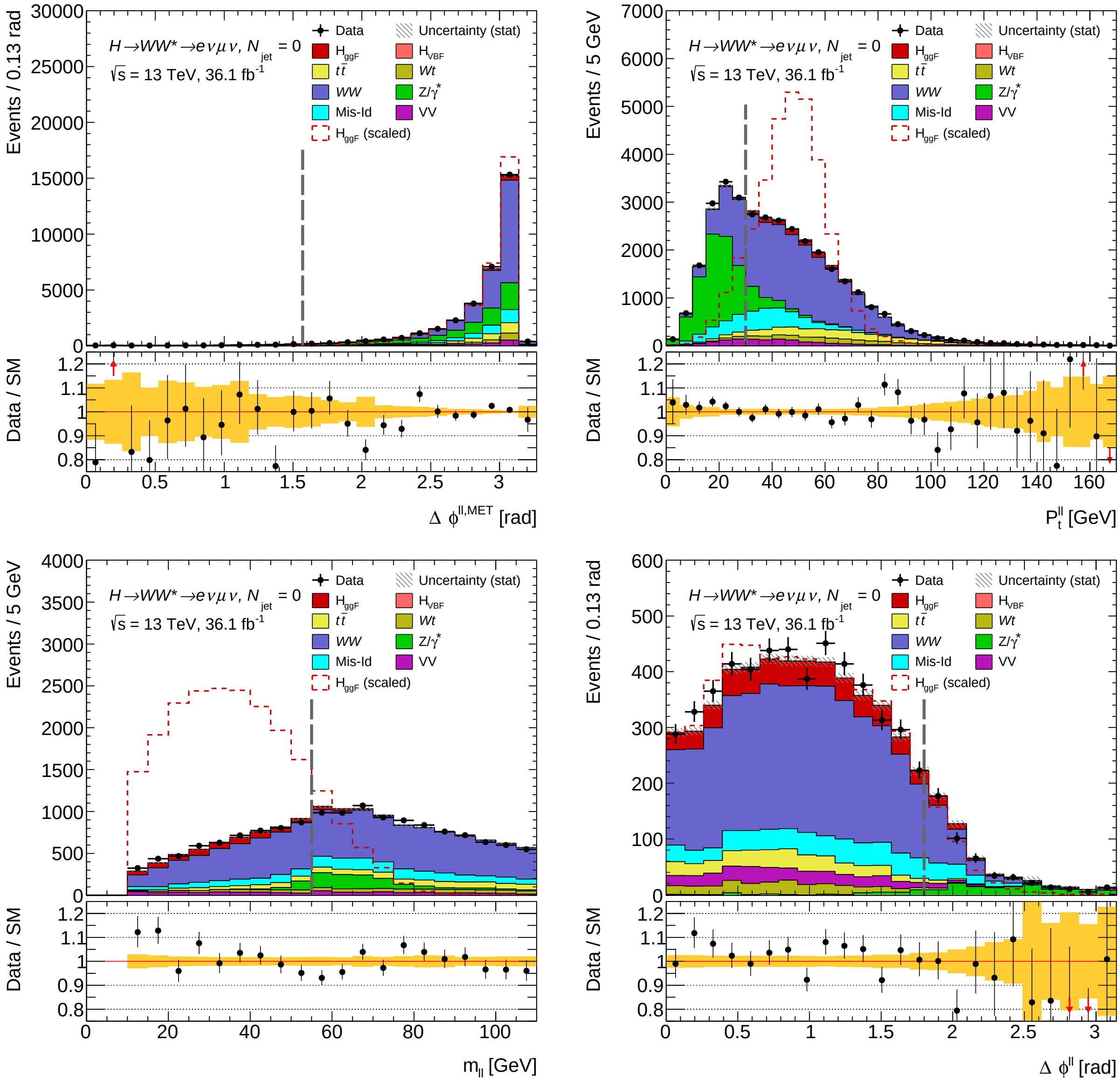

Figure 4.5.: Distributions of quantities used to enrich ggF $H \to WW^*$ events in the 0-jet category. Each distribution is shown at a selection level just before the selection based on that variable. The order of these selections follows that of Tab. 4.4. Stacked estimates are normalized to their prediction with exception of the WW, top, and Z/γ^* which are scaled to measured data in control regions, resulting in scaling factors listed in Tab. 4.5. Selection thresholds for the signal regions are indicated by the vertical gray dashed line. Uncertainties shown include statistical uncertainties only. The overlaid ggF signal distribution is scaled to the integral of the stacked contributions. Red arrows in the bottom panels indicate the direction of ratio points outside the range shown.

Table 4.5.: Background scaling factors used for distributions and yields shown in Sec. 4.4. No uncertainties are given as the factors are used only for visualization prior to a full likelihood-based treatment.

	0-jet	1-jet	$\geq$ 2-jet
WW	1.07	1.00	-
top	0.99	1.02	1.00
Z/γ^*	0.86	0.86	0.90

The top control region represents a simplification compared to the Run 1 analysis [115] where multiple regions are used to estimate a jet-veto survival probability. No reduction in analysis sensitivity due to this change is found.

Distributions and event yields given in this section include scaling factors for backgrounds for which a control region of the same jet multiplicity is defined. Their values are listed in Tab. 4.5 and are only used to provide a refined comparison between observed and modeled distributions and yields. These scaling factors are not used in the likelihood fit in Sec. 4.5, but instead normalization factors are determined in-situ. The scaling factors used for visualization are determined by subtracting the predicted yields $n_{\text{other},i}$ of processes not to be scaled from the observed yields d_i in the control regions denoted by i. Let S_j denote the scale factor for process j and n_{ij} the predicted yield of that process in control region i. Then the S_j are obtained by solving a set of linear equations

$$d_i - n_{\text{other},i} = d'_i = n_{ij} S_j.$$

In the 1-jet category again events containing b-tagged jets with $p_{\text{T}} > 20\,\text{GeV}$ are vetoed. The larger of the individual leptons' transverse masses ($\max(m_{\text{T}}^{\ell})$) is used to select events where at least one lepton originates from a W boson. The $Z/\gamma^* \to \tau\tau$ background is further reduced via a requirement on the invariant mass of a hypothesized pair of tau leptons $m_{\tau\tau}$ which is calculated in the collinear approximation [158][5]. If for a given kinematic configuration $m_{\tau\tau}$ cannot be computed it is treated equivalently to $m_{\tau\tau} = 0$. As in the 0-jet category the azimuthal angle between the two leptons $\Delta\phi_{\ell\ell}$ and their invariant mass $m_{\ell\ell}$ exploit the $H \to WW^*$ spin correlation. Distributions of these quantities used to enrich the signal are presented in Figs. 4.4 and 4.6. The expected event yields at each selection step after preselection as well as in the control regions are shown in Tab. 4.6. In the signal regions the WW and top processes make the largest contributions to the background rate.

[5] As this approximation fails if the suspected τ leptons are emitted in a back-to-back topology $m_{\tau\tau}$ is not employed in the 0-jet category due to the lack of a recoil object.

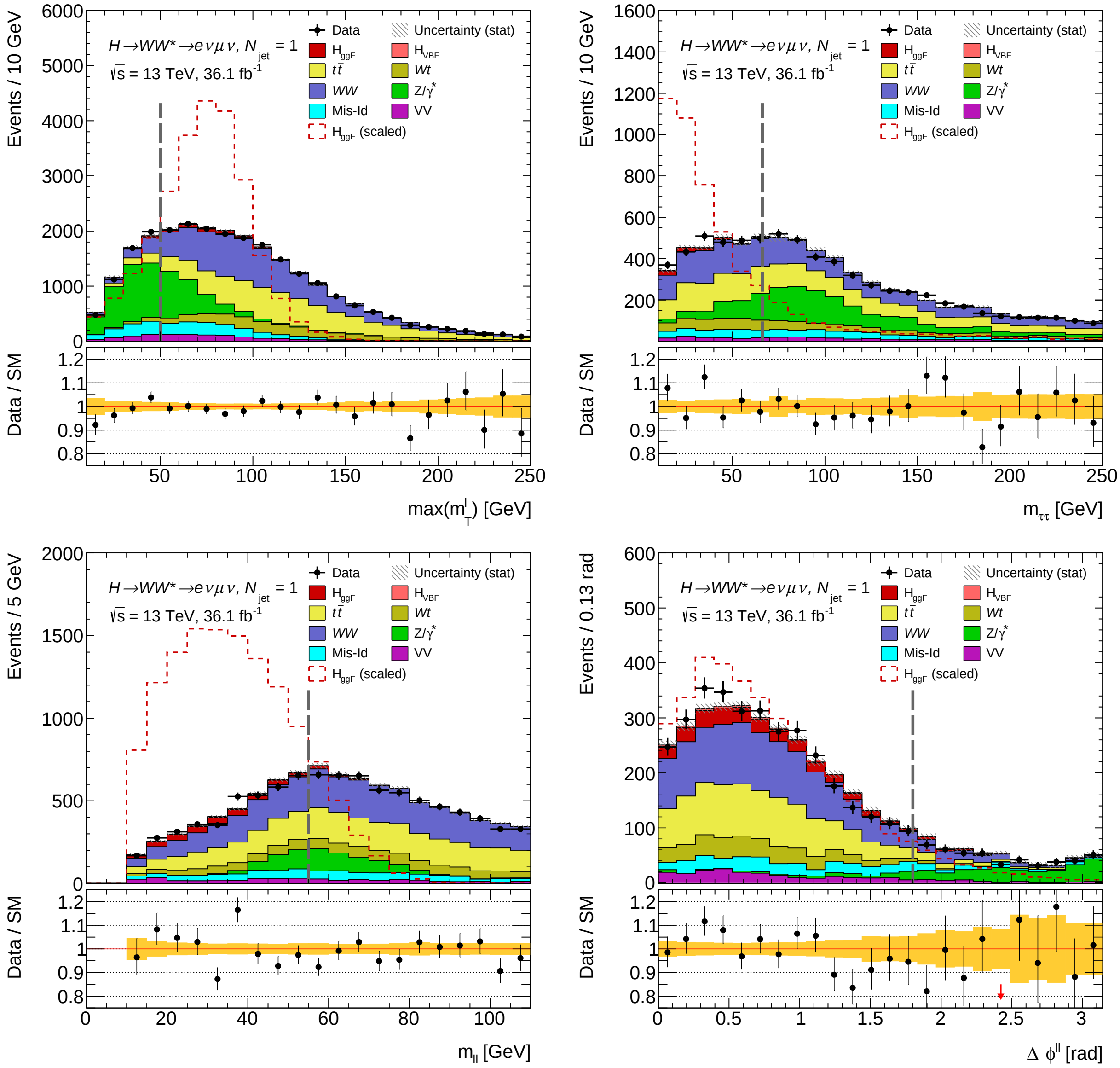

Figure 4.6.: Distributions of quantities used to enrich ggF $H \to WW^*$ events in the 1-jet category. Each distribution is shown at a selection level just before the selection based on that variable. The order of these selections follows that of Tab. 4.4. Stacked estimates are normalized to their prediction with exception of WW, top, and Z/γ^* which are scaled to measured data in control regions, resulting in scaling factors listed in Tab. 4.5. Selection thresholds for the signal regions are indicated by the vertical gray dashed line. Uncertainties shown include statistical uncertainties only. The overlaid ggF signal distribution is scaled to the integral of the stacked contributions. Red arrows in the bottom panels indicate the direction of ratio points outside the range shown.

Analogously to the 0-jet category 1-jet control regions are defined to constrain background event rates using data with the same jet multiplicity as the corresponding signal region. The following changes with respect to the selection for the signal region are applied. Criteria ensuring orthogonality with respect to the signal region are again enquoted.

1-**jet** WW **CR** No requirements on $\Delta\phi_{\ell\ell}$, loosened $|m_{\tau\tau} - m_Z| > 25\,\mathrm{GeV}$, and "$m_{\ell\ell} > 80\,\mathrm{GeV}$".

1-**jet top CR** No requirements on $\Delta\phi_{\ell\ell}$, and $m_{\ell\ell}$, and modified b-tagging requirements $N_{b-\mathrm{jets},20-30} = 0$, $N_{b-\mathrm{jets},30} = 1$. The split b-tag requirement ensures no extrapolation is being performed with respect to low p_T jets where uncertainties of the b-tagging efficiency are much larger than starting from 30 GeV [96].

1-**jet** Z/γ^* **CR** No $p_\mathrm{T}^\mathrm{miss}$, $\Delta\phi_{\ell\ell}$ requirements, loosened $m_{\ell\ell} < 80$, and "$m_{\tau\tau} > m_Z - 25\,\mathrm{GeV}$".

4.4.2. Categories Targeting Production via Vector-Boson Fusion

For the signal region targeted at VBF production the same requirement as for the 1-jet signal region is imposed on the number of b-jets $N_{b-\mathrm{jets},20} = 0$. The two jets with the highest p_T in this category are considered as the *tagging jets* characteristic for the VBF process. A central jet veto is applied, *i.e.*, events are rejected if a jet with p_T of at least 20 GeV is found within the pseudorapidity gap spanned by the two tagging jets. The leptons are required to be within the pseudorapidity range delimited by the pseudorapidity of these jets (*outside lepton veto*). The $Z/\gamma^* \to \tau\tau$ background is reduced by demanding $m_{\tau\tau} < m_Z - 25\,\mathrm{GeV}$. Distributions of these quantities and criteria are shown in Fig. 4.7. After this selection a boosted decision tree (BDT) is used as the final discriminant. Variables used in this BDT are

m_{jj} the invariant mass of the two tagging jets and

Δy_{jj} their rapidity separation to exploit the topology of the highly energetic tagging jets.

$m_{\ell\ell}$, $\Delta\phi_{\ell\ell}$ The invariant mass and azimuthal angular spacing of the dilepton system are used for the same reasons as in the 0-jet and 1-jet categories.

$\sum_\ell C_\ell$ The lepton η-centrality where $C_\ell = \frac{|2\eta_\ell - \sum_j \eta_j|}{\Delta\eta_{jj}}$ and

$\sum m_{\ell j}$ the sum of invariant masses of all four lepton + tagging jet combinations: while the tagging jets are usually found at high $|\eta|$ the W bosons from the Higgs decay and the resulting leptons are produced mostly central, *i.e.* at low $|\eta|$ resulting in larger mass sums and smaller η-centrality values compared to

Table 4.6.: Expected and observed event yields at different stages of the event selection for the $H \to WW^*$ analysis. Uncertainties shown are statistical uncertainties due to finite MC and data sample sizes. The total background (bkg) represents the sum of all processes not producing a Higgs boson. Yields of the WW (only in 0-jet and 1-jet categories), top, and Z/γ^* processes are scaled to measured data in control regions. The 0-jet and 1-jet signal regions are additionally shown split into cases where the subleading lepton ℓ_1 is either an electron or a muon.

	ggF	VBF	other H	WW	other VV	$t\bar{t}$	Wt	Z/γ^*	Mis-Id (e)	Mis-Id (μ)	$V\gamma$	Total Bkg	Data/Bkg	Data
Preselection	1617±4	166.4±0.5	504.8±2.0	35210±70	2902±28	286280±240	26930±70	85260±250	8280±110	9170±90	2630±70	456700±400	0.9776±0.0017	446444
$p_{\mathrm{T}}^{\mathrm{miss}} > 20\,\mathrm{GeV}$	1506±4	157.1±0.5	296.9±1.5	29970±70	2331±25	266440±230	25150±60	21660±140	6260±90	6010±70	1340±40	359150±310	0.9967±0.0019	357965
0-jet	782.2±3.2	9.33±0.12	82.9±0.8	17380±60	867±14	5495±33	2259±19	8290±80	1890±40	1848±32	533±27	38560±120	1.024±0.006	39474
b-jet veto	760.1±3.1	8.84±0.12	79.2±0.8	17020±50	836±14	2512±22	1403±15	8020±80	1790±40	1749±31	516±26	33840±120	1.025±0.007	34679
$\Delta\phi^{\ell\ell,\mathrm{MET}} > \pi/2$	756.2±3.1	8.72±0.12	76.1±0.7	16910±50	787±13	2470±22	1389±15	7610±80	1740±35	1668±30	494±26	33070±110	1.026±0.007	33943
$p_{\mathrm{T}}^{\ell\ell} > 30\,\mathrm{GeV}$	673.1±3.0	7.93±0.11	36.6±0.4	13710±50	613±12	2236±21	1254±14	1090±40	1220±28	1032±20	265±19	21410±80	1.025±0.008	21949
$m_{\ell\ell} < 55\,\mathrm{GeV}$	575.2±2.7	6.77±0.10	10.44±0.18	3313±23	194±6	340±8	226±6	152±11	296±13	301±10	115±12	4936±35	1.136±0.017	5607
$\Delta\phi_{\ell\ell} < 1.8$	534.8±2.6	6.42±0.10	9.43±0.17	3064±22	181±6	326±8	219±6	23±5	254±12	237±9	106±11	4409±32	1.154±0.018	5089
$\Delta\Phi_{\ell\ell} < 1.8$, only $\ell_1 = \mu$	316.2±2.1	3.76±0.08	5.33±0.12	1748±17	108±5	185±6	128±4	11.6±2.8	127±10	191±7	44±7	2542±24	1.130±0.024	2874
$\Delta\Phi_{\ell\ell} < 1.8$, only $\ell_1 = e$	218.6±1.6	2.66±0.06	4.10±0.11	1316±14	72.6±3.4	142±5	91±4	10.9±3.5	127±7	46±6	62±9	1867±21	1.186±0.028	2215
WW CR 0-jet	86.8±1.1	1.03±0.04	10.34±0.23	4973±29	209±7	676±11	402±8	334±19	380±16	304±11	83±11	7360±40	1.013±0.013	7461
Ztt CR 0-jet	44.0±0.7	0.491±0.026	102.80±1.00	921±12	163±6	41.3±3.1	25.7±1.9	40710±140	827±33	1880±40	750±40	45320±150	1.003±0.006	45463
top CR 0-jet	18.7±0.6	0.389±0.025	1.71±0.09	245±8	19.9±2.6	2278±22	671±11	49±6	55±9	49±6	10±4	3378±29	1.006±0.019	3399
1-jet	465.0±2.3	53.33±0.29	106.9±0.9	8080±40	784±15	45320±100	10450±40	6070±70	1590±50	1526±35	458±25	74280±150	0.991±0.004	73635
b-jet veto	421.8±2.1	48.75±0.27	93.4±0.8	7449±35	700±14	6597±35	2225±19	5400±70	1095±32	1043±27	402±24	24920±100	1.009±0.008	25135
$\max(m_{\mathrm{T}}^{\ell}) > 50\,\mathrm{GeV}$	347.7±1.9	37.92±0.24	63.1±0.7	6864±33	561±12	6184±34	2089±18	2250±40	779±26	627±20	214±17	19570±80	1.008±0.008	19733
$m_{\tau\tau} < m_Z - 25\,\mathrm{GeV}$	326.3±1.9	34.99±0.23	28.8±0.4	4909±28	375±9	4336±28	1475±15	820±25	502±21	389±15	133±14	12940±60	1.0170±0.0100	13166
$m_{\ell\ell} < 55\,\mathrm{GeV}$	282.2±1.8	30.69±0.22	14.73±0.32	1246±14	135±6	996±13	369±7	300±14	163±11	168.0±10	85±10	3461±31	1.087±0.020	3762
$\Delta\phi_{\ell\ell} < 1.8$	263.9±1.7	29.14±0.21	12.74±0.30	1133±13	120±5	942±13	350±7	63±7	140±10	129±8	73.0±10	2949±27	1.107±0.022	3264
$\Delta\Phi_{\ell\ell} < 1.8$, only $\ell_1 = \mu$	150.8±1.3	16.22±0.16	7.38±0.22	631±10	67±4	533.0±10	206±6	33±5	69±8	95±6	29±6	1663±20	1.101±0.029	1831
$\Delta\Phi_{\ell\ell} < 1.8$, only $\ell_1 = e$	113.1±1.1	12.92±0.14	5.36±0.20	502±9	52.8±3.0	409±8	145±5	29±6	71±6	34±5	44±8	1286±18	1.114±0.033	1433
WW CR 1-jet	1.56±0.14	0.189±0.018	11.75±0.24	3829±25	260±8	3689±27	1193±14	194±16	371±18	195±10	54±9	9780±50	1.000±0.011	9784
$Z \to \tau\tau$ CR 1-jet	25.8±0.5	3.50±0.07	39.3±0.6	322±7	52±4	212±6	67.2±3.2	2570±40	97±12	162±13	91±11	3570±50	1.000±0.021	3571
top CR 1-jet	20.6±0.5	2.03±0.06	3.54±0.17	243±7	26.4±3.3	14450±50	4252±27	69±7	206±21	173±14	7.2±2.5	19430±70	1.000±0.008	19428

	ggF	VBF	other H	WW	other VV	$t\bar{t}$	Wt	Z/γ^*	Mis-Id (e)	Mis-Id (μ)	Mis-Id correction	$V\gamma$	Total Bkg	Data/Bkg	Data
2-jet	276.4±1.7	99.7±0.4	130.20±1.00	6210±17	751±15	232330±220	13400±50	6870±60	3090±80	2950±50	−513±14	429±23	265520±250	0.9962±0.0022	264515
b-jet veto	228.5±1.5	86.1±0.4	103.4±0.8	5178±16	586±14	12330±50	1630±16	5510±60	776±29	718±24	−259±8	354±21	26830±90	0.978±0.007	26229
central jet veto	168.5±1.3	66.13±0.32	78.1±0.7	3700±14	394±9	8110±40	1215±14	4040±50	554±24	537±21	−188±8	239±18	18610±80	0.983±0.008	18301
outside lepton veto	44.3±0.7	51.25±0.28	24.01±0.34	642±6	81±4	1749±18	254±6	860±24	117±12	120±10	−39.9±2.5	55.0±10	3840±40	0.994±0.019	3813
$m_{\tau\tau} < m_Z - 25\,\mathrm{GeV}$	39.3±0.6	44.22±0.26	6.31±0.20	400±5	48.5±3.2	1139±14	164±5	295±16	67±8	69±7	−27.2±2.0	29±8	2185±26	0.990±0.024	2164
$Z \to \tau\tau$ CR	2.89±0.16	4.10±0.08	5.79±0.16	22.0±1.0	6.5±1.0	50.1±2.9	6.7±0.9	367±14	19±5	9±5	−5.2±0.8	12.7±2.8	488±17	1.03±0.06	501
top CR	5.42±0.26	5.090±0.100	1.46±0.12	52.5±1.7	7.8±1.2	6720±40	640±10	49±5	94±13	96.0±10	−10±4	3.8±1.5	7660±40	1.002±0.013	7668

backgrounds where leptons and jets are produced in closer relation to each other, *e.g.*, from the decay of a top quark.

$p_{\mathrm{T}}^{\mathrm{tot}}$ The magnitude of the vectorial sum of transverse momenta of all selected leptons, jets and $\vec{E}_{\mathrm{T}}^{\mathrm{miss}}$.

m_{T} In Eq. (4.2) the transverse mass is given for a single lepton. For a system of visible decay products with mass m^{vis}, vectorial sum of transverse momenta $\vec{p}_{\mathrm{T}}^{\mathrm{vis}}$, and $E_{\mathrm{T}}^{\mathrm{vis}} = \sqrt{|\vec{p}_{\mathrm{T}}^{\,\mathrm{vis}}|^2 + m^{\mathrm{vis}}}$ this can be generalized to[6]

$$m_{\mathrm{T}}^{\mathrm{vis}} = \sqrt{\left(E_{\mathrm{T}}^{\mathrm{vis}} + E_{\mathrm{T}}^{\mathrm{miss}}\right)^2 - \left|\vec{p}_{\mathrm{T}}^{\,\mathrm{vis}} + \vec{E}_{\mathrm{T}}^{\,\mathrm{miss}}\right|^2}.$$

The transverse mass of the dilepton system is denoted by m_{T} and included in the BDT.

Distributions of these quantities are presented in Fig. 4.8 and in the Appendix in Fig. D.1.

For the $\geq$ 2-jet category only the rates of the Z/γ^* and top backgrounds are constrained by dedicated control regions. The selection of events for the top control region is identical to that of the signal region except for the requirement $N_{b\text{−jets},20} = 1$. For the Z/γ^* control region the $m_{\tau\tau}$ criterion is changed to $|m_{\tau\tau} - m_Z| < 25\,\mathrm{GeV}$ and $m_{\ell\ell} < 80\,\mathrm{GeV}$ is required in addition to the remaining selection criteria also applied for the signal region. The predicted and observed event yields after the different selection steps towards the VBF signal region as well as in the corresponding control regions are given in Tab. 4.6. The dominant background in the VBF signal region originates from top processes. However, as can be seen from Tab. 4.8, in the highest BDT bin the contributions from WW and top processes are similar. Contributions due to misidentified leptons in this bin are smaller compared to WW and top yields, yet these are highly relevant due to large systematic uncertainties associated with this background.

Contributions from other Higgs boson production or decay modes are predominantly VH, $H \to WW^*$ and $H \to \tau\tau$. While their yields exceed those of the signal processes in some control regions they are still negligible compared to the total yields in these regions.

4.5. Statistical Analysis

The cross sections times branching ratio $\sigma_{\mathrm{ggF}} \cdot \mathcal{B}_{H\to WW^*}$ and $\sigma_{\mathrm{VBF}} \cdot \mathcal{B}_{H\to WW^*}$ are extracted by means of a maximum likelihood fit as introduced in Sec. 2.4. In this

[6] Up to masses of the individual visible particles

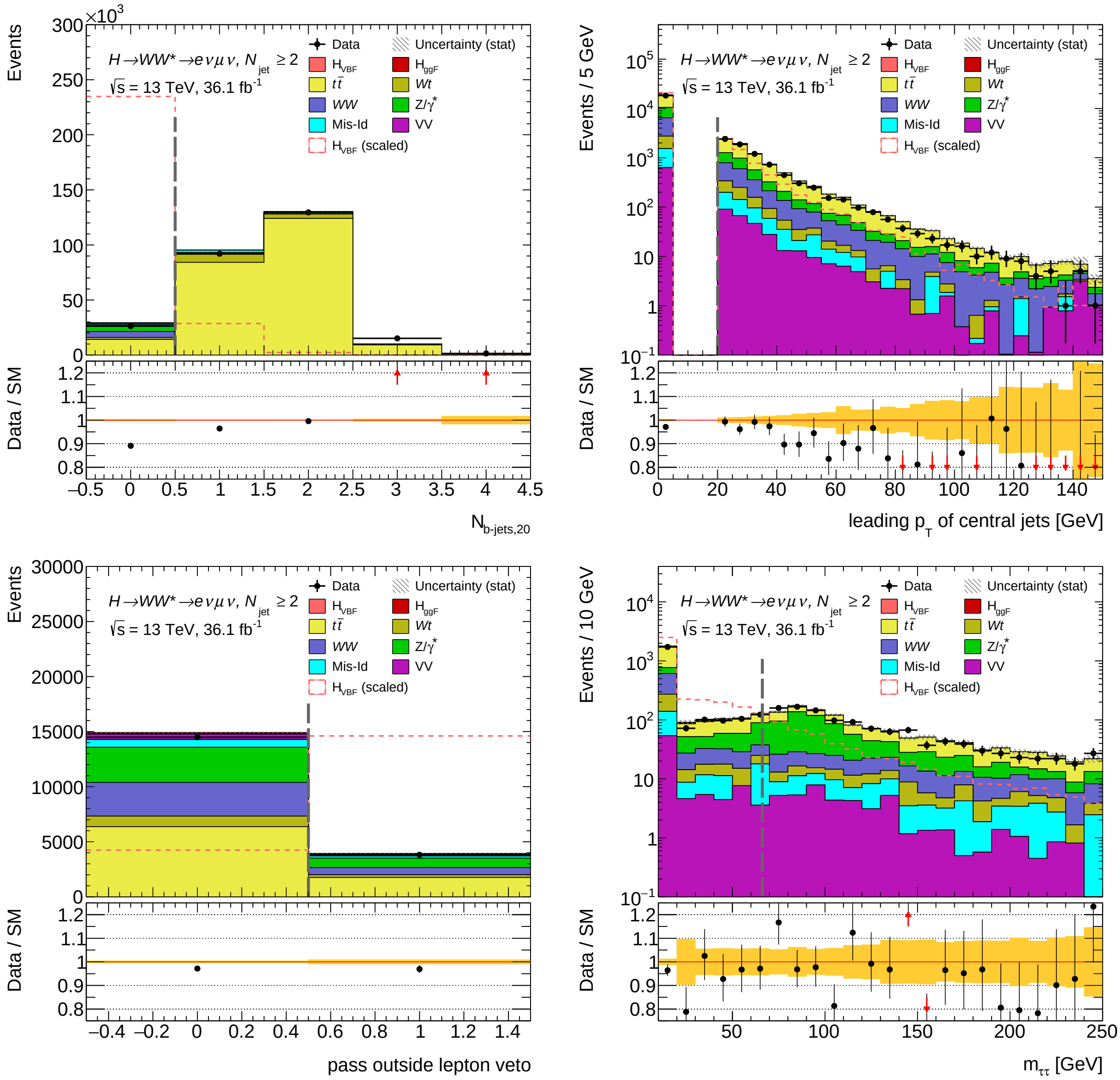

Figure 4.7.: Distributions of selection variables used to enrich VBF $H \to WW^*$ events in the $\geq$ 2-jet category. Each distribution is shown at a selection level just before the selection based on that variable. The order of these selections and graphics shown here follows that in the text. Stacked estimates are normalized to their prediction with exception of top, and Z/γ^* which are scaled to measured data in control regions, resulting in scaling factors listed in Tab. 4.5. Selection thresholds for the signal regions are indicated by the vertical gray dashed line. The leading p_{T} of central jets shows a gap as only jets with $p_{\mathrm{T}} > 20$ GeV are considered. Events to the right of this gap are rejected by the central jet veto. Uncertainties shown include statistical uncertainties only. The overlaid VBF signal distribution is scaled to the integral of the stacked contributions. Red arrows in the bottom panels indicate the direction of ratio points outside the range shown.

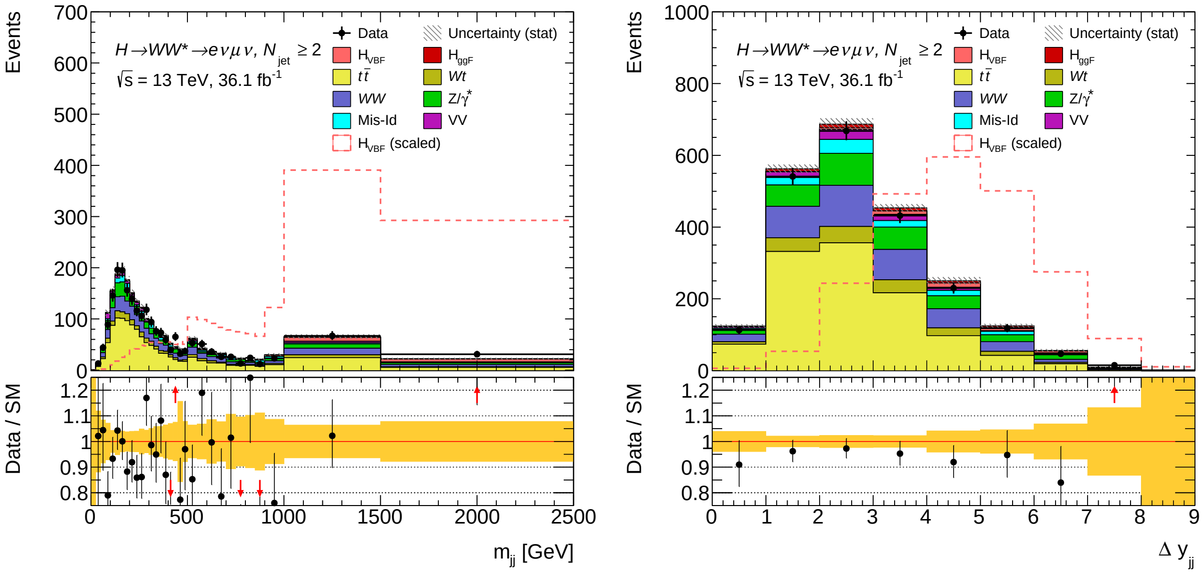

Figure 4.8.: Pre-fit distributions of variables used in the VBF BDT in the $H \rightarrow WW^*$ analysis. Stacked estimates are normalized to their prediction with exception of top, and Z/γ^* which are scaled to measured data in control regions with scaling factors shown in Tab. 4.5. Uncertainties shown include statistical uncertainties only.

section the construction of the individual likelihoods for the ggF and VBF enriched regions are described.

4.5.1. Splitting of Signal Regions and Binning

The 0-jet and 1-jet signal regions are each subdivided into a total of 16 subregions to enhance the discrimination of the ggF signal process with respect to the various background processes. The splits are performed using criteria discussed in the following.

- $m_{\ell\ell} < 30\,\text{GeV}$, $m_{\ell\ell} \geq 30\,\text{GeV}$ The non-resonant WW production increases towards larger values of $m_{\ell\ell}$. Hence, this split allows for better discrimination between the WW background and the $H \rightarrow WW^*$ signal which is enriched at low values of $m_{\ell\ell}$, yet produced at relevant rates in the range $30\,\text{GeV} < m_{\ell\ell} < 55\,\text{GeV}$.
- $\ell_1 = e$, $\ell_1 = \mu$ The signal regions are split based on the flavor of the subleading lepton ℓ_1. As can be seen from Tab. 4.6 for the mis-ID background the subleading lepton is more likely to be the one misidentified. Uncertainties regarding misidentified electrons are largely uncorrelated to those regarding

Table 4.7.: Optimization of the sensitivity of the ggF $H \to WW^*$ analysis with respect to the $p_{\mathrm{T}}^{\ell 1}$ split in the 0-jet and 1-jet signal regions. The quoted significances and uncertainties of the ggF signal strength are obtained from a preliminary implementation of this analysis and fits to Asimov datasets. Only statistical, systematic uncertainties from experimental sources as well as ggF signal modeling uncertainties defined in the WG1 scheme are considered.

$p_{\mathrm{T}}^{\ell 1}$ split [GeV]	$\sigma_{\mu,\mathrm{ggF}}$ [%]	expected significance Z_0
18	18.9	6.24
19	18.9	6.23
20	18.9	6.21
21	18.9	6.20
22	18.9	6.21
23	19.0	6.19
24	19.0	6.18
25	19.1	6.15

misidentified muons. Separating the signal region based on the flavor of the subleading lepton therefore provides separate handles in regards to these sizeable uncertainties.

- $p_{\mathrm{T}}^{\ell 1} < 20\,\mathrm{GeV}$, $p_{\mathrm{T}}^{\ell 1} \geq 20\,\mathrm{GeV}$ The split based on the transverse momentum of the subleading lepton is performed for a similar reason as the split based on the subleading lepton flavor. While both the ggF signal process and the mis-ID background are enriched at low values of $p_{\mathrm{T}}^{\ell 1}$ the latter drops off more rapidly as $p_{\mathrm{T}}^{\ell 1}$ increases as can be seen in Fig. 4.9. The particular choice of the split at $p_{\mathrm{T}}^{\ell 1} = 20\,\mathrm{GeV}$ is identical to the Run 1 analysis [115]. A validation of this choice based on a preliminary version of this Run 2 analysis is shown in Tab. 4.7. The threshold is kept consistent with the Run 1 analysis as no significant improvement is found for other thresholds.

In each of the so defined signal subregions the transverse mass m_{T} is used as a final discriminant. In each of the 0-jet (1-jet) subregions 8 (6) bins are used with boundaries constructed such that roughly the same number of signal events are expected in each bin of the same subregion. These *remapped* m_{T} distributions are created starting from histograms with bins of width 1 GeV in the range $80\,\mathrm{GeV} < m_{\mathrm{T}} < 130\,\mathrm{GeV}$. Starting from the underflow bin $m_{\mathrm{T}} < 80\,\mathrm{GeV}$ bins of increasing m_{T} are combined until a fraction $1/N_{\mathrm{bins}}$ of the total ggF signal is accumulated. This fraction is typically not exactly met due to the finite initial bin sizes. Hence, two options are considered to either include or exclude the bin leading to exceeding $1/N_{\mathrm{bins}}$. For both variants the procedure is applied iteratively until the desired number of bins is reached. Out of the emerging variants the one with the smallest squared differences with respect to a uniform distribution is

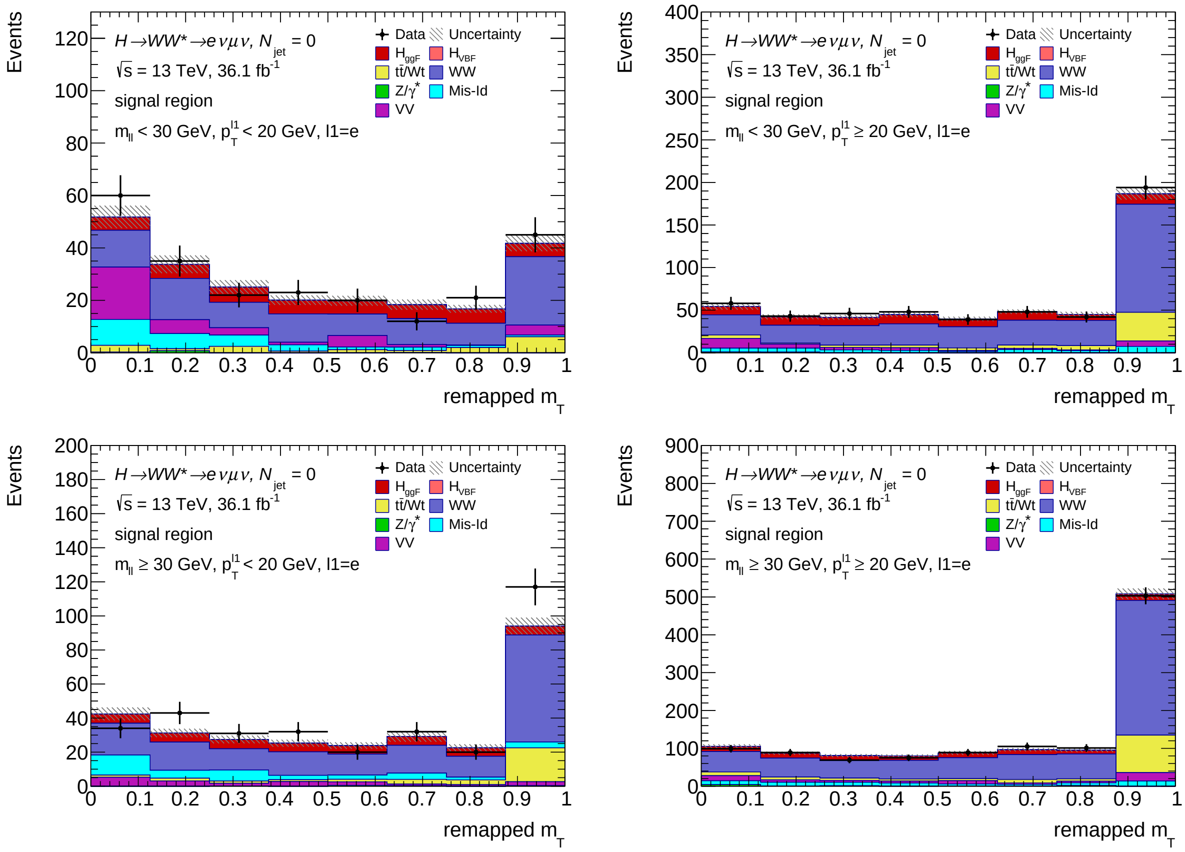

Figure 4.9.: Remapped m_{T} post-fit distributions in the 0-jet signal region of the $H \to WW^*$ analysis. The distributions shown are those in the subregions where the subleading lepton is an electron. The graphics on the left show the $p_{\mathrm{T}}^{\ell 1} < 20\,\mathrm{GeV}$ subregions, the ones on the right the subregions with $p_{\mathrm{T}}^{\ell 1} \geq 20\,\mathrm{GeV}$. At the top and bottom the regions with $m_{\ell\ell} < 30\,\mathrm{GeV}$ and $m_{\ell\ell} \geq 30\,\mathrm{GeV}$, respectively, are shown.

eventually used. The resulting remapped m_{T} distributions in the 0-jet subregions where $\ell_1 = e$ are shown in Fig. 4.9. The full set of remapped m_{T} distributions in all signal regions can be found in App. C together with the m_{T} bin boundaries of the remapped m_{T} distributions.

In the $\geq$ 2-jet signal region the BDT response is used as the final discriminant in four bins with boundaries $[-1.0, 0.26, 0.61, 0.86, 1.0]$. Background-like events are enriched towards low values while VBF-like events are primarily found at high values. The so binned distribution is shown in Fig. 4.10.

For the $\geq$ 2-jet top control region the same binning using the BDT response is used as for the VBF signal region in order to further constrain the shape of the

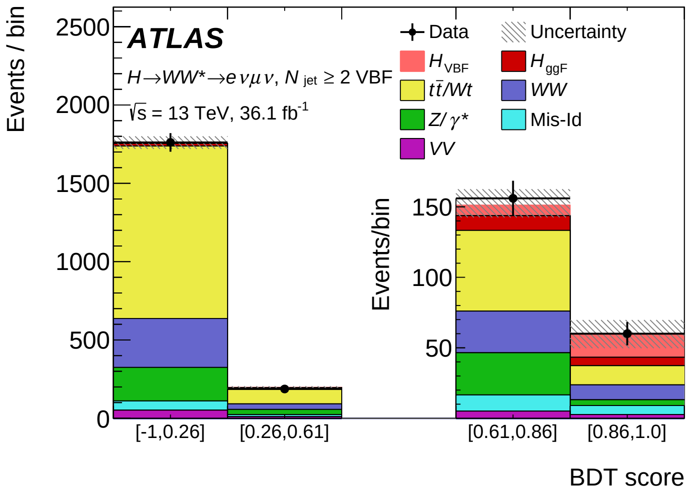

Figure 4.10.: Post-fit distribution of the BDT score in the $\geq$ 2-jet signal region of the $H \to WW^*$ analysis. The shaded uncertainty band includes statistical and systematic uncertainties. Published in Ref. [112].

top background. All other control regions are included in the fit as single bins. Distributions showing the post-fit modeling in these control regions are shown in Fig. 4.11 (0-jet, 1-jet) and Fig. 4.12($\geq$ 2-jet).

4.5.2. Parametrization of Likelihood and Uncertainties

The structure of the binned likelihood used in this analysis follows the general structure in Eq. (2.10) with bins described in Sec. 4.5.1. Eight normalization factors (NFs) in total are included for the WW (only in 0-jet and 1-jet categories), top, and Z/γ^* backgrounds. Analogously to the scaling factors in Tab. 4.5, these scale all contributions of the respective processes within a particular N_{jets} category. In contrast to the scaling factors in Tab. 4.5, however, these are determined *in-situ* during the maximization of the likelihood. These parameters are freely floating and mainly constrained from the respective control regions, *i.e.*, no dedicated external constraint terms C_k are included. These NFs not only mitigate uncertainties regarding the inclusive cross sections of the normalized processes[7] but also correct for potentially mismodeled acceptances common to signal and control regions where the same NF is applied.

In general sources of uncertainties affect both signal and control regions. With respect to the stability of the numerical minimization of the NLL, however, it

[7] up to the relative contributions for different processes being normalized together, *i.e.*, $gg \to WW/qq \to WW$ and $t\bar{t}/Wt$.

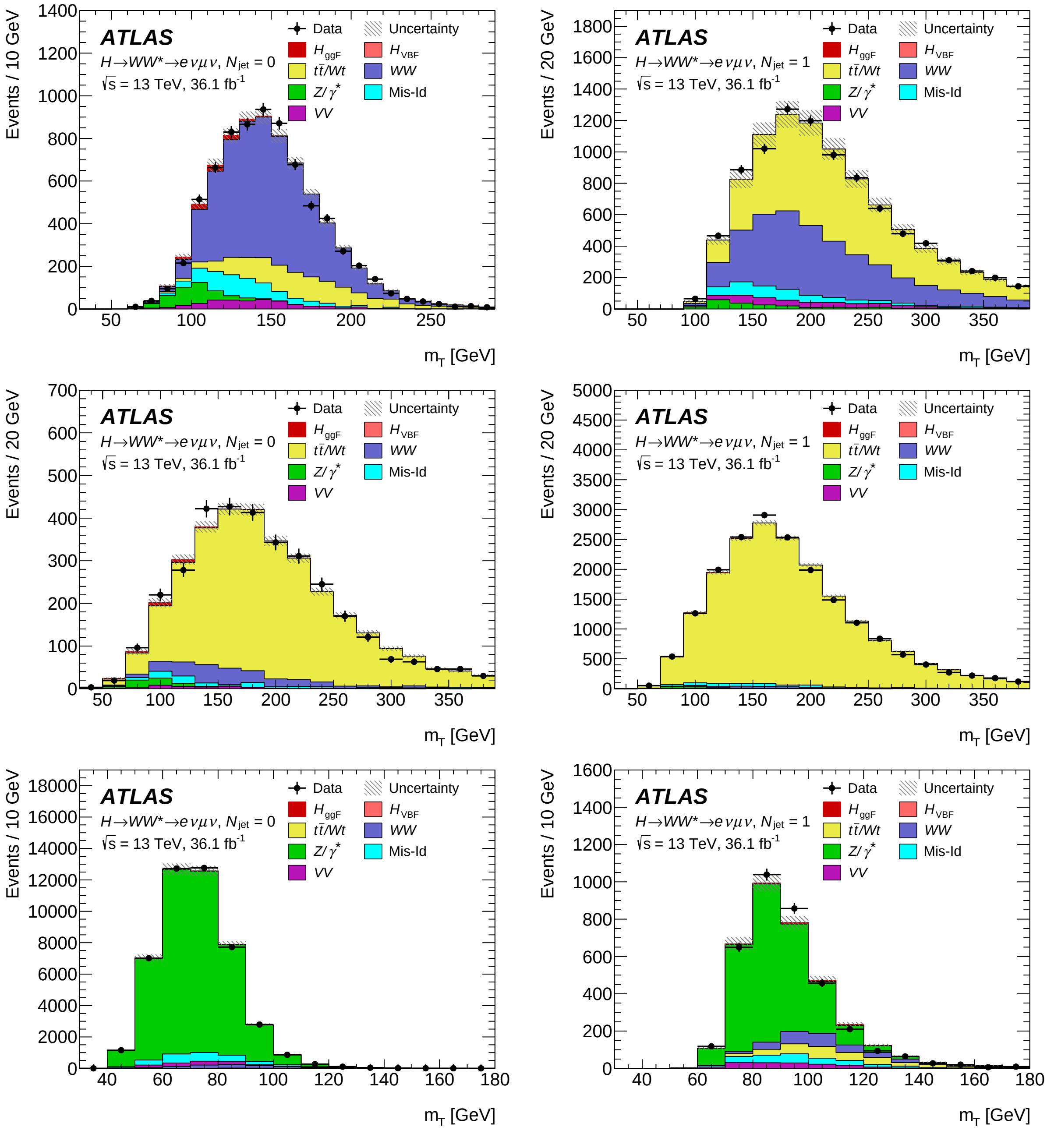

Figure 4.11.: Post-fit m_{T} distributions in the 0-jet (left) and 1-jet (right) control regions of the $H \to WW^*$ analysis. The WW control regions are shown in the top row, the top control regions in the middle, and the Z/γ^* control regions in the bottom. The shaded uncertainty band includes statistical and systematic uncertainties. Published in Ref. [112].

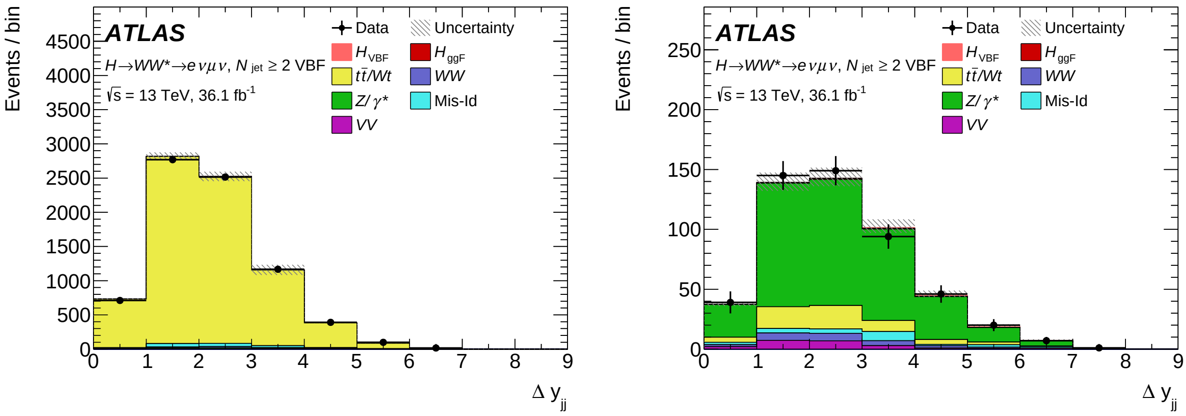

Figure 4.12.: Post-fit Δy_{jj} distributions $\geq$ 2-jet control regions of the $H \to WW^*$ analysis. The top control region is shown on the left, the Z/γ^* control region is shown on the right. The shaded uncertainty band includes statistical and systematic uncertainties. Published in Ref. [112].

can be favorable to transform the uncertainty such that its effect is vanishing in one control region in order to reduce the (anti-)correlation with a NF. Usually such uncertainties are theoretical modeling uncertainties concerning only a single background process. Such a transformation to some extent voids the interpretability of the NF, *e.g.*, in terms of a relative cross section measurement of the normalized process. Without the transformation any pull of the nuisance parameter associated with the uncertainty in question is compensated by a change of the NF value to the extent of the uncertainty's effect common to signal and control regions. The best-fit value of the NF therefore depends on the exact implementation of individual uncertainties and should be considered an abstract parameter. As long as the transformation only concerns background processes and leaves their post-fit yields unchanged the interpretability of extracted signal parameters remains unaffected.

The parameters of interest are the *signal strengths*

$$\mu_s = \frac{(\sigma_s \cdot \mathcal{B}_{H\to WW^*})_{\text{observed}}}{(\sigma_s \cdot \mathcal{B}_{H\to WW^*})_{\text{SM}}}, \quad s = \text{ggF, VBF} \tag{4.3}$$

for the ggF and VBF production modes respectively. Similarly to background normalization factors these parameters scale the modeled yields of the respective signal process. The μ_s parameters, however, are shared across all N_{jets} categories in order to extract the total signal strengths and cross sections. The measured cross sections are then in turn obtained via Eq. (4.3) and removing theoretical uncertainties concerning the predicted value of $(\sigma \cdot \mathcal{B}_{H\to WW^*})_{\text{SM}}$.

Uncertainties arising from finite sample sizes used to model individual contributions are accounted for by one parameter γ_i per bin as implemented in Ref. [71]. As events in these samples are generally weighted with weights w_j the variance in each bin i is given by

$$\sigma^2_{i,\text{stat.}} = \sum_{\text{event } j \in \text{ bin } i} w_j^2.$$

With $n_i = \sum w_j$ the constraint terms are Poisson distributions $P'(x|k)$ where the parameters are given by

$$x = \gamma_i \frac{n_i^2}{\sigma^2_{i,\text{stat.}}}, \text{ and } k = \frac{n_i^2}{\sigma^2_{i,\text{stat.}}}.$$

As x can assume non-integer values the factorial $x!$ in the Poisson distribution is replaced by the Gamma function $\Gamma(x+1)$.

Experimental sources of systematic uncertainties are considered for objects described in Sec. 3.3 and used in this analysis. The effect of these uncertainties on the final distributions used in the statistical analysis are obtained through reprocessing of the simulated samples with modified efficiency scale factors or modified kinematic properties for the objects concerned by a particular uncertainty. The former variation only affects the weights of the simulated events. The latter affects, *e.g.*, energy scales and can therefore introduce migrations of individual simulated events into, out of, or between categories and bins. The resulting differences between the nominal and varied distributions are then taken as the $\pm 1\sigma$ variations of the nuisance parameter associated with the uncertainty. Between these values the effect is interpolated as a function of the nuisance parameter following the default implementation in Ref. [71]. Sets of such $\pm 1\sigma$ variations are provided by the respective ATLAS *Combined Performance* groups. In several cases individual variations represent a combination of multiple sources of uncertainties for a particular object type. These variations correspond to eigenvalue decompositions of covariance matrices of the uncertain quantities[8]. Such decompositions can significantly reduce the complexity of the likelihood constructed from the variations. A short summary of uncertainties regarding the different objects is given in the following.

electrons For electrons kinematic uncertainties are considered regarding the energy scale and resolution with six nuisance parameters. Additionally uncertainties are included concerning the efficiency of the used electron and dilepton

[8] efficiencies, energy and momentum scales, ...

triggers, the reconstruction, isolation, and identification efficiencies. In total 32 nuisance parameters in regards to electron efficiencies are considered.

muons Besides a kinematic uncertainty regarding the overall momentum scale of muons additional parameters account for uncertainties related to the momentum measurement in the inner detector and the muon spectrometer. Other uncertainties in the context of muons are related to their trigger, reconstruction and identification, and isolation efficiencies as well as the efficiency of the association of muon tracks to the primary vertex.

jets An uncertainty regarding the jet energy resolution (JER) as well as 21 nuisance parameters describing uncertainties regarding the jet energy scale (JES) are considered. In particular these include uncertainties regarding dependencies on pile-up and the jets' flavors are included. In the 0-jet and 1-jet categories JES uncertainties affect mainly the top and VBF processes and correspond to yield variations of $5 - 8\%$. One additional nuisance parameter is included for the efficiencies of each the JVT and fJVT.

flavor tagging Uncertainties are assigned to the efficiencies of b, c, or light jets being tagged by the MV2c10 algorithm. The largest effect is associated with the b-jet tagging efficiency. In regions with b-vetos the $\pm 1\sigma$ variations of the most relevant nuisance parameter correspond to a change in the yield from top processes by up to 15%.

missing transverse momentum Resolution and momentum scale uncertainties of unassigned soft tracks entering the calculation of $\vec{E}_{\mathrm{T}}^{\mathrm{miss}}$ and $\vec{p}_{\mathrm{T}}^{\mathrm{miss}}$ are explicitly included. In addition these quantities are recalculated for kinematic variations of electrons, muons, and jets.

luminosity A flat uncertainty of 2.1% [159] is assigned to all processes estimated from MC and not normalized to data in a control region.

pile-up A dedicated uncertainty is included to account for the modeling of pile-up interactions. It is obtained by reweighting simulated samples to pile-up profiles with average numbers of interactions increased or decreased by about 10%.

Further details on individual sources of uncertainties can be found in Sec. 3.3 and the references given therein.

A set of experimental uncertainties specific to this analysis is related to the data-driven estimation of mis-ID leptons as introduced in Sec. 4.3. Variations of the fake factors are employed to describe

- statistical uncertainties in the estimation of the fake factors,

- uncertainties regarding the subtraction of real leptons in the estimation of fake factors, *i.e.*, the number of WZ events in the Z+jets enriched sample, and
- uncertainties regarding the correction factors due to the different flavor composition of the misidentified objects in Z+jets and W+jets enriched samples.

An additional uncertainty is applied on the correction for events where both leptons are misidentified (*double fakes*) in the $\geq$ 2-jet signal region. It is conservatively chosen as the full size of the correction and amounts to about 25% of the final mis-ID estimate. In the 0-jet and 1-jet regions the number of such events is found to be negligible.

The effects of these experimental uncertainties on the modeled yields and distributions are evaluated per processes or sums of similar processes representing minor backgrounds. These individual processes in this sense are the signal processes ggF, and VBF, the WW backgrounds $gg \rightarrow WW$, and $qq \rightarrow WW$, top backgrounds $t\bar{t}$, and Wt, the Z/γ^* background, the mis-ID background, the sum of diboson backgrounds excluding WW, as well as summed contaminations from other Higgs boson production and decay modes.

No significant effects of experimental uncertainties on the shape of the remapped m_{T} distributions in 0-jet and 1-jet signal subregions are found for any of the aforementioned groups of processes. To this end a χ^2 fit of a constant is performed to the ratio of the nominal and varied distributions, considering only statistical uncertainties of the nominal histogram. A potential shape effect is removed if the probability of finding a χ^2 value lower than the one found in the respective χ^2 fit is less than 5%. Hence, nuisance parameters representing experimental uncertainties in these regions are implemented to only act on the total yields of each process group and subregion. Relative differences between the signal subregions as well as control regions, however, are fully taken into account unless *pruned*. In order to make the convergence of the minimization of the NLL more robust, effects of uncertainties are pruned if that effect on the yield of a process group within a region is below 0.5%. Such small effects may lead to unphysical (anti-)correlations between different regions due to relative sign changes. Artifacts in the modeling of systematic uncertainties may also lead to unphysically strong constraints on nuisance parameters in particular if their effect is overestimated in regions with high event yields. Variations of kinematic quantities can often lead to the migration of individual events in or out of a region. In particular for simulated samples with large event weights this can introduce unphysical effects. If such an unphysical variation is in a region or bin with large event yields the corresponding nuisance parameter can be constrained from this region leading to an underestimation of the uncertainty in other regions. Therefore, effects of uncertainties obtained from variations of kinematic quantities are removed if

$$\frac{\delta_{\text{variation}}}{\sigma_{\text{stat}}} < 0.2 \; .$$

Here $\delta_{\text{variation}}$ denotes the variation in the event yield of a sample in some region and σ_{stat} the statistical uncertainty of the corresponding sample. An uncertainty is only dropped completely if it is pruned in all regions for all processes. The effects of the applied pruning have been examined at various steps and found to be either negligible or to resolve unphysically strong constraints on some nuisance parameters.

Theoretical uncertainties concerning the modeling of the ggF signal are parametrized following the "WG1" scheme in Ref. [60, 160] for the 0-jet and 1-jet categories. It accounts for perturbative uncertainties regarding resummation [60, 161,162], migration between jet bins, the shape of the p_{T}^{H} distribution, the treatment of the top quark mass, and an additional uncertainty for VBF like topologies. For the $\geq$ 2-jet categories perturbative uncertainties are derived via the Stewart-Tackmann method [163]. In this method uncertainties of the inclusive cross sections $\sigma_{\geq N-\text{jet}}$ and $\sigma_{\geq N+1-\text{jet}}$ are assumed to be independent. Therefore the uncertainty of the exclusive cross section $\sigma_{N-\text{jet}} = \sigma_{\geq N-\text{jet}} - \sigma_{\geq N+1-\text{jet}}$ is given by the uncertainties of the inclusive cross sections added in quadrature. The QCD scale uncertainties (3.9% for ggF) as well as combined PDF+α_s uncertainties of 3.2% (ggF) [60] regarding the total cross section are assigned only for the measurement of signal strengths. Independent parameters are included for corresponding acceptance uncertainties and applied for both, measurements of signal strengths and cross sections. In regards to the PDF set, eigenvector variations of PDF4LHC [119] are added in quadrature and additionally comparisons to other PDF sets (CT10 [147], MMHT14 [164], and NNPDF3.0 [143] are used to derive uncertainties. Independent variations of factorization and renormalization scales by factors 0.5 and 2 are used to derive QCD scale acceptance uncertainties. Uncertainties due to the generator choice and the modeling of underlying event and parton showers are derived from the comparisons indicated in Tab. 4.2.

Acceptance uncertainties of the VBF signal arising from PDFs, choice of the generator, and parton showers are derived analogously to those for the ggF signal. Uncertainties of the total cross section of 2.1% for (PDF+α_s) and QCD scales are again taken from Ref. [60].

For the $qq \to WW$ background QCD scale uncertainties are derived from variations of these scales by factors of 0.5 and 2 in samples produced with MG5_aMC@NLO [133,134] and PYTHIA8 [57] with the constraint $0.5 \leq \mu_F/\mu_R \leq 2$. The resulting extrapolation uncertainties from the 0-jet and 1-jet control regions to the corresponding signal regions amounts to between 0.1% and 3.1%. Uncertainties of the matrix element are derived via comparisons of the nominal Sherpa [141,142,144,145] sample to samples produced with Powheg and Pythia8 or Herwig++ for the 0-jet and 1-jet categories. For the $\geq$ 2-jet categories comparisons to MG5_aMC@NLO are used. Parton shower uncertainties are determined through variation of the *ckkw* parameter in Sherpa [141, 165, 166]. PDF uncertainties are determined from variations provided in the NNPDF3.0 set and comparison to the CT14 set [167].

The $gg \to WW$ background constitutes about 10% of the total WW background in the signal regions of this analysis. It is normalized to the total cross section in Ref. [146] and a conservative extrapolation uncertainty of 26% (39%) is assigned in the 0-jet (1-jet) signal regions based on Ref. [168].

For the top backgrounds uncertainties related to parton shower radiation are assessed through variations of internal parameters of the respective nominal generators including variations of the QCD scales μ_F and μ_R by factors of 0.5 and 2. Uncertainties regarding matrix elements and parton showers are determined through the comparisons indicated in Tab. 4.2. Uncertainties regarding the treatment of Feynman diagrams shared between $t\bar{t}$ and Wt are applied based on a comparison of samples produced with diagram subtraction and diagram removal prescriptions described in Ref. [169]. PDF uncertainties for the $t\bar{t}$ process are again estimated from variations provided in NNPDF3.0 and comparisons to MMHT14, CT14, and PDF4LHC. For the Wt process internal variations of NNPDF3.0 and comparisons of CT10 to NNPDF3.0, and MSTW2008 [170] are employed to derive an uncertainty. As the resulting PDF uncertainties are found to be negligible they are dropped.

For the WZ/γ^* background uncertainties are obtained through variations of Sherpa parameters regarding renormalization, factorization, and resummation scales as well as parton shower matching and tunes. The scales are independently varied by the usual factory of 0.5 and 2. For the $W\gamma$ background a comparison of the Sherpa sample to one generated with MG5_aMC@NLO accounts for both, matrix element and parton shower uncertainties. As for other processes QCD scale uncertainties are assessed through variations of these scales by factors of 0.5 and 2, however, excluding the combinations $(0.5, 2)$ and $(2, 0.5)$. PDF uncertainties are obtained from internal variations and comparisons of NNPDF to CT14 and MMHT14.

From a comparison of samples produces with Sherpa and MG5_aMC@NLO+Pythia8 for the Z/γ^* process in the 0-jet and 1-jet an uncertainty between 5% and 25% in the signal and control regions is found. It shows opposite signs between signal and control regions as well as between the N_{jets} bins. For the signal regions it is only evaluated for the sum of the subregions of each jet multiplicity due to the very limited size of the samples.

Contaminations from Higgs boson production or decay modes other than the signal processes are tiny in this analysis. Hence, no dedicated theoretical uncertainties are assigned.

Comparisons used to estimate the effect of these sources of theoretical uncertainties are largely performed using generator level samples with selections closely resembling those for the reconstructed samples unless sufficiently large reconstructed samples are available.

After applying the b-jet veto in addition to the preselection criteria in the $\geq$ 2-jet category a mismodeling of the m_{jj} shape is found and an uncertainty corresponding the full relative size of this mismodeling is applied to all but the VBF processes in this category.

Effects and rankings of uncertainties with respect to the parameters of interest in this analysis are elaborated on in Sec. 4.6.

4.6. Results

The cross sections times branching ratios and signal strengths are determined simultaneously for the ggF and VBF $H \to WW^*$ processes by minimization of NLL described in Sec. 4.5 using the RooFit package [70]. The observed cross sections times branching ratio

$$\begin{aligned}(\sigma_{\mathrm{ggF}} \cdot \mathcal{B}_{H\to WW^*})_{\mathrm{obs}} &= 11.4\,^{+1.2}_{-1.1}(\text{stat.})\,^{+1.2}_{-1.1}(\text{th. syst.})\,^{+1.4}_{-1.3}(\text{exp. syst.})\,\text{pb} \\ &= 11.4\,^{+2.2}_{-2.1}\,\text{pb},\ \text{and} \\ (\sigma_{\mathrm{VBF}} \cdot \mathcal{B}_{H\to WW^*})_{\mathrm{obs}} &= 0.50\,^{+0.24}_{-0.22}(\text{stat.}) \pm 0.10(\text{th. syst.})\,^{+0.12}_{-0.13}(\text{exp. syst.})\,\text{pb} \\ &= 0.50\,^{+0.29}_{-0.28}\,\text{pb}\end{aligned}$$

are in good agreement with the predicted values [60]

$$\begin{aligned}(\sigma_{\mathrm{ggF}} \cdot \mathcal{B}_{H\to WW^*})_{\mathrm{SM}} &= 10.4 \pm 0.6\,\text{pb},\ \text{and} \\ (\sigma_{\mathrm{VBF}} \cdot \mathcal{B}_{H\to WW^*})_{\mathrm{SM}} &= 0.81 \pm 0.02\,\text{pb}.\end{aligned}$$

The contours of the 68% and 95% confidence levels in the $(\sigma_{\mathrm{ggF}} \cdot \mathcal{B}_{H\to WW^*}) \times (\sigma_{\mathrm{VBF}} \cdot \mathcal{B}_{H\to WW^*})$ plane are shown Fig. 4.13. The respective signal strengths are

$$\begin{aligned}\mu_{\mathrm{ggF}} &= 1.10\,^{+0.10}_{-0.09}(\text{stat.})\,^{+0.13}_{-0.11}(\text{th. syst.})\,^{+0.14}_{-0.13}(\text{exp. syst.}) &&= 1.10\,^{+0.21}_{-0.20},\ \text{and} \\ \mu_{\mathrm{VBF}} &= 0.62\,^{+0.29}_{-0.27}(\text{stat.})\,^{+0.12}_{-0.13}(\text{th. syst.}) \pm 0.15(\text{exp. syst.}) &&= 0.62\,^{+0.36}_{-0.35}.\end{aligned}$$

The significances of the signal processes over the respective null hypotheses are observed (expected) to be $Z_{\mathrm{ggF}} = 6.0$ (5.3) and $Z_{\mathrm{VBF}} = 1.8$ (2.6).

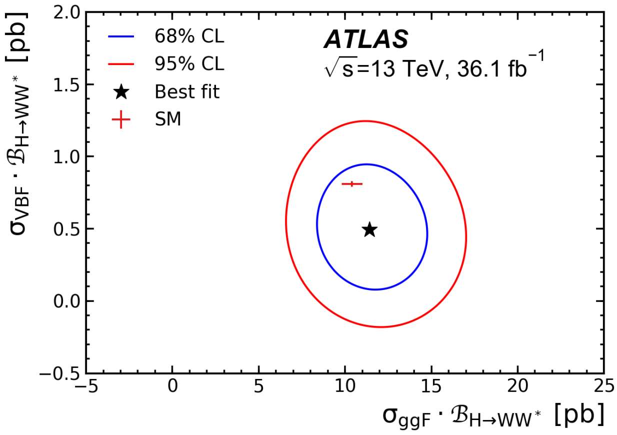

Figure 4.13.: Two dimensional confidence levels of $\sigma_{\mathrm{ggF}} \cdot \mathcal{B}_{H\to WW^*}$ and $\sigma_{\mathrm{VBF}} \cdot \mathcal{B}_{H\to WW^*}$. The SM prediction with corresponding theoretical uncertainties [60] is given by the red marker. The correlation between the two POIs is small due to the purity and higher accuracy of the ggF signal. Published in Ref. [112].

The post-fit event yields in the three signal regions are shown in Tab. 4.8. Numbers for the individual 0-jet and 1-jet subregions can be found in the Appendix in Tab. C.2. Post-fit distributions in the control regions are shown in Fig. 4.11 and Fig. 4.12. The post-fit distributions in the VBF signal region are presented in Fig.4.10, the post-fit modelling of the Δy_{jj} and m_{jj} distributions used in the BDT is shown in Fig. D.2 in the Appendix. The sum of the 0-jet and 1-jet ggF signal regions is presented in Fig. 4.14. Distributions of m_{T}, $p_{\mathrm{T}}^{\ell 1}$, and $m_{\ell\ell}$ in the 0-jet and 1-jet signal regions each are shown in Fig. C.5 in the Appendix.

The total uncertainty for the VBF production mode is dominated by statistical uncertainties, yet systematic uncertainties are not negligible. For the gluon-fusion measurement the relevance of both, experimental and theoretical, systematic uncertainties is at the level or even larger than the statistical uncertainties. A more detailed breakdown into different sources of uncertainties is given in Tab. 4.9, impacts of leading individual uncertainties and their pulls are presented in Fig. 4.15. The difference between impact and breakdown values[9] for individual parameters are found to be generally small.

Uncertainties Affecting Measurement of the VBF Signal

The VBF measurement at this point is dominated by statistical uncertainties arising from the finite size of the available data sample. To a smaller, yet relevant, extent

[9]The terms *impact* and *breakdown* refer to the corresponding prescriptions presented in Sec. 2.4.3.

Table 4.8.: Post-fit event yields in the signal regions of the $H \to WW^*$ analysis. In addition to the full signal regions the highest BDT bin in the $\geq$ 2-jet signal region is shown. Uncertainties include statistical and systematic uncertainties, and correlations amongst corresponding nuisance parameters. The latter are also the reason why the uncertainties of the total yields are smaller than those of some individual contributions. Published in Ref. [112].

Process	0-jet SR	1-jet SR	$\geq$ 2-jet SR	$\geq$ 2-jet SR BDT > 0.86
H_{ggF}	639 ± 110	285 ± 51	42 ± 16	6 ± 3
H_{VBF}	7 ± 1	31 ± 2	28 ± 16	16 ± 6
WW	3016 ± 203	1053 ± 206	400 ± 60	11 ± 2
VV	333 ± 38	208 ± 32	70 ± 12	3 ± 1
$t\bar{t}/Wt$	588 ± 130	1397 ± 179	1270 ± 80	14 ± 2
Mis-Id	447 ± 77	234 ± 49	90 ± 30	6 ± 2
Z/γ^*	27 ± 11	76 ± 24	280 ± 40	4 ± 1
Total	5067 ± 80	3296 ± 61	2170 ± 50	60 ± 10
Observed	5089	3264	2164	60

a second source of statistical uncertainties is affecting this analysis. The size of the available MC samples, foremost those of the Z/γ^* background, affect the analysis to an extent that exceeds the combination of all sources of theoretical uncertainties.

The most important theoretical uncertainties are related to the non-resonant WW background and the ggF $H \to WW^*$ contamination in the $\geq$ 2-jet VBF signal region. For both of these processes a dedicated control or signal region in the $\geq$ 2-jet category is highly desirable for future iterations of this analysis. For the WW background the inclusion of such a control region has been considered but no definition with sufficient purity and sample size was found. With the almost 140 fb^{-1} of data recorded in the full Run 2 campaign the latter is likely to be alleviated. Additionally recent theoretical progress [171, 172] may reduce uncertainties in this regard. The inclusion of a $\geq$ 2-jet ggF signal region not only supports the VBF measurement by reducing extrapolation uncertainties. It is also desirable in regards to measurements in the *simplified template cross-sections* (STXS) scheme [60] in order to cover more of the Higgs boson production categories defined therein.

Experimental uncertainties are of even lower relevance. While uncertainties related to the mis-ID background represent the largest contribution in this group their effect in regards to the final result is small. The conservative choice of the double fakes uncertainty is partially motivated by a negligible effect on the total uncertainty.

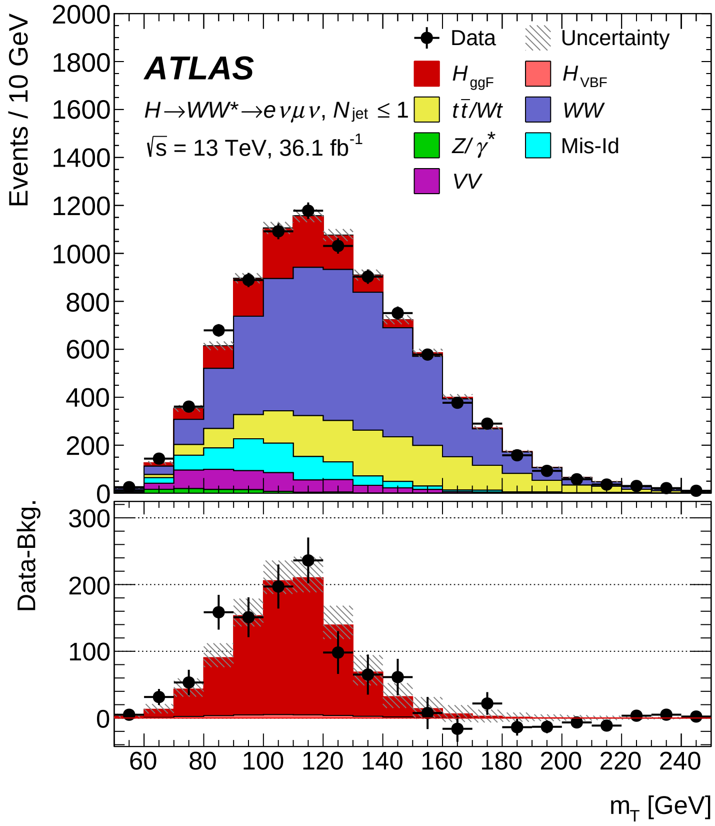

Figure 4.14.: Post-fit m_{T} distribution in the combined 0-jet and 1-jet signal regions in the $H \to WW^*$ analysis. Uncertainties represented by the hatched bands include statistical uncertainties, systematic uncertainties, and correlations amongst these. The bottom panel shows a comparison of background subtracted data and the $H \to W^{\mp}W^{\pm *} \to \ell^- \bar{\nu}\ell'^+\nu'$ signal. Contributions from other Higgs production or decay modes are omitted in the graphic as they are too small to be visible. Published in Ref. [112].

Uncertainties Affecting Measurement of the ggF Signal

The precision of the measurement of the ggF production mode is affected by statistical, experimental, and theoretical systematic uncertainties in almost equal parts. The most relevant theoretical uncertainties are related to the modeling of the ggF signal itself as well as the dominant background processes WW (0-jet) and top (1-jet). In regards to the WW background the leading contribution is an uncertainty on the extrapolation from the control regions to the respective signal regions. For this analysis at $\sqrt{s} = 13\,\mathrm{TeV}$ the applied uncertainty is taken as the larger of the estimates for $\sqrt{s} = 8, 14\,\mathrm{TeV}$ in Ref. [168] as no dedicated estimates for

Table 4.9.: Breakdown of uncertainties in the $H \to WW^*$ analysis. Values are given in percent of the respective cross section times $H \to WW^*$ branching ratio and obtained as described in Sec. 2.4.3. The effect of statistical uncertainties in control regions refers to the breakdown of the free background normalization parameters. MC statistical uncertainties include statistical uncertainties arising from the ID+anti-ID data sample used to estimate the contribution from misidentified leptons. Published in Ref. [112].

Source	ggF	VBF
Data sample size	10	46
CR sample size	7	9
MC sample size	6	21
Theoretical uncertainties	10	19
ggF	5	13
VBF	< 1	4
WW	6	12
$t\bar{t}/Wt$	5	5
Experimental uncertainties	8	9
b-tagging	4	6
Modeling of pile-up	5	2
Jet	2	2
Lepton	3	< 1
Misidentified leptons	6	9
Luminosity	3	3
Total	18	57

$\sqrt{s} = 13\,\text{TeV}$ are given. Dedicated estimations in addition to theoretical advances as already discussed for the VBF measurement are likely to reduce this uncertainty. Leading uncertainties related to the $t\bar{t}$ production enter indirectly via the ≥ 2-jet category. While the ggF measurement mainly relies on the lower jet multiplicities the ≥ 2-jet category allows to constrain jet bin migrations to some extent.

The modelling of the $t\bar{t}$ process in the ≥ 2-jet category affects the 0-jet and 1-jet categories by an additional intermediary: the b-tagging efficiency represents one of the largest experimental uncertainties. The 0-jet category provides the largest sensitivity to the ggF production mode. In this category only jets with $20\,\text{GeV} < p_{\text{T}} < 30\,\text{GeV}$ are available for the rejection of events from top backgrounds by means of a b-veto. In just this kinematic region uncertainties of the tagging efficiency are much larger than for higher p_{T} as can be seen in Ref. [96]. The leading experimental uncertainty is given by the modeling of pile-up. The current definition of this uncertainty is generally considered conservative as pile-up effects are already included in uncertainties regarding individual physics objects. Leading

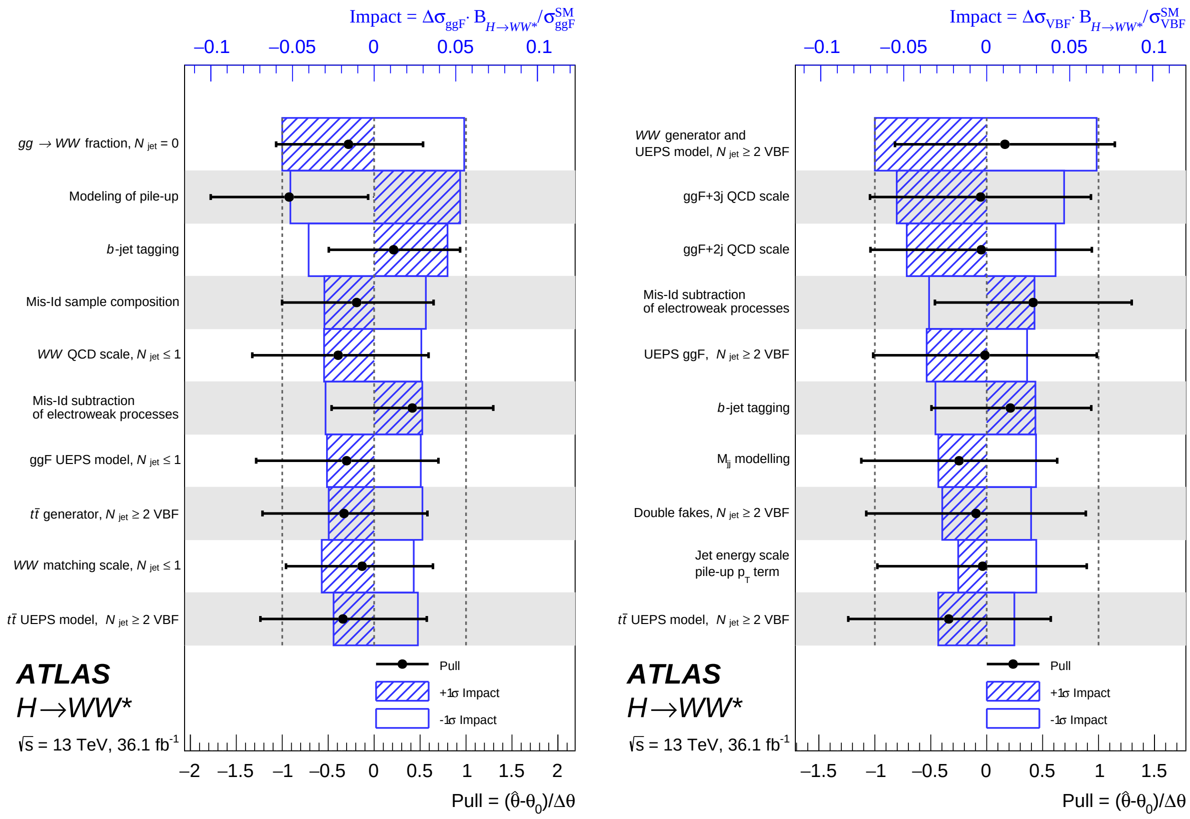

Figure 4.15.: Impacts and pulls of individual nuisance parameters in the $H \to WW^*$ analysis. Post-fit impacts on ggF cross section are shown on the left, impacts on the VBF cross section on the right as blue boxes and are derived as described in Sec. 2.4.3. The black markers represent the best-fit values of the parameters, the attached error bars their post-fit uncertainties. The N_{jets} suffixes indicate parameters either only applicable in certain regions or decorrelated between different N_{jets} categories. Published in Ref. [112].

uncertainties entering the analysis via the estimate of mis-ID events are related to the subtraction of prompt leptons in the estimation of the fake factors and the jet flavor composition difference between the Z+jets and W+jets samples. The former can be reduced through independent optimization of event selection criteria for the estimation of misidentified electrons and muons. In order to reduce the latter progress in the theoretical prediction of the flavor composition represents one possible way of improvement. A different approach could be to make use of dilepton events currently unused by the analysis in order to estimate fake factors from samples with a mis-ID composition closer to that in the main analysis.

Comparison to other Measurements

An analysis targeting the same production and decay modes of the Higgs boson has been performed by the ATLAS Collaboration already based on the Run 1 dataset corresponding to $25\,\text{fb}^{-1}$ at $\sqrt{s} = 7,\ 8\,\text{TeV}$ [115]. The therein reported signal strengths are $\mu_{\text{ggF}} = 1.02 \pm 0.19(\text{stat.})\,^{+0.22}_{-0.18}(\text{syst.})$ and $\mu_{\text{VBF}} = 1.27\,^{+0.44}_{-0.40}(\text{stat.})\,^{+0.30}_{-0.21}(\text{syst.})$. The measurement presented here features significantly reduced statistical and slightly reduced systematic uncertainties. At the same time it is simplified in several aspects. Some of the main differences are listed in the following.

- The Run 2 analysis benefits from a larger dataset due to the increased integrated luminosity as well as due to increased cross sections due to the increased center-of-mass energy. The increase, however, applied to the signal cross sections to a similar extent as for backgrounds as can be seen in Fig. 2.10.
- In the Run 1 analysis not only final states with one electron and one muon but also those with two electrons or two muons are considered. While this doubles the signal acceptance the gain in sensitivity is much smaller as the same-flavor categories come at the cost of much larger background contamination from $Z/\gamma^* \to ee, \mu\mu$.
- While the Run 2 analysis presented here requires $p_{\text{T}}^{\ell 1} > 15\,\text{GeV}$ this requirement is looser in the Run 1 equivalent with $p_{\text{T}}^{\ell 1} > 10\,\text{GeV}$ increasing the signal acceptance [115]. The harsher pile-up conditions in Run 2, however, make an accurate estimate of the mis-ID background in this region very challenging.
- The jet definition in the Run 2 analysis is simplified to use a threshold of $p_{\text{T}} > 30\,\text{GeV}$ instead of different thresholds depending on the pseudorapidity η.
- The 0-jet and 1-jet top control regions in the Run 2 analysis are defined using simple b-tag requirements instead of complex estimation procedures for the different jet bins in the Run 1 analysis. During the development of the present analysis no significant difference in sensitivity has been found.

The corresponding Run 2 analysis performed by the CMS Collaboration [173] also includes final states with two same-flavor leptons and covers additionally the WH and ZH production modes. The measured signal strengths are $\mu_{\text{ggF,CMS}} = 1.38\,^{+0.21}_{-0.24}$ and $\mu_{\text{VBF,CMS}} = 0.29\,^{+0.66}_{-0.29}$ [173]. While analysis strategies differ in some aspects similar absolute precision is found for the ggF production mode while for the VBF production mode the uncertainty is larger by a factor of 1.8 in terms of the observed absolute uncertainty. For the CMS result only the upper uncertainty is considered in this factor as the lower uncertainty is truncated at $\mu = 0$.

5 Projections for Measurements of Higgs Boson Couplings at the HL-LHC

In this chapter projections for the expected sensitivities of measurements of Higgs boson cross sections and couplings at the High Luminosity LHC (HL-LHC) [6] are presented. These projections have been performed in view of the *European Strategy for Particle Physics Update 2018-2020* [174]. They are intended to estimate the achievable precision with the expected final datasets corresponding to integrated luminosities of $3000 - 4000\,\mathrm{fb}^{-1}$ [6] at $\sqrt{s} = 14\,\mathrm{TeV}$ delivered to the ATLAS and CMS experiments each.

The results presented in this section comprise a subset of projections of ATLAS measurements of Higgs boson cross sections and couplings. The projections are performed based on the corresponding Run 2 analyses as of early summer 2018. The results of these projections are published in Ref. [175] which is part of Ref. [176] together with expected detector performances [177] and projections for other analyses performed in ATLAS and CMS. The Higgs boson related results are again summarized in Ref. [178]. The selection of results shown here largely corresponds to the author's areas of contribution: the projection of the ggF and VBF $H \to WW^*$ analysis presented in Chap. 4 and its combination with projections of analyses targeting other Higgs boson production and decay modes.

5.1. Prescriptions and Assumptions

The estimation of the future sensitivities of the various analyses is performed largely through adjustments to the statistical models and maximum likelihood fits to the resulting Asimov datasets. Performing these studies based on such high-level models is owed to the time scale available for these studies. This restricts adjustments from the Run 2 to the HL-LHC conditions and datasets to be mostly accounted for by means of uniform or only coarsely binned scaling factors described in the following.

Table 5.1.: Cross-section scaling factors approximating $\sigma(14\,\text{TeV})/\sigma(13\,\text{TeV})$ for background processes used in projections estimating the sensitivity of Higgs boson related analyses at the HL-LHC. The scale factors used for the projection of the $H \to WW^*$ analysis are annotated with the processes they are applied to. Based on Ref. [125].

$\sqrt{\hat{s}}$	gluon initiated	quark initiated
125 GeV	1.12	1.08
	($gg \to WW$)	($qq \to WW$, VV, $V\gamma$, mis-ID, Z/γ^*)
300 GeV	1.16	1.10
	($t\bar{t}$)	(Wt)
600 GeV	1.21	1.13

The central values of detector, reconstruction, and identification and isolation efficiencies as well as misidentification rates are assumed to be unchanged at the HL-LHC compared to their current values. While parts of the detectors will be upgraded the resulting gain is expected to roughly compensate for the more challenging pile-up conditions at the HL-LHC with up to 200 average interactions per bunch crossing [6].

The yields of all processes considered are scaled to an integrated luminosity of $3000\,\text{fb}^{-1}$. To account for the center-of-mass energy of $\sqrt{s} = 14\,\text{TeV}$ instead of $\sqrt{s} = 13\,\text{TeV}$ the total cross sections of background processes are scaled based on the ratio of parton luminosities in Ref. [125]. As the projections are performed largely on the level of the statistical models approximate scaling factors listed in Tab. 5.1 are applied. These scale factors depend on the typical hard scatter center-of-mass $\sqrt{\hat{s}}$ and whether a process is quark or gluon initiated. Changes in kinematic distributions and resulting changes, *e.g.*, in acceptances are neglected. For the projection of the $H \to \gamma\gamma$ analysis [179] the background is estimated from side bands in data and its composition is not accurately known. The effect of different choices of cross-section scaling factors has therefore been studied for this channel and found to be negligible.

For the signal processes, *i.e.*, different Higgs boson production modes, the expected yields are scaled by the ratio of their cross sections at $\sqrt{s} = 14$ and $13\,\text{TeV}$ in Ref. [60]. The production cross sections and their ratios are shown in Tab. 5.2. Again, kinematic changes due to the increased center-of-mass energy are neglected.

The limited size of MC samples available is a source of considerable uncertainties already in current analyses such as the one presented in Chap. 4. Providing and processing sufficiently large sets of simulated events for analyses using even larger measured datasets represents a large challenge discussed, *e.g.*, in Ref. [180]. The

Table 5.2.: Higgs boson production cross sections at $\sqrt{s} = 13$ and $14\,\text{TeV}$ and their ratios. Based on Ref. [60].

	ggF	VBF	WH	$qq \to ZH$	$gg \to ZH$	$t\bar{t}H$
$\sigma(14\,\text{TeV})/\,\text{pb}$	54.67	4.278	1.513	0.8418	0.1443	0.6137
$\sigma(13\,\text{TeV})/\,\text{pb}$	48.58	3.782	1.373	0.762	0.1227	0.5071
$\sigma(14\,\text{TeV})/\sigma(13\,\text{TeV})$	1.125	1.131	1.102	1.105	1.176	1.210

projections presented here, however, are focused towards the physics potential disregarding such challenges. Therefore statistical uncertainties arising from finite sizes of simulated samples are neglected for these studies. The same holds for so called *spurious signal* uncertainties in the $H \to \gamma\gamma$ analysis [179]. These uncertainties account for potential biases in the extracted signal yields due to the choice of function for the analytic background model. Their current magnitude is driven by the size of simulated samples from which it is estimated. For this reason, as well as anticipated improvements in terms of background parametrization, these uncertainties are neglected here.

Statistical uncertainties of the assumed datasets inherently scale as $\sqrt{L_{\text{Run 2}}/L_{\text{HL-LHC}}}$ where L denotes the integrated luminosity used in the current Run 2 analysis ($36 - 80\,\text{fb}^{-1}$) and at the end of the LH-LHC programme respectively. In terms of systematic uncertainties two scenarios are considered. In the scenario S1 systematic uncertainties are kept at their values used in the Run 2 analyses extrapolated from. In scenario S2 systematic uncertainties are reduced by scaling factors documented in Ref. [177]. Their assumed values are coordinated with those used by analogous projections performed in the CMS Collaboration.

Reduction factors for uncertainties of parton distribution functions are given in Ref. [177] for different ranges of hard scatter center-of-mass energies and different initial states. They are provided in two sets assuming no (a factor 2.5) improvement in uncertainties of experimental inputs to the determination of the PDFs. Over the largest range of center-of-mass energies between 40 GeV and 1 TeV these factors range between 0.38 (0.27) and 0.49 (0.42). Outside of this range the reduction is more modest for most initial states. For the $H \to WW^*$ projection the most relevant backgrounds are non-resonant but can be expected to be largely contained in this central interval. For the VBF enriched region with large dijet invariant mass the range $> 1\,\text{TeV}$ can also be expected to be relevant. Hence, a rather conservative reduction factor of 0.50 is used for the $H \to WW^*$ projection. The same reduction factor of 0.5 is also applied to remaining theoretical uncertainties for all projected analyses. This applies to acceptances, shapes of fitted distributions as well as inclusive cross sections.

Experimental uncertainties of the jet energy scales (JES) are either unchanged, halved, or expected to become negligible depending on the particular source of uncertainty. The jet energy resolution (JER) is reduced by a factor 0.5. Uncertainties regarding the flavor tagging of jets are reduced to a third of their value at Run 2. The uncertainty regarding the modeling of pile-up interactions is halved. The total integrated luminosity is assumed to be measured with an uncertainty of 1.0% corresponding to a reduction by about half of its uncertainty in Run 2. Methodological uncertainties such as those related to the mis-ID estimate in the $H \to WW^*$ analysis are unchanged with exception of the statistical uncertainties of the fake factors which are scaled like statistical uncertainties of the dataset in the main measurement. Uncertainties regarding the efficiencies of electrons, photons, and muons are unchanged. Here improvements are expected to largely cancel with more challenging conditions at the HL-LHC. Uncertainties of the energy scale and resolution of electrons and photons are kept unchanged or are halved if they are dominant. For the extrapolation of the $H \to \mu\mu$ analysis an improved resolution of the dimuon invariant mass of $15 - 30\%$ is assumed due to expected improvements of the inner detector.

In order to allow for a simplified combination of the expected sensitivities of the ATLAS and CMS Collaborations expected uncertainties of parameters of interest (POIs) are split into statistical uncertainties, experimental uncertainties, and theoretical uncertainties acting either on signal processes or background processes. A full likelihood based combination or taking correlations of individual nuisance parameters into account was again prohibited by the timeline for these projections and the European Strategy Update. The combination documented in Ref. [178] is performed using the BLUE method [181–183] where the effect of theoretical uncertainties is assumed to be fully correlated between the two experiments, the experimental and statistical uncertainties are assumed to be uncorrelated for this combination. The effects of the individual groups on a POI are determined following largely the breakdown method described in Sec. 2.4. In order to apply the BLUE method it is required that the square sum of a single experiment's breakdown values reproduces the experiment's total uncertainty.

Hence, a modified breakdown prescription is used for uncertainties split into these groups. In Sec. 2.4 the POI's uncertainties are compared between the fully unconditional fit and fits where one group of nuisance parameters is set constant. For the grouping also used for the combination a sequential approach is used where in each step additional nuisance parameters are fixed and the POI's uncertainties are compared to those from the previous step. In this sequence theoretical uncertainties affecting background processes are fixed in the first iteration, signal theory uncertainties in the second, and experimental uncertainties in the last iteration. The quoted breakdown of background theory uncertainties is then taken as the square difference of the POI's uncertainties between the unconditional fit and the first iteration. The breakdown of the signal theory group is the square difference between the first and second iteration. Analogously the breakdown of experimental uncertainties is defined. In case the uncertainty of the luminosity is quoted individually it is excluded from the group of experimental uncertainties and set constant in the very last iteration. The residual uncertainties after fixing all nuisance parameters corresponding to systematic uncertainties are quoted as the statistical component. While this prescription by construction yields closure when adding the groups' breakdowns in quadrature it also introduces a dependence on the order of the chosen sequence. The size of this dependence is discussed for the projected $H \to WW^*$ analysis in Sec. 5.2.

5.2. Projection of the $H \to WW^*$ Analysis

In this section the expected sensitivity at the HL-LHC is presented based on the $H \to WW^*$ analysis described in Chap. 4. The evolution of the total uncertainties as well as different groups of uncertainties for different values of the integrated luminosity is shown in Fig. 5.1 for the measurement of the ggF and VBF Higgs boson production cross section times branching ratio $\mathcal{B}_{H\to WW^*}$. Contributions from systematic uncertainties can be found to be reduced with larger datasets for multiple reasons.

- Some uncertainties considered as systematic uncertainties in the cross section or signal strength measurement are in turn statistical uncertainties of an orthogonal subset of the recorded dataset. Their magnitude therefore inherently reduces as the inverse square root of the integrated luminosity. In the $H \to WW^*$ analysis this applies to the statistical components of the fake factor uncertainties.
- As the relative statistical uncertainties resulting from the dataset decrease, nuisance parameters can be significantly constrained *in-situ* beyond the level given by their corresponding constraint term. In 5.2 and Figs. 5.3 this is particularly prominent for the *muon fake factor EW subtraction*. As this uncertainty is considered conservative in the Run 2 analysis and has not been explicitly reduced, the increased constraint is considered appropriate here. Sensitivity to this parameter is largely given by the choice of discriminant variables in the ggF categories described in Sec. 4.5.1 which are chosen as to provide separation between contributions from processes with prompt or misidentified leptons. Similarly non-negligible constraints of other nuisance parameters have been checked for plausibility as the used statistical model may not be sufficiently detailed for the largely increased dataset. In the $H \to WW^*$

projection presented here constraints are found to be at reasonable levels. A contrasting example is found in the extrapolation of the $t\bar{t}H$, $H \to b\bar{b}$ channel [175,176] where the effect of an uncertainty regarding the modeling of the $t\bar{t}$+heavy flavor background is implicitly reduced beyond plausible levels when assuming a $3000\,\mathrm{fb}^{-1}$ dataset. In this case an additional uncertainty acting directly on the $t\bar{t}H$ signal is injected to emulate a more modest reduction and provide a more accurate comparison between the different channels' sensitivities.

- Often systematic uncertainties affect different regions considered in a fit to different extents. The precision in regions with low yields of the signal process but also small systematic uncertainties may outweigh that in high-yield regions with large systematic uncertainties given a sufficiently larger dataset. Hence, even without increased constraints of nuisance parameters the relevance of systematic uncertainties can be reduced in the projections compared to the Run 2 result.

In general improvements in expected uncertainties below the effect of systematic uncertainties in the Run 2 analysis are related to a non-trivial combination of these reasons. The rankings base on the breakdown method of individual sources of uncertainties for the projected cross section and signal strength measurements are shown in Fig. 5.2 (ggF) and Fig. 5.3) (VBF) when assuming an integrated luminosity of $3000\,\mathrm{fb}^{-1}$.

For the VBF production the finite size of the available dataset remains the leading source of uncertainty amongst the groups shown throughout most of the anticipated data taking campaign. It is becoming subdominant around $2500\,\mathrm{fb}^{-1}$. With the full $3000\,\mathrm{fb}^{-1}$ all categories contribute to similar levels between 2.5% and 4%. The most relevant individual sources of systematic uncertainties are related to the modeling of the WW background, the VBF signal and contaminations from the ggF signal in the VBF categories. The leading experimental uncertainty is the flavor composition dependence of the jet energy scale (JES) in samples enriched in jets from heavy quarks. The uncertainty regarding the m_{jj} modeling is unchanged compared to the analysis presented in Chap. 4 as the origin of the corresponding mismodeling is not well known. As several leading sources of uncertainties contribute to a similar or slightly larger extent the effect of this choice on the total expected uncertainties is small.

In the current ggF $H \to WW^*$ analysis effects of experimental and theoretical systematic uncertainties are already at the same level as statistical uncertainties due to the finite size of the recorded dataset. As especially for theoretical uncertainties a sizeable reduction is assumed in scenario S2, these initially appear as subdominant in Fig. 5.1 for the ggF production mode. The breakdown values of many sources of uncertainties are very similar for this production mode. Hence, even the inclusion

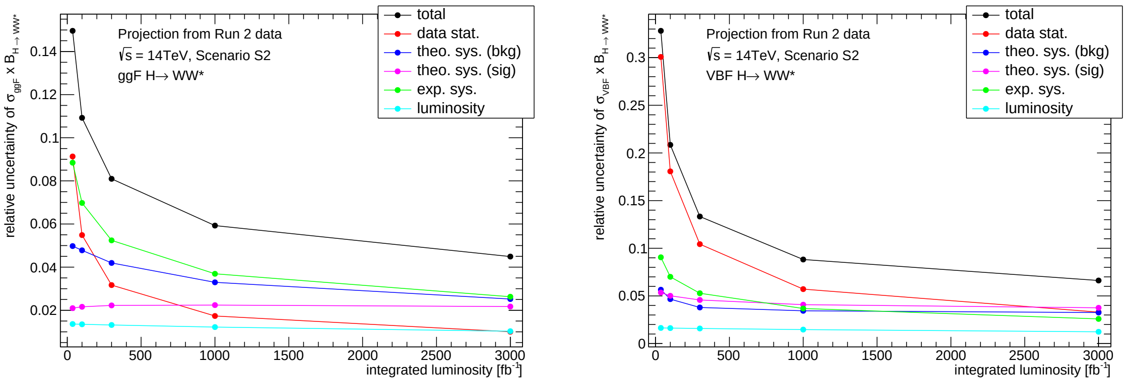

Figure 5.1.: Expected relative uncertainties of measurements of the cross section of ggF (left) and VBF (right) Higgs boson production times $H \to WW^*$ branching ratio in scenario S2. The contributions of subsets of uncertainties are obtained via a sequential breakdown as described in Sec. 5.1. The actually evaluated points are represented by the markers and correspond to integrated luminosities of 36.1, 100, 300, 1000, and 3000 fb^{-1}.

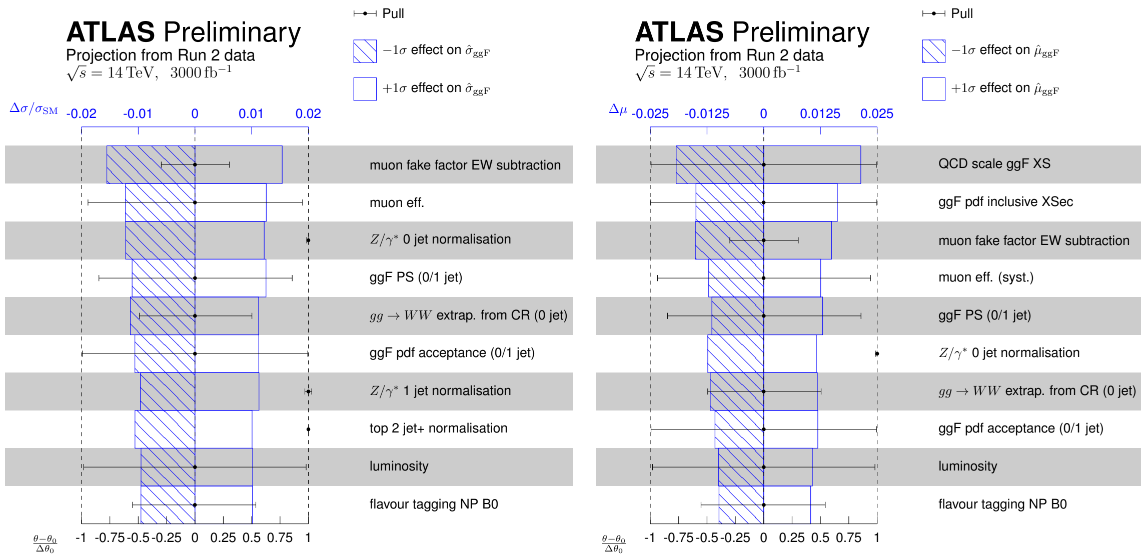

Figure 5.2.: Ranking of leading sources of uncertainties in the projected ggF $H \to WW^*$ analysis at the HL-LHC with a dataset corresponding to 3000 fb^{-1}. The rankings are obtained via the breakdown method and refer to measurements of the cross section times branching ratio $\sigma_{\mathrm{ggF}} \times \mathcal{B}_{H\to WW^*}$ (left) and signal strength $\mu_{\mathrm{ggF,H\to WW^*}}$ (right). Published in Refs. [175, 176].

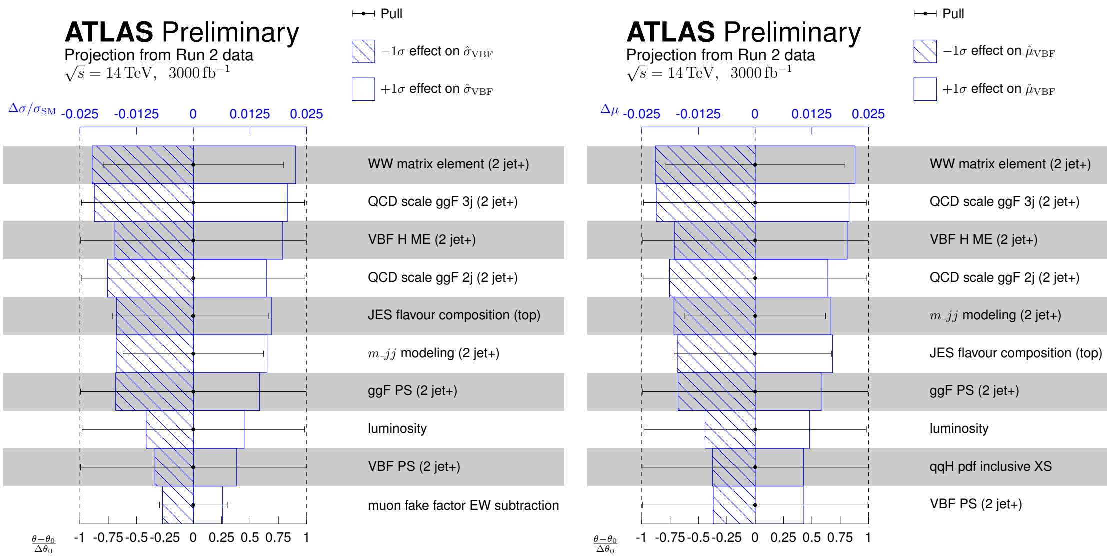

Figure 5.3.: Ranking of leading sources of uncertainties in the projected VBF $H \to WW^*$ analysis at the HL-LHC with a dataset corresponding to 3000 fb^{-1}. The rankings are obtained via the breakdown method and refer to measurements of the cross section times branching ratio $\sigma_{\mathrm{VBF}} \times \mathcal{B}_{H\to WW^*}$ (left) and signal strength $\mu_{\mathrm{VBF,H\to WW^*}}$ (right). Published in Refs. [175, 176].

of uncertainties of the total signal cross section can slightly change the order in which uncertainties appear in the rankings shown in Fig. 5.2 due to finite numeric precision in the minimization of the NLL. Similarly the contribution of groups with initially small breakdown values may seem to slightly increase with higher luminosity in Fig. 5.1 since at lower luminosity values the subtraction in quadrature is performed from two values which are large compared to their difference.

The leading experimental uncertainty for measurements targeting the ggF production mode is given by the uncertainty due to the subtraction of real leptons (EW subtraction) when estimating the muon fake factor (*c.f.* Sec. 4.3). As a methodological uncertainty it has not been modified for scenario S2. Improved descriptions of the WZ production and improved rejection of this process during the estimation of the fake factors are likely to reduce this uncertainty in the future. At least to some extent such improvements are implicitly included in these projections as the corresponding nuisance parameter is strongly constrained. The leading theoretical uncertainty of a background process is related to the gluon induced, non-resonant WW production. This uncertainty is conservatively estimated in the Run 2 analysis. It is significantly constrained in this extrapolation even after being reduced to half of its magnitude in the Run 2 analysis. Hence, even a less conservative estimate may still lead to a sizeable effect in the future unless additional measures are taken. Besides this background related modeling uncertainty, several uncertainties regarding the ggF signal process itself are found amongst the leading uncertainties. In case of a signal strength measurement the two leading sources of uncertainties relate to the total cross section of the ggF signal. Improvements beyond the already assumed reduction by a scaling factor of 0.5 may be achievable for uncertainties from PDFs and α_s due to future experimental and theoretical improvements in their determination. In regards to the uncertainty related to QCD scales the here assumed reduction by 50% may be considered optimistic as already the Run 2 analysis uses the prediction calculated at N3LO in QCD [60].

A comparison of the expected uncertainties in the scenarios S1 and S2 at HL-LHC and S1 with a dataset equivalent to the Run 2 analysis is shown in Tab. 5.3. As discussed in Sec. 5.1 these breakdowns into different groups of uncertainties are performed in a sequential manner which introduces a dependence on the chosen sequence. Several variants of possible sequences are compared in Tab. 5.4. The contribution to the total uncertainty attributed to a group of systematic uncertainties is found to be larger the earlier it appears in the chosen sequence. The differences of the respective contribution are up to 15% between the sequences resulting in the largest and smallest values. For the combination of projections from ATLAS and CMS the order described in Sec. 5.1 can therefore be considered to be conservative as the uncertainty groups fixed first are those considered fully correlated between the experiments' individual results.

The observed effect of order dependence can be understood in terms of correlations emerging between different nuisance parameters when fitting a dataset. Fixing a group of parameters to their best fit value therefore inherently strengthens constraints on remaining parameters which, in the fully unconditional fit, are correlated to the ones being fixed to their best-fit values. It should be noted that these correlations do not necessarily need to appear as linear correlation coefficients, *i.e.*, non-vanishing off-diagonal elements in the inverse Hessian matrix. Instead the effect of order dependence may also be (partially) introduced by terms of an expansion of the NLL beyond quadratic order.

5.3. Other Projected Analyses

Analogously to the projection presented in Sec. 5.2 projections of the individual $H \to \gamma\gamma$ [179], $H \to ZZ^*$ [184], $H \to \tau\tau$ [185], $VH,\ H \to b\bar{b}$ [32], and $t\bar{t}H$ [186,187] analyses as well as the $H \to \mu\mu$ [188] and $H \to Z\gamma$ [189] searches have been performed [175, 176].

The rare decay modes $H \to \mu\mu$ and $H \to Z\gamma$ have not been formally observed, yet. The signal strength of the $H \to \mu\mu$ decay is expected to be measured with an uncertainty of 13% in scenario S2 with a dataset corresponding to $3000\,\text{fb}^{-1}$ at

Table 5.3.: Comparison of expected uncertainties of the cross sections times branching ratio in the ggF and VBF $H \to WW^*$ channels for different scenarios. Values given are relative uncertainties of the cross section times $H \to WW^*$ branching ratio. If the signal strength is measured the column $\Delta\mu_{\text{sig}}$ replaces $\Delta_{\text{sig}}/(\sigma \cdot \mathcal{B})_{\text{SM}}$. Here, "Run 2" refers to $36.1\,\text{fb}^{-1}$ at $\sqrt{s} = 13\,\text{TeV}$ and "HL-LHC" refers to $3000\,\text{fb}^{-1}$ at $\sqrt{s} = 14\,\text{TeV}$. The groups of uncertainties are denoted by the subscripts *stat* (statistical), *exp* (experimental), *sig* (signal theory), and *bkg* (background theory). Published in Refs. [175, 176].

Prod. mode	Scenario	$\frac{\Delta_{\text{tot}}}{(\sigma\cdot\mathcal{B})_{\text{SM}}}$	$\frac{\Delta_{\text{stat}}}{(\sigma\cdot\mathcal{B})_{\text{SM}}}$	$\frac{\Delta_{\text{exp}}}{(\sigma\cdot\mathcal{B})_{\text{SM}}}$	$\frac{\Delta_{\text{sig}}}{(\sigma\cdot\mathcal{B})_{\text{SM}}}$	$\frac{\Delta_{\text{bkg}}}{(\sigma\cdot\mathcal{B})_{\text{SM}}}$	$\Delta\mu_{\text{sig}}$
ggF	Run 2, S1	$^{+0.191}_{-0.189}$	$^{+0.099}_{-0.098}$	$^{+0.112}_{-0.110}$	$^{+0.047}_{-0.036}$	$^{+0.092}_{-0.096}$	$^{+0.077}_{-0.058}$
	HL-LHC, S1	$^{+0.064}_{-0.065}$	$^{+0.010}_{-0.010}$	$^{+0.037}_{-0.037}$	$^{+0.040}_{-0.039}$	$^{+0.033}_{-0.036}$	$^{+0.068}_{-0.064}$
	HL-LHC, S2	$^{+0.046}_{-0.044}$	$^{+0.010}_{-0.010}$	$^{+0.030}_{-0.029}$	$^{+0.023}_{-0.020}$	$^{+0.025}_{-0.025}$	$^{+0.035}_{-0.033}$
VBF	Run 2, S1	$^{+0.391}_{-0.360}$	$^{+0.332}_{-0.311}$	$^{+0.122}_{-0.110}$	$^{+0.115}_{-0.098}$	$^{+0.106}_{-0.093}$	$^{+0.119}_{-0.099}$
	HL-LHC, S1	$^{+0.108}_{-0.109}$	$^{+0.033}_{-0.033}$	$^{+0.055}_{-0.048}$	$^{+0.070}_{-0.067}$	$^{+0.056}_{-0.064}$	$^{+0.073}_{-0.070}$
	HL-LHC, S2	$^{+0.067}_{-0.066}$	$^{+0.033}_{-0.033}$	$^{+0.029}_{-0.029}$	$^{+0.038}_{-0.037}$	$^{+0.032}_{-0.033}$	$^{+0.039}_{-0.038}$

Table 5.4.: Comparison of expected uncertainties of the cross sections times branching ratio in the ggF $H \to WW^*$ channel for different choices of breakdown sequences. Values given are relative uncertainties of the cross section times $H \to WW^*$ branching ratio. The groups of uncertainties are denoted by the shorthands *exp* (experimental), *sig* (signal theory), and *bkg* (background theory). The uncertainty of the integrated luminosity is considered as a separate group and fixed in an additional, last step in all sequences. In all cases its breakdown value is 1%. The scenario is S2 with $3000\,\text{fb}^{-1}$ at $\sqrt{s} = 14\,\text{TeV}$.

Sequence	$\frac{\Delta_{\text{exp}}}{(\sigma\cdot\mathcal{B})_{\text{SM}}}$	$\frac{\Delta_{\text{sig}}}{(\sigma\cdot\mathcal{B})_{\text{SM}}}$	$\frac{\Delta_{\text{bkg}}}{(\sigma\cdot\mathcal{B})_{\text{SM}}}$
bkg→exp→sig	$^{+0.029}_{-0.028}$	$^{+0.019}_{-0.018}$	$^{+0.025}_{-0.025}$
bkg→sig→exp	$^{+0.027}_{-0.026}$	$^{+0.022}_{-0.021}$	$^{+0.025}_{-0.025}$
exp→bkg→sig	$^{+0.030}_{-0.029}$	$^{+0.019}_{-0.018}$	$^{+0.024}_{-0.024}$
exp→sig→bkg	$^{+0.030}_{-0.029}$	$^{+0.021}_{-0.019}$	$^{+0.023}_{-0.023}$
sig→bkg→exp	$^{+0.027}_{-0.026}$	$^{+0.023}_{-0.020}$	$^{+0.025}_{-0.025}$
sig→exp→bkg	$^{+0.029}_{-0.028}$	$^{+0.023}_{-0.020}$	$^{+0.023}_{-0.023}$

Table 5.5.: Summary of expected total uncertainties of Higgs boson production cross section times branching ratio measurements at the HL-LHC. The quoted values are total relative uncertainties in scenario S2 with an assumed dataset of $3000\,\mathrm{fb}^{-1}$ at $\sqrt{s} = 14\,\mathrm{TeV}$. For the $t\bar{t}H(+tH)$ production mode the $H \to ZZ^*$, $H \to WW^*$ and $H \to \tau\tau$ decay modes are summarized as a *multi-lepton* category which is then split based on the presence of a hadronically decaying τ lepton. The $H \to ZZ^*$ contribution in these categories is given by events where no four-lepton invariant mass can be calculated. The $t\bar{t}H$, $H \to b\bar{b}$ channel is split into single (1ℓ) and dilepton (2ℓ) categories. Based on Refs. [175, 176].

<table>
<tr><th></th><th>$H \to \gamma\gamma$</th><th>$H \to ZZ^*$</th><th>$H \to WW^*$</th><th>$H \to \tau\tau$</th><th>$H \to b\bar{b}$</th></tr>
<tr><td>ggF</td><td>$^{+0.04}_{-0.03}$</td><td>$^{+0.043}_{-0.043}$</td><td>$^{+0.046}_{-0.044}$</td><td>$^{+0.123}_{-0.108}$</td><td>-</td></tr>
<tr><td>VBF</td><td>$^{+0.10}_{-0.09}$</td><td>$^{+0.125}_{-0.117}$</td><td>$^{+0.067}_{-0.066}$</td><td>$^{+0.080}_{-0.076}$</td><td>-</td></tr>
<tr><td>WH</td><td rowspan="3">$^{+0.09}_{-0.09}$</td><td rowspan="3">$^{+0.190}_{-0.178}$</td><td>-</td><td>-</td><td>$^{+0.104}_{-0.100}$</td></tr>
<tr><td>$q\bar{q} \to ZH$</td><td>-</td><td>-</td><td>$^{+0.121}_{-0.118}$</td></tr>
<tr><td>$gg \to ZH$</td><td>-</td><td>-</td><td>$^{+0.432}_{-0.433}$</td></tr>
<tr><td rowspan="2">$t\bar{t}H$</td><td rowspan="2">$^{+0.08}_{-0.08}$</td><td>$^{+0.226}_{-0.202}$</td><td colspan="2"></td><td>$^{+0.18}_{-0.15}$ (1ℓ)</td></tr>
<tr><td colspan="3">$^{+0.17}_{-0.17}$ (0τ), $^{+0.25}_{-0.25}$ $(\geq 1\tau)$</td><td>$^{+0.23}_{-0.20}$ (2ℓ)</td></tr>
</table>

$\sqrt{s} = 14\,\mathrm{TeV}$. Even with the full HL-LHC dataset the measurement is expected to be dominated by statistical uncertainties. The decay $H \to Z\gamma$ represents an even larger challenge. For this decay mode the cross section times branching ratio is expected to be measured with an uncertainty of 23% in scenario S1 using the full expected single-experiment dataset. The projections indicate a signal significance for the $H \to Z\gamma$ decay of 4.9σ. With additional advances in the analysis strategy a formal observation of this process with significance $\geq 5.0\sigma$ can be expected assuming Standard Model production and decay rates. The dominant source of uncertainties are again statistical uncertainties of the dataset. As the systematic uncertainties are expected to remain subdominant no extrapolation of this channel has been performed for S2.

An overview of expected precisions of the remaining individual analyses is shown in Tab. 5.5. The most precise individual channels overall are the $H \to \gamma\gamma$, $H \to ZZ^*(\to 4\ell)$, and $H \to WW^*$ channels with Higgs boson production via gluon-fusion. Their expected total uncertainties of cross section times branching ratio range between 3 and 5%. Each of these channels is expected to achieve a precision similar to the precision of the current prediction of the ggF cross section with an uncertainty of 5% [60].

The $H \rightarrow WW^*$ analysis features the smallest expected uncertainties for the VBF production mode. In the corresponding $H \rightarrow ZZ^*$ category statistical uncertainties are the largest contribution to the total uncertainty in this combination of production and decay channels. In the $H \rightarrow \gamma\gamma$ channel the expected statistical, experimental and signal modeling systematic uncertainties exceed those in the projected VBF $H \rightarrow WW^*$ analysis by 0.01 to 0.03 each. In the $H \rightarrow \tau\tau$ analysis the sensitivity to the VBF production mode exceeds that for the ggF production mode and is close to the expected sensitivity in the $H \rightarrow WW^*$ channel.

The ggF $H \rightarrow \tau\tau$ process is measured primarily in a boosted regime effectively canceling benefit of the higher production cross section compared to VBF. It is therefore also much more strongly affected by signal modeling uncertainties. Furthermore the $H \rightarrow \tau\tau$ analysis categories provide only modest separation between events from either ggF or VBF production modes resulting in strong anti-correlations between the measured ggF and VBF cross sections [185].

The measurement of the associated production with a vector boson is limited by statistical uncertainties in the $H \rightarrow ZZ^*$ channel. Statistical uncertainties are also dominating in the $H \rightarrow \gamma\gamma$ measurement while the expected total uncertainty of 9% is much lower than the expected uncertainty of 18% in the $H \rightarrow ZZ^*$ channel. The expected sensitivities in the projected $VH,\ H \rightarrow b\bar{b}$ analysis are derived for the different subprocesses $WH, q\bar{q} \rightarrow ZH$, and $gg \rightarrow ZH$ individually. The expected total uncertainties of the WH and $q\bar{q} \rightarrow ZH$ cross sections in the $H \rightarrow b\bar{b}$ decay channel similar to that in the combined $VH,\ H \rightarrow \gamma\gamma$ case. Leading sources of uncertainties are related to the modeling of background processes (WH) and statistical uncertainties ($q\bar{q} \rightarrow ZH$). The sensitivity to the gluon induced ZH production is very low as the analysis extrapolated from is not designed to separate the two ZH production processes.

The $H \rightarrow \gamma\gamma$ decay channel is expected to allow for the highest accuracy in the $t\bar{t}H$ production mode. The main benefits for this channel are the distinct signature of the $H \rightarrow \gamma\gamma$ decay as well as the parametric background model extracted directly from data. While the $H \rightarrow b\bar{b}$ decay features better statistical precision it is limited by uncertainties of the background modeling, in particular the $t\bar{t}$+heavy flavor backgrounds.

A feature that can be found across several decay channels is the relevance of the modeling of contaminations from the ggF production mode in phase spaces targeted at the other production modes VBF, VH, and $t\bar{t}H$. Similar to the VBF $H \rightarrow WW^*$ case shown in Fig. 5.3 leading uncertainties for the subdominant production modes include one or multiple nuisance parameters related to the modeling of the ggF production mode in the $H \rightarrow \gamma\gamma$ and $H \rightarrow ZZ^*$ analyses.

5.4. Combination

In the previous sections 5.2 and 5.3 expected sensitivities of individual Higgs boson analyses at the HL-LHC are presented. In this section results are presented from a statistical combination of the individual extrapolated ATLAS analyses. A large set of different parametrizations of the Higgs boson signals has been published in Refs. [175, 176].

5.4.1. Parametrizations

The combination procedure largely follows that of a recent ATLAS combination of Run 2 results in Ref. [190]. The combined likelihood is essentially a product of the individual analyses' likelihoods except for constraint terms of nuisance parameters which are considered correlated between multiple analyses. For such parameters and corresponding uncertainties the constraint term is only included once in the product likelihood. The $t\bar{t}H$, $H \to b\bar{b}$ channel introduces large, unrealistic constraints on various experimental uncertainties and the corresponding nuisance parameters are therefore decorrelated from those acting on the remaining channels. As an additional simplification, nuisance parameters in the $H \to Z\gamma$ analysis are decorrelated from other channels as the $H \to Z\gamma$ analysis has only been extrapolated assuming scenario S1, *i.e.*, for combined results including this analysis no reduction of systematic uncertainties in the corresponding regions is included. As the extrapolated $H \to Z\gamma$ analysis is still dominated by statistical uncertainties this is expected to have negligible effects on the estimated sensitivities.

Uncertainties of the predicted production cross sections and decay branching ratios of the Higgs boson are included depending on the parametrization.

- For the measurement of production cross sections the yield contributions from different decay modes are combined according to their SM branching ratios and corresponding uncertainties are assigned. For these measurements the analyses targeting the rare decays $H \to \mu\mu$ and $H \to Z\gamma$ are not included as their contribution to the sensitivity is negligible here.
- Analogously, for measurements of the different branching ratios, processes are correlated in their production mode according to their SM predictions and uncertainties regarding the total cross section of the different production modes are assigned.
- When measuring the product of individual production cross sections times branching ratios no theoretical uncertainties regarding either of these apply.

- Both groups of uncertainties, regarding production and decay, are included when quoting signal strengths μ or a reparametrization thereof in terms of the κ *framework* [125, 190, 191].

The κ parameters correspond to coupling modifiers inspired by couplings in the leading order Feynman graphs [125]:

$$(\sigma \cdot \mathcal{B})_{if} = \kappa_i^2 \sigma_i^{\mathrm{SM}} \cdot \frac{\kappa_f^2 \Gamma_f^{\mathrm{SM}}}{\kappa_H^2 \Gamma_H^{\mathrm{SM}}},$$

or equivalently

$$\mu_{if} = \frac{\kappa_i^2 \kappa_f^2}{\kappa_H^2}.$$

Here, the superscript SM refers to the Standard Model values of the Higgs boson production cross section via process i (σ_i^{SM}), the partial width of decay into final state f (Γ_f^{SM}) and the total width Γ_H^{SM} of the Higgs boson. Multiple variants of this type of parametrization can be employed. For example, the modifiers κ_g, κ_γ, and $\kappa_{Z\gamma}$ refer to the effective (loop induced) couplings to gluons, photons, and $Z\gamma$ respectively. In order to resolve these effective couplings in terms of fundamental couplings the different relative contributions from SM particles in the loops need to be considered. For example, the $H \to \gamma\gamma$ decay involves significant contributions from Feynman diagrams with either a top quark or a W boson in the loop. Numeric values allowing to determine the different relative contributions when resolving these effective couplings are given in Ref. [125] calculated at NLO. An overview of the resulting parametrization of the different production and decay modes in terms of effective and fundamental couplings can be found in Ref. [191]. Another parametrization employs a single modifier for couplings to massive vector bosons ($\kappa_V = \kappa_W = \kappa_Z$) and massive fermions ($\kappa_F$) each.

The total width modifier κ_H^2 can be written as [175, 191]

$$\kappa_H^2 = \frac{\sum_f \kappa_f^2 \cdot \mathcal{B}_{H\to f}}{1 - \mathcal{B}_{\mathrm{BSM}}} \tag{5.1}$$

where $\mathcal{B}_{\mathrm{BSM}}$ accounts for deviations in SM couplings not measured as well as BSM decays which are invisible to the detector. An exception is the $H \to ZZ^* \to 4\nu$ decay where relevant parameter κ_Z is constrained via the $H \to ZZ^* \to 4\ell$ channel. The at hadron colliders experimentally inaccessible $H \to gg$ decay is constrained from the ggF production mode. The Standard Model corresponds to all κ parameters being 1 and $\mathcal{B}_{\mathrm{BSM}} = 0$. When allowing $\mathcal{B}_{\mathrm{BSM}} > 0$ one needs to impose the condition $\kappa_{W,Z} \leq 1$ in order to be able to constrain κ_H, *i.e.*, the Higgs boson total width, without introducing degeneracies in the parametrization. The assumption that $\kappa_{W,Z} \leq 1$ holds in a range of possible extensions to the SM [125].

The expected precision of parametrizations shown in the following refer to the more optimistic scenario S2 and a dataset corresponding to $3000\,\mathrm{fb}^{-1}$ at $\sqrt{s} = 14\,\mathrm{TeV}$. The more conservative scenario S1 is included in Refs. [175, 176].

5.4.2. Global Signal Strength

The global signal strength combining all Higgs boson production and decay modes and scaling all $\sigma \cdot \mathcal{B}$ by the common factor μ_H is expected to be measured as

$$\mu_H = 1^{+0.025}_{-0.024} = 1 \pm 0.006(\mathrm{stat}) \ \pm 0.013(\mathrm{exp}) \ \pm 0.017(\mathrm{sig}) \pm 0.010(\mathrm{bkg}). \quad (5.2)$$

Uncertainties regarding the signal processes are dominating as this parametrization depends on the predicted individual cross sections and branching ratios. It therefore includes sizeable uncertainties regarding production and decay ratios. As the individual analyses use orthogonal subsets of the full dataset their statistical uncertainties are inherently uncorrelated and therefore the statistical uncertainty of such a combined measurement is greatly reduced. Similarly uncertainties from the modeling of background processes and, to a lesser extent, experimental uncertainties are only partially correlated between the individual channels due to different final state signatures [175, 176]. In a recent ATLAS combination using up to $80\,\mathrm{fb}^{-1}$ of Run 2 data the global signal strength was determined to be

$$\mu_H = 1.11^{+0.09}_{-0.08} = 1.11 \pm 0.05(\mathrm{stat}) \ ^{+0.05}_{-0.04}(\mathrm{exp}) \ ^{+0.05}_{-0.04}(\mathrm{sig}) \pm 0.03(\mathrm{bkg}) \ \ [192].$$

5.4.3. Production Cross Sections and Branching Ratios

The expected precision of combined measurements of the production cross sections and decay branching ratios is shown in Fig. 5.4. The relative total expected uncertainty of the measured ggF cross section of 2.4% is almost identical to the uncertainty of the inclusive signal strength in Eq. (5.2). However, the latter includes a sizeable uncertainty of the predicted ggF cross section of around 2.5% (QCD scales + PDF + α_s). The measurements of most production mode cross section are expected to be dominated by systematic uncertainties with exception of the ZH production mode where the size of statistical and systematic uncertainties are almost identical.

When measuring the Higgs boson branching ratios only the rare decay modes $H \to \mu\mu$ and $H \to Z\gamma$ are still limited by statistical uncertainties. The common

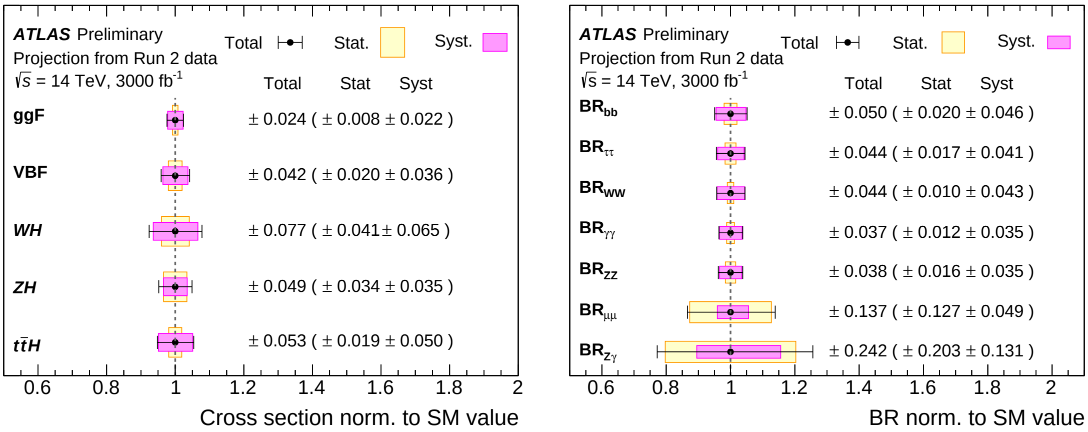

Figure 5.4.: Expected uncertainties of combined measurements of Higgs boson production cross sections (left) or branching ratios (right) at the HL-LHC. The expected uncertainties are shown as total uncertainties (black) as well as statistical (yellow boxes) and systematic components (pink). Published in Refs. [175,176].

decay modes $H \to b\bar{b}$, $H \to WW^*$, $H \to ZZ^*$ and $H \to \gamma\gamma$ are expected to be measured with uncertainties between 4 and 5%.

Expected total uncertainties and their breakdowns into statistical, experimental, signal, and background modeling uncertainties are shown in Tab. 5.6 for production cross sections times branching ratios which can be measured in this combination. For easier comparison of different channels the results are additionally visualized in Fig. 5.5. Background uncertainties of the $H \to \mu\mu, Z\gamma$ decays are vanishing due to their parametric background estimate, and either small vanishing correlations with other channels. While in the $H \to \gamma\gamma$ channel similar parametric background models are used, this channel is less affected by statistical uncertainties and shares several sources of systematic uncertainties with other channels. Fixing background related nuisance parameters therefore leads also to a small indirect reduction of uncertainties of the cross sections in the $H \to \gamma\gamma$ channel.

Statistical uncertainties are only expected to be dominant for very rare decay modes ($H \to \mu\mu, Z\gamma$) or combinations of rare production and decay modes ($VH/t\bar{t}H$, $H \to ZZ^*$ and VH, $H \to \gamma\gamma$). For most other combinations systematic uncertainties dominate over statistical ones.

5.4.4. Interpretations in the κ Framework

In this section interpretations of the projected results in the κ framework described in Sec. 5.4.1 are presented.

Table 5.6.: Expected uncertainties of the cross sections times branching ratios in the combination of analyses projected to the anticipated HL-LHC dataset. The scenario is S2 with $3000\,\text{fb}^{-1}$ at $\sqrt{s} = 14\,\text{TeV}$. Adapted from version published in Refs. [175, 176].

Production	Decay	$\frac{\Delta_{\text{tot}}}{(\sigma\cdot\mathcal{B})_{\text{SM}}}$	$\frac{\Delta_{\text{stat}}}{(\sigma\cdot\mathcal{B})_{\text{SM}}}$	$\frac{\Delta_{\text{exp}}}{(\sigma\cdot\mathcal{B})_{\text{SM}}}$	$\frac{\Delta_{\text{sig}}}{(\sigma\cdot\mathcal{B})_{\text{SM}}}$	$\frac{\Delta_{\text{bkg}}}{(\sigma\cdot\mathcal{B})_{\text{SM}}}$
ggF	$H \to \gamma\gamma$	$^{+0.037}_{-0.035}$	$^{+0.017}_{-0.017}$	$^{+0.031}_{-0.029}$	$^{+0.009}_{-0.009}$	$^{+0.006}_{-0.005}$
	$H \to ZZ^*$	$^{+0.039}_{-0.039}$	$^{+0.020}_{-0.020}$	$^{+0.030}_{-0.030}$	$^{+0.011}_{-0.010}$	$^{+0.010}_{-0.009}$
	$H \to WW^*$	$^{+0.044}_{-0.043}$	$^{+0.012}_{-0.012}$	$^{+0.027}_{-0.027}$	$^{+0.021}_{-0.020}$	$^{+0.024}_{-0.024}$
	$H \to \tau\tau$	$^{+0.085}_{-0.080}$	$^{+0.033}_{-0.033}$	$^{+0.045}_{-0.044}$	$^{+0.058}_{-0.051}$	$^{+0.028}_{-0.026}$
	$H \to \mu\mu$	$^{+0.187}_{-0.183}$	$^{+0.179}_{-0.179}$	$^{+0.031}_{-0.023}$	$^{+0.047}_{-0.029}$	$^{+0.000}_{-0.000}$
	$H \to Z\gamma$	$^{+0.346}_{-0.320}$	$^{+0.311}_{-0.311}$	$^{+0.059}_{-0.039}$	$^{+0.139}_{-0.062}$	$^{+0.000}_{-0.000}$
VBF	$H \to \gamma\gamma$	$^{+0.093}_{-0.085}$	$^{+0.044}_{-0.044}$	$^{+0.058}_{-0.051}$	$^{+0.056}_{-0.051}$	$^{+0.009}_{-0.008}$
	$H \to ZZ^*$	$^{+0.122}_{-0.115}$	$^{+0.098}_{-0.094}$	$^{+0.053}_{-0.048}$	$^{+0.047}_{-0.042}$	$^{+0.014}_{-0.011}$
	$H \to WW^*$	$^{+0.066}_{-0.065}$	$^{+0.033}_{-0.033}$	$^{+0.029}_{-0.028}$	$^{+0.040}_{-0.040}$	$^{+0.028}_{-0.028}$
	$H \to \tau\tau$	$^{+0.079}_{-0.076}$	$^{+0.037}_{-0.037}$	$^{+0.050}_{-0.046}$	$^{+0.033}_{-0.031}$	$^{+0.037}_{-0.035}$
	$H \to \mu\mu$	$^{+0.370}_{-0.353}$	$^{+0.325}_{-0.325}$	$^{+0.142}_{-0.092}$	$^{+0.104}_{-0.104}$	$^{+0.000}_{-0.000}$
	$H \to Z\gamma$	$^{+0.677}_{-0.688}$	$^{+0.625}_{-0.619}$	$^{+0.153}_{-0.065}$	$^{+0.208}_{-0.293}$	$^{+0.000}_{-0.000}$
WH	$H \to \gamma\gamma$	$^{+0.141}_{-0.136}$	$^{+0.132}_{-0.130}$	$^{+0.037}_{-0.030}$	$^{+0.030}_{-0.026}$	$^{+0.007}_{-0.006}$
	$H \to b\bar{b}$	$^{+0.102}_{-0.099}$	$^{+0.044}_{-0.043}$	$^{+0.042}_{-0.040}$	$^{+0.044}_{-0.040}$	$^{+0.070}_{-0.068}$
ZH	$H \to \gamma\gamma$	$^{+0.161}_{-0.153}$	$^{+0.151}_{-0.147}$	$^{+0.036}_{-0.028}$	$^{+0.041}_{-0.034}$	$^{+0.006}_{-0.005}$
	$H \to b\bar{b}$	$^{+0.052}_{-0.051}$	$^{+0.035}_{-0.035}$	$^{+0.020}_{-0.019}$	$^{+0.022}_{-0.021}$	$^{+0.024}_{-0.024}$
VH	$H \to ZZ^*$	$^{+0.187}_{-0.176}$	$^{+0.177}_{-0.168}$	$^{+0.037}_{-0.031}$	$^{+0.043}_{-0.039}$	$^{+0.018}_{-0.016}$
$t\bar{t}H$	$H \to \gamma\gamma$	$^{+0.076}_{-0.072}$	$^{+0.047}_{-0.046}$	$^{+0.043}_{-0.040}$	$^{+0.041}_{-0.038}$	$^{+0.005}_{-0.005}$
	$H \to WW^*, \tau\tau$	$^{+0.213}_{-0.191}$	$^{+0.063}_{-0.063}$	$^{+0.189}_{-0.170}$	$^{+0.052}_{-0.034}$	$^{+0.054}_{-0.048}$
	$H \to ZZ^*$	$^{+0.203}_{-0.183}$	$^{+0.196}_{-0.177}$	$^{+0.035}_{-0.026}$	$^{+0.041}_{-0.035}$	$^{+0.010}_{-0.009}$
	$H \to b\bar{b}$	$^{+0.151}_{-0.133}$	$^{+0.032}_{-0.032}$	$^{+0.034}_{-0.033}$	$^{+0.047}_{-0.041}$	$^{+0.135}_{-0.118}$

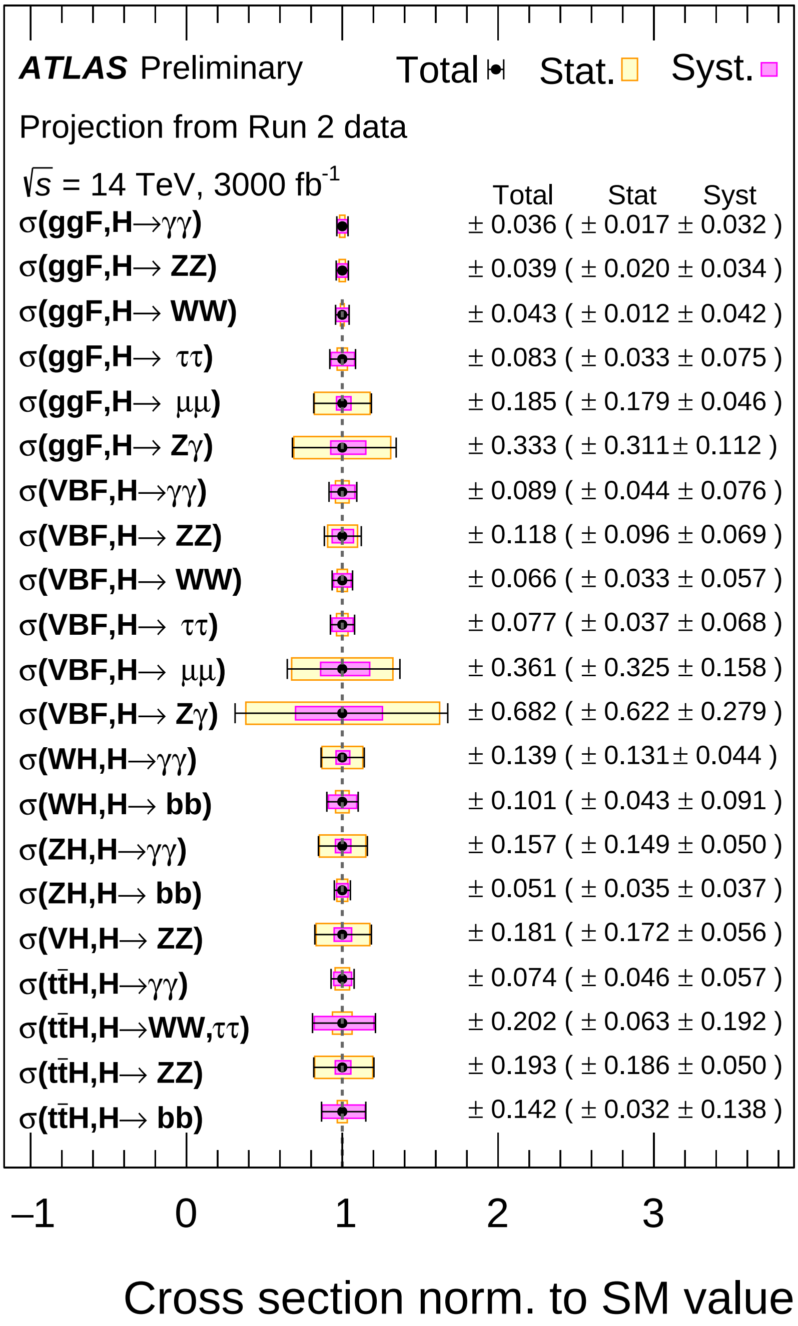

Figure 5.5.: Expected uncertainties of combined measurements of Higgs boson production cross sections times branching ratios at the HL-LHC. The expected uncertainties are shown as total uncertainties (black) as well as statistical (yellow boxes) and systematic components (pink). Published in Refs. [175,176].

The Higgs-fermion vertices in the Standard Model are proportional to $\kappa_f \cdot \lambda/\sqrt{2} = \kappa_f \cdot m_f/v$. The couplings of the Higgs boson to the massive vector bosons are proportional to $\kappa_V m_V^2/v$. Hence the reduced couplings $\kappa_f m_f/v$ (fermions) and $\sqrt{\kappa_V} m_V/v$ are expected to show a linear dependence on the particles' masses as illustrated in Fig. 5.6, comparing the already achieved precision to that projected for the HL-LHC programme. The reduced coupling $\kappa_f m_f/v$ is expected to be measured with an uncertainty of about 7% for muons. In the Run 2 combination [190] performed at a similar time as the studies presented here, only an upper limit of $\kappa_\mu < 1.63$ at 95% confidence level is achieved. Similarly the expected uncertainties of couplings of other particles to the Higgs boson are expected to be greatly reduced. In this case shown in Fig. 5.6 the loop structure as predicted by the SM is assumed to resolve the effective couplings of gluons and photons to the Higgs boson. The $H \to Z\gamma$ analysis and corresponding decay mode are not included as their contribution to the sensitivity is expected to be negligible.

The expected uncertainties shown in Fig. 5.7 are obtained with parametrizations leaving the gluon and photon couplings to the Higgs boson unresolved, *i.e.*, κ_g, κ_γ parameters scaling their effective couplings are included. The $\mathcal{B}_{\mathrm{BSM}}$ term is fixed to 0. Using such a parametrization the measurement becomes sensitive to contributions to the loops from new particles which might even be too heavy for direct production. The expected uncertainties of 2.4% (κ_γ) and 3.1% (κ_g) are about a fourth of those reported in Ref. [190]. The expected two dimensional confidence levels in the κ_g, κ_γ-plane are shown in Fig. 5.8.

When allowing $\mathcal{B}_{\mathrm{BSM}} \neq 0$ in Eq. (5.1) this parameter is expected to be measured with an uncertainty of 3.3%. No dedicated searches for invisible decays of the Higgs boson are included here. In Ref. [190] a corresponding 95% confidence level limit of $\mathcal{B}_{\mathrm{BSM}} < 0.26$ is quoted based on up to $80\,\mathrm{fb}^{-1}$ of Run 2 data. Assuming that the corresponding profiled NLL is approximately parabolic[1] this corresponds again to an expected improvement by a factor of about 4. Uncertainties of κ parameters are reduced, both, in Ref. [190] and here, when including a $\mathcal{B}_{\mathrm{BSM}}$ term. This feature can be related to the imposed conditions $\kappa_{W,Z} \leq 1$.

In Fig. 5.9 expected uncertainties are shown for measurements of ratios of κ parameters $\lambda_{ij} := \kappa_i/\kappa_j$, $j = g, Z$. The $gg \to H \to ZZ^*$ process serves as a reference process with $\kappa_{gZ} := \kappa_g \kappa_Z/\kappa_H$ connecting the coupling ratios λ_{ij} to absolute cross sections. Again, to avoid degeneracies all of these parameters are assumed to be positive with exception of λ_{tg} and λ_{WZ}. In this parametrization the total width of the Higgs boson drops out and therefore no assumptions regarding this width need to be made. The loop induced processes are again treated via effective coupling modifiers κ_g, κ_γ, $\kappa_{Z\gamma}$. For comparison Fig. 5.9 also includes

[1]That is, the 95% confidence level corresponds to approximately 2 standard deviations.

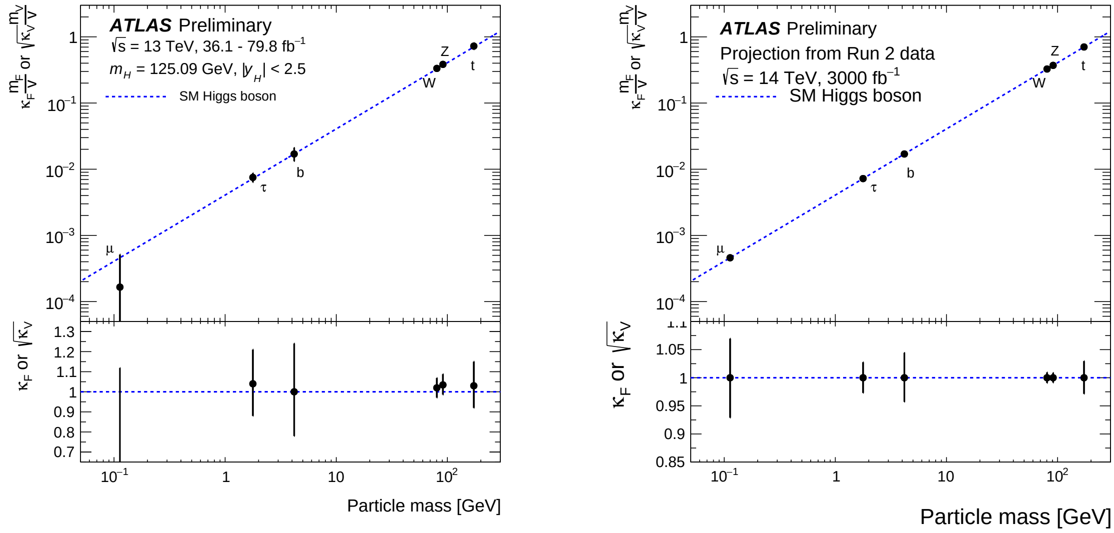

Figure 5.6.: Test of relation between coupling strengths of particles to the Higgs boson and their masses. The vertical axis shows the reduced couplings $\kappa_f \cdot m_f/v$ for fermions and $\sqrt{\kappa_V} \cdot m_V/v^a$ for massive vector bosons with the vacuum expectation value $v = 246\,\text{GeV}$. The left hand side shows a recent ATLAS measurement (from Ref. [190]) using up to $80\,\text{fb}^{-1}$ of Run 2 data, the right hand side (published in Refs. [175, 176]) the expected precision at the HL-LHC in scenario S2. In both cases no BSM effects are considered and the SM structure is assumed for loop induced effective couplings $gg \to H$ and $H \to \gamma\gamma$ which are expressed in terms of the fundamental couplings to fermions and weak vector bosons. The dashed lines indicate the SM prediction, the ratios to which are shown in the bottom panels.

[a] Here, the power of the constant v is adjusted to create a dimensionless quantity and to make the linear relations for fermion and vector boson masses coincide.

expected uncertainties for a largely analogous measurement of ratios of production cross sections and branching ratios. In contrast to the λ parametrization the analyses of the rare decay channels $H \to \mu\mu$, $Z\gamma$ are not included in this case.

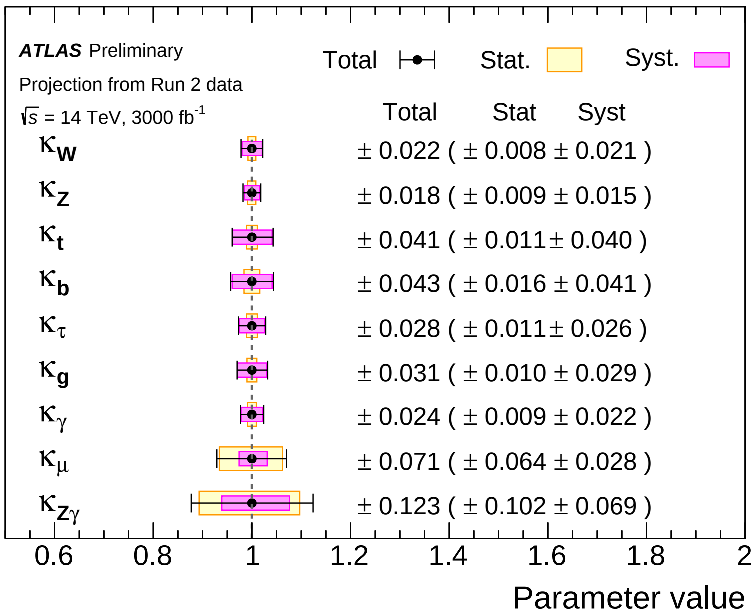

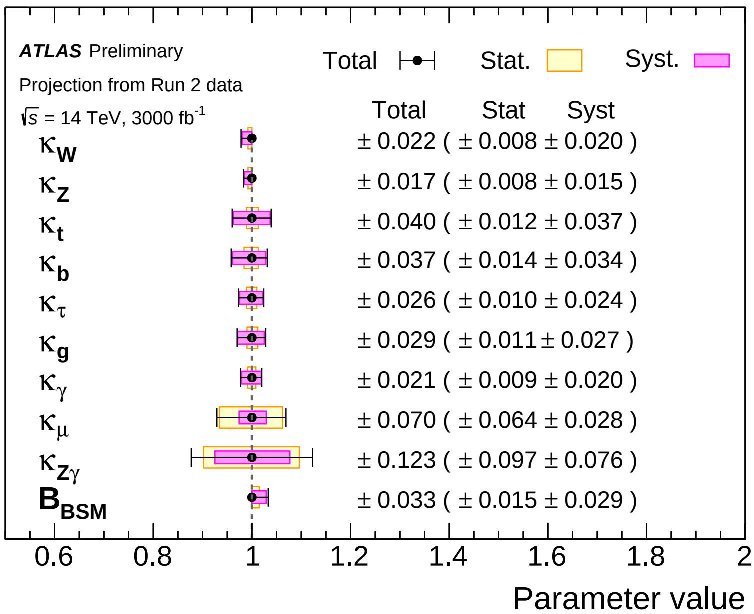

Figure 5.7.: Expected uncertainties of scaling factors κ of Higgs boson couplings at the HL-LHC in scenario S2 with (bottom graphic) and without (top graphic) inclusion of a generic BSM term accounting for undetected decay modes. In the former case the conditions $\mathcal{B}_{\mathrm{BSM}} \geq 0$ and $\kappa_{W,Z} \leq 1$ are imposed. Published in Refs. [175, 176].

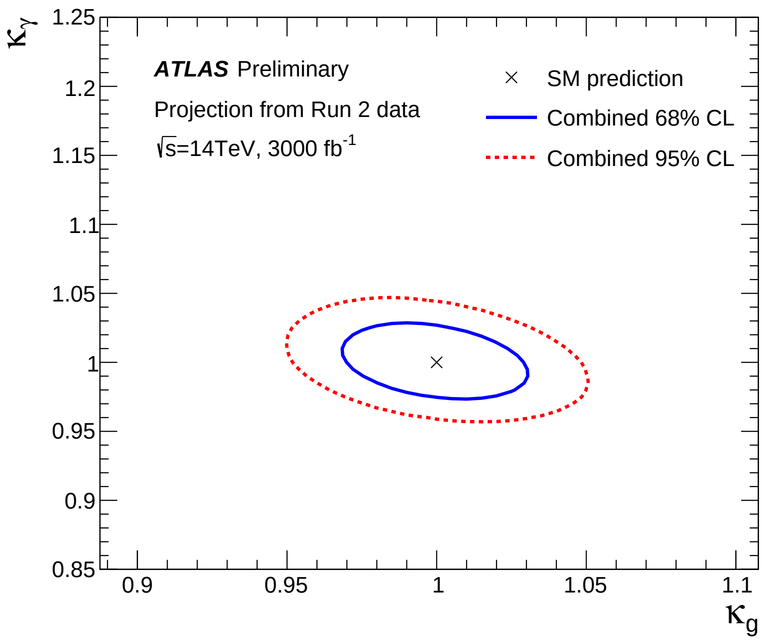

Figure 5.8.: Expected 68% and 95% confidence levels in the κ_g, κ_γ-plane at the HL-LHC in scenario S2. Published in Refs. [175, 176].

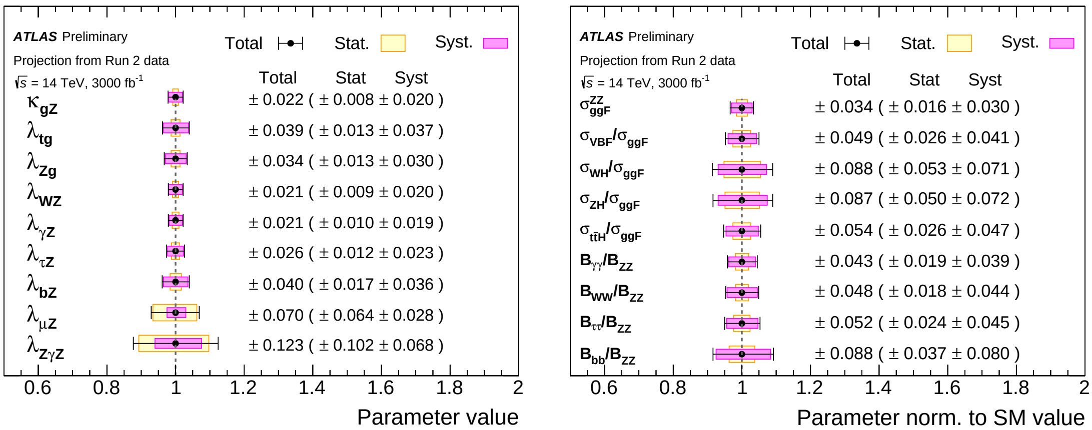

Figure 5.9.: Expected uncertainties of ratios $\lambda_{ij} = \kappa_i/\kappa_j$ (left), and ratios of production cross sections and branching ratios (right) measured at the HL-LHC in scenario S2. In both cases the $gg \to H \to ZZ^*$ process is used as a reference fixing absolute cross sections. In both graphics the scenario is S2. Published in Refs. [175, 176].

6 Summary and Conclusions

The set of experimentally confirmed particles in the Standard Model of particle physics was completed in 2012 with the discovery of a neutral resonance of $m_H \approx 125\,\mathrm{GeV}$ by the ATLAS [1] and CMS [2] Collaborations. By now being considered as the Higgs boson of the Standard Model, it is since a topic of a broad set of experimental investigations. Its unique role in the Standard Model renders it a prime subject for studies in regards to potential extensions of the Standard Model. Amongst these studies measurements of production cross sections and branching ratios and their interpretation in terms of couplings to other Standard Model particles represent an important baseline for further studies. The Brout-Englert-Higgs (BEH) mechanism predicting the existence of the Higgs boson is not only studied in processes producing a Higgs boson. Feynman diagrams involving the exchange of a Higgs boson are crucial for the self-consistency of the SM in processes such as the scattering of vector bosons.

Studies are presented evaluating the potential for improvements of the charge reconstruction of highly energetic electrons in the ATLAS detector. Charge misreconstruction in this regard leads to significant background contributions in analyses investigating some of the rarest processes by exploiting signatures with two electrons or muons carrying identical electric charge. In particular in cases where the electron emits a hard bremsstrahlung photon converting to an e^+e^- pair in the detector material, the choice of the charge-defining track is non-trivial. Potential gains by means of an improved, MVA based, ambiguity resolution at the level of already reconstructed tracks are found to be limited.

In detailed studies the dominant origin of charge misidentification is instead found to be in the reconstruction of the used track candidates. Charge misidentification is found to be strongly linked to the presence of hybrid tracks which are partially composed of hits from a prompt electron and partially of hits from electrons produced in the conversion of a bremsstrahlung photon.

A measurement of the gluon-fusion (ggF) and vector-boson fusion (VBF) Higgs boson production cross sections times $H \to WW^*$ branching ratio is presented based on data corresponding to an integrated luminosity of $36.1\,\mathrm{fb}^{-1}$ at $\sqrt{s} = 13\,\mathrm{TeV}$ taken in the years 2015 and 2016. To this end final states with one electron and one muon are used in categories of different jet multiplicities targeting either the ggF or VBF production mode. The estimation of background contributions from events with misidentified leptons is performed using a fake factor method. In the category targeting the VBF production mode a boosted decision tree is used to enhance the separation of signal events from those from background processes. The cross sections times branching ratio are determined simultaneously using a binned profile likelihood fit which for which binning and parametrization are discussed in detail. High sensitivity in regions targeting the ggF production mode is achieved in this fit through the use of of distributions in multiple dimensions. The obtained values read

$$\begin{aligned}
\sigma_{\text{ggF}} \cdot \mathcal{B}_{H\to WW^*} &= 11.4\,^{+1.2}_{-1.1}(\text{stat.})\,^{+1.2}_{-1.1}(\text{th. syst.})\,^{+1.4}_{-1.3}(\text{exp. syst.})\,\text{pb} \\
&= 11.4\,^{+2.2}_{-2.1}\,\text{pb}, \\
&\text{and} \\
\sigma_{\text{VBF}} \cdot \mathcal{B}_{H\to WW^*} &= 0.50\,^{+0.24}_{-0.22}(\text{stat.}) \pm 0.10(\text{th. syst.})\,^{+0.12}_{-0.13}(\text{exp. syst.})\,\text{pb} \\
&= 0.50\,^{+0.29}_{-0.28}\,\text{pb}.
\end{aligned}$$

The corresponding signal strengths, *i.e.*, the ratio of the aforementioned result to the prediction in the Standard Model are

$$\begin{aligned}
\mu_{\text{ggF}} &= 1.10\,^{+0.10}_{-0.09}(\text{stat.})\,^{+0.13}_{-0.11}(\text{th. syst.})\,^{+0.14}_{-0.13}(\text{exp. syst.}) &&= 1.10\,^{+0.21}_{-0.20}, \text{ and} \\
\mu_{\text{VBF}} &= 0.62\,^{+0.29}_{-0.27}(\text{stat.})\,^{+0.12}_{-0.13}(\text{th. syst.}) \pm 0.15(\text{exp. syst.}) &&= 0.62\,^{+0.36}_{-0.35}.
\end{aligned}$$

The results are well compatible with the Standard Model predictions. Leading uncertainties are discussed for both production modes. The accuracy of the here obtained results is briefly compared to earlier measurements by the ATLAS Collaboration and to a recent measurement pubished by the CMS Collaboration.

An extensive outlook for studying the Higgs boson is given in Chap. 5. Projections of expected sensitivities at the HL-LHC are presented exemplary based on the $H \to WW^*$ analysis for interpretations in terms of cross sections times branching ratio and signal strengths. Furthermore a statistical combination with such projections for other Higgs boson analyses is presented. The expected precisions are derived for parameters of various interpretation schemes including Higgs boson production cross sections, Higgs boson branching ratios, and combinations thereof.

The results are also interpreted in various parametrizations of the κ-framework which introduces multiplicative modifiers for the coupling strengths of the Higgs boson to other particles. Based on this framework the couplings of the Higgs boson to the massive vector bosons and the third generation fermions are anticipated to be measured with uncertainties between 1.8% and 4.3%. For the loop induced effective couplings to photons and gluons expected uncertainties of 2.4% and 3.1%

are found, providing unprecedented sensitivity to effects of new physics possibly contributing to these loops. Similarly decays of the Higgs boson to undetected final states are expected to be measurable with an uncertainty of 3.3%.

Systematic uncertainties are expected to become a limiting factor for most of these measurements even with some assumed significant improvements. Further more, the sensitivity of inclusive measurements and interpretations, *e.g.*, in the κ-framework to effects of new physics is limited. A rich set of more sophisticated analyses and interpretations should therefore be envisioned. Fiducial measurements in restricted phase spaces can reduce uncertainties due to the extrapolation from the experimentally covered phase space to the inclusive processes. Additionally, in differential measurements individual cross sections are extracted in multiple bins of selected variables. Many systematic uncertainties affect primarily overall event rates while their effect on shapes of distributions may be small. As a consequence, *e.g.*, differential measurements allow for the extraction of additional shape information whereas the shape of signal processes is largely fixed in measurement such as those projected.

Similarly additional information can be extracted in the so called simplified template cross section (STXS) scheme [60] determining individual cross sections in multiple disjoint phase space regions. The STXS scheme, being agreed upon between theorists and experimentalists from different experiments, is particularly suitable for further interpretations including results from several analyses. Such interpretations are usually performed in terms of Effective Field Theories (EFT) such as SMEFT [193].

Appendix

A. Relation between χ^2 Distribution for 1 Degree of Freedom and Gaussian Confidence Intervals

In this section a connection between the cumulative density function (CDF) of a χ^2 distribution with one degree of freedom and the symmetric integrals of a standard normal distribution is shown. For one degree of freedom the χ^2 distribution reads (see, *e.g.*, Ref. [67])

$$f(\chi^2, 1) = \frac{1}{\sqrt{2\pi}} \frac{e^{-\chi^2/2}}{\sqrt{\chi^2}}.$$

Its CDF α with $x := \chi^2$ can be expressed as

$$\begin{aligned}
\alpha &= \frac{1}{\sqrt{2\pi}} \int_0^{x'} dx\, \frac{e^{-x/2}}{\sqrt{x}} \\
&\overset{y^2:=x}{=} \frac{1}{\sqrt{2\pi}} \int_0^{y'} dy\, \frac{dy^2}{dy} \frac{e^{-y^2/2}}{y}, \; y' = \sqrt{x'} \\
&= \frac{1}{\sqrt{2\pi}} \int_0^{y'} dy\, 2e^{-y^2/2}.
\end{aligned}$$

The so transformed integrand is symmetric with respect to 0 and the expression can, hence, be written as a symmetric integral

$$\alpha = \frac{1}{\sqrt{2\pi}} \int_{-y'}^{y'} dy\, e^{-y^2/2},$$

which is nothing but the integral over a standard normal distribution between $\pm y' = \pm\sqrt{\chi^{2\prime}}$. Hence, the probability $p = 1 - \alpha$ to find $\chi^2 > \chi^{2\prime}$ is the same as the probability for a normal distributed quantity to be found outside the interval $[-\sqrt{\chi^{2\prime}}, \sqrt{\chi^{2\prime}}]$.

B. Input Distributions for Electron Track Selection BDT

In this Section distributions of input quantities of the track selection BDT in Sec. 3.3.6 are shown. For better comparison of their shapes the distributions of different types of tracks are normalized, their integral before normalization is given in the legends. All entries are unweighted counts. All distributions are obtained from a sample of simulated single electron events with overlaid pileup collisions.

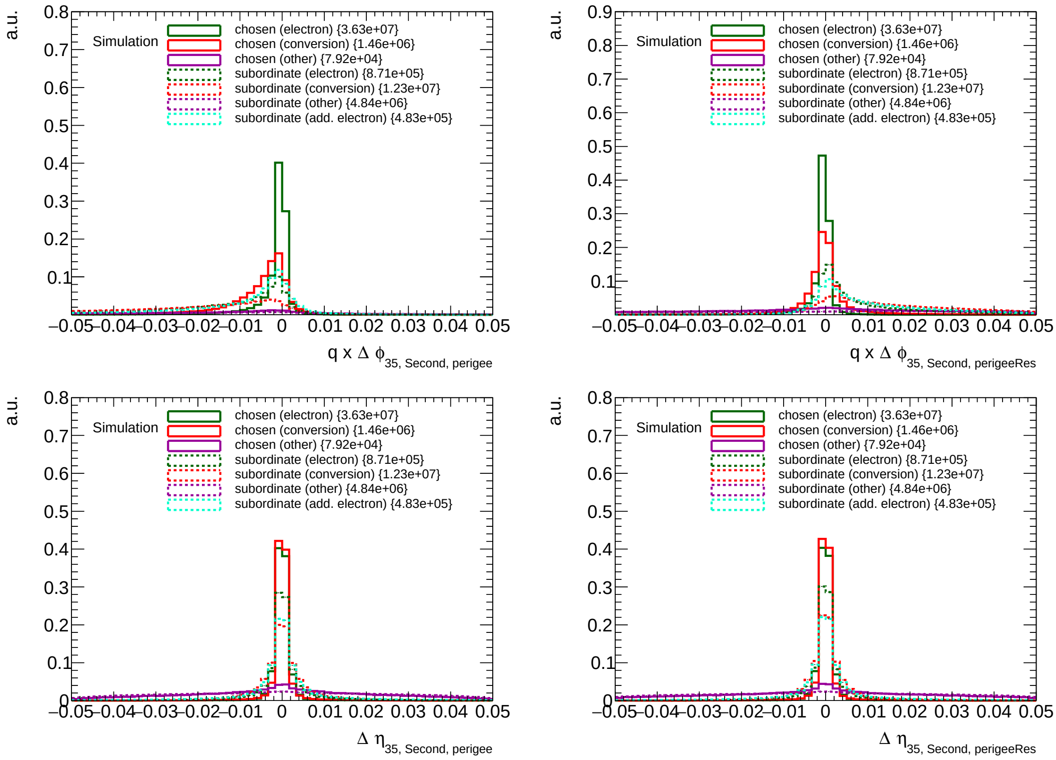

Figure B.1.: Distributions of distances in ϕ and η between the barycenter of the electron's $\eta \times \phi = 3 \times 5$ cells calorimeter cluster and the extrapolated track position. The cluster's barycenter and the tracks' η and ϕ values are taken at the second layer of the electromagnetic calorimeter. Tracks are either directly extrapolated from the perigee or extrapolated from the perigee after rescaling their momentum to the cluster's energy. The distances in ϕ direction are multiplied by the track's reconstructed charge to account for the interplay of different direction of curvature for different charges and radiative energy losses. The tracks' parameters are taken from the GSF fit.

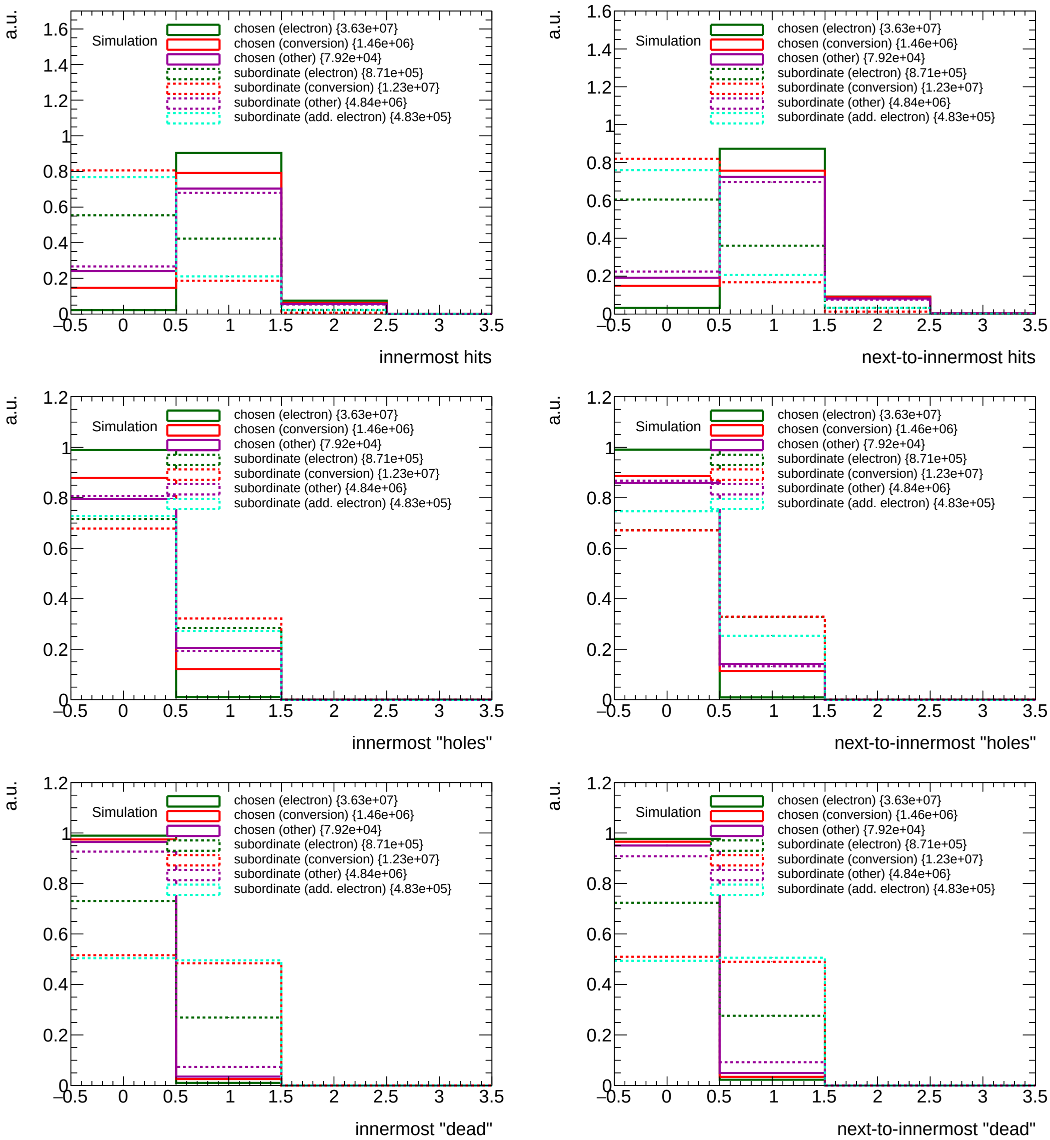

Figure B.2.: Distributions of number of hits, missing hits and known dead modules for different tracks in the innermost and next-to-innermost tracking detector layers. More than one hit in one detector layer can be found due to slight overlap of the modules of each layer to ensure full ϕ coverage.

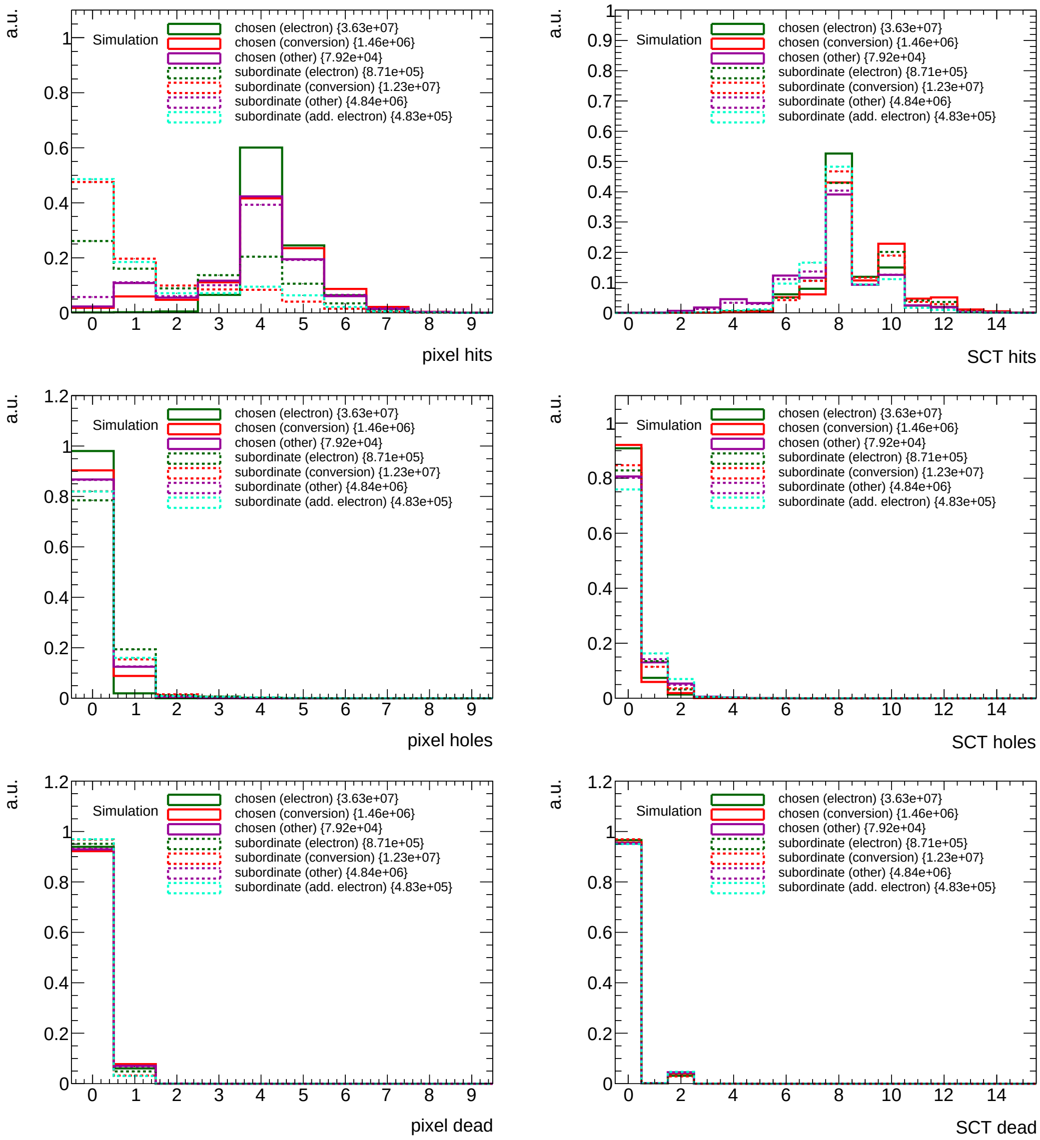

Figure B.3.: Distributions of number of hits, missing hits and known dead modules for different tracks in the pixel and silicon strip (SCT) tracking detectors.

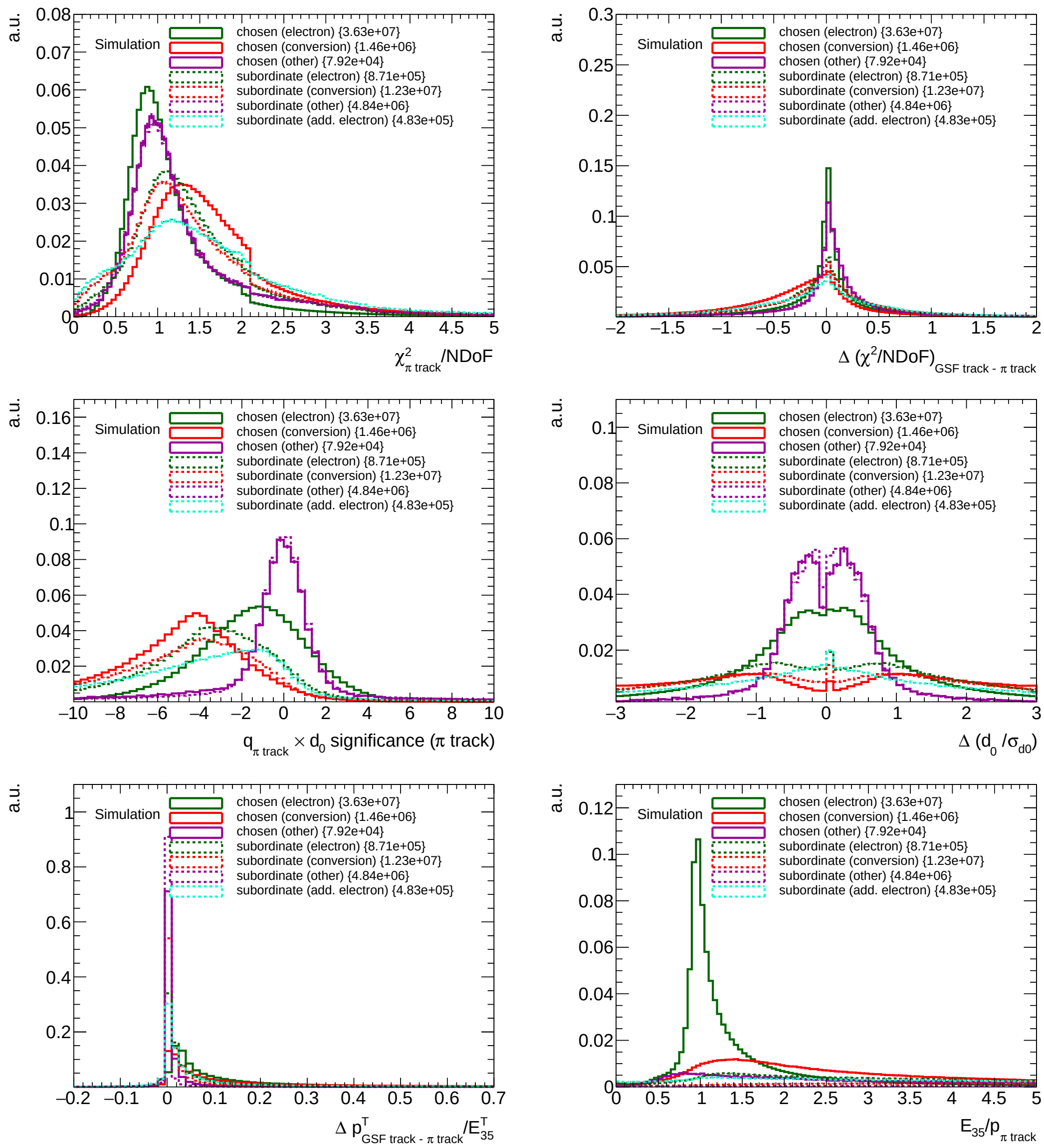

Figure B.4.: Distributions of remaining input quantities to the track selection BDT. Distributions of differences indicated by a Δ refer to the difference of the quantity in question between the pion-hypothesis track fit and the GSF fit. E_{35} refers to the energy measurement in the $\eta \times \phi = 3 \times 5$ cells sized calorimeter cluster. While the GSF fit is designed to improve the parameter estimates for electron tracks it is found to provide much stronger differences for non-electron tracks compared to the pion-hypothesis fit.

C. Additional Distributions Regarding the ggF $H \to WW^*$ Analysis

In Tab. C.1 bin boundaries used to create the remapped m_T distribution used in the ggF $H \to WW^*$ statistical analysis are listed. The algorithm used to obtain these boundaries is described in Sec. 4.5. The post-fit distributions of the remapped m_T are shown in Figs. C.1 and C.2 for the 0-jet signal subregions and in Figs. C.3 and C.4 for the 1-jet signal subregions. The corresponding yields including also those from other Higgs boson production or decay modes[1] are given in Tab.C.2 based on a fit to the 0-jet and 1-jet regions only where the VBF process is fixed to the SM prediction.

Additional post-fit distributions in the 0-jet and 1-jet signal regions are shown in Fig. C.5. Again the hatched uncertainty bands include statistical uncertainties, systematic uncertainties and correlations thereof. Edges in the $p_\mathrm{T}^{\ell 1}$ distributions are related to different thresholds of the triggers used.

[1]Contributions from other Higgs processes are omitted in the presented graphics as their contribution would not be visible.

Table C.1.: Bin boundaries of the m_T distributions in the ggF $H \to WW^*$ signal subregions. Numeric values are given in GeV. The lowest m_T bins start at 0, the highest bins run until ∞.

N_jets	$m_{\ell\ell}$	$p_\mathrm{T}^{\ell 1}$	ℓ_1	m_T boundaries
0	< 30	< 15	e	$84, 92, 98, 103, 108, 114, 121$
			μ	$82, 89, 95, 101, 107, 113, 122$
		≥ 15	e	$93, 101, 107, 113, 118, 124, 130$
			μ	$93, 101, 107, 112, 117, 123, 130$
	≥ 30	< 15	e	$87, 95, 101, 106, 111, 117, 124$
			μ	$86, 94, 100, 106, 111, 117, 125$
		≥ 15	e	$94, 102, 108, 113, 118, 124, 130$
			μ	$93, 101, 107, 112, 117, 123, 130$
1	< 30	< 15	e	$80, 91, 101, 111, 123$
			μ	$80, 91, 101, 110, 121$
		≥ 15	e	$85, 96, 107, 116, 129$
			μ	$85, 97, 107, 117, 130$
	≥ 30	< 15	e	$86, 97, 106, 115, 125$
			μ	$87, 97, 105, 114, 125$
		≥ 15	e	$89, 99, 108, 118, 130$
			μ	$89, 100, 109, 119, 130$

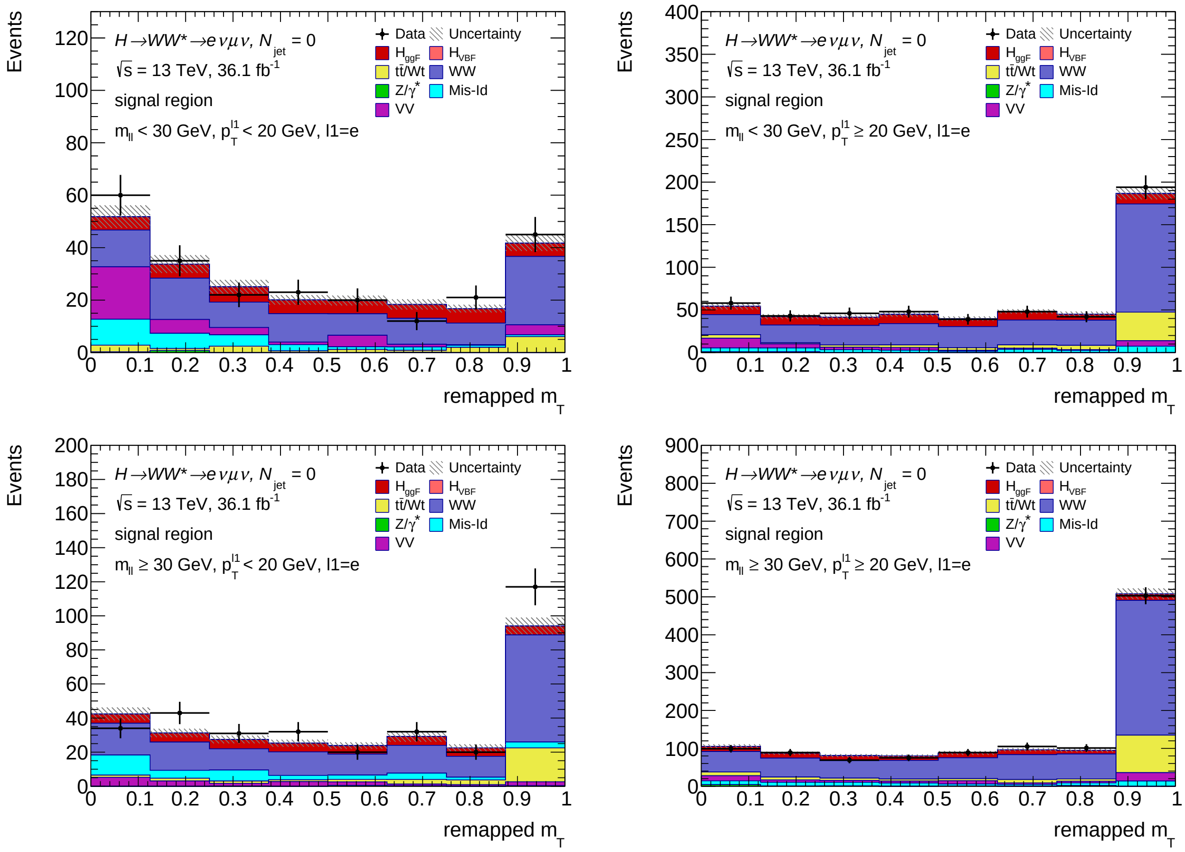

Figure C.1.: Remapped m_{T} post-fit distributions in the 0-jet signal region of the $H \to WW^*$ analysis. The distributions shown are those in the subregions where the subleadig lepton is an electron. The graphics on the left show the $p_{\mathrm{T}}^{\ell 1} < 20\,\mathrm{GeV}$ subregions, the ones on the right the subregions with $p_{\mathrm{T}}^{\ell 1} \geq 20\,\mathrm{GeV}$. At the top and bottom the regions with $m_{\ell\ell} < 30\,\mathrm{GeV}$ and $m_{\ell\ell} \geq 30\,\mathrm{GeV}$ respectively are show.

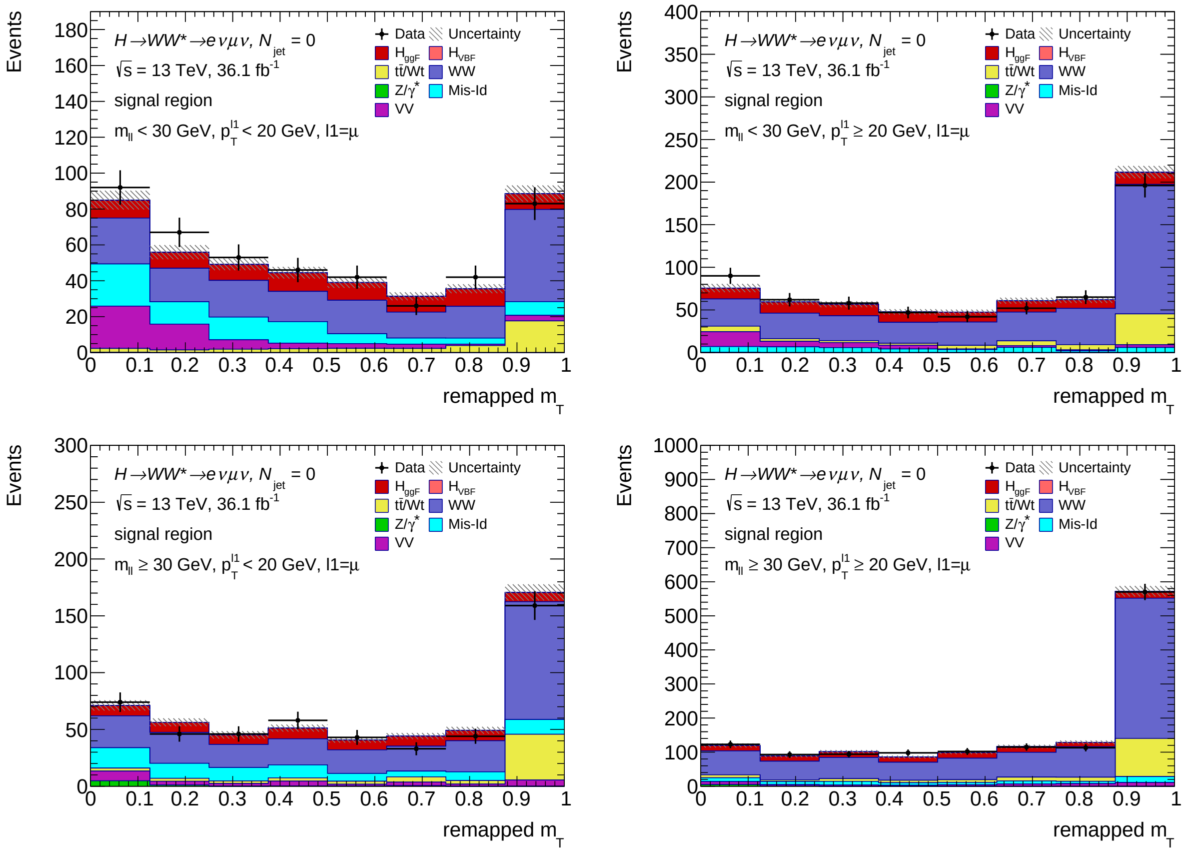

Figure C.2.: Remapped m_{T} post-fit distributions in the 0-jet signal region of the $H \rightarrow WW^*$ analysis. The distributions shown are those in the subregions where the subleadig lepton is a muon. The graphics on the left show the $p_{\mathrm{T}}^{\ell 1} < 20\,\mathrm{GeV}$ subregions, the ones on the right the subregions with $p_{\mathrm{T}}^{\ell 1} \geq 20\,\mathrm{GeV}$. At the top and bottom the regions with $m_{\ell\ell} < 30\,\mathrm{GeV}$ and $m_{\ell\ell} \geq 30\,\mathrm{GeV}$ respectively are show.

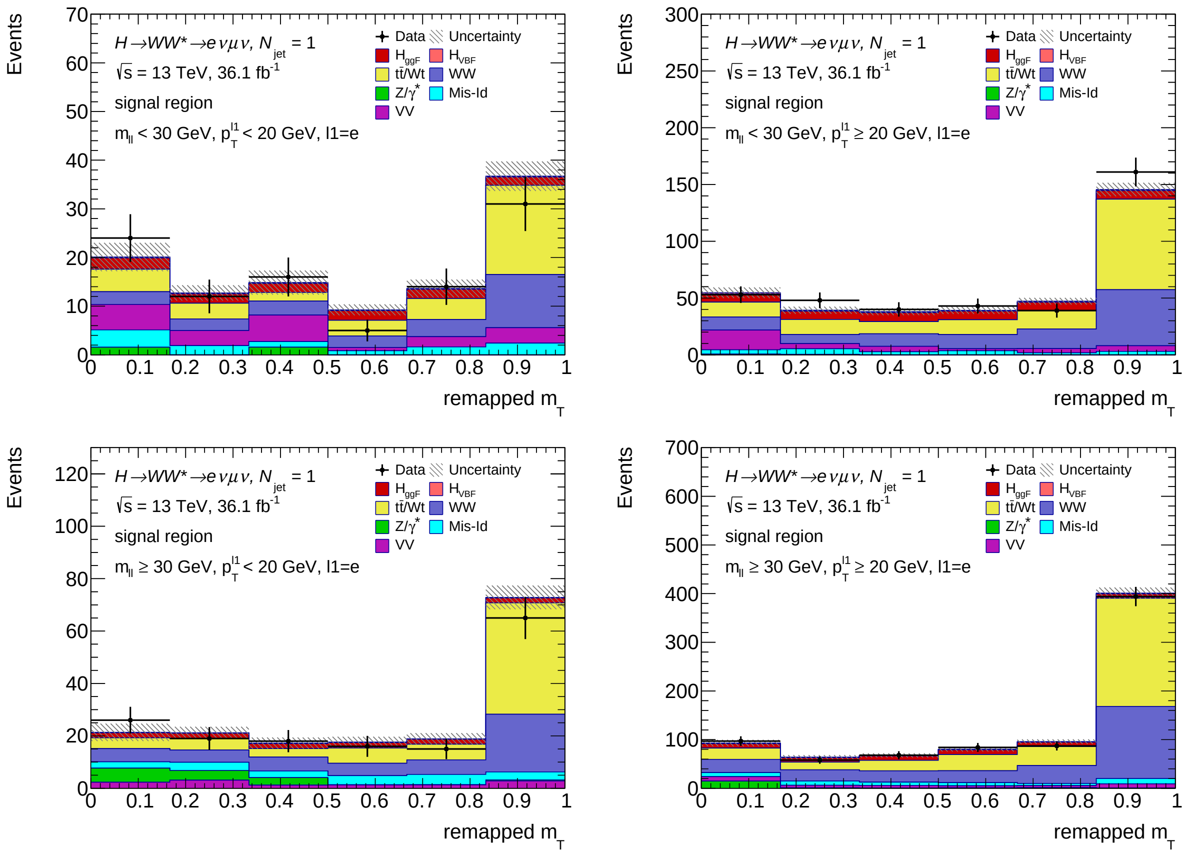

Figure C.3.: Remapped m_{T} post-fit distributions in the 1-jet signal region of the $H \to WW^*$ analysis. The distributions shown are those in the subregions where the subleadig lepton is an electron. The graphics on the left show the $p_{\mathrm{T}}^{\ell 1} < 20\,\mathrm{GeV}$ subregions, the ones on the right the subregions with $p_{\mathrm{T}}^{\ell 1} \geq 20\,\mathrm{GeV}$. At the top and bottom the regions with $m_{\ell\ell} < 30\,\mathrm{GeV}$ and $m_{\ell\ell} \geq 30\,\mathrm{GeV}$ respectively are show.

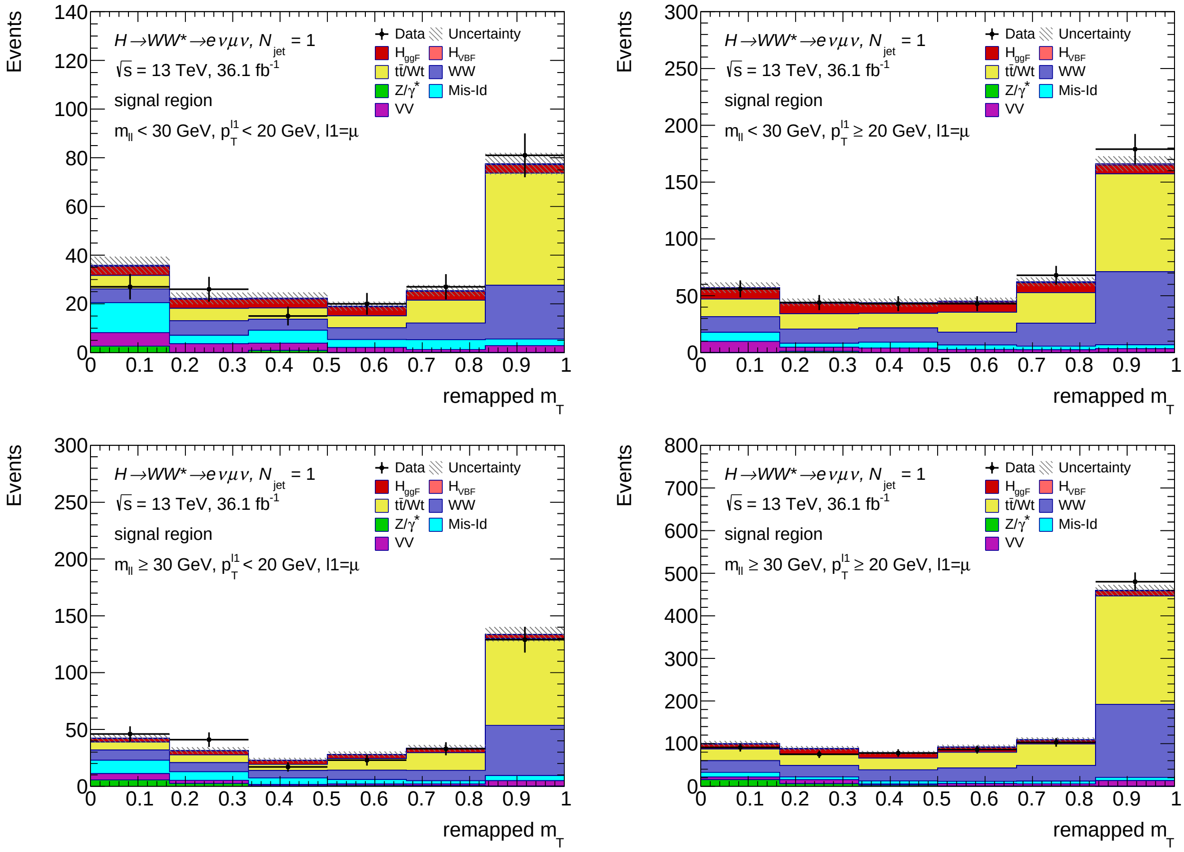

Figure C.4.: Remapped m_{T} post-fit distributions in the 1-jet signal region of the $H \to WW^*$ analysis. The distributions shown are those in the subregions where the subleadig lepton is a muon. The graphics on the left show the $p_{\mathrm{T}}^{\ell 1} < 20\,\mathrm{GeV}$ subregions, the ones on the right the subregions with $p_{\mathrm{T}}^{\ell 1} \geq 20\,\mathrm{GeV}$. At the top and bottom the regions with $m_{\ell\ell} < 30\,\mathrm{GeV}$ and $m_{\ell\ell} \geq 30\,\mathrm{GeV}$ respectively are show.

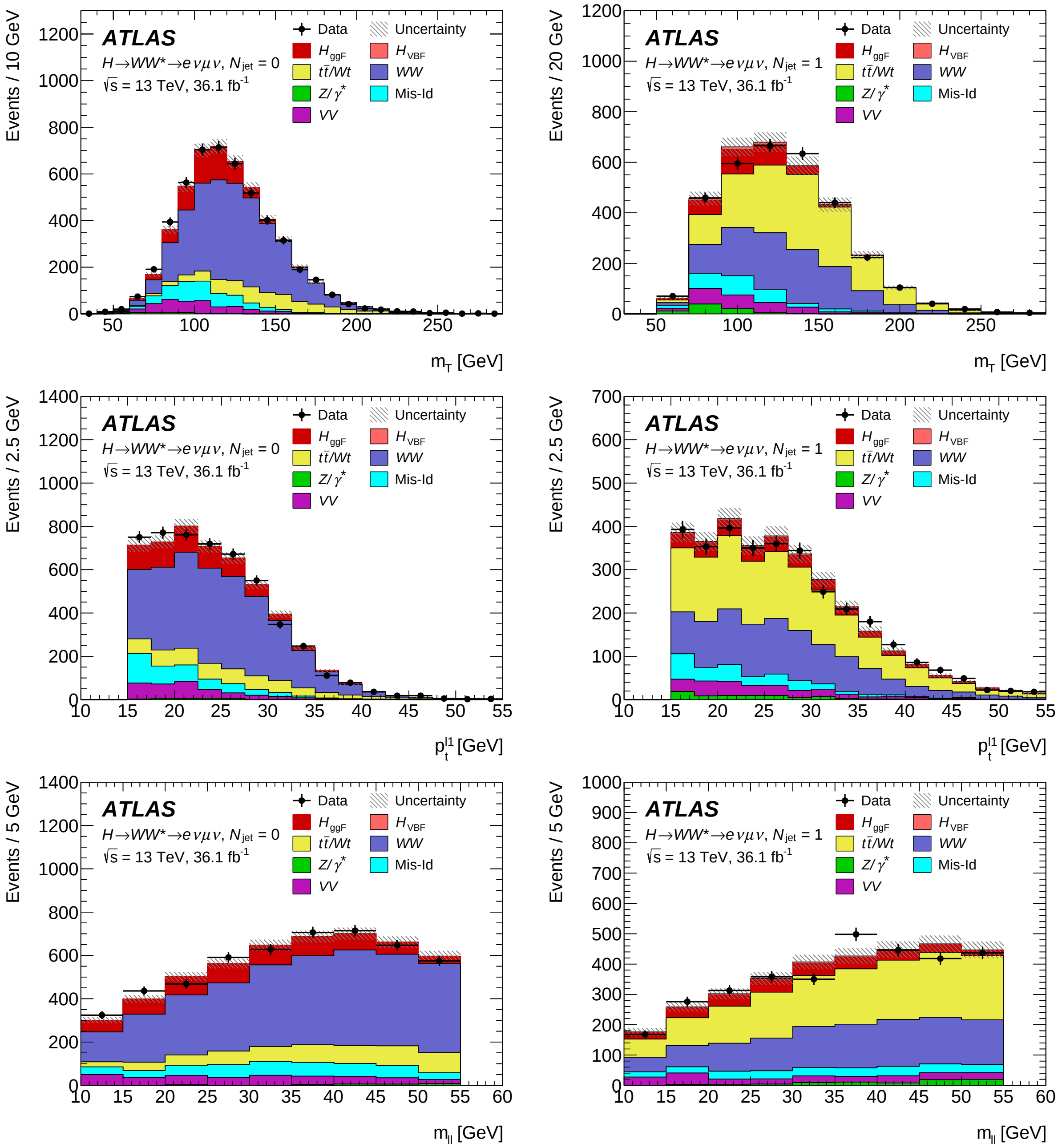

Figure C.5.: Post-fit distributions in the 0-jet and 1-jet signal regions of the $H \to WW^*$ analysis. The distributions shown are m_{T} (top), $p_{\mathrm{T}}^{\ell 1}$ (middle), $m_{\ell\ell}$ (bottom). The 0-jet signal region is shown on the left, the 1-jet signal region on the right. Uncertainties include statistical and systematic uncertainties as well as correlations between these. Published in Ref. [112].

Table C.2.: Detailed post-fit event yields in the 0-jet and 1-jet categories in the $H \to WW^*$ analysis. The values are obtained from a fit to only those categories with the VBF process fixed to the SM prediction. Uncertainties include all statistical and systematic uncertainties considered in the analysis.

	H_{ggF}	H_{VBF}	other H	$t\bar{t}/Wt$	WW	Z/γ^*	Mis-Id	VV	Data
CR, 0j, WW	104 ± 19	1.10 ± 0.13	10.0 ± 1.0	1180 ± 200	4900 ± 270	350 ± 50	600 ± 130	318 ± 33	7461
CR, 0j, Ztt	53 ± 9	0.55 ± 0.06	107 ± 4	71 ± 14	910 ± 60	41100 ± 600	2300 ± 600	970 ± 80	45463
CR, 0j, top	21 ± 4	0.45 ± 0.08	1.70 ± 0.32	2960 ± 170	240 ± 40	48 ± 16	89 ± 22	33 ± 7	3399
CR, 1j, WW	1.82 ± 0.35	0.196 ± 0.018	10.7 ± 0.5	5100 ± 600	3600 ± 700	200 ± 50	480 ± 120	350 ± 60	9784
CR, 1j, Ztt	28 ± 5	3.64 ± 0.20	39.3 ± 1.5	302 ± 33	300 ± 60	2530 ± 80	220 ± 60	147 ± 22	3571
CR, 1j, top	22 ± 5	2.18 ± 0.30	3.4 ± 0.5	18800 ± 400	220 ± 50	75 ± 14	320 ± 80	32 ± 6	19428
0-jet signal regions									
$m_{\ell\ell} < 30\,\mathrm{GeV}$, $p_{\mathrm{T}}^{\ell 1} < 20\,\mathrm{GeV}$, $\ell_1 = e$	42 ± 7	0.45 ± 0.05	0.30 ± 0.09	16 ± 4	103 ± 9	1.1 ± 0.4	26 ± 5	38 ± 4	238
$m_{\ell\ell} < 30\,\mathrm{GeV}$, $p_{\mathrm{T}}^{\ell 1} < 20\,\mathrm{GeV}$, $\ell_1 = \mu$	75 ± 13	0.72 ± 0.09	0.53 ± 0.05	34 ± 7	184 ± 14	0.11 ± 0.04	81 ± 12	55 ± 6	451
$m_{\ell\ell} < 30\,\mathrm{GeV}$, $p_{\mathrm{T}}^{\ell 1} \geq 20\,\mathrm{GeV}$, $\ell_1 = e$	78 ± 13	0.94 ± 0.11	0.88 ± 0.08	57 ± 11	303 ± 20	1.9 ± 0.6	30 ± 8	32 ± 4	518
$m_{\ell\ell} < 30\,\mathrm{GeV}$, $p_{\mathrm{T}}^{\ell 1} \geq 20\,\mathrm{GeV}$, $\ell_1 = \mu$	100 ± 18	1.10 ± 0.16	1.07 ± 0.09	66 ± 12	371 ± 26	0.15 ± 0.05	41 ± 9	41 ± 6	612
$m_{\ell\ell} \geq 30\,\mathrm{GeV}$, $p_{\mathrm{T}}^{\ell 1} < 20\,\mathrm{GeV}$, $\ell_1 = e$	41 ± 7	0.37 ± 0.04	0.37 ± 0.06	32 ± 7	165 ± 13	1.1 ± 0.6	37 ± 7	18.8 ± 2.7	329
$m_{\ell\ell} \geq 30\,\mathrm{GeV}$, $p_{\mathrm{T}}^{\ell 1} < 20\,\mathrm{GeV}$, $\ell_1 = \mu$	70 ± 12	0.66 ± 0.06	0.67 ± 0.06	61 ± 11	272 ± 19	7.1 ± 3.1	87 ± 14	30 ± 4	503
$m_{\ell\ell} \geq 30\,\mathrm{GeV}$, $p_{\mathrm{T}}^{\ell 1} \geq 20\,\mathrm{GeV}$, $\ell_1 = e$	103 ± 18	1.22 ± 0.17	1.40 ± 0.12	149 ± 28	740 ± 50	9.2 ± 3.1	67 ± 17	69 ± 7	1130
$m_{\ell\ell} \geq 30\,\mathrm{GeV}$, $p_{\mathrm{T}}^{\ell 1} \geq 20\,\mathrm{GeV}$, $\ell_1 = \mu$	129 ± 22	1.52 ± 0.16	1.59 ± 0.12	172 ± 32	880 ± 60	6.1 ± 2.7	78 ± 19	49 ± 7	1308
1-jet signal regions									
$m_{\ell\ell} < 30\,\mathrm{GeV}$, $p_{\mathrm{T}}^{\ell 1} < 20\,\mathrm{GeV}$, $\ell_1 = e$	11.7 ± 2.3	1.01 ± 0.06	0.44 ± 0.06	36 ± 5	25 ± 5	3.1 ± 1.5	11.5 ± 2.3	19.7 ± 2.9	102
$m_{\ell\ell} < 30\,\mathrm{GeV}$, $p_{\mathrm{T}}^{\ell 1} < 20\,\mathrm{GeV}$, $\ell_1 = \mu$	22 ± 4	2.04 ± 0.14	0.81 ± 0.06	76 ± 9	50.0 ± 10.0	3.6 ± 1.7	31 ± 4	18.1 ± 3.3	196
$m_{\ell\ell} < 30\,\mathrm{GeV}$, $p_{\mathrm{T}}^{\ell 1} \geq 20\,\mathrm{GeV}$, $\ell_1 = e$	45 ± 8	5.12 ± 0.34	1.66 ± 0.19	146 ± 16	110 ± 20	1.2 ± 0.6	20 ± 6	37 ± 5	384
$m_{\ell\ell} < 30\,\mathrm{GeV}$, $p_{\mathrm{T}}^{\ell 1} \geq 20\,\mathrm{GeV}$, $\ell_1 = \mu$	52 ± 9	5.7 ± 0.4	2.36 ± 0.17	172 ± 20	134 ± 24	1.06 ± 0.33	27 ± 9	26 ± 6	433
$m_{\ell\ell} \geq 30\,\mathrm{GeV}$, $p_{\mathrm{T}}^{\ell 1} < 20\,\mathrm{GeV}$, $\ell_1 = e$	11.6 ± 2.3	1.08 ± 0.07	0.55 ± 0.11	66 ± 8	47 ± 9	13 ± 4	19 ± 4	12.0 ± 2.7	159
$m_{\ell\ell} \geq 30\,\mathrm{GeV}$, $p_{\mathrm{T}}^{\ell 1} < 20\,\mathrm{GeV}$, $\ell_1 = \mu$	20 ± 4	1.88 ± 0.11	0.96 ± 0.07	122 ± 14	85 ± 16	10 ± 5	36 ± 6	17 ± 4	289
$m_{\ell\ell} \geq 30\,\mathrm{GeV}$, $p_{\mathrm{T}}^{\ell 1} \geq 20\,\mathrm{GeV}$, $\ell_1 = e$	55 ± 10	6.4 ± 0.4	2.38 ± 0.15	360 ± 40	280 ± 50	19 ± 6	46 ± 11	36 ± 7	788
$m_{\ell\ell} \geq 30\,\mathrm{GeV}$, $p_{\mathrm{T}}^{\ell 1} \geq 20\,\mathrm{GeV}$, $\ell_1 = \mu$	67 ± 12	7.3 ± 0.5	3.00 ± 0.26	420 ± 50	320 ± 60	25 ± 7	44 ± 14	42 ± 7	913

D. Additional Distributions Regarding the VBF $H \to WW^*$ Analysis

In Fig. D.1 distributions are shown for variables used in the BDT for the VBF targeted signal regions in the $H \to WW^*$ analysis. The remaining BDT input variables are shown in Fig. 4.8 in Sec. 4.4.2. The overlaid VBF signal distributions are scaled to the same integral as the stacked entries. Distributions are shown after all hard selections for the VBF signal region are applied. Stacked estimates are normalized to their prediction with exception of top, and Z/γ^* which are scaled to measured data in control regions. Uncertainties shown include statistical uncertainties only. The yellow or hatched gray bands represent the statistical uncertainties of the modeled contributions. Red arrows in the bottom panels indicate the direction of ratio points outside the range shown.

Post-fit distributions for the dijet rapidity separation Δy_{jj} and the dijet invariant mass m_{jj} are shown in Fig. D.2. Here, the uncertainty bands include statistical and systematic uncertainties as well as correlations between these.

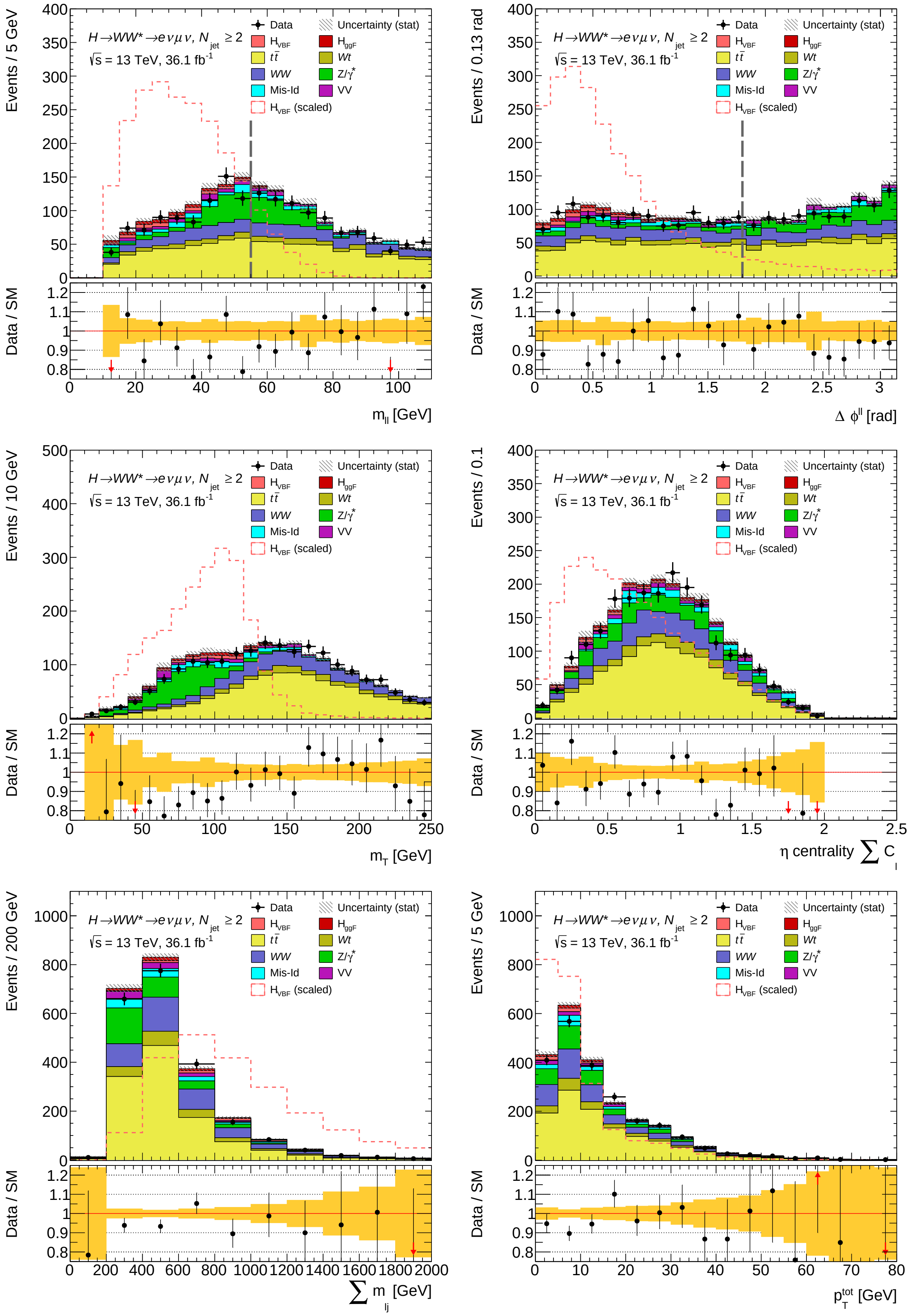

Figure D.1.: Pre-fit distributions of variables used in the VBF BDT in the $H \to WW^*$ analysis. Uncertainties shown include statistical uncertainties only.

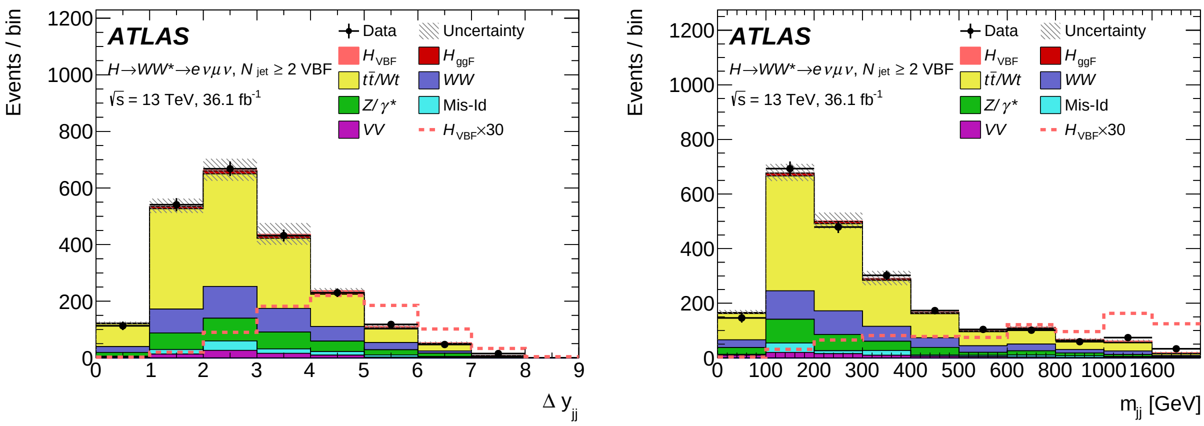

Figure D.2.: Post-fit distributions of Δy_{jj} and m_{jj} in the $\geq$ 2-jet VBF signal region of the $H \to WW^*$ analysis. The hatched uncertainty bands include statistical and systematic uncertainties as well as correlations thereof. Published in Ref. [112].

List of Figures

List of Tables

Bibliography

[1] **ATLAS Collaboration**, "Observation of a new particle in the search for the Standard Model Higgs boson with the ATLAS detector at the LHC", *Physics Letters B* **716** no. 1, (2012) 1 – 29. `http://www.sciencedirect.com/science/article/pii/S037026931200857X`.

[2] **CMS Collaboration**, "Observation of a new boson at a mass of 125 GeV with the CMS experiment at the LHC", *Physics Letters B* **716** no. 1, (2012) 30 – 61. `http://www.sciencedirect.com/science/article/pii/S0370269312008581`.

[3] P. W. Higgs, "Broken Symmetries and the Masses of Gauge Bosons", *Phys. Rev. Lett.* **13** (Oct, 1964) 508–509. `http://link.aps.org/doi/10.1103/PhysRevLett.13.508`.

[4] P. W. Higgs, "Spontaneous Symmetry Breakdown without Massless Bosons", *Phys. Rev.* **145** (May, 1966) 1156–1163. `http://link.aps.org/doi/10.1103/PhysRev.145.1156`.

[5] **ATLAS Collaboration and CMS Collaboration**, "Combined Measurement of the Higgs Boson Mass in pp Collisions at $\sqrt{s} = 7$ and 8 TeV with the ATLAS and CMS Experiments", *Phys. Rev. Lett.* **114** (May, 2015) 191803. `http://link.aps.org/doi/10.1103/PhysRevLett.114.191803`.

[6] G. Apollinari *et al.*, *High-Luminosity Large Hadron Collider (HL-LHC): Technical Design Report V. 0.1*. CERN Yellow Reports: Monographs. CERN, Geneva, 2017. `http://cds.cern.ch/record/2284929`.

[7] A. Einstein, "Die Grundlage der allgemeinen Relativitätstheorie", *Annalen der Physik* **354** no. 7, (1916) 769–822, `https://onlinelibrary.wiley.com/doi/pdf/10.1002/andp.19163540702`.

[8] NobelPrize.org, "The Nobel Prize in Physics 2007", Aug, 2019. `https://www.nobelprize.org/prizes/physics/2007/summary/`.

[9] T. Haberer, J. Debus, H. Eickhoff, O. Jäkel, D. Schulz-Ertner, and U. Weber, "The hei-
delberg ion therapy center", *Radiotherapy and Oncology* **73** (2004) S186 – S190, `http://www.sciencedirect.com/science/article/pii/S016781400480046X`. Carbon-Ion Theraphy.

[10] T. J. Berners-Lee, "Information management: a proposal", CERN-DD-89-001-OC, CERN, Geneva, Mar, 1989. `http://cds.cern.ch/record/369245`.

[11] M. Planck, "Ueber das Gesetz der Energieverteilung im Normalspectrum", *Annalen der Physik* **309** no. 3, (1901) 553–563. `https://onlinelibrary.wiley.com/doi/abs/10.1002/andp.19013090310`.

[12] A. Einstein, "Über einen die Erzeugung und Verwandlung des Lichtes betreffenden heuristischen Gesichtspunkt", *Annalen der Physik* **322** no. 6, (1905) 132–148. `https://onlinelibrary.wiley.com/doi/abs/10.1002/andp.19053220607`.

[13] NobelPrize.org, "The Nobel Prize in Physics 1918", Aug, 2019. `https://www.nobelprize.org/prizes/physics/1918/summary/`.

[14] NobelPrize.org, "The Nobel Prize in Physics 1921", Aug, 2019. `https://www.nobelprize.org/prizes/physics/1921/summary/`.

[15] A. Einstein, "Zur Elektrodynamik bewegter Körper", *Annalen der Physik* **322** no. 10, (1905) 891–921. `https://onlinelibrary.wiley.com/doi/abs/10.1002/andp.19053221004`.

[16] E. Fermi, "Versuch einer Theorie der β-Strahlen. I", *Zeitschrift für Physik* **88** no. 3, (Mar, 1934) 161–177. `https://doi.org/10.1007/BF01351864`.

[17] S. L. Glashow, "Partial-symmetries of weak interactions", *Nuclear Physics* **22** no. 4, (1961) 579 – 588. `http://www.sciencedirect.com/science/article/pii/0029558261904692`.

[18] A. Salam and J. Ward, "Electromagnetic and weak interactions", *Physics Letters* **13** no. 2, (1964) 168 – 171. `http://www.sciencedirect.com/science/article/pii/0031916364907115`.

[19] S. Weinberg, "A Model of Leptons", *Phys. Rev. Lett.* **19** (Nov, 1967) 1264–1266. `http://link.aps.org/doi/10.1103/PhysRevLett.19.1264`.

[20] F. J. Hasert *et al.*, "Observation of Neutrino Like Interactions Without Muon Or Electron in the Gargamelle Neutrino Experiment", *Phys. Lett.* **B46** (1973) 138–140. [,5.15(1973)].

[21] **UA1 Collaboration**, "Experimental Observation of Lepton Pairs of Invariant Mass Around 95 GeV/c^2 at the CERN SPS Collider", *Phys. Lett.* **126B** (1983) 398–410. [,7.55(1983)].

[22] **UA2 Collaboration**, "Evidence for $Z^0 \rightarrow e^+e^-$ at the CERN anti-p p Collider", *Phys. Lett.* **129B** (1983) 130–140. [,7.69(1983)].

[23] **UA1 Collaboration**, "Experimental observation of isolated large transverse energy electrons with associated missing energy at s=540 GeV", *Physics Letters B* **122** no. 1, (1983) 103 – 116. `http://www.sciencedirect.com/science/article/pii/0370269383911772`.

[24] NobelPrize.org, "The Nobel Prize in Physics 1979", Aug, 2019. `https://www.nobelprize.org/prizes/physics/1979/summary/`.

[25] NobelPrize.org, "The Nobel Prize in Physics 1983", Aug, 2019. `https://www.nobelprize.org/prizes/physics/1983/summary/`.

[26] F. Englert and R. Brout, "Broken Symmetry and the Mass of Gauge Vector Mesons", *Phys. Rev. Lett.* **13** (Aug, 1964) 321–323. `http://link.aps.org/doi/10.1103/PhysRevLett.13.321`.

[27] G. S. Guralnik *et al.*, "Global Conservation Laws and Massless Particles", *Phys. Rev. Lett.* **13** (Nov, 1964) 585–587. `https://link.aps.org/doi/10.1103/PhysRevLett.13.585`.

[28] P. W. Anderson, "Plasmons, Gauge Invariance, and Mass", *Phys. Rev.* **130** (Apr, 1963) 439–442. `https://link.aps.org/doi/10.1103/PhysRev.130.439`.

[29] NobelPrize.org, "The Nobel Prize in Physics 2013", Aug, 2019. `https://www.nobelprize.org/prizes/physics/2013/summary/`.

[30] **ATLAS Collaboration**, "Observation of Higgs boson production in association with a top quark pair at the LHC with the ATLAS detector", *Phys. Lett.* **B784** (2018) 173–191, `arXiv:1806.00425 [hep-ex]`.

[31] **CMS Collaboration**, "Observation of $\mathrm{t\bar{t}H}$ production", *Phys. Rev. Lett.* **120** no. 23, (2018) 231801, `arXiv:1804.02610 [hep-ex]`.

[32] **ATLAS Collaboration**, "Observation of $H \rightarrow b\bar{b}$ decays and VH production with the ATLAS detector", *Physics Letters B* **786** (2018) 59 – 86. `http://www.sciencedirect.com/science/article/pii/S0370269318307056`.

[33] **CMS Collaboration**, "Observation of Higgs boson decay to bottom quarks", *Phys. Rev. Lett.* **121** no. 12, (2018) 121801, `arXiv:1808.08242 [hep-ex]`.

[34] T. Kajita *et al.*, "Establishing atmospheric neutrino oscillations with Super-Kamiokande", *Nuclear Physics B* **908** (2016) 14 – 29. `http://www.sciencedirect.com/science/article/pii/S0550321316300554`.

[35] Y. Sofue, *Mass Distribution and Rotation Curve in the Galaxy*, pp. 985–1037. Springer Netherlands, Dordrecht, 2013. https://doi.org/10.1007/978-94-007-5612-0_19.

[36] **ATLAS Collaboration**, "Measurements of the Higgs boson production and decay rates and coupling strengths using pp collision data at $\sqrt{s} = 7$ and 8 TeV in the ATLAS experiment", *Eur. Phys. J.* **C76** no. 1, (2016) 6, arXiv:1507.04548 [hep-ex].

[37] **The Gfitter Group**, J. Haller *et al.*, "Update of the global electroweak fit and constraints on two-Higgs-doublet models", *The European Physical Journal C* **78** no. 8, (Aug, 2018) 675. https://doi.org/10.1140/epjc/s10052-018-6131-3.

[38] D. J. Griffiths, *Introduction to elementary particles.* TextBook Physics. Wiley, New York, NY, 1987. https://cds.cern.ch/record/1260972.

[39] F. Halzen and A. D. Martin, *Quarks and Leptons: An Introductory Course in Modern Particle Physics.* Wiley (1984), New York, NY, 1984.

[40] M. E. Peskin and D. V. Schroeder, *An introduction to quantum field theory.* Westview, Boulder, CO, 1995. https://cds.cern.ch/record/257493.

[41] E. Noether, "Invariante Variationsprobleme", *Nachrichten d. Königlichen Gesellschaft d. Wissenschaften zu Göttingen, Mathematisch-Physikalische Klasse* (1918) 235–257.

[42] **Particle Data Group**, M. Tanabashi *et al.*, "Review of Particle Physics", *Phys. Rev. D* **98** (Aug, 2018) 030001. https://link.aps.org/doi/10.1103/PhysRevD.98.030001.

[43] M. Gell-Mann, "A schematic model of baryons and mesons", *Physics Letters* **8** no. 3, (1964) 214 – 215. http://www.sciencedirect.com/science/article/pii/S0031916364920013.

[44] G. Zweig, "An SU_3 model for strong interaction symmetry and its breaking; Version 1", CERN-TH-401, CERN, Geneva, Jan, 1964. http://cds.cern.ch/record/352337.

[45] M. Szleper, "The Higgs boson and the physics of WW scattering before and after Higgs discovery", arXiv:1412.8367 [hep-ph].

[46] H. Yukawa, "On the Interaction of Elementary Particles I", *Proc. Phys. Math. Soc. Jap.* **17** (1935) 48–57. [Prog. Theor. Phys. Suppl.1,1(1935)].

[47] A. Djouadi, "The Anatomy of electro-weak symmetry breaking. I: The Higgs boson in the standard model", *Phys. Rept.* **457** (2008) 1–216, arXiv:hep-ph/0503172 [hep-ph].

[48] N. Cabibbo, "Unitary Symmetry and Leptonic Decays", *Phys. Rev. Lett.* **10** (Jun, 1963) 531–533.
`http://link.aps.org/doi/10.1103/PhysRevLett.10.531`.

[49] M. Kobayashi and T. Maskawa, "CP-Violation in the Renormalizable Theory of Weak Interaction", *Progress of Theoretical Physics* **49** no. 2, (1973) 652–657,
`http://ptp.oxfordjournals.org/content/49/2/652.full.pdf+html`.

[50] Y. L. Dokshitzer, "Calculation of the Structure Functions for Deep Inelastic Scattering and e+ e- Annihilation by Perturbation Theory in Quantum Chromodynamics.", *Sov. Phys. JETP* **46** (1977) 641–653. [Zh. Eksp. Teor. Fiz.73,1216(1977)].

[51] V. Gribov and L. Lipatov, "Deep inelastic electron scattering in perturbation theory", *Physics Letters B* **37** no. 1, (1971) 78 – 80. `http://www.sciencedirect.com/science/article/pii/0370269371905764`.

[52] G. Altarelli and G. Parisi, "Asymptotic Freedom in Parton Language", *Nucl. Phys.* **B126** (1977) 298–318.

[53] R. K. Ellis, W. J. Stirling, and B. R. Webber, *QCD and collider physics*. Cambridge monographs on particle physics, nuclear physics, and cosmology. Cambridge University Press, Cambridge, 2003.
`https://cds.cern.ch/record/318585`. Photography by S. Vascotto.

[54] S. Höche, "Introduction to parton-shower event generators", in *Proceedings, Theoretical Advanced Study Institute in Elementary Particle Physics: Journeys Through the Precision Frontier: Amplitudes for Colliders (TASI 2014): Boulder, Colorado, June 2-27, 2014*, pp. 235–295. 2015.
`arXiv:1411.4085 [hep-ph]`.

[55] A. Ortiz and L. V. Palomo, "Universality of the underlying event in *pp* collisions", *Phys. Rev. D* **96** (Dec, 2017) 114019.
`https://link.aps.org/doi/10.1103/PhysRevD.96.114019`.

[56] M. Cacciari, G. P. Salam, and G. Soyez, "The anti-ktjet clustering algorithm", *Journal of High Energy Physics* **2008** no. 04, (Apr, 2008) 063–063. `https://doi.org/10.1088%2F1126-6708%2F2008%2F04%2F063`.

[57] T. Sjostrand *et al.*, "A Brief Introduction to PYTHIA 8.1", *Comput. Phys. Commun.* **178** (2008) 852–867, `arXiv:0710.3820 [hep-ph]`.

[58] **ATLAS Collaboration**, "Summary of ATLAS Pythia 8 tunes", ATL-PHYS-PUB-2012-003, CERN, Geneva, Aug, 2012.
`https://cds.cern.ch/record/1474107`.

[59] **ATLAS Collaboration**, "Standard Model Summary Plots Spring 2019", ATL-PHYS-PUB-2019-010, CERN, Geneva, Mar, 2019. `http://cds.cern.ch/record/2668559`.

[60] **LHC Higgs Cross Section Working Group**, D. de Florian *et al.*, *Handbook of LHC Higgs Cross Sections: 4. Deciphering the Nature of the Higgs Sector*. CERN Yellow Reports: Monographs. Oct, 2016. `http://cds.cern.ch/record/2227475`.

[61] **ATLAS Collaboration**, "Cross-section measurements of the Higgs boson decaying into a pair of τ-leptons in proton-proton collisions at $\sqrt{s} = 13$ TeV with the ATLAS detector", *Phys. Rev. D* **99** (Apr, 2019) 072001. `https://link.aps.org/doi/10.1103/PhysRevD.99.072001`.

[62] **CMS Collaboration**, "Observation of the Higgs boson decay to a pair of τ leptons with the CMS detector", *Physics Letters B* **779** (2018) 283 – 316. `http://www.sciencedirect.com/science/article/pii/S0370269318301035`.

[63] **ATLAS Collaboration**, "Observation of $H \rightarrow b\bar{b}$ decays and VH production with the ATLAS detector", *Physics Letters B* **786** (2018) 59 – 86. `http://www.sciencedirect.com/science/article/pii/S0370269318307056`.

[64] **CMS Collaboration**, "Observation of Higgs Boson Decay to Bottom Quarks", *Phys. Rev. Lett.* **121** (Sep, 2018) 121801. `https://link.aps.org/doi/10.1103/PhysRevLett.121.121801`.

[65] **ATLAS Collaboration**, "Measurement of the Higgs boson mass in the $H \rightarrow ZZ^* \rightarrow 4\ell$ and $H \rightarrow \gamma\gamma$ channels with $\sqrt{s} = 13$ TeV pp collisions using the ATLAS detector", *Phys. Lett.* **B784** (2018) 345–366, `arXiv:1806.00242 [hep-ex]`.

[66] **CMS Collaboration**, "Measurements of properties of the Higgs boson decaying into the four-lepton final state in pp collisions at $\sqrt{s} = 13$ TeV.", *JHEP* **11** no. CMS-HIG-16-041. CMS-HIG-16-041-003, (Jun, 2017) 047. 55 p. `https://cds.cern.ch/record/2272260`.

[67] R. Bock and W. Krischer, *The Data Analysis BriefBook*. Accelerator Physics. Springer Berlin Heidelberg, 2013.

[68] G. Cowan, K. Cranmer, E. Gross, and O. Vitells, "Asymptotic formulae for likelihood-based tests of new physics", *The European Physical Journal C* **71** no. 2, (Feb, 2011) 1554. `https://doi.org/10.1140/epjc/s10052-011-1554-0`.

[69] S. S. Wilks, "The Large-Sample Distribution of the Likelihood Ratio for Testing Composite Hypotheses", *Ann. Math. Statist.* **9** no. 1, (03, 1938) 60–62. `https://doi.org/10.1214/aoms/1177732360`.

[70] W. Verkerke and D. P. Kirkby, "The RooFit toolkit for data modeling", *eConf* **C0303241** (2003) MOLT007, `arXiv:physics/0306116 [physics]`. [,186(2003)].

[71] **ROOT**, K. Cranmer *et al.*, "HistFactory: A tool for creating statistical models for use with RooFit and RooStats", .

[72] R. Barlow and C. Beeston, "Fitting using finite Monte Carlo samples", *Computer Physics Communications* **77** no. 2, (1993) 219 – 228. `http://www.sciencedirect.com/science/article/pii/001046559390005W`.

[73] L. Evans and P. Bryant, "LHC Machine", *JINST* **3** (2008) S08001.

[74] "LEP Design Report: Vol.2. The LEP Main Ring", `https://cds.cern.ch/record/102083`.

[75] E. Mobs, "The CERN accelerator complex", `https://cds.cern.ch/record/2197559`.

[76] **ATLAS Collaboration**, "Luminosity Public Results Run 2." Website, 2018. `https://twiki.cern.ch/twiki/bin/view/AtlasPublic/LuminosityPublicResultsRun2?rev=64`.

[77] J. Wenninger, "Approaching the Nominal Performance at the LHC", in *Proceedings, 8th International Particle Accelerator Conference (IPAC 2017): Copenhagen, Denmark, May 14-19, 2017*.

[78] "CERN Annual report 2017", Tech. Rep., CERN, Geneva, 2018. `http://cds.cern.ch/record/2624296`.

[79] **ATLAS Collaboration**, "The ATLAS Experiment at the CERN Large Hadron Collider", *JINST* **3** (2008) S08003.

[80] **LHCb Collaboration**, "The LHCb Detector at the LHC", *Journal of Instrumentation* **3** no. 08, (Aug, 2008) S08005–S08005. `https://doi.org/10.1088%2F1748-0221%2F3%2F08%2Fs08005`.

[81] **ALICE Collaboration**, "The ALICE experiment at the CERN LHC", *Journal of Instrumentation* **3** no. 08, (Aug, 2008) S08002–S08002. `https://doi.org/10.1088%2F1748-0221%2F3%2F08%2Fs08002`.

[82] **CMS Collaboration**, "The CMS experiment at the CERN LHC", *JINST* **3** (2008) S08004.

[83] **ATLAS Collaboration**, "Production and integration of the ATLAS Insertable B-Layer", *JINST* **13** no. 05, (2018) T05008, `arXiv:1803.00844 [physics.ins-det]`.

[84] **ATLAS Collaboration**, A. R. Martínez, "The Run-2 ATLAS Trigger System", *J. Phys. Conf. Ser.* **762** no. 1, (2016) 012003.

[85] **ATLAS Collaboration**, "The ATLAS Inner Detector commissioning and calibration", *The European Physical Journal C* **70** no. 3, (2010) 787–821. `http://dx.doi.org/10.1140/epjc/s10052-010-1366-7`.

[86] **ATLAS Collaboration**, M. Capeans, G. Darbo, K. Einsweiller, M. Elsing, T. Flick, M. Garcia-Sciveres, C. Gemme, H. Pernegger, O. Rohne, and R. Vuillermet, "ATLAS Insertable B-Layer Technical Design Report", CERN-LHCC-2010-013. ATLAS-TDR-19, Sep, 2010. `http://cds.cern.ch/record/1291633`.

[87] G. Avoni *et al.*, "The new LUCID-2 detector for luminosity measurement and monitoring in ATLAS", *Journal of Instrumentation* **13** no. 07, (Jul, 2018) P07017–P07017. `https://doi.org/10.1088%2F1748-0221%2F13%2F07%2Fp07017`.

[88] **ATLAS Collaboration**, "The ATLAS Simulation Infrastructure", *The European Physical Journal C* **70** no. 3, (Dec, 2010) 823–874. `https://doi.org/10.1140/epjc/s10052-010-1429-9`.

[89] S. Agostinelli *et al.*, "Geant4—a simulation toolkit", *Nuclear Instruments and Methods in Physics Research Section A: Accelerators, Spectrometers, Detectors and Associated Equipment* **506** no. 3, (2003) 250 – 303. `http://www.sciencedirect.com/science/article/pii/S0168900203013688`.

[90] **ATLAS Collaboration**, "Performance of the ATLAS track reconstruction algorithms in dense environments in LHC Run 2", *The European Physical Journal C* **77** no. 10, (Oct, 2017) 673. `https://doi.org/10.1140/epjc/s10052-017-5225-7`.

[91] **ATLAS Collaboration**, "Reconstruction of primary vertices at the ATLAS experiment in Run 1 proton–proton collisions at the LHC", *Eur. Phys. J.* **C77** no. 5, (2017) 332, `arXiv:1611.10235 [physics.ins-det]`.

[92] **ATLAS Collaboration**, "Topological cell clustering in the ATLAS calorimeters and its performance in LHC Run 1", *Eur. Phys. J.* **C77** (2017) 490, `arXiv:1603.02934 [hep-ex]`.

[93] **ATLAS Collaboration**, "Jet reconstruction and performance using particle flow with the ATLAS Detector", *The European Physical Journal C* **77** no. 7, (Jul, 2017) 466. `https://doi.org/10.1140/epjc/s10052-017-5031-2`.

[94] **ATLAS Collaboration**, "Jet energy scale measurements and their systematic uncertainties in proton-proton collisions at $\sqrt{s} = 13$ TeV with the ATLAS detector", *Phys. Rev. D* **96** (Oct, 2017) 072002. https://link.aps.org/doi/10.1103/PhysRevD.96.072002.

[95] **ATLAS Collaboration**, "Jet energy resolution in proton-proton collisions at $\sqrt{s} = 7$ TeV recorded in 2010 with the ATLAS detector", *Eur. Phys. J.* **C73** no. 3, (2013) 2306, arXiv:1210.6210 [hep-ex].

[96] **ATLAS Collaboration**, "Measurements of b-jet tagging efficiency with the ATLAS detector using $t\bar{t}$ events at $\sqrt{s} = 13$ TeV", *JHEP* **08** (2018) 089, arXiv:1805.01845 [hep-ex].

[97] **ATLAS Collaboration**, "Muon reconstruction performance of the ATLAS detector in proton–proton collision data at $\sqrt{s}$ =13 TeV", *Eur. Phys. J.* **C76** no. 5, (2016) 292, arXiv:1603.05598 [hep-ex].

[98] **ATLAS Collaboration**, "Measurement of the tau lepton reconstruction and identification performance in the ATLAS experiment using *pp* collisions at $\sqrt{s} = 13$ TeV", ATLAS-CONF-2017-029, CERN, Geneva, May, 2017. http://cds.cern.ch/record/2261772.

[99] **ATLAS Collaboration**, "Electron reconstruction and identification in the ATLAS experiment using the 2015 and 2016 LHC proton-proton collision data at $\sqrt{s} = 13$ TeV", *Eur. Phys. J.* **C79** no. 8, (2019) 639, arXiv:1902.04655 [physics.ins-det].

[100] **ATLAS Collaboration**, "Electron and photon energy calibration with the ATLAS detector using 2015–2016 LHC proton-proton collision data", *JINST* **14** no. 03, (2019) P03017, arXiv:1812.03848 [hep-ex].

[101] T. G. Cornelissen *et al.*, "The global χ^2 track fitter in ATLAS", *J. Phys. Conf. Ser.* **119** (2008) 032013.

[102] **ATLAS Collaboration**, "Improved electron reconstruction in ATLAS using the Gaussian Sum Filter-based model for bremsstrahlung", ATLAS-CONF-2012-047, CERN, Geneva, May, 2012. https://cds.cern.ch/record/1449796.

[103] **ATLAS Collaboration**, "Observation of electroweak production of a same-sign W boson pair in association with two jets in *pp* collisions at $\sqrt{s} = 13$ TeV with the ATLAS detector", arXiv:1906.03203 [hep-ex].

[104] **ATLAS Collaboration**, "Athena", https://doi.org/10.5281/zenodo.2641997.

[105] **ATLAS Collaboration**, "Performance of the ATLAS track reconstruction algorithms in dense environments in LHC Run 2", *The European Physical Journal C* **77** no. 10, (Oct, 2017) 673. https://doi.org/10.1140/epjc/s10052-017-5225-7.

[106] **ATLAS Collaboration**, "Search for new phenomena in events with same-charge leptons and b-jets in pp collisions at $\sqrt{s} = 13$ TeV with the ATLAS detector", *JHEP* **12** (2018) 039, arXiv:1807.11883 [hep-ex].

[107] A. Hoecker *et al.*, "TMVA: Toolkit for Multivariate Data Analysis", *PoS* **ACAT** (2007) 040, arXiv:physics/0703039.

[108] **ATLAS Collaboration**, "IBL Efficiency and Single Point Resolution in Collision Events", ATL-INDET-PUB-2016-001, CERN, Geneva, Aug, 2016. http://cds.cern.ch/record/2203893.

[109] M. Muskinja, "Search for new physics processes with same charge leptons in the final state with the ATLAS detector using proton–proton collisions at $\sqrt{s} = 13$ TeV. Iskanje procesov nove fizike s pari enako nabitih leptonov v končnem stanju z detektorjem ATLAS s trki protonov pri energiji $\sqrt{s} = 13$ TeV", Aug, 2018. http://cds.cern.ch/record/2643902. Presented 20 Sep 2018.

[110] P. Calafiura *et al.*, "TrackML: A High Energy Physics Particle Tracking Challenge", in *Proceedings, 14th International Conference on e-Science: Amsterdam, Netherlands, October 29-November 1, 2018*, p. 344. 2018.

[111] **ATLAS Collaboration**, "Performance of missing transverse momentum reconstruction with the ATLAS detector using proton-proton collisions at $\sqrt{s} = 13$ TeV", *Eur. Phys. J.* **C78** no. 11, (2018) 903, arXiv:1802.08168 [hep-ex].

[112] **ATLAS Collaboration**, "Measurements of gluon-gluon fusion and vector-boson fusion Higgs boson production cross-sections in the $H \to WW^* \to e\nu\mu\nu$ decay channel in pp collisions at $\sqrt{s} = 13$ TeV with the ATLAS detector", *Phys. Lett.* **B789** (2019) 508–529, arXiv:1808.09054 [hep-ex]. Additional Figures are available at https://atlas.web.cern.ch/Atlas/GROUPS/PHYSICS/PAPERS/HIGG-2016-07/.

[113] **ATLAS Collaboration**, "Performance of pile-up mitigation techniques for jets in pp collisions at $\sqrt{s} = 8$ TeV using the ATLAS detector", *The European Physical Journal C* **76** no. 11, (Oct, 2016) 581. https://doi.org/10.1140/epjc/s10052-016-4395-z.

[114] **ATLAS Collaboration**, "Identification and rejection of pile-up jets at high pseudorapidity with the ATLAS detector", *The European Physical Journal C* **77** no. 9, (Sep, 2017) 580. https://doi.org/10.1140/epjc/s10052-017-5081-5.

[115] **ATLAS Collaboration**, "Observation and measurement of Higgs boson decays to WW^* with the ATLAS detector", *Phys. Rev. D* **92** (Jul, 2015) 012006. http://link.aps.org/doi/10.1103/PhysRevD.92.012006.

[116] K. Hamilton *et al.*, "NNLOPS simulation of Higgs boson production", *JHEP* **10** (2013) 222, arXiv:1309.0017 [hep-ph].

[117] J. M. Campbell *et al.*, "NLO Higgs Boson Production Plus One and Two Jets Using the POWHEG BOX, MadGraph4 and MCFM", *JHEP* **07** (2012) 092, arXiv:1202.5475 [hep-ph].

[118] S. Catani and M. Grazzini, "An NNLO subtraction formalism in hadron collisions and its application to Higgs boson production at the LHC", *Phys. Rev. Lett.* **98** (2007) 222002, arXiv:hep-ph/0703012 [hep-ph].

[119] J. Butterworth *et al.*, "PDF4LHC recommendations for LHC Run II", *Journal of Physics G: Nuclear and Particle Physics* **43** no. 2, (Jan, 2016) 023001. https://doi.org/10.1088%2F0954-3899%2F43%2F2%2F023001.

[120] P. Nason and C. Oleari, "NLO Higgs boson production via vector-boson fusion matched with shower in POWHEG", *JHEP* **02** (2010) 037, arXiv:0911.5299 [hep-ph].

[121] K. Hamilton *et al.*, "Finite quark-mass effects in the NNLOPS POWHEG+MiNLO Higgs generator", *JHEP* **05** (2015) 140, arXiv:1501.04637 [hep-ph].

[122] **ATLAS Collaboration**, "Measurement of the Z/γ^* boson transverse momentum distribution in pp collisions at $\sqrt{s} = 7$ TeV with the ATLAS detector", *JHEP* **09** (2014) 145, arXiv:1406.3660 [hep-ex].

[123] A. Djouadi *et al.*, "HDECAY: a program for Higgs boson decays in the Standard Model and its supersymmetric extension", *Computer Physics Communications* **108** no. 1, (1998) 56 – 74. http://www.sciencedirect.com/science/article/pii/S0010465597001239.

[124] A. Djouadi *et al.*, "HDECAY: Twenty$_{++}$ years after", *Comput. Phys. Commun.* **238** (2019) 214–231, arXiv:1801.09506 [hep-ph].

[125] **LHC Higgs Cross Section Working Group**, S. Heinemeyer *et al.*, *Handbook of LHC Higgs Cross Sections: 3. Higgs Properties: Report of the LHC Higgs Cross Section Working Group*. CERN Yellow Reports: Monographs. Jul, 2013. https://cds.cern.ch/record/1559921.

[126] C. Anastasiou *et al.*, "Higgs Boson Gluon-Fusion Production in QCD at Three Loops", *Phys. Rev. Lett.* **114** (2015) 212001, `arXiv:1503.06056 [hep-ph]`.

[127] C. Anastasiou *et al.*, "High precision determination of the gluon fusion Higgs boson cross-section at the LHC", *JHEP* **05** (2016) 058, `arXiv:1602.00695 [hep-ph]`.

[128] S. Actis *et al.*, "NLO Electroweak Corrections to Higgs Boson Production at Hadron Colliders", *Phys. Lett.* **B670** (2008) 12–17, `arXiv:0809.1301 [hep-ph]`.

[129] C. Anastasiou *et al.*, "Mixed QCD-electroweak corrections to Higgs boson production in gluon fusion", *JHEP* **04** (2009) 003, `arXiv:0811.3458 [hep-ph]`.

[130] M. Ciccolini *et al.*, "Strong and electroweak corrections to the production of Higgs + 2jets via weak interactions at the LHC", *Phys. Rev. Lett.* **99** (2007) 161803, `arXiv:0707.0381 [hep-ph]`.

[131] M. Ciccolini *et al.*, "Electroweak and QCD corrections to Higgs production via vector-boson fusion at the LHC", *Phys. Rev.* **D77** (2008) 013002, `arXiv:0710.4749 [hep-ph]`.

[132] P. Bolzoni *et al.*, "Higgs production via vector-boson fusion at NNLO in QCD", *Phys. Rev. Lett.* **105** (2010) 011801, `arXiv:1003.4451 [hep-ph]`.

[133] J. Alwall *et al.*, "The automated computation of tree-level and next-to-leading order differential cross sections, and their matching to parton shower simulations", *JHEP* **07** (2014) 079, `arXiv:1405.0301 [hep-ph]`.

[134] R. Frederix and S. Frixione, "Merging meets matching in MC@NLO", *JHEP* **12** (2012) 061, `arXiv:1209.6215 [hep-ph]`.

[135] J. Bellm *et al.*, "Herwig 7.0/Herwig++ 3.0 release note", *Eur. Phys. J.* **C76** no. 4, (2016) 196, `arXiv:1512.01178 [hep-ph]`.

[136] T. Han and S. Willenbrock, "QCD correction to the p p $\rightarrow$ W H and Z H total cross-sections", *Phys. Lett.* **B273** (1991) 167–172.

[137] O. Brein *et al.*, "NNLO QCD corrections to the Higgs-strahlung processes at hadron colliders", *Phys. Lett.* **B579** (2004) 149–156, `arXiv:hep-ph/0307206 [hep-ph]`.

[138] M. L. Ciccolini *et al.*, "Electroweak radiative corrections to associated WH and ZH production at hadron colliders", *Phys. Rev.* **D68** (2003) 073003, `arXiv:hep-ph/0306234 [hep-ph]`.

[139] G. Luisoni and other, "$HW^{\pm}$/HZ + 0 and 1 jet at NLO with the POWHEG BOX interfaced to GoSam and their merging within MiNLO", *JHEP* **10** (2013) 083, `arXiv:1306.2542 [hep-ph]`.

[140] F. Cascioli *et al.*, "Precise Higgs-background predictions: merging NLO QCD and squared quark-loop corrections to four-lepton + 0,1 jet production", *JHEP* **01** (2014) 046, `arXiv:1309.0500 [hep-ph]`.

[141] T. Gleisberg *et al.*, "Event generation with SHERPA 1.1", *Journal of High Energy Physics* **2009** no. 02, (2009) 007. `http://stacks.iop.org/1126-6708/2009/i=02/a=007`.

[142] T. Gleisberg and S. Hoeche, "Comix, a new matrix element generator", *JHEP* **12** (2008) 039, `arXiv:0808.3674 [hep-ph]`.

[143] **NNPDF**, R. D. Ball *et al.*, "Parton distributions for the LHC Run II", *JHEP* **04** (2015) 040, `arXiv:1410.8849 [hep-ph]`.

[144] S. Schumann and F. Krauss, "A Parton shower algorithm based on Catani-Seymour dipole factorisation", *JHEP* **03** (2008) 038, `arXiv:0709.1027 [hep-ph]`.

[145] S. Hoeche *et al.*, "QCD matrix elements + parton showers: The NLO case", *JHEP* **04** (2013) 027, `arXiv:1207.5030 [hep-ph]`.

[146] F. Caola *et al.*, "QCD corrections to W^+W^- production through gluon fusion", *Phys. Lett.* **B754** (2016) 275–280, `arXiv:1511.08617 [hep-ph]`.

[147] H.-L. Lai *et al.*, "New parton distributions for collider physics", *Phys. Rev. D* **82** (Oct, 2010) 074024. `https://link.aps.org/doi/10.1103/PhysRevD.82.074024`.

[148] S. Hoeche *et al.*, "Hard photon production and matrix-element parton-shower merging", *Phys. Rev.* **D81** (2010) 034026, `arXiv:0912.3501 [hep-ph]`.

[149] M. Czakon *et al.*, "Total Top-Quark Pair-Production Cross Section at Hadron Colliders Through $\mathcal{O}(\alpha_s^4)$", *Phys. Rev. Lett.* **110** (2013) 252004, `arXiv:1303.6254 [hep-ph]`.

[150] S. Frixione *et al.*, "A Positive-weight next-to-leading-order Monte Carlo for heavy flavour hadroproduction", *JHEP* **09** (2007) 126, `arXiv:0707.3088 [hep-ph]`.

[151] E. Re, "Single-top Wt-channel production matched with parton showers using the POWHEG method", *Eur. Phys. J.* **C71** (2011) 1547, `arXiv:1009.2450 [hep-ph]`.

[152] T. Sjöstrand *et al.*, "PYTHIA 6.4 physics and manual", *Journal of High Energy Physics* **2006** no. 05, (2006) 026. `http://stacks.iop.org/1126-6708/2006/i=05/a=026`.

[153] K. Melnikov and F. Petriello, "Electroweak gauge boson production at hadron colliders through $\mathcal{O}(\alpha(s)^2)$", *Phys. Rev.* **D74** (2006) 114017, `arXiv:hep-ph/0609070 [hep-ph]`.

[154] C. Anastasiou *et al.*, "High precision QCD at hadron colliders: Electroweak gauge boson rapidity distributions at NNLO", *Phys. Rev.* **D69** (2004) 094008, arXiv:hep-ph/0312266 [hep-ph].

[155] S. Alioli *et al.*, "NLO vector-boson production matched with shower in POWHEG", *JHEP* **07** (2008) 060, arXiv:0805.4802 [hep-ph].

[156] M. L. Mangano *et al.*, "ALPGEN, a generator for hard multiparton processes in hadronic collisions", *Journal of High Energy Physics* **2003** no. 07, (2003) 001. http://stacks.iop.org/1126-6708/2003/i=07/a=001.

[157] J. Pumplin *et al.*, "New Generation of Parton Distributions with Uncertainties from Global QCD Analysis", *Journal of High Energy Physics* **2002** no. 07, (2002) 012. http://stacks.iop.org/1126-6708/2002/i=07/a=012.

[158] T. Plehn *et al.*, "A Method for identifying $H \to \tau^+\tau^- \to e^\pm\mu^\mp p_T$ at the CERN LHC", *Phys. Rev.* **D61** (2000) 093005, arXiv:hep-ph/9911385 [hep-ph].

[159] **ATLAS Collaboration**, "Luminosity determination in pp collisions at $\sqrt{s} = 13$ TeV using the ATLAS detector at the LHC", ATLAS-CONF-2019-021, CERN, Geneva, Jun, 2019. http://cds.cern.ch/record/2677054.

[160] **LHC Higgs cross section working group**, "WG1 ggF subgroup meeting: uncertainties in kinematic regions", Tech. Rep., 2017. https://indico.cern.ch/event/618048/.

[161] G. Luisoni and S. Marzani, "QCD resummation for hadronic final states", *J. Phys.* **G42** no. 10, (2015) 103101, arXiv:1505.04084 [hep-ph].

[162] P. E. L. Rakow and B. R. Webber, "Noncollinearity of Jets in Quantum Chromodynamics", *Phys. Rev. Lett.* **43** (Dec, 1979) 1695–1697. https://link.aps.org/doi/10.1103/PhysRevLett.43.1695.

[163] I. W. Stewart and F. J. Tackmann, "Theory Uncertainties for Higgs and Other Searches Using Jet Bins", *Phys. Rev.* **D85** (2012) 034011, arXiv:1107.2117 [hep-ph].

[164] L. A. Harland-Lang and other, "Parton distributions in the LHC era: MMHT 2014 PDFs", *Eur. Phys. J.* **C75** no. 5, (2015) 204, arXiv:1412.3989 [hep-ph].

[165] S. Catani *et al.*, "QCD matrix elements + parton showers", *JHEP* **11** (2001) 063, arXiv:hep-ph/0109231 [hep-ph].

[166] F. Krauss, "Matrix elements and parton showers in hadronic interactions", *JHEP* **08** (2002) 015, arXiv:hep-ph/0205283 [hep-ph].

[167] S. Dulat *et al.*, "New parton distribution functions from a global analysis of quantum chromodynamics", *Phys. Rev.* **D93** no. 3, (2016) 033006, `arXiv:1506.07443 [hep-ph]`.

[168] T. Melia *et al.*, "Gluon Fusion contribution to W^+W^-+jet production", *JHEP* **08** (2012) 115, `arXiv:1205.6987 [hep-ph]`.

[169] S. Frixione *et al.*, "Single-top hadroproduction in association with a W boson", *JHEP* **07** (2008) 029, `arXiv:0805.3067 [hep-ph]`.

[170] A. D. Martin *et al.*, "Parton distributions for the LHC", *Eur. Phys. J.* **C63** (2009) 189–285, `arXiv:0901.0002 [hep-ph]`.

[171] T. Gehrmann *et al.*, "W^+W^- Production at Hadron Colliders in Next to Next to Leading Order QCD", *Phys. Rev. Lett.* **113** no. 21, (2014) 212001, `arXiv:1408.5243 [hep-ph]`.

[172] M. Grazzini *et al.*, "W^+W^- production at the LHC: fiducial cross sections and distributions in NNLO QCD", *JHEP* **08** (2016) 140, `arXiv:1605.02716 [hep-ph]`.

[173] **CMS Collaboration**, "Measurements of properties of the Higgs boson decaying to a W boson pair in pp collisions at s=13TeV", *Physics Letters B* **791** (2019) 96 – 129. `http://www.sciencedirect.com/science/article/pii/S0370269319301169`.

[174] "European Strategy for Particle Physics Update 2018-2020." `http://europeanstrategyupdate.web.cern.ch/`.

[175] **ATLAS Collaboration**, "Projections for measurements of Higgs boson cross sections, branching ratios, coupling parameters and mass with the ATLAS detector at the HL-LHC", Tech. Rep., CERN, Geneva, Dec, 2018. `http://cds.cern.ch/record/2652762`.

[176] **CMS Collaboration, ATLAS Collaboration**, "Report on the Physics at the HL-LHC and Perspectives for the HE-LHC", Tech. Rep., CERN, Geneva, 2019. `https://cds.cern.ch/record/2651134`. Presented at "The HL/HE-LHC Physics Workshop: final jamboree, 1 March 2019".

[177] **ATLAS Collaboration**, "Expected performance of the ATLAS detector at the High-Luminosity LHC", ATL-PHYS-PUB-2019-005, CERN, Geneva, Jan, 2019. `http://cds.cern.ch/record/2655304`.

[178] **HL/HE WG2 group**, M. Cepeda *et al.*, "Higgs Physics at the HL-LHC and HE-LHC", `arXiv:1902.00134 [hep-ph]`.

[179] **ATLAS Collaboration**, "Measurements of Higgs boson properties in the diphoton decay channel using 80 fb^{-1} of *pp* collision data at $\sqrt{s} = 13$ TeV with the ATLAS detector", ATLAS-CONF-2018-028, CERN, Geneva, Jul, 2018. `https://cds.cern.ch/record/2628771`.

[180] **HEP Software Foundation**, J. Albrecht *et al.*, "A Roadmap for HEP Software and Computing R&D for the 2020s", *Comput. Softw. Big Sci.* **3** no. 1, (2019) 7, `arXiv:1712.06982 [physics.comp-ph]`.

[181] L. Lista, "The bias of the unbiased estimator: A study of the iterative application of the BLUE method", *Nuclear Instruments and Methods in Physics Research Section A: Accelerators, Spectrometers, Detectors and Associated Equipment* **764** (2014) 82 – 93. `http://www.sciencedirect.com/science/article/pii/S0168900214008638`.

[182] L. Lista, "Corrigendum to "The bias of the unbiased estimator: A study of the iterative application of the BLUE method" [Nuclear Instruments and Methods in Physics Research Section A 764 (2014) 82–93]", *Nuclear Instruments and Methods in Physics Research Section A: Accelerators, Spectrometers, Detectors and Associated Equipment* **773** (2015) 87 – 96. `http://www.sciencedirect.com/science/article/pii/S0168900214013424`.

[183] A. Valassi, "Combining correlated measurements of several different physical quantities", *Nuclear Instruments and Methods in Physics Research Section A: Accelerators, Spectrometers, Detectors and Associated Equipment* **500** no. 1, (2003) 391 – 405. `http://www.sciencedirect.com/science/article/pii/S0168900203003292`. NIMA Vol 500.

[184] **ATLAS Collaboration**, "Measurements of the Higgs boson production, fiducial and differential cross sections in the 4ℓ decay channel at $\sqrt{s} = 13$ TeV with the ATLAS detector", ATLAS-CONF-2018-018, CERN, Geneva, Jun, 2018. `https://cds.cern.ch/record/2621479`.

[185] **ATLAS Collaboration**, "Cross-section measurements of the Higgs boson decaying into a pair of τ-leptons in proton-proton collisions at $\sqrt{s} = 13$ TeV with the ATLAS detector", *Phys. Rev.* **D99** (2019) 072001, `arXiv:1811.08856 [hep-ex]`.

[186] **ATLAS Collaboration**, "Search for the standard model Higgs boson produced in association with top quarks and decaying into a $b\bar{b}$ pair in pp collisions at $\sqrt{s} = 13$ TeV with the ATLAS detector", *Phys. Rev. D* **97** (Apr, 2018) 072016. `https://link.aps.org/doi/10.1103/PhysRevD.97.072016`.

[187] **ATLAS Collaboration**, "Evidence for the associated production of the Higgs boson and a top quark pair with the ATLAS detector", *Phys. Rev. D* **97** (Apr, 2018) 072003. `https://link.aps.org/doi/10.1103/PhysRevD.97.072003`.

[188] **ATLAS Collaboration**, "A search for the rare decay of the Standard Model Higgs boson to dimuons in *pp* collisions at $\sqrt{s} = 13$ TeV with the ATLAS Detector", ATLAS-CONF-2018-026, CERN, Geneva, Jul, 2018. https://cds.cern.ch/record/2628763.

[189] **ATLAS Collaboration**, "Searches for the Zγ decay mode of the Higgs boson and for new high-mass resonances in pp collisions at $\sqrt{s} = 13$ TeV with the ATLAS detector", *Journal of High Energy Physics* **2017** no. 10, (Oct, 2017) 112. https://doi.org/10.1007/JHEP10(2017)112.

[190] **ATLAS Collaboration**, "Combined measurements of Higgs boson production and decay using up to 80 fb^{-1} of proton-proton collision data at $\sqrt{s} = 13$ TeV collected with the ATLAS experiment", ATLAS-CONF-2018-031, CERN, Geneva, Jul, 2018. https://cds.cern.ch/record/2629412.

[191] **ATLAS Collaboration, CMS Collaboration**, "Measurements of the Higgs boson production and decay rates and constraints on its couplings from a combined ATLAS and CMS analysis of the LHC pp collision data at $\sqrt{s} = 7$ and 8 TeV", *JHEP* **08** (2016) 045, arXiv:1606.02266 [hep-ex].

[192] **ATLAS Collaboration**, "Combined measurements of Higgs boson production and decay using up to 80 fb^{-1} of proton-proton collision data at $\sqrt{s} = 13$ TeV collected with the ATLAS experiment", arXiv:1909.02845 [hep-ex].

[193] I. Brivio, Y. Jiang, and M. Trott, "The SMEFTsim package, theory and tools", *JHEP* **12** (2017) 070, arXiv:1709.06492 [hep-ph].